Control-Oriented Modelling of an Integrated Attitude and Vibration Suppression Architecture for Large Space Structures

A PhD Dissertation
Submitted in Partial Fulfilment of the Requirements for the Degree of

Doctor of Philosophy

In Aeronautical and Space Engineering

Authored by

Federica Angeletti

Supervised by

Prof. Paolo Gasbarri

Co-advised by

Prof. Fabio Celani

XXXIII Cycle
2018-2020

Department of Mechanical and Aerospace Engineering (DIMA)
Sapienza University of Rome

Sapienza
Università di Roma

TABLE OF CONTENTS

ABSTRACT

This thesis is divided into two parts. The main focus of the research, namely active vibration control for large flexible spacecraft, is exposed in *Part I* and, in parallel, the topic of machine learning techniques for modern space applications is described in *Part II*. In particular, this thesis aims at proposing an end-to-end general architecture for an integrated attitude-vibration control system, starting from the design of structural models to the synthesis of the control laws. To this purpose, large space structures based on realistic missions are investigated as study cases, in accordance with the tendency of increasing the size of the scientific instruments to improve their sensitivity, being the drawback an increase of its overall flexibility. An active control method is therefore investigated to guarantee satisfactory pointing and maximum deformation by avoiding classical stiffening methods. Therefore, the instrument is designed to be supported by an active deployable frame hosting an optimal minimum set of collocated smart actuators and sensors. Different spatial configurations for the placement of the distributed network of active devices are investigated, both at closed-loop and open-loop levels. Concerning closed-loop techniques, a method to optimally place the poles of the system via a Direct Velocity Feedback (DVF) controller is proposed to identify simultaneously the location and number of active devices for vibration control with an in-cascade optimization technique. Then, two general and computationally efficient open-loop placement techniques, namely Gramian and Modal Strain Energy (MSE)-based methods, are adopted as opposed to heuristic algorithms, which imply high computational costs and are generally not suitable for high-dimensional systems, to propose a placement architecture for generically shaped tridimensional space structures. Then, an integrated robust control architecture for the spacecraft is presented as composed of both an attitude control scheme and a vibration control system. To conclude the study, attitude manoeuvres are performed to excite main flexible modes and prove the efficacy of both attitude and vibration control architectures. Moreover, *Part II* is dedicated to address the problem of improving autonomy and self-awareness of modern spacecraft, by using machine-learning based techniques to carry out Failure Identification for large space structures and improving the pointing performance of spacecraft (both flexible satellite with sloshing models and small rigid platforms) when performing repetitive Earth Observation manoeuvres.

LIST OF FIGURES

LIST OF TABLES

Chapter 1
INTRODUCTION

This thesis mainly focuses on the design of a general architecture for the implementation of a distributed active vibration control system on different types of Large Space Structures (LSSs), starting from the design of the flexible appendages, addressing the problem of optimal placement of a network of actuators/sensors for vibration suppression, developing an integrated simulation environment and finally testing related control strategies. Eventually, a second macro area is researched, which involves the application of machine learning-based strategies to modern satellite problems, such as damage identification on large flexible structures and attitude control in repetitive re-orientation manoeuvres. In this Chapter, the framework of the research activities is presented in Sec. 1.1 and the main contents of the thesis are highlighted in Sec. 1.2.

1.1 THESIS CONTEXT

Lately, the tendency of implementing large structures on in-orbit spacecraft while, at the same time, narrowing their performance requirements has significantly affected space activities. Therefore, investigating methods aimed at coping with the interaction between platform control and system flexible dynamics is a topic of current interest. The Control/Structure Interaction (CSI) can arise in various situations, thus leading to a relevant deterioration of on-orbit performance: in-flight instability phenomena and even failure of the mission are undesired potential scenarios. Both latter and former have concerned

telecommunication missions, with loss of operations time and achievable data. Hence, satellites equipped with wide lightweight flexible elements, as hoop reflector antennas, booms and long masts, call for the capacity of performing fast and precise manoeuvres without losing a strict control over flexible parts. However, spacecraft equipped with such highly flexible appendages are generally characterized by closely spaced low structural modes and overlapping bandwidth, which could interfere with the bandwidth of the attitude controller. Consequently, considering the CSI problem when designing satellites control systems is of paramount importance.

Current studies and on-going projects involving large flexible appendages share strict pointing, guidance and instruments requirements, such as not crossing the limit of maximum displacement in some points of the structure, avoiding coupling low Attitude and Orbital Control System (AOCS) bandwidth with very low structural frequencies, guaranteeing AKE (Absolute Knowledge Error) and APE (Absolute Pointing Error) constraints are met with enough margin. Moreover, a wide variety of an Earth Observation (EO) spacecraft is currently using and will profit by large antenna systems supported by masts or beam-like structures with low stiffness. To cite some of them, SWOT (Surface Water Ocean Topography) is an ocean altimetry and hydrography mission jointly developed by NASA and CNES expected to be launched in 2021. The main satellite objective is to realize the first global survey of the Earth's surface water. Two radar antennae are positioned at either end of a 10-meter mast to measure the elevation of the surface and two gyroscopes are mounted in the payload, so to observe the mast oscillations and accurately retrieve radar data. This case demonstrates the current need of limiting undesired elastic oscillations to accurately acquire and process scientific information. The Ocean Surface Current Mission (OSCM) is a future mission to direct a mapping of global ocean currents at sub-mesoscale resolution. This spacecraft is a representative case of the SAR (Synthetic Aperture Radar) EO instruments family, to which Italy has widely contributed participating in the realization of Sentinel SAR-type satellites in the frame of Copernicus project. Growing interest is currently being addressed at national level towards EO missions, proved by the establishment of the Italian National User Forum to share satellite observation data to all core services, from civil protection to agriculture. To effectively taking advantage of in-orbit data, the new SAR-equipped satellites shall satisfy improved performance requirements, as enhanced platform stability and extremely accurate precision (micrometer) for length and position of the

antennae phase centers. As for that, intensive thermal and mechanical testing are often required to demonstrate the antenna displacements are actually lower than the imposed limit. In this context, the future European BIOMASS mission will be carrying a P-band mesh reflector also developed by U.S. companies. In detail, a deployable mesh reflector is an antenna instrument characterized by a circular truss-based platform supporting a large parabolic reflective surface, usually with diameter higher than 6 meters. The Soil Moisture Active Passive (SMAP) mission, accoutred with the patented Astromesh® reflector, developed by NASA and Northrop Grumman, is the typical example of such an EO system. It was launched in 2015 to measure the amount of water in the top layer of soil. In particular, the technology needed to realize a flight-ready antenna is mainly prerogative of U.S. industry. Therefore, the LEA (Large European Antenna) Horizon 2020 project aims towards European non-dependence in large deployable reflectors. The awarded consortium will develop a 6 m deployable antenna prototype, ready to be launched from 2021. This tender endorses the vivid interest in studying innovative solutions to improve European capabilities in the field of space antenna systems. Furthermore, in the frame of the Copernicus program many satellites with different Earth observation purposes (radar, hyperspectral) already have configurations that, in Low-Earth Orbit (LEO), might experience control/structure interaction, either because of their instrument or solar arrays. Indeed, the already available Copernicus space segment (the sentinel satellites series) and the Copernicus space segment evolution (CHIME, ROSE-L) will make use of a wide variety of instruments (optics, SAR, multispectral) with configurations often including large flexible solar arrays. In this perspective, to minimize the problem of undesired vibrations affecting the precision of the aforementioned scientific instruments, the GNC design calls either for a very expensive baseline with high-precision sensors both at platform and distributed level or a system contemplating active control of the flexible structure to ensure acceptable deformations. However, according to the current state-of-the-art for already flown missions, the payloads supporting structures are manufactured by using passive materials. Hence, the second solution represents still an open and challenging research field.

From a control point of view, in recent years, advancements in counteracting CSI led to a significant increase of spacecraft reliability and operative life in modern space missions. Be it as it may, there exist a lack in alternative solutions other than classical suppression by feedback control system of the main rigid platform implemented on flown space mission. According to the current state of

the art, most widely used techniques are single loop frequency design methods, in particular a PID control for the rigid platform coupled with filters to eliminate resonant peaks of predominant elastic modes. Moreover, frequency separation techniques are used to ensure the control system bandwidth is well separated from the first fundamental frequency of the flexible appendage, yet increasing the mass and stiffness of the part in the design process. An effective alternative solution could consist in actively rigidizing flexible appendages by implementing a network of smart actuators/sensors to counteract undesired elastic vibrations. Indeed, most of current space missions, large antennas are supported by passive Extendable Supporting Structures (ESSs), thus unable to react to disturbances originated from platform operations and environmental perturbations. In more detail, in this thesis the attention has been focused on a specific kind of actuators, i.e. linear piezo-electric stacks, where a small physical expansion along their length occurs when applying a voltage potential. This actuators category is currently available on the international market as devices to be used both in vacuum and extreme temperatures, thus representing a viable solution to address the problem of vibration control of such large space structures.

Concerning the second macro area treated in this thesis, the improvement of spacecraft autonomy is one of the major research areas related to future space missions. Nowadays, the possibility to interact with in-orbit satellite is limited by several factors, as availability and state of the connection to the ground station, power budgets, communication latency. Moreover, modern missions – especially those devoted to Earth Observation tasks - rely on downlinking to the ground a huge amount of scientific and telemetry data in limited time windows. Therefore, achieving a certain level of autonomy for on-board operations will be crucial to foster the development of space activities in the next decades. Indeed, it has been proven - by several studies by space agencies and companies worldwide - that introducing in space missions' autonomous systems leads to a relevant increase of operations efficiency, in terms of reliability and required efforts. Hence, there exists a current need to make the spacecraft more self-aware and autonomous. Both such aspects are addressed in this thesis.

The first one is investigated by proposing an architecture based on Deep Learning to make the satellite aware of possible failures in its appendages at structural level. At present, on-board detection capabilities are being investigated to the purpose of allowing a prompt response to damage or emergency situation

which may compromise mission performance. At the same time, a rapid autonomous on-board identification of structural damages or not nominal operations - on instruments such as antennas and telescopes - could help in discarding specific batch of data, so to avoid processing the traditionally huge amount of telemetry and scientific data downlinked to the ground. Moreover, growing interest is currently being reserved to emerging technologies enabling future space maintenance missions. In this perspective, assessing the current status of a spacecraft could assist in the selection of suitable/convenient spacecraft candidates for repairing.

The second aspect is addressed by introducing a computationally efficient method (suitable to be implemented also on small platforms as CubeSats, as opposed to traditional machine learning solutions) aiming at improving the tracking performance for repetitive attitude manoeuvres, typical for Earth Observation missions. In this scenario, spacecraft are often called to perform iterative re-orientation profiles to acquire scientific data of specific terrestrial areas, with the same inclination and light conditions. Therefore, they can be considered as periodically actuated dynamic system, affected by periodic disturbances, such as flexibility, sloshing and orbital generalized forces. A convenient algorithm can then be applied to learn from data collected from past orbits to improve spacecraft attitude tracking performance for the next observation tasks, based on generally available measurements, such as attitude and rates.

1.2 THESIS OVERVIEW AND MAIN CONTRIBUTIONS

This thesis is divided into two parts. In detail, *Part I* focuses on the problem of active vibration suppression for a spacecraft equipped with very large flexible structures. This research aims at proposing an end-to-end general architecture for an integrated attitude-vibration control system, from the design of structural models to the synthesis and testing of the control laws on an in-orbit simulation environment. *Part II* addresses the problem of improving spacecraft awareness and autonomy, by paying attention to two specific issues of modern space activities.

Chapter 2 is devoted to a literature review inherent to the subjects covered in *Part I*. Indeed, the section introduces the research domain related to the control of

large space structures, by providing background about the state-of-the-art of both attitude and vibration control system architectures. Moreover, it identifies prospective flexible payload candidates from real missions to test the proposed control strategy.

Chapter 3 recalls the mathematical instruments needed to address the themes discussed throughout the research. In more details, it provides mechanical models for modelling star-like (one central hub and different appendages) assembled flexible structures and piezoelectric substructures, while describing main concepts of non-linear mechanics and flexible dynamics for an in-orbit flexible spacecraft. In particular, a mass/inertia formulation available in literature is extended to take into consideration the presence of a distributed vibration control system when assembling the substructures. Finally, a linearized model to be deployed in most common control design frameworks is presented.

Chapter 4 and *Chapter 5* address the theme of optimal placement of a network of smart actuators and sensors required to guarantee high precision pointing and limit maximum deformation of the flexible structures. Different spatial configurations are investigated according to two different approaches: *closed loop* and *open loop* placement. More thoroughly, Chapter 4 examines the optimal placement of piezoelectric actuators in closed loop by using pole placement techniques, by testing different optimization algorithms. Among them, a Reinforcement Learning algorithm is tested to search the best configuration for the devices. In this regard, an approach is proposed to perform in-cascade optimizations to identify at the same time both the location and the gain of the Direct Velocity Feedback (DVF) active vibration controller. The robustness of the final configuration to damage and failure of the devices is tested as well. Conversely, Chapter 5 explores the possibility to apply straightforward and computationally efficient placement strategies, namely Gramian and Modal Strain Energy (MSE)-based methods, as opposed to heuristic algorithms, generally not suitable for high-dimensional systems. In this chapter, the main contribution lies in underlining a general framework to allow a fast and efficient positioning of actuators and sensors by using two parallel methods for further cross-check and validation. The results obtained by using different schemes are compared and discussed.

Chapter 6 introduces a general framework to synthetize an integrated attitude and vibration control scheme based on $\boldsymbol{\mu}$-synthesis approach. In detail, a strategy

to perform an automatic assembly of different substructures to a central platform is presented and tested by synthetizing a controller on a linear dynamic system, and also applied to a non-linear system to prove its efficacy.

Chapter 7 is dedicated to the development of a simulation environment reproducing the in-orbit behaviour of space structures. Such a tool includes the full non-linear dynamics of the assembled spacecraft, orbit propagation, actuators and sensors non-linear models and attitude and vibration control laws implementation. In this regard, a convenient model of an interface for piezoelectric stack actuators is implemented in Simulink environment and tested by performing different simulations.

Chapter 8 focusses on the application of a machine learning-based algorithms to the solution of issues in modern space activities. In detail, attention has been paid to two main fields: Failure Detection and Identification (FDI) based on Deep Learning (DL) and Iterative Learning Control (ILC) scheme to perform attitude manoeuvres for both large and small satellite. In the first case, a Long Short-Term Memory (LSTM) Neural Network, state of the art of the current DL methods, is trained to classify possible failures in large space flexible structure at local level. The second subject aims at using a computationally efficient strategy, suitable to be run on-board satellites, also on small platform as CubeSats, to improve their pointing performance when required to perform repetitive attitude re-orientation manoeuvres for Earth Observation (EO) missions.

Finally, the last part of the thesis, consisting of the *Conclusions* chapter is devoted to discussing and resuming the main achieved results, to propose some additional considerations and to provide comments for future investigations in the field. Also, the section *Appendix* supplements the thesis by including more in-depth information about the developed mathematical models.

Part I

Chapter 2
LITERATURE REVIEW

The study of the Control/Structure Interaction problem may be structured in two major branches: modelling and control of large flexible structures. This chapter focuses on investigating the state-of-the-art of both fields, by highlighting the related main approaches and practical applications. Based on consequently drawn conclusions, this chapter aims at identifying promising models to design and implement an end-to-end architecture for controlling in-orbit structures.

The simultaneous tendency of implementing large structures on spacecraft and narrowing performance requirements has significantly affected space activities lately. Thus, a consistent investigation aimed at coping with the interaction between platform control and flexible dynamics of the system is currently needed. The Control/Structure Interaction (CSI) can arise in various situations, thus entailing a deterioration of in-orbit performance of space systems [1][2]. In recent years, advancements in counteracting CSI have led to a significant increase of spacecraft reliability and operative life in modern space missions.

2.1 FLEXIBLE SPACE SYSTEMS

The first section of this literature review aims at providing an overview of the structural designs that have been conceived to build-up large appendages for several space missions, at both simulation and test levels. According to [3], a Large Space Structure (LSS) can be defined as a "structure in space which consists of a large number of structural elements configured in such a way to provide a space platform for on-going scientific payloads". Generally, such a structure is highly

flexible and may have a large number of controlled structural modes when subjected to narrow mission requirements. Large Space Structures (LSSs) are mainly deployable, as the launchers' fairings dimensions are a major constraint in the spacecraft design. Many reviews concerning deployable structures can be found in literature [4][5][6]. Nevertheless, according to G.E. Fenci and N.G. Currie from the University of Salford [7] it is evident that an up-to-date complete survey on this topic is currently lacking, being the latest but not the most comprehensive review by R. Andover dating back to 2015 [8]. However, the most detailed classification seems to have been presented by Hanaor and Levy in 2011 [9], thus omitting the cutting-edge technologies that have been developed in recent years. This section will be based on the aforementioned reviews, yet it will be focussed in particular on those deployable structures that find applications in present space missions and related research studies. Thus, the broad classification criteria used by Pellegrino in [4] will be taken as a reference in this thesis and will be further extended by referring to recent literature since the review does not mention recent fundamental deployable as tensegrities, for instance. An overview of several contemplated categories is reported in Fig. 2-1.

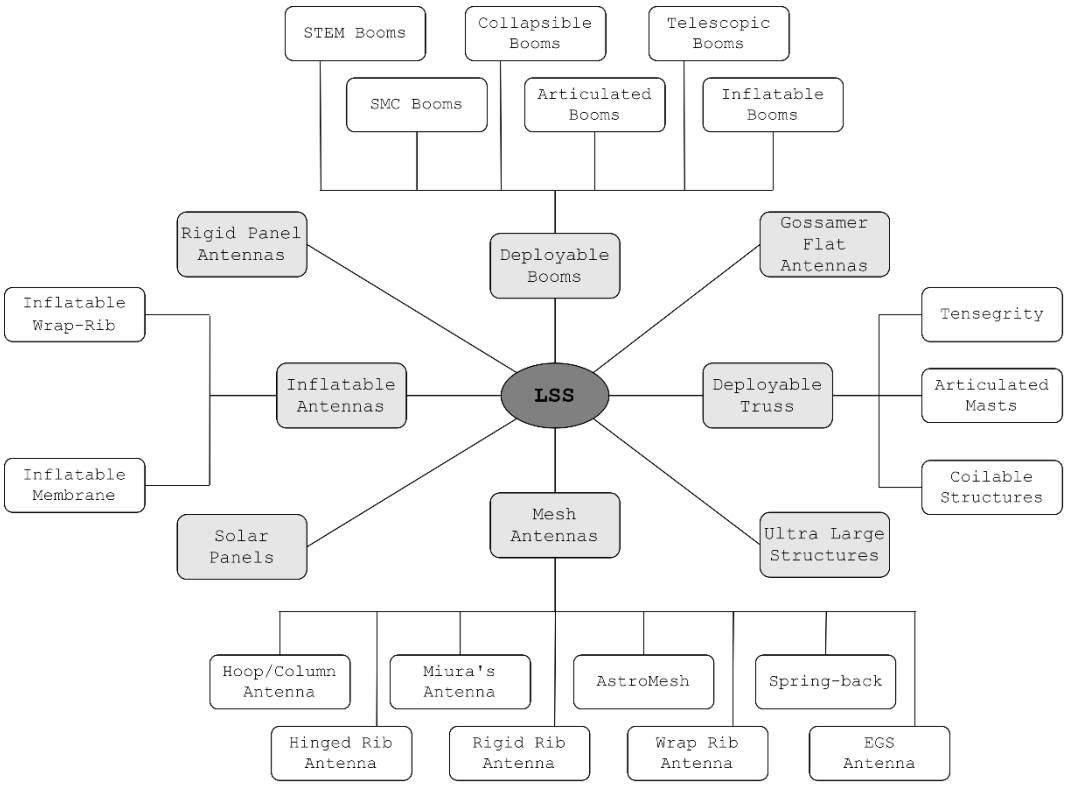

Fig. 2-1: Broad classification of LSS concepts

Flexible space appendages are here summarized in eight main classes, namely Deployable Booms, Gossamer Flat Antennas, Deployable Trusses, Mesh Antennas, Rigid Panels Antennas, Inflatables Antennas, Solar Panels and Ultra Large Structures. Some information on each class will be presented hereafter.

Deployable Booms surely represent a wide class of space extendable structures. Also referring to the review written by Puig et al. [10], a possible classification is presented in Fig. 2-1. *Inflatable booms* have been mainly adopted as solutions to deploy light structures (typically membranes under 10 kg) and have relatively low deployment accuracy and post-deployment stability. On the other hand, they are extremely lightweight with a very high packaging ratio. The concept of inflatable structures was used by NASA scientists for the 28m long booms of the Inflatable Antenna Experiment on-board SPARTAN satellite in 1996 (see Fig. 2-2). Conversely, *Telescopic Booms* are typically much stiffer and stable than most other deployable solutions, but they are much heavier and have a low packaging ratio. However, recent solutions, as Astro Aerospace's Telescopic Tube Mast (TTM) by Northrop-Grumman, may guarantee a stiff and yet lightweight solution, fully retractable on-orbit for masts up to 34.4m in length, having however a very low first natural frequency of 0.1 Hz [11]. *Shape Memory Composite (SMC) Booms* are already available for deploying solar sails or solar shields. Indeed, they cannot deploy heavy structures and have relatively low pointing accuracy and post-deployment stability [10]. Recently, the DLR developed several versions of Carbon Fiber Reinforced Polymer (CFRP) *Collapsible Tube Masts (CTMs)*, with different scales and applications. In preparation for the deployment of a 20m x 20m solar sail mission (Gossamer-2), DLR tested 14m CFRP CTMs in simulated space and launch environment [12]. *Storable Extendible Tubular Member (STEM)* structures are generally composed of a laminate that can be rolled up flat on a drum and that is able to return to its circular shape on deployment via motors.

Fig. 2-2: Deployment sequence of Inflatable Antenna Experiment (IAE) (image credit: NASA)

Finally, systems as deployable jointed arms, of which the Mobile Servicing System (MSS) (the international space station (ISS) robotic arm, better known as the Canadarm2) is maybe the most famous example, can be described as an *Articulated Boom.* Keeping in line with such concepts, SWOT (Surface Water Ocean Topography, joint venture of NASA's JPL, CNES and TAS-F) spacecraft equips two deployable booms (see Fig. 2-3) for its Ka-Band Radar Interferometer (Karin), being the two antennas placed at the end point of the arms connected to the central hub of the satellite. Novel concepts are also under investigation, as for ATHENA (Advanced Telescope for High Energy Astrophysics) mission in the frame of Cosmic Vision 2015-2025. In particular, three tubular arms, each with two sections and three joints, are stowed on the outside of the service module, extending over the fixed telescope structure.

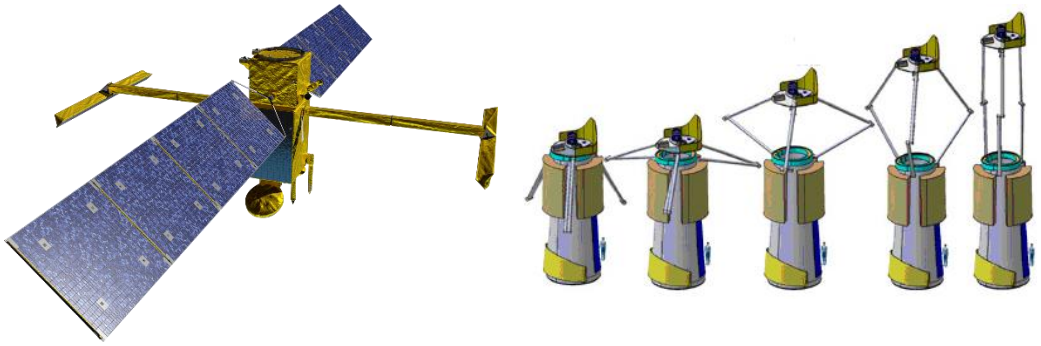

(a) (b)

Fig. 2-3: (a) SWOT spacecraft. Image credits: NASA (b) ATHENA mission. Image credits: ESA

Deployable Truss structures contain a certain number of pinned joints instead of rigid joints to provide several degrees of freedom for storage and deployment of the structure itself. A possible classification is shown in Fig. 2-1. Among them, *Tensegrity* structures use cables instead of conventional struts where only traction forces are applied. Such a solution allows developing light weight masts extending up to several tens of meters. However, tip axial and lateral translation are typically of the order of the centimeter, thus preventing from using this concept for precision deployment systems. Another very common concept for deployable trusses is the *Articulated Masts*: they consist of longerons (vertical members aligned with the longitudinal mast direction), connecting circumferential battens and further supporting diagonals. The NuSTAR mission (2012, [13]) is a famous example of space deployable mast (more than 10-meters long), aiming at centroiding errors of about 50 microns, pointing stability of 80 microns and detection of translation of 25 microns. The *Coilable Mast* technology relies on some

full length longerons that are coiled as springs in the stowed configuration [10]. Indeed, coiling the longerons (by applying an elastic deformation) provides the strain energy necessary for their deployment, while the stiffness and weight can also be selected by modifying the boom's diameter for each specific application. For instance, Northrop-Grumman's AstroMast (see Fig. 2-4) is a coilable mast with a 120° twisted deployed configuration.

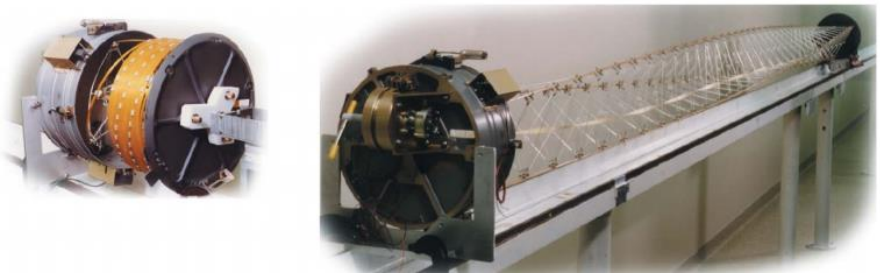

Fig. 2-4: AstroMast in stowed and deployed configuration. Image credits: Northrop-Grumman

In recent years, the original concept of a *Mesh Reflector* [14] has received further modifications to be adapted to current space mission requirements and objectives. Indeed, the idea of a *Miura's Antenna* was selected to be the basic design of the HALCA satellite's antenna, an 8-meter large deployable reflector launched in 1997. Nowadays, growing interest is being addressed to the topic of deployment, shape optimization and control of large mesh reflectors [16]. In this context, Large Space Structure (LSS) UG is currently developing a large deployable reflector (LDR) technology under an ESA project aiming at LDR concepts with sizes up to 18 m diameter [15]. Among mesh-type reflectors, a family of patented perimeter truss deployable mesh reflectors designed by Northrop Grumman's Astro Aerospace is particularly mature concerning design and flight heritage: *AstroMesh*® antennas, which flew on several missions, as THURAYA, INMARSAT and SMAP. Harris Corporation developed the *Rigid Rib Antenna (RRA)* for the NASA Tracking and Data Relay Satellite (TDRS) and NASA Galileo mission to Jupiter. The two antennas are almost identical, with a diameter of 5 m. In particular, the RRA is an umbrella type antenna with 16 parabolic, tubular CFRP ribs attached to a central hub and a reflective mesh between the ribs. The *Wrap-Rib Antenna* is an umbrella-type instrument with a central hub, parabolic CFRP and a reflective mesh, developed at NASA's Jet Propulsion Laboratory (JPL) in the 1970s. The ribs are deployed by cutting a restraining cable placed around the hub. A 9.1 m diameter 60 kg WRA was launched in 1974 on-board the Applications Technology Satellite 6 (ATS-6). Harris Corporation developed the *Hinged-Rib Antenna (HRA)* for the

Asia Cellular Satellite (ACeS) system [17]. In this concept, the ribs are hinged along their length, which produce a smaller height of the stowed package. Currently, Harris is working on a refined version of the HRA, called Advanced Folding Rib Antenna (AFRA), with the same deployed diameter as the ACeS HRA, but with lower mass and smaller stowed diameter and height. Moreover, NASA Langley Research Center (LaRC) and Harris Corporation developed the *Hoop/Column Antenna (HCA)* concept around 1980: a simple tension and compression preloaded structure, where a central column and a large-diameter hoop are the compression members, which maintain pre-tension in a cable network, supporting and shaping the RF reflective mesh surface. A totally different antenna concept, without moveable connections, was developed by the Hughes Space and Communication Company [17]. The *Spring-Back Antenna (SBA)* consists of a thin graphite mesh dish with an integral lattice of ribs and a stiffening hoop along the rim. The folding concept is both simple and effective: since there are no joints or hinges, it is simply folded elastically about a central axis, like a taco shell, as it is also often called. When in orbit, the reflector deploys by cutting the tie cables, which releases its stored elastic strain energy. Such antenna concept is used in NASA's next generation TDRS, where the 5 m diameter RRAs are replaced by 4.6 m diameter SBAs. Another concept is the Russian-Georgian company Energia-GPI-Space *(EGS) Antenna*, consisting of a circular pantograph ring and radial tensioned membrane ribs connecting to a central hub.

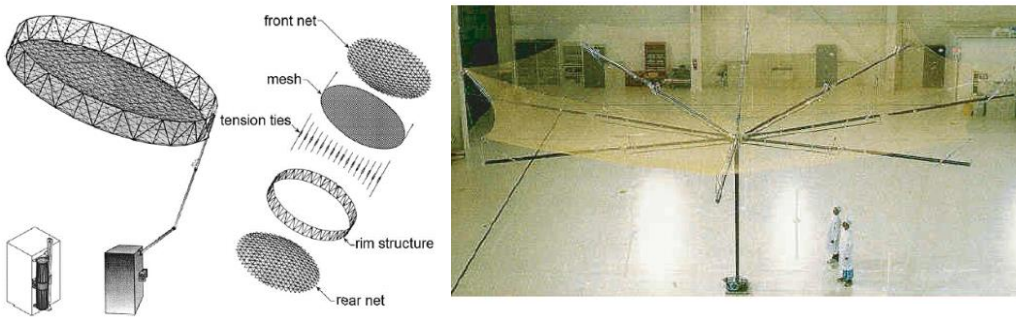

(a) (b)

Fig. 2-5: (a) AstroMesh® design concept (b) HRA design concept [17]

Inflatable Antennas would potentially give the smallest package size and the lowest mass [17]. Generally, they are composed of a thin flexible material which is folded before launch and then deployed by inflation when in-orbit. However, the main drawback of inflatable antennas is the difficulty of achieving high shape accuracy for the reflective surface. *Inflatable Wrap Rib Antenna (IWRA)* is a type of

structure where the inflatable reflector antenna is made of thin film, and the precision of off-set parabolic reflector is maintained by tension tailored CFRP ribs with a central hub and an outer inflatable torus [18]. In space applications, very often the membranes are supported by a frame of *Inflatable Booms*. The concept was studied by NASA's JPL and L'Garde, however the program for inflatable reflectors was abandoned mainly because large thin shell inflatable reflector antennas seem to show a criticality concerning buckling aspects.

(a) (b)

Fig. 2-6: (a) Inflatable membrane antenna [19] (b) DAISY antenna: folded and deployed configurations [21]

Antenna applications operating at frequencies over about 40 GHz require high surface accuracy. Solid material is usually chosen for their reflective surface. A possible concept is the Deployable Antenna Integral System (DAISY) by ESA and Dornier [20]. Here, each panel is connected to the central hub by a revolute joint, which allows the panels to fold by nesting in front of the hub. The truss structure on the back of each panel provides additional stiffness for better surface accuracy. Harris Corp. [22] has recently developed a novel concept called the flexible precision reflector realised in TEMBO © Elastic Memory Composite material. The FPR includes a thin-composite reflector surface that is furled in a pleated fashion, like an umbrella.

Satellite SAR (Synthetic Aperture Radar) Flat Gossamer Antennas are widely applied in Earth Observation missions. Deployable support structures (DSSs) or Extendable Supporting Structures (ESSs) are then key components for supporting and rigidizing such antennas. As known, a progressive improvement in observation resolution requirements can be observed nowadays, and designing high-rigidity, large-scale, and simple-motion ESS has increasingly become necessary. The most famous example of such a concept are RADARSAT-1 and RADARSAT-2 satellites. Although their deployment need only one movement, their single-wing designs can support only two antenna panels, and their large-

scale capacities are poor. In [23], a single-wing design was developed to support four antenna panels, by aiming at a Modular Deployable Truss Structure (MDTS) antenna capable of obtaining a resolution ranging from 0.3 to 1 m, requiring a 28 m long antenna, as depicted in Fig. 2-7.

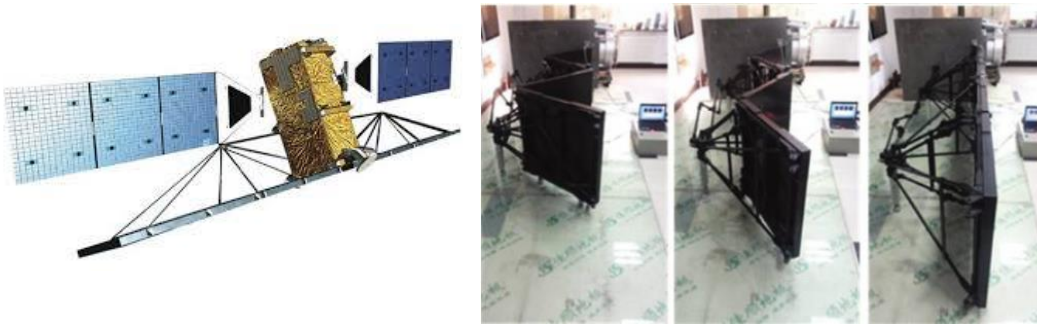

(a) (b)

Fig. 2-7: (a) RADARSAT-2 spacecraft. Image credits: Canadian Space Agency (b) Deployment model of the scaled version of MDTS [23]

Solar panels often have a high degree of flexibility and low natural frequencies, especially in the case of equipment devoted to power-hungry mission that should realize quite large areas to capture solar energy. In these cases, the solar array is usually attached to the main body of the satellite by an axial boom that can be rotated by the Solar Array Drive Mechanism (SADM) and the deployment mechanism provides a self-locking gear to avoid unexpected movements if this is still in working condition.

Ultra Large Structure are theoretical concepts considering the possibility of realizing flexible appendages extending for hundreds of meters. Research is being performed about this class of structures, characterized by very low frequencies and stiffness. However, such an idea has not found an implementation in the real world yet. An example is the academic research carried out at Bejing Institute of Technology [24], where the first fundamental frequency of a 280 m wide deployed solar array is 0.044 Hz, while the one of the 150 m diameter antenna is 0.073 Hz.

2.1.1 CONCLUSIONS

Generally, a lower mass combined with a higher structural stiffness implies a higher first natural frequency of the structure, which is desirable to separate the structural and attitude control system frequencies, as in the case of EGS

Pantograph Antenna (first frequency of about 17 Hz). However, as can be deducted by observing the data reported in Fig. 2.8, in general the first fundamental frequency of large space antennas is below 1 Hz, the lower values for the very large antenna systems. Concerning flat SAR antennas, the introduction in the structural configuration of a backbone structure (named before as ESS) has led to a relevant stiffening of the system, which is also much heavier, so that the first frequencies of the antenna are generally above 2 Hz. Moreover, there exist other limit cases with first fundamental frequencies much higher than standard antennas, as SWOT payload, with first frequency of above 5 Hz.

In each class of LSS, several different concepts have been proposed throughout years. However, only a limited number of them have proven to be viable and even fewer have actually flown: the most successful concepts from each category are contemplated and summarized in Fig. 2.8 according to their first natural frequency and aperture.

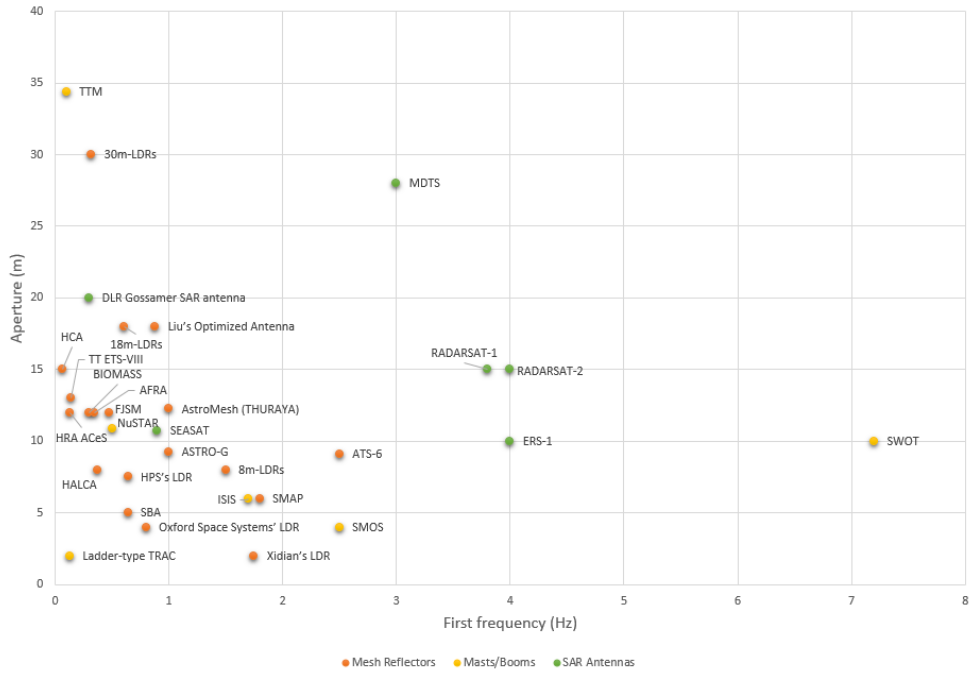

Fig. 2-8: Classification of different LSSs according to their natural frequency and aperture

The available collected data is indeed further partitioned into three groups: Mesh Reflectors, Synthetic Aperture Radar (SAR) antennas and Masts/booms antennas, according to the maturity and flown heritage of the correspondent LSS concept. In general, the larger the aperture of an antenna is, the higher will be its sensitivity

and performance. However, by observing Fig. 2.8, it can be noticed a lack of literature (and experiments) concerning large space antenna models with apertures above 15 meters, and frequency range below 2 Hz. Therefore, a wide prospective research area can be identified for antenna concepts with such a characteristic.

2.2 CONTROL OF FLEXIBLE STRUCTURES

Currently, the domain of space structures control is still a very active research field, due to the continuous development of modern space activities and the consequent evolution of mission needs and requirements. To guarantee better performance, the control laws should take the modifications of the system dynamics related to its flexibility into account [1]. In particular, applications of control of large structures include pointing control, adaptive optics, retargeting of flexible appendages, motion of flexible space manipulators, precision attitude control and vibration control. In this thesis, a particular attention is dedicated to the last two areas.

Generally, during a spacecraft attitude manoeuvre, large space structures are subjected to non-negligible flexible deformations that may generate additional disturbance torques for the attitude control system. In this scenario, and to improve the geometric stability and precision of the structural system, it is of utter importance to design a control system counteracting negative effects originated by Control/Structure Interactions. Typically, space missions involving such an issue are:

- Earth Observation (EO) missions (optical, military, etc.) requiring agile manoeuvres (up to 2°/sec). In general, spacecraft agility is often limited by the tranquilization time, that is the time required for all the perturbed states of the satellite (as flexible oscillations, sloshing, etc.) to be successfully damped out;
- Missions equipping large antennas/radar requiring an accurate and fast retrieving of scientific measurements of ice, ocean, soil, biomass monitoring.

In this context, a possible classification of current methods for controlling LSSs is reported in Fig. 2-9.

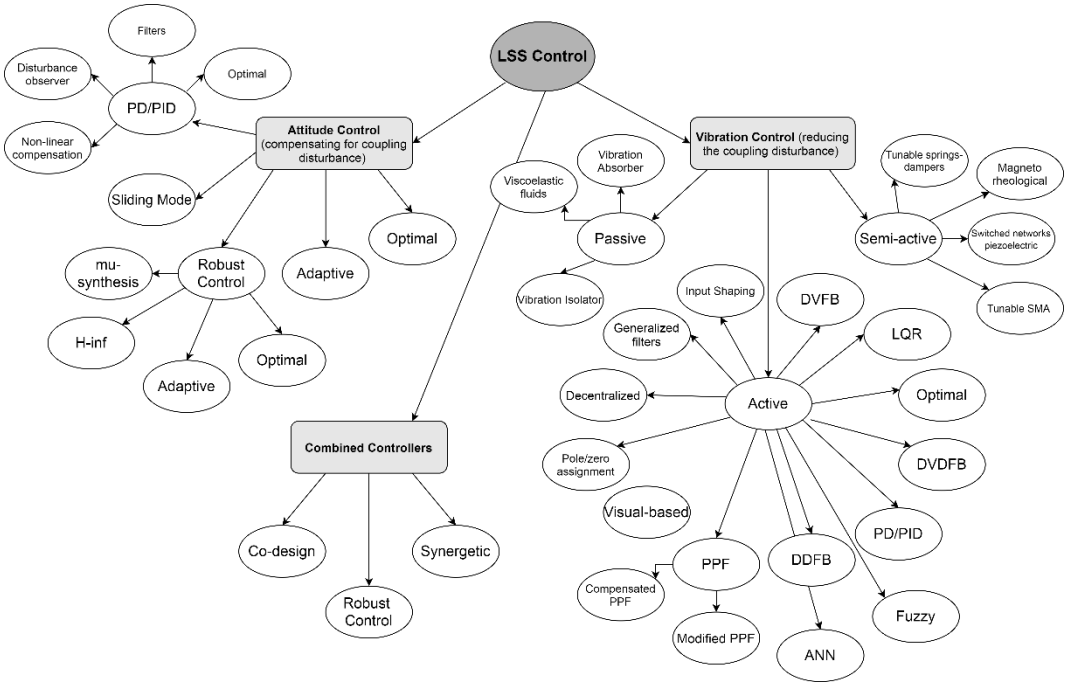

Fig. 2-9: Broad classification of control solutions for LSSs

First, the different strategies are distinguished among *attitude control*, aiming at compensating for disturbances originated by the coupling with the flexible parts of the spacecraft, *vibration control*, whose purpose is to suppress the coupling disturbance, usually in parallel to the attitude control system, and *combined controllers*, taking advantage of both the previous approaches at the same time. In the next section, more details concerning the presented methods will be introduced.

2.2.1 Attitude Control of Flexible Spacecraft

Nowadays, the current standard for CSI management by using only actuators/sensors located at platform level may be summarized in two approaches: *frequencies separation* and *disturbances rejection*. The first method consists in identifying the bandwidth of the dominant flexible modes, and in designing the flexible appendages and the spacecraft motion closed loop such that the control bandwidth is sufficiently separated from the structural one. To cite an example, in SMAP (Soil Moisture Active Passive) mission [25], launched in 2015, the satellite is equipped with a spinning mesh reflector, which sets the first mode of the system. Due to the controller bandwidth and the disturbance sources, frequency

separation is the key to ensure reliable and predictable performance. As for that, the first mode of the Reflector and Boom Assembly (RBA) was required to be higher than 1.45 Hz when attached to the spacecraft in a free-free configuration, giving a decade separation between the observatory first mode and the bandwidth of the spin controller (see Fig. 2-10). Additionally, the RBA was required to have a minimum of 0.2 Hz of separation between its first two modes such that they not interact.

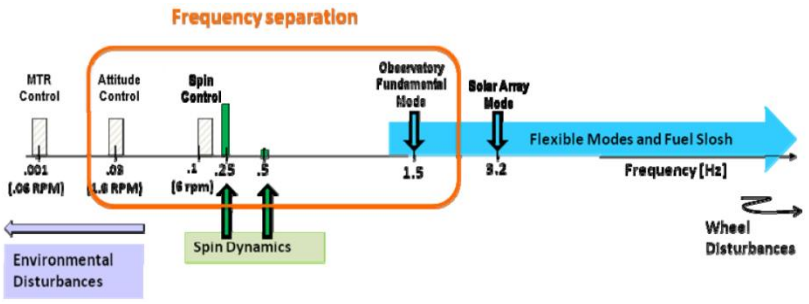

Fig. 2-10: Frequency separation approach for SMAP spacecraft [25]

As far as the second approach is concerned, the flexible phenomena are seen as external disturbances affecting the spacecraft attitude motion. Therefore, the controller may be designed according to robust criteria (i.e. $\boldsymbol{H}_\infty$ theory [26], $\boldsymbol{\mu}$-synthesis methods [27], optimal robust control [28] and adaptive robust control [29] and others) to attenuate the input disturbances in the bandwidth of dominant flexible modes. Another possibility is to couple classical controllers (as Proportional Integrative Derivative (PID) [30], Linear Quadratic Regulators (LQR) [31], adaptive control, and optimal control etc.) with Gain and/or Phase compensation methods to attenuate the flexible modes, by validating the architecture with worst-case analysis techniques. The main idea is to design low-pass and notch filters to suppress the resonant peaks of relevant structural modes. For instance, in the GNC design of BIOMASS satellite [32] the control actions and sensors are collocated at the platform level, thus aiming at reducing the impact of flexible modes on the spacecraft dynamics by implementing proper filters.

However, such approaches, while being mature from a state-of-the-art point of view, are generally characterized by several drawbacks. Indeed, filter tuning procedures, while being intuitive, are often time consuming and there exists no guarantee the multivariable robustness margins are always met. When applying both approaches, an iterative co-design of structural and control parameters is often required to define the final architecture of the spacecraft, thus entailing

relevant computational time and labour efforts, while not ensuring an optimal solution may be always reached. Furthermore, missions requiring very narrow pointing precision, as the NuSTAR spacecraft, which is required to maintain its attitude within 1 arcsec during the observation phase, are expected to have consequently a slow slew speed of about 0.06 deg/sec (= 3.6 deg/min = 50 min for a 180 degrees manoeuvre) [33]. Indeed, Control/Structure Interaction problem also limits torques to be exerted on the spacecraft and imposes narrow restrictions for choosing control algorithms and actuators (namely thrusters and Reaction Wheels, RWs). In most cases, to avoid over-exciting the flexible modes of the structures, thrusters are excluded from the control loop in case of pointing or stabilization attitude manoeuvres, thus limiting de facto the available manoeuvre speed.

2.2.2 VIBRATION CONTROL OF LARGE SPACE STRUCTURES

A different solution consists in including in the design of the overall control system also the equations describing the elastic deformations of the parts of interest, while conceiving a control law able to suppress the flexible vibrations as fast as possible, with eventually the use of distributed control on the structure. Although it may be considered as an independent domain, vibration suppression for large space structures is actually an area fully interconnected to attitude control. Indeed, perturbations impacting flexible appendages are mostly originated by manoeuvres and, at the same time, by reducing unwanted vibrations actively rigidizing the structure, stability and performance of attitude controllers are improved. Vibration reduction can be achieved by adopting different strategies, according to the investigated problems [34]. The most common strategies may be divided in *stiffening*, that consists in shifting the resonance frequency of the structure beyond the frequency band of excitation, *damping*, aiming at reducing the resonance peaks by dissipating vibration energy and *isolation*, which prevents the propagation of disturbances to sensitive parts of the system, often adopted for adaptive optics and high-precision telescopes.

Furthermore, vibration suppression may be further achieved by following different philosophies:

- *Passively*, by implementing vibration absorbing materials, such as fluids and viscoelastic materials, on the spacecraft structure or by adopting Dynamic

Vibration Absorbers (DVA) to transfer kinetic energy. Moreover, passive solutions can be also obtained by using smart materials, either through energy coupling in shunt circuits or superelasticity. Indeed, vibration energy can be either converted into electrical energy to be dissipated in electrical circuits or stored by carrying out energy harvesting strategies. Passive vibration control, on the other hand, is not adaptive to the variation of system parameters and uncertainties in vibration sources;

- *Semi-actively*, when passive devices with controllable properties are used. Recently, Magneto-Rheological (MR) fluid were adopted, as well as piezoelectric transducers with switched electrical networks. Semi-active vibration control overcomes passive damping limitations by creating tunable springs or dampers. As the semi-active mechanisms do not directly act against the vibration sources, little or no external power is required [35]. Smart materials integrated with passive mechanisms have been implemented in semi-active vibration control. Giurgiutiu et al [36] connected shape memory alloys with morphing mechanisms to mitigate structural vibrations in helicopter blades. However, shape memory alloys exhibit a low operating frequency and need a mechanism to provide restoring forces. Recent studies have presented other possible semi-active vibration control methods by directly tuning the material properties of smart materials. Magnetorhelogical (MR) materials, which are iron particles embedded elastomers or fluids, can provide magnetically-tunable stiffness and damping coefficient [37][38]. Asnani et al [39] showed that the stiffness and damping coefficient of piezoelectric materials can be continuously tuned by adjusting electrical shunts;
- *Actively*, by generating a force to counteract the vibration. Such a method is generally employed when high performance is needed, as in the case of space domain. To perform active vibration control, a set of sensors (acceleration, strain, velocity, force, etc.) and actuators (inertial, strain, force, etc.) are needed to be coupled by a control algorithm, which may work either in a feedback or in a feedforward fashion.

Among them, *active vibration suppression* will be the focus of this thesis, as this philosophy can generally lead to higher suppression performance and guarantee a robust architecture in case of properties modification of the system. Research has been carried out in this field in last years: Proportional–Integral–Derivative (PID)-based control [40], Positive Position Feedback (PPF) [41], Direct Velocity Feedback

(DVFB) [42], linear quadratic Gaussian (LQG) control [43], structural filtering [44], pole/zero placement [45], input shaping [46][47] are examples of the most widespread approaches. Recently, intelligent control techniques have attracted growing interest and have been applied to the problem of active control of space structures. In 2018, Luo et al. [48] investigated a fuzzy algorithm to damp out the vibration of a hoop truss antenna during a lab test in ground conditions. In 2017, Xu et al. [49] implemented smart devices to perform vibration control of a Gossamer space structure and tested it in laboratory. Furthermore, model-based controllers are realized to include a dynamic model both for the rigid and the elastic dynamics [50].

2.2.3 COMBINED CONTROL/STRUCTURE DESIGN

Integrated controllers are becoming more and more suitable to engineer control solutions for large space structures, by tying together spacecraft flexible dynamics and attitude control laws. Traditionally, when used in early phases of the satellite design, such methods are also referred to as Plant-Controller Optimization (PCO) or Co-Design (CD) [51]. Indeed, structural models and control techniques can be merged to maximize the performance of the system: improve the robustness and stability of the spacecraft while minimizing structure mass and costs. In the last decades, CD methods started to use $\boldsymbol{H}_\infty$-controllers to optimize structural parameters and control configuration [52][53][54]. Such approaches are currently used in several studies, as the ones from Alazar et al. [55], where optimization of the attitude control system and of the Finite Element (F.E.) model are performed using optimization algorithms, as a genetic algorithm. The mentioned strategies make use of full order and unstructured controllers, but lately, with the broadening of Linear Matrix Inequality (LMI) approaches [56], also structured controllers (as PID) have been contemplated in the CD process. In Hiramoto et al. [57] the complexity of the design was increased by adding optimal actuator/sensor placement, and ICSD was performed to compute optimal structural parameters, collocated actuator placement and vibration control of a supported beam. Nowadays, the CD problem is generally set as a multi-channel $\boldsymbol{H}_\infty$ scheme where constraints to tuneable parameters (both at structure and control level) are defined in the frequency domain [58][59].

However, the same approaches may be used in advanced phases of the

satellite design to synthetize a robust and stable attitude controller also integrating information about the flexible dynamics of the system, once the structural project of the spacecraft is concluded [60]. Other approaches may be used in such sense. A Variable Structure Control (VSC) technique is used in [61] to integrate the command input shaping and the technique of dynamic variable structure output feedback control, to achieve the elimination of residual vibration by modifying the existing command. In [62], an attitude control system based on two fundamental control schemes (proportional-derivative (PD) control, with nonadaptive band-stop filters, and wave-based control) is applied to the problem of controlling spacecraft with sloshing propellant. Recently, Sabatini et al. [63] have proposed and experimentally tested an alternative approach in which two sets of actuators (attitude and structural devices) are commanded by means of a single model-based control law in a synergetic way. In this context, concerning the integrated attitude control/structure design, few works have been performed by considering integrated attitude and distributed vibration control system based on a multi-channel $\boldsymbol{H}_\infty$ scheme. Therefore, one of the objectives of this thesis is to provide a possible framework to perform control/structure distributed control of flexible space structures.

2.2.4 Active Control Devices

Actuators and sensors selected for space missions must satisfy requirements covering a wide range of applications. In general, most satellites host scientific instruments calling for strict pointing requirements, such as targeting, refocusing of mirrors, scanning mechanisms or optical path adjustments. In this context, electric motors have been widely employed gaining a substantial flight heritage and reliability, especially concerning appendages deployment and rotation or reorienting of solar arrays. Lately, smart materials and cutting-edge technologies have started to prove their benefits if applied to space missions. Be as it may, current concrete applications to space are still rather limited, thus indicating that the technological transfer from terrestrial devices has not still fully occurred yet. However, where extremely high precision is requested in combination with low mass and long operational life, smart materials have been seen as an approach which could make the mission viable [64]. In particular, this section is intended to provide a brief overview of the state of the art of current actuators and sensors

used in the space field, with a particular attention to the devices suitable to apply active vibration control for LSSs.

Concerning space actuators, the main categories may be distinguished in: Electric Motors, Proof-mass and Smart materials. In the class of *Electric Motors* several devices and application may be accounted, as brushless/brushed DC motors and stepper motors. The range of application may include Reaction Wheels (RWs), Micro Wheels (MWs), Energy Wheels, De-spun platforms, Solar Array Drive Mechanisms (SADM) used to rotate solar panels, Antenna Pointing Mechanisms (APMs) and different Deployment Mechanisms (DMs). While RWs and MWs are usually characterized by high continuous and often variable rotational speed, SADMs, APMs and DMs operates mostly in low speed, the latter being used in a single shot operation.

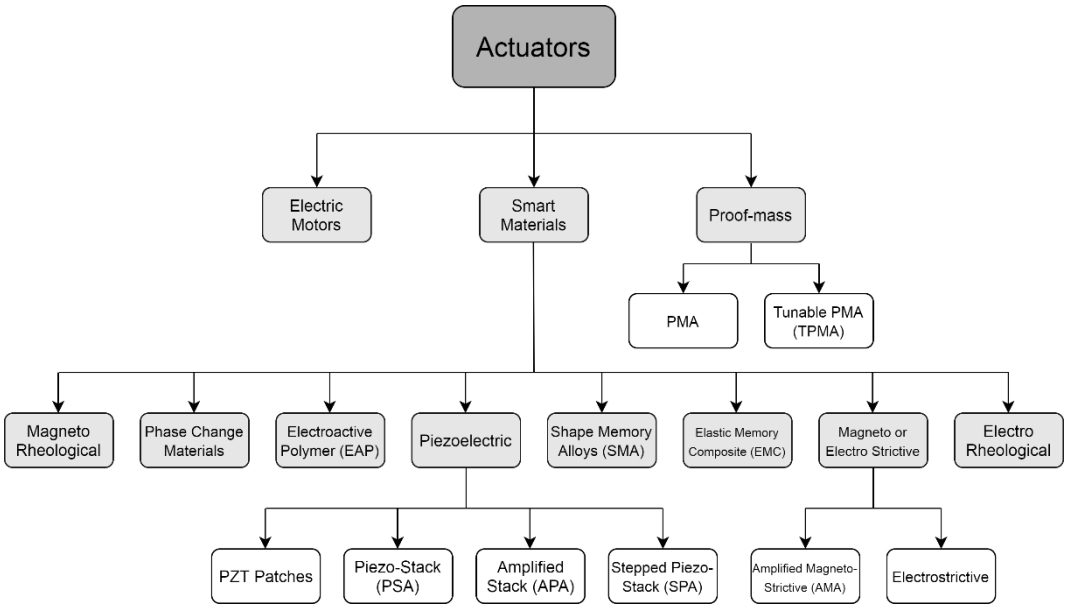

Fig. 2-11: Broad classification of actuators type for vibration control

Proof-mass actuators (PMAs) are promising devices to perform active vibration control. In general, a proof mass actuator is composed of a parallel arrangement of a spring and an active element pushing/pulling against a mass (known as proof mass or inertial mass). However, the actuator must be specifically sized for a particular structure [65]. This process is complex, due to the need to avoid PMA may run against its stops and reach the condition of stroke saturation, implying a further shock to the structure a damage to the actuator itself. The capacity of the

actuator is intimately linked to the moving mass, the stroke length, and the maximum force available from the electromechanical subsystem [66]. However, the operations at low frequencies (being the case for most flexible space structures) require a large stroke, which is technically difficult. Furthermore, such actuators demand often for a high mass to damp out vibrations for very large structures.

Research is currently being performed on smart materials, thus allowing them to become a more and more interesting and mature technology for a near future breakthrough as space sensors and actuators. Unlike other devices, smart materials enable vibration control strategies with small packaging size, broad frequency bandwidth, and high reliability. Their characteristics highly depend on the considered material and related properties; however, a scheme representing a general control architecture by using different types of smart devices is reported in Fig. 2-12.

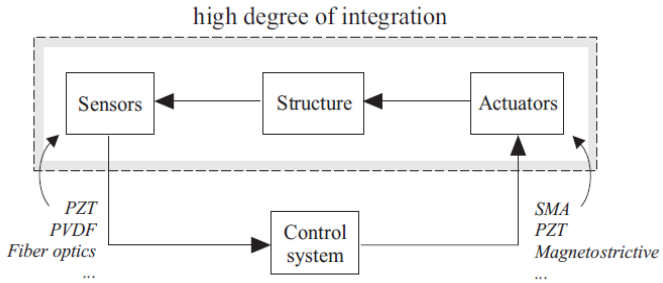

Fig. 2-12: Structure equipped with smart material control architecture [34]

Smart materials may be classified in several groups, according to their physical behaviour. The most relevant classes are listed in Fig. 2-11. Among them, some may be suitable for space applications. However, also regarding vibration control, piezoelectric devices represent the most mature technology. They have successfully flown and qualified for flight in different scenarios and projects, such as for microvibration cancellation for PICARD and Solar Orbiter missions. More thoroughly, a variety of applications has been already implemented in flown missions: pointing mechanisms (such as in ARTEMIS and PHARAO missions), laser control (as in AEOLUS and PHARAO spacecraft), free-floating object handling (LISA-PF, FOTON M3) and generally instrumentation (ROSETTA, MISSE7, CURIOSITY missions) [64].

The main features of actuators and sensors, which are relevant for a prospective space application, are listed in Table 2-1.

Table 2-1: Comparison of smart actuators properties

Type	Drive Voltage	Response Time	Force	Stroke	Power	Def.	Freq.	Mass
PMA	0-100 V	Fast (ms)	Up to 300 N	Up to 4 mm	Low/ Medium	n.a.	Medium/High	~ kg
TPMA	n.a.	Fast (ms)	Up to 1kN	Up to 10mm	Medium	n.a.	High to low	~ kg
PZT-P	-30-70 V	Very Fast (sub-ms)	Up to 110 MPa	up to 1mm (bending)	Low	0.2 %	Medium/High	~ g
PSA	-30-1000 V	Very Fast (sub-ms)	500/3000 N	Up to 180 μm	Low/ Medium	0.1-0.3%	High to low	~ g
APA	-30-150 V	Fast (ms)	30 N/ 1500 N	1.5 mm/ 25 μm	Low/ Medium	Up to 10%	High to low	~ g
SPA	0-150 V	Fast (ms)	30 N	>10 mm	Low/ Medium	>10%	High to low	~ g
SMA	5-20 V	Slow (s to min)	Up to 700 MPa	Up to cm	Medium/ High (cooling)	<8%	Very low	~ g
EMC	0-30 V	Slow (s to min)	n.a.	Up to cm	Medium	n.a.	Very low	~ g
AMA	0-50 V	Fast (ms)	70MPa	Up to 200 μm	n.a.	0.2%	High to low	~ g
EAP	4-7 V	Very Fast (μ to s)	0.1-3 MPa	n.a.	High	>10%	Low	~ g

PMA: Proof Mass Actuators, *TPMA: Tunable-PMA*, *PZT-P: Piezo-electric Patches*, *PSA: Piezo Stack Actuators*, *APA: Amplified Piezo Actuator*, *SPA: Stepper Piezo Actuator*, *SMA: Shape Memory Alloys*, *EMC: Elastic Memory Composite*, *AMA: Amplified Magneto-strictive Actuators*, *EAP: Electro-Active Polymers.*

However, it is worth noting that some of the actuators mentioned in the table are currently under development and are not available as commercial devices (as EAPs and Magnetostrictive devices), and that the effect of PMAs is highly dependent on the mass of the actuator itself (resulting in massive devices to have high performance) and its saturation stroke limit. Consequently, it is worth noting that the most promising actuators to be used in this study are the piezoelectric devices. In particular, the PSA actuators configured in OPSA setup (see Par. 5.5.1.2), due to the possibility to exert not only axial forces but also bending moments, they can benefit at the same time of the properties of both PSA and PZT-P devices.

Concerning vibration sensing, sensors can be classified in contact and non-contact devices. The first ones work when mounted or bonded accurately to the vibrating structure, while the second type does not need a direct contact with it. Among *contact sensors*, the accelerometer is by far the most diffused device. Such a sensor measures the level of accelerations and may be classified in three types: MEMS, piezoelectric and piezoresistive. However, the latter materials are also commonly used to detect strain caused by structural vibrations [67]. In detail,

piezoelectric sensors may be further distinguished in PZT (with high value of the piezoelectric constant, but high stiffness and brittleness), PVDF (low Young modulus, easily deformable, but low piezoelectric coefficient) and MFC (high flexibility and low sensing bandwidth, suitable to sense low frequencies vibration for space structures). Another type of sensor is the strain gauge, which works as a foil with an electrically conductive grid that can be stretched or compressed, thus changing the electrical resistance of the grid. It is worth noting that most of piezoelectric stack actuator solutions offer a strain gauge position sensor for inner closed loop control, which actually provides information about the position of the actuator during dynamic operations.

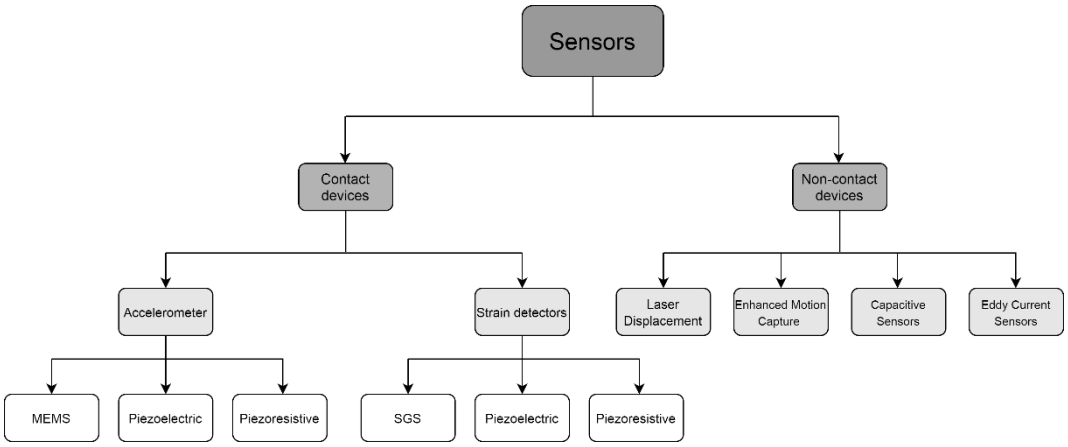

Fig. 2-13: Broad classification of sensors for vibration control

Also, *non-contact devices* can be used to measure vibration levels, such as acoustic pressure sensors, laser displacement sensors, optical systems (as cameras and motion capture methods), eddy current and capacity displacement sensors. However, a few of them are currently suitable to space environment and yet they present some drawbacks. Indeed, optical techniques are likely to be impacted by light conditions depending on the specific orbital environment in terms of saturation of detectors by direct sunlight and noisy environment background for light presence. Moreover, optical metrology may pose some limits to the design of a collocated vibration control system with regard to which actuator to select, and implies considerable interface/harness issues between actuators and corresponding sensors. Concerning laser displacement sensors, their measurements are intrinsically mono-dimensional (the observed movement is along the direction of the laser beam propagation). In addition, in a space application, the source would need to be located near the point whose

displacement should be measured (as the precision of such a metrology system is significantly affected by the distance from the target), thus leading to the need for a support likely offered by a boom or other deployable structure, involving indeed additional flexibility. Capacitive sensors have similar benefits and drawbacks as lasers for vibration testing.

On the other hand, piezoelectrics can be used to sense also very low frequencies while equipped to a suitable external electric circuit to hold the charge during slow oscillations (hold&store mechanism). Furthermore, they have the relevant advantage to be self-powered (even if an amplification stage is required to obtain the voltage to be used in the control chain). Also, accelerometers are devices used to measure accelerations in some points of the structure (as in the Nodes of Interest (NOIs), see Par. 3.4.1) and to derive also velocities and positions, when located at the tip of the antenna reflector. On the contrary, when placed near the root of the mast, the acceleration levels could be lower than the device noise itself and so not easily detectable. Also, strain gauge sensors could be used for active vibration purposes, even though they would be generally produce few nominal millivolt output per each volt of excitation and be highly dependent on temperature status. In particular, strain sensors based on piezoelectric materials have low mass, but higher stiffness if compared to strain gauge foils (i.e. very low impact on the structure). Ultimately, piezo strain sensors, accelerometers and also foil gauge appear to be the most promising solutions to be implemented in a closed loop vibration control architecture. In this thesis, both piezoelectric sensors and accelerometers will be considered as available sensors.

2.3 STUDY CASES

In this context, suitable study cases are selected to develop an overall attitude and vibration control architecture. Two candidates of particular interests have been identified as mesh reflectors and radar interferometers. As far as the former are concerned, such a deployable antenna instrument is characterized by a circular truss structure supporting a large parabolic antenna reflector, usually with diameter higher than 6 meters (as the AstroMesh® family). As mentioned in Par. 1.1, the current interest towards this type of structure is proved by the development of a LEA (Large European Antenna) project in the frame of a Horizon 2020 project. Moreover, among the available data (see Fig. 2-8), it can be noticed

the only observable case with a first natural frequency above 5 Hz is the Surface Water Ocean Topography (SWOT) mission, joint venture of the Jet Propulsion Laboratory (JPL), the National Centre for Space Studies (CNES) and Thales Alenia Space to be launched in 2021. In detail, SWOT spacecraft will equip a 10-meters long radar interferometer having first fundamental frequency of about 7 Hz, much stiffer than all the antennas with similar aperture to avoid CSI issues.

The two candidates have been considered as testbeds to verify the improvement the systems could receive by implementing an active vibration control system. Indeed, the aim of this research is to investigate the possibility of designing an enhanced spacecraft, by improving its current performance, according to the logic presented in Fig. 2-14.

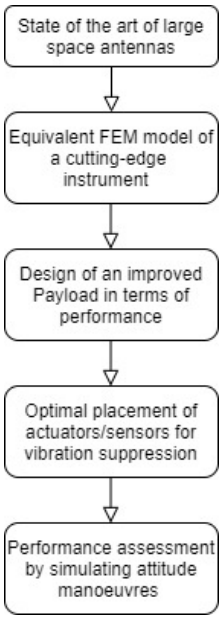

Fig. 2-14: Work logic of the research

In addition, an active vibration control system will be investigated to avoid a conservative design in terms of mass and stiffness of the structure, thus entailing a lowering of its first natural frequencies. More details on the designed structures may be found in Par. 5.6.

BIBLIOGRAPHY

[1] G.L. Ketner, *Survey of historical incidents with Control-Structures Interaction and recommended technology improvements needed to put hardware in space*, prepared for Control Structures Interaction Office, NASA, Langley Research Center, Washington, 1989.

[2] P. A. Belloch, N. R. Beagley, *Tools for analysis of control structure interaction*, *Computer-Aided Engineering Journal*, Vol. 7, Issue 4, August 1990;

[3] American Society of Civil Engineers, *Identification of Large Space Structures in Orbit*, Final Report prepared for Air Force Rocket Propulsion Laboratory, Sept. 1985, New York

[4] S. Pellegrino, *Deployable structures in engineering*, Pellegrino S (ed.) Deployable structures. Vienna: Springer, 2001, pp. 1–35;

[5] C. M. Stevenson, *Morphological principles: current kinetic architectural structures*, London: Adaptive Architecture, The Building Centre, 2011, pp. 1–12;

[6] A. E. Del Grosso and P. Basso, *Deployable structures*, Adv. Sci. Tech. 2013; 83: 122–131;

[7] G. E. Fenci and N.C. Currie, *Deployable structures classification: A review*, International Journal of Space Structures, Vol. 32, Issue 2, pages 112-130, 2017;

[8] E. R. Adrover, *Deployable Structures*, London: Laurence King Publishing, 2015;

[9] A. Hanaor and R. Levy, *Evaluation of deployable structures for space enclosures*, Int. J. Space Struct. 2001; 16: 211–229;

[10] L. Puig, A. Barton, N. Rando, *A review on large deployable structures for astrophysics*, Acta Astronautica 67 (2010), 12-26, 2010;

[11] M. Mobrem, C. Spier, *Design and Performance of the Telescopic Tubular Mast*, Proceedings of the 41st Aerospace Mechanisms Symposium, Jet Propulsion Laboratory, May 16-18, 2012;

[12] F. Del Campo and J. I. R. Urien, *Collapsible Tube Mast Technology Demonstration Program*, Space Technology-Industrial and Commercial Application, pp. 61-76, Jan 1993;

[13] O. R. Stohlman and S. Pellegrino, *Shape accuracy of a joint-dominated deployable mast*, 51st AIAA/ASME/ASCE/AHS/ASC Structures, Structural Dynamics and Materials Conference, 12-15 April 2010, Orlando, FL, AIAA-2010-2605;

[14] K. Miura, Y. Miyazaki, *Concept of the tension truss antenna*, AIAA Journal, Vol. 28, pp. 1098-1104, 1990;

[15] L. Datashvili, N. Maghaldadze, S. Ender; J Pauw, P. He, H. Baier, A. Ihle, J. S.

Prowald, *Advances in Mechanical Architectures of Large Precision Space Apertures*, European Conference on Spacecraft Structures, Materials & Environmental Testing, 2014;

[16] Y. Zhang, D. Yang, S. Li, *An integrated control and structural design approach for mesh reflector deployable space antennas*, Mechatronics 35 (2016) 71–81;

[17] G. Tibert, *Deployable Tensegrity Structures for Space Applications*, Doctoral Thesis, Royal Institute of Technology, Department of Mechanics, Stockholm, 2002;

[18] J. Yu et al., *Dynamic Testing of an Inflatable Wrap-rib Reflector Antenna*, Procedia Engineering Volume 199, 2017, Pages 483-488;

[19] Straubel, *Design and methods for deployable space antennas,* Doctoral Dissertation, July 2012;

[20] S. D. Guest and S. Pellegrino, *A new concept for solid surface deployable antennas*, Acta Astronautica 38, 2 (1996), 103–113;

[21] Z. You, *Deployable structures for masts and reflector antennas*, PhD thesis, University of Cambridge, Cambridge, UK, 1994;

[22] L.N. Keller, M.S. Lake, D. Codell, R. Barrett, R. Taylor and M.R. Schultz, *Development of Elastic Memory Composite Stiffeners for a Flexible Precision Reflector*, Composites in Manufacturing, Vol. 23, N°2, 2007;

[23] Y. Wang et al., *Design and Deployment Analysis of Modular Deployable Structure for Large Antennas*, Journal of Spacecraft and Rockets 52(4):1-11, July 2015;

[24] Q. Hu et al., *Decentralized simple adaptive control for large space structures*, Journal of Sounds and Vibration, Vol. 472, 2018, pages 95-119;

[25] M. Mobrem, S. Kuehn, C. Spier, E. Slimko, *Design and Performance of Astromesh Reflector Onboard Soil Moisture Active Passive Spacecraft*, 2012 IEEE Aerospace Conference, 3-10 March 2012, Big Sky, USA;

[26] R. L. Kosut, H. Salzewedel, A. E. Neini, *Robust Control of Flexible Spacecraft*, Vol. 6, N. 2, March 1983;

[27] T. Ohtani et al., *Robust Attitude Control Using Mu-Synthesis for the Large Flexible Satellite ETS-VIII*, Journal of Space Technology and Science, Vol. 25 (2011), Issue 1;

[28] K. Steen, J. Høgsberg, *Optimal resonant control of flexible structures*, J. Sound Vib. 323 (2009) 530–554.

[29] M.H. Toodeshki, J. Askari, S. Hosseinnia, *Adaptive robust H ∞ control of time delay systems with unknown uncertainty bounds*, Int. J. Control. Autom. Syst. 10 (2012) 158–165.

[30] S. Sakai, N. Bando, *Attitude Control System Design for Fast Rest-to-Rest Attitude*

Maneuver, Approaching Micro-Arcsecond Resolution with VSOP-2, Astrophysics and Technology ASP Conference Series, Vol. 402, c 2009;

[31] Y. Yang, *Analytic LQR Design for Spacecraft Control System Based on Quaternion Model*, Journal of Aerospace Engineering, Vol. 25, issue 3, 2012;

[32] S. Bennani, F. Ankersen, M. Arcioni, M. Casasco, L. Massotti, P. Silvestrin, *Robust Attitude Control Design for the BIOMASS Satellite (Earth Explorer Core Mission Candidate*), Proceedings of the 18th World Congress The International Federation of Automatic Control (IFAC) , Milano (Italy), Aug. 28: Sept. 2, 2011;

[33] C. C. Liebe et al., *Metrology system for measuring mast motions on the NuSTAR mission*, 2010 IEEE Aerospace Conference, Big Sky, MT, 2010, pp. 1-11, doi: 10.1109/AERO.2010.5446898;

[34] A. Preumont, *Vibration Control of Active Structures*, Solid Mechanics and Its Applications, Third Edition, Springer Netherlands, 2011;

[35] Z. Deng and M. J. Dapino, *Review of magnetostrictive materials for structural vibration control*, 2018 Smart Mater. Struct. 27 113001;

[36] V. Giurgiutiu, Z. Chaudhry and C. A. Rogers, *Engineering feasibility of induced strain actuators for rotor blade active vibration control*, J. Intell. Mater. Syst. Struct. 6 583–97;

[37] J. D. Carlson and M. R. Jolly, *Fluid, foam and elastomer devices*, Mechatronics 10 555–69, 2000;

[38] C. Y. Lai and W. H. Liao, *Vibration control of a suspension system via a magnetorheological fluid damper*, Modal Analysis 8 527–47, 2002;

[39] V. M. Asnani, Z. Deng, J. J. Scheidler and M. J. Dapino, *Experimental comparison of piezoelectric and magnetostrictive shunt dampers*, Proceedings of SPIE, 2016;

[40] W. Gawronski, *Advanced Structural Dynamics and Active Control of Structures*. New York: Springer Science & Business Media, 2004;

[41] J. L. Fanson and T. K. Caughey, *Positive position feed-back control for large space structures*. AIAA Journal 28: 717–724, 1990;

[42] T. Nagashio et al., *Optimal Static Output Feedback Control for Large Space Structures and Its Application to Local Control*, Trans. Japan Soc. Aero. Space Sci. Vol. 47, No. 155, pp. 1–8, 2004;

[43] A. Koszewnik, *The active vibration control of the plate structure by using LQG controller and piezo-stripes*, 2017 22nd International Conference on Methods and Models in Automation and Robotics (MMAR), 28-31 Aug. 2017, Miedzyzdroje, Poland;

[44] B. Wie, K. Byun, *New generalized structural filtering concept for active vibration control synthesis*, J. Guid. Control Dyn. 12 (1989) 147–154;

[45] B. Wie, A.E. Ryson, *Pole-zero modeling of flexible space structures*, J. Guid. Control Dyn. 11 (1988) 554–561.

[46] W. Singhose, R. Eloundou, J. Lawrence, *Command generation for flexible systems by input shaping and command smoothing*, J. Guid. Control Dyn. 33 (2010) 1697–1707.

[47] W. Singhose, *Command shaping for flexible systems: a review of the first 50 years*, Int. J. Prec. Eng. Manuf. 10 (2009) 153–168.

[48] Y. Luo et al., *Active vibration control of a hoop truss structure with piezoelectric bending actuators based on a fuzzy logic algorithm*, Smart Mater. Struct., vol. 27, no. 8, p. 085030, 2018.

[49] R. Xu, D. Li, J. Jiang, and J. Zou, *Decentralized adaptive fuzzy vibration control of smart gossamer space structure*, J. Intell. Mater. Syst. Struct., vol. 28, no. 12, pp. 1670–1681, Jul. 2017.

[50] Z.H. Wang, M. Xu, Y.H. Jia, S.J. Xu, L. Tang, *Vibration suppression-based attitude control for flexible spacecraft,* Aerosp. Sci. Technol., 70 (2017), pp. 487-496;

[51] J. A. Perez-Gonzalez, *Integrated Control/Structure Design of a Flexible Satellite Using Structured Robust Control Synthesis*, Doctoral Thesis, ISAE Institut Superieur de l'Aeronautique et de l'Espace, 2016;

[52] A. Falcoz et al., *Integrated Control and Structure design framework for spacecraft applied to Biomass satellite*, 19th IFAC Symposium on Automatic Control in Aerospace September 2-6, 2013. Würzburg, Germany

[53] K. Tsujioka, I. Kajiwara and A. Nagamatsu, *Integrated Optimum Design of Structure and H-infinity Control System*. AIAA Journal, vol. 34, no. 1, pages 159–165, January 1996. 22, 167

[54] S.V. Savant and H.H. Asada. *Integrated Structure/Control Design Based on Model Validity and Robustness Margin*, Proceedings of the American Control Conference, San Diego, California, June 1999.

[55] D. Alazard, T. Loquen, H. De Plinval, C. Cumer, C. Toglia and P. Pavia. *Optimal Co-Design for Earth Observation Satellites with Flexible Appendages*, AIAA Guidance, Navigation, and Control (GNC) Conference, 2013.

[56] C. Scherer, P. Gahinet and M. Chilali. *Multiobjective Output-Feedback Control via LMI Optimization,* Automatic Control, IEEE Transactions, vol. 42, no. 7, pages 896–911, 1997

[57] K. Hiramoto, J. Mohammadpour and K.M. Grigoriadis, *Integrated Design of System Parameters, Control and Sensor Actuator Placement for Symmetric Mechanical Systems*, In 48th IEEE Conference on Decision and Control, Shanghai, China, December 2009.

[58] P. Gahinet and Pierre Apkarian, *Structured $\boldsymbol{H}_\infty$ Synthesis using MATLAB*, 18th IFAC World Congress, Milano, Italy, August 2011

[59] D. Alazard, T. Loquen, H. De Plinval & C. Cumer, *Avionics/Control Co-Design for Large Flexible Space Structures*, AIAA Guidance, Navigation, and Control (GNC) Conference, Boston, Massachusetts, USA, August 2013.

[60] N. Guy, D. Alazard, C. Cumer, C. Charbonnel, *A new attitude control design approach for flexible satellites*, IFAC Proceedings Volumes, Volume 46, Issue 19, 2013, Pages 500-505;

[61] Q. L Hu, P. Shi, and H. J. Gao, *Adaptive variable structure and commanding shaped vibration control of flexible spacecraft*, Journal of Guidance, Control, and Dynamics, vol. 30, no. 3, pp. 804–815, 2007.

[62] A. Colagrossi, M. Lavagna, *Integrated vibration suppression attitude control for flexible spacecrafts with internal liquid sloshing*, Multibody Syst Dyn (2020). https://doi.org/10.1007/s11044-020-09755-9

[63] M. Sabatini, G.B. Palmerini, P. Gasbarri, *Synergetic approach in attitude control of very flexible satellites by means of thrusters and PZT devices*, Aerospace Science and Technology, Vol. 96, pages 2-11, January 2020;

[64] C. Allegranza, L. Gaillard, R. Le Letty, S. Patti, L. Scolamiero , M. Toso, *Actuators for Space Applications: State of the Art and New Technologies*, 1 1 ATG-Europe B.V., Noordwijk, The Netherlands 2 European Space Agency, Noordwijk, The Netherlands;

[65] C. L. Kirk and M. S. Lee, *Proof-Mass Actuator Control of Shuttle-based AstroMast*, Acta Astronautica, Vol. 32, N° 2, pp 97-106, 1994;

[66] D. K. Lindner, *Performance And Control Of Proof-Mass Actuators Accounting For Stroke Saturation*, AIAA Journal of Guidance, Dynamics, and Control Vol. 17, No. 5, September - October, 1994, pp. 1103: 1108;

[67] S. Kon et al., *Piezoresistive and Piezoelectric MEMS Strain Sensors for Vibration Detection*, Sensors and Smart Structures Technologies for Civil, Mechanical, and Aerospace Systems 2007, edited by Masayoshi Tomizuka, Chung-Bang Yun, Victor Giurgiutiu, Proc. of SPIE Vol. 6529, 65292V, (2007);

Chapter 3
DYNAMICS OF FLEXIBLE SPACE SYSTEMS

In this chapter, the instruments needed to address the themes discussed throughout the research are introduced. In detail, the main concepts of non-linear mechanics and flexible dynamics for an in-orbit flexible spacecraft are here recalled, to arrive to a linearized model to be deployed in most common control design frameworks.

In order to describe the problems arising when manoeuvring an in-orbit flexible spacecraft, necessary knowledge about the coupling between attitude dynamics and flexible mechanics is here retained. In this thesis, the classical non-linear formulation for flexible in-orbit spacecrafts has been further developed by including the presence of smart distributed actuators and sensors.

3.1 FLEXIBLE SPACECRAFT DYNAMICS

In the last decades, modern space missions have been calling for progressively more performant technology to observe the Earth and the Universe, thus leading to longer extendable elements, larger antennas and wider solar panels. In this context, the flexibility of the system cannot be neglected and should be considered when deriving the equations of motion of a spacecraft. The main approaches to derive the dynamics of a flexible structure are the Euler-Lagrange theory [2][3], the Newton-Euler method [4] and the Ritz-Galerkin technique [5][6]. In this thesis, a Lagrangian approach complemented with the Finite Element Method (FEM) has been chosen to derive the full dynamics of a spacecraft equipped with flexible

appendages, also including embedded piezoelectric active materials.

In general, the Lagrangian $\mathcal{L}$ of a system can be written as the difference between its kinetic energy K and its potential energy functional Π as

$$\mathcal{L} = K - \Pi \tag{3.1}$$

Therefore, the Lagrangian equations can be derived as

$$\frac{d}{dt}\frac{\partial \mathcal{L}}{\partial \dot{S}} - \frac{\partial \mathcal{L}}{\partial S} = Q \tag{3.2}$$

where $S = \left[{}^{I}X_0, \Xi, \eta \right]$ is the set of Lagrangian generalized coordinates, with ${}^{I}X_0$ vector indicating the origin O of the Body reference frame with respect to the Inertial frame, where the left subscript indicates it is written in the Inertial reference frame, $\Xi_{i=1,..,3}$ describing the attitude of the spacecraft via Euler's angles and η vector of the N_m modal amplitudes of the flexible system. The term Q represents the generalized Lagrangian forces, which are not included in the potential energy functional. They are computed from the physical forces using $QdS = dL$ where dL is the virtual work of the physical forces on the virtual displacement field generated by a virtual variation dS of the Lagrangian coordinates.

In detail, different types of interaction are considered in the frame of Lagragian equations. According to [3], four specific categories may be identified as: conservative internal body interactions (i.e. the interaction among different particles of the body), conservative external interactions (as the gravity force), non-conservative internal body interactions (i.e. damping) and non-conservative external interactions (as the forces exerted by mass-ejection systems). Furthermore, it is stated that any conservative interaction, which is derived from a potential, can be considered either inside the Lagrangian or as a Lagrangian force. In this thesis, the conservative internal body interactions are assumed to be inside the Lagrangian, while the conservative external interactions are equated to generalized Lagrangian forces. According to this approach, the potential energy may be split in two terms $\Pi = \Pi_I + \Pi_E$, where the first term refers to internal conservative actions, while the second one to external interactions. Therefore, eq. (3.2) may be rewritten as

$$\frac{d}{dt}\frac{\partial K}{\partial \dot{S}} - \frac{\partial K}{\partial S} + \frac{\partial \Pi_I}{\partial S} + \frac{\partial \mathcal{F}}{\partial \dot{S}} = Q \tag{3.3}$$

with $\mathcal{F}$ dissipation function which is considered as a potential of the internal dissipative forces, function of the internal variables and their time derivatives, and

$$Q = -\frac{\partial \Pi_E}{\partial S} + F^{n.c.} \tag{3.4}$$

where $F^{n.c.}$ are the non-conservative external forces.

The main steps needed to describe the satellite dynamics are:

a. Introduction to adopted Reference frames;
b. Definition of kinematics parameters;
c. Definition of kinetic, elastic, piezoelectric and gravitational functionals, including the formulation of FEM piezoelectric elements;
d. Definition of the Lagrangian;
e. Writing of governing equations.

3.1.1 REFERENCE FRAMES

To outline the motion of satellites, specific reference frames are generally adopted to universally develop the expression of their dynamics. In this section, the main reference frames involved in spacecraft attitude and orbit description are briefly introduced.

3.1.1.1 INERTIAL REFERENCE FRAME (I)

The first system to be defined is an Inertial Reference Frame I: (O_I, X_I, Y_I, Z_I), where the equations of motion may be naturally written. In the aerospace field, such an inertial frame is generally associated to an Earth-fixed set of axes, namely Earth Centered Inertial (ECI) reference system. This frame is assumed quasi-inertial, being the main non-inertial acceleration due to the Sun-Earth gravitational attraction. Indeed, while such a reference might be not suitable to the mathematical description of interplanetary physics, or when other celestial bodies are involved, it is revealed particularly useful to describe the dynamics of satellites orbiting around the Earth.

In detail,

- The origin O_I is placed in correspondence of the center of the Earth;

- The X_I axis lies on the Earth's equatorial plane and is permanently pointed towards the Aries Constellation;
- The Z_I axis is parallel to the Earth's rotation axis and aligned to the direction of Geographical Nord;
- The Y_I axis is aligned to form a right-handed orthogonal frame.

3.1.1.2 LOCAL ORBITAL REFERENCE FRAME (LORF)

To describe the motion of a satellite orbiting the Earth, the Local Orbital Reference Frame (LORF): ($O_{LORF}, X_{LORF}, Y_{LORF}, Z_{LORF}$) may be considered. Such a system is defined by the position and velocity of a spacecraft. The attitude of a satellite in such reference frame is described by means of some Keplerian parameters, namely the Right Ascension of the Ascending Node Ω, the inclination of the orbit i, the perigee argument ω and the true anomaly υ. In detail,

- The origin O_{LORF} is in a spacecraft reference point, generally the Center of Mass;
- The X_{LORF} axis is aligned to the orbital radius;
- The Y_{LORF} axis is perpendicular to X_O in the nominal direction of flight, so to be approximately aligned with the spacecraft velocity vector;
- The Z_{LORF} axis forms a right-handed orthogonal frame with the other axes.

The transformation between the Inertial and Orbital frames is defined through the rotation matrix $T_{LORF \leftarrow I}$. Such a matrix is obtained by assuming a 3-1-3 rotation sequence:

- A first counter-clockwise rotation around the Z_I axis represented by the Ω parameter;
- A second counter-clockwise rotation around the X_I axis represented by the i parameter;
- A last counter-clockwise rotation around the Z_I axis represented by the parameter $\varpi = \omega + \upsilon$, equal to the sum of the perigee argument and the true anomaly.

3.1.1.3 LOCAL VERTICAL LOCAL HORIZON REFERENCE FRAME (LVLH)

A more convenient approach is to define the attitude of the spacecraft with respect to the Earth's surface. To this purpose, the Local Vertical Local Horizon (LVLH) frame: ($O_{LVLH}, X_{LVLH}, Y_{LVLH}, Z_{LVLH}$) may be adopted. In detail,

- The origin O_{LVLH} is in a spacecraft reference point, generally the Center of Mass;
- The Z_{LVLH} axis points toward the Earth's center (negative position vector of the satellite along the orbit);
- The X_{LVLH} is perpendicular to Z_{LVLH} in the nominal direction of flight, so it is approximately aligned with the spacecraft velocity vector;
- The Y_{LVLH} axis forms a right-handed orthogonal frame with the other two axes.

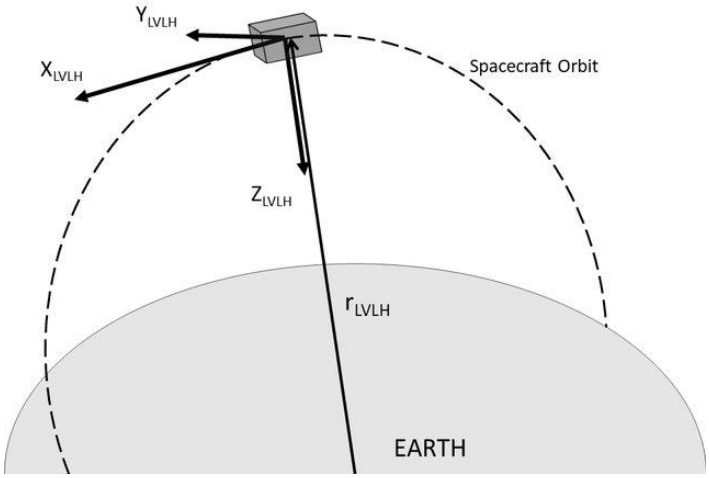

Fig. 3-1: Local Vertical Local Horizon reference frame

According to this configuration, the $X_{LVLH}, Y_{LVLH}, Z_{LVLH}$ axes are commonly known as Roll, Pitch and Yaw (φ, θ, ϕ) axes respectively. The attitude of a spacecraft with respect to the LVLH frame can be obtained from the LOFR reference system by using a $T_{LVLH \leftarrow LORF}$ transformation:

- A first clockwise 90-degrees rotation around the Y_{LORF} axis;
- A second counter-clockwise 90-degrees rotation around the Z_{LORF} axis.

3.1.1.4 SPACECRAFT REFERENCE FRAME (S/C)

This fixed coordinate system S/C: ($O, X_{SC}, Y_{SC}, Z_{SC}$), is used to define hardware location within the satellite. Referring to such a frame is useful to assemble different parts (as payload, solar panels, antennas, etc.) to a central body. Indeed, when building the dynamic model of a spacecraft, each part may be considered connected to a central platform by means of some attachment points, defined with respect to the S/C reference frame. The origin O is located at the centre of the launch vehicle interface circle, i.e. at the bottom of the interface cylinder and the top of the launch vehicle specific interface frame. The directions of the coordinated axes may vary according to the specific type of satellite. However, typically the naming is given such that, when the S/C frame is aligned to the LVLH frame during some operational phase, we have the same axes names in both the systems (as in the case of Roll, Pitch and Yaw axes). In general, the Z_{SC} axis is assumed perpendicular to the launch vehicle interface plane and pointed towards the Nadir direction when the satellite is in orbit, one of the other axis X_{SC} or Y_{SC} is considered parallel to the longitudinal direction of solar arrays and the third one aligned to form a right-handed orthogonal frame.

3.1.1.5 BODY REFERENCE FRAME (B)

The Body Reference Frame B: (G, X_B, Y_B, Z_B) is a reference frame joined to the body, with an origin attached to a generic point G of the spacecraft (usually the Center of Mass, CoM, of the system). Such frame is generally obtained by translating the S/C frame to the point G, by maintaining the same orientation of the coordinated axes.

3.1.1.6 APPENDAGE REFERENCE FRAME (A)

Generally, a spacecraft is equipped with one or more flexible appendage, each of which is usually designed and built according to its Appendage reference frame A_i: ($O_{A_i}, X_{A_i}, Y_{A_i}, Z_{A_i}$). The origin O_{A_i} of such system is often placed at the attachment point of the substructure with the satellite platform. The position of the attachment points is usually defined in the S/C reference frame. The directions of the

coordinated axes depend on the specific geometry or needs of the appendages. An example of how different appendages are positioned with respect to a spacecraft platform (i.e. the S/C reference frame) is presented in Fig. 3-2, where the system PL: ($P_1, X_{PL}, Y_{PL}, Z_{PL}$) represents the Payload, with origin in the attachment point P_1, while the systems SA1: ($P_2, X_{SA1}, Y_{SA1}, Z_{SA1}$) and SA2: ($P_3, X_{SA2}, Y_{SA2}, Z_{SA2}$) indicate the two solar arrays attached in correspondence of points P_2 and P_3.

However, to develop the system dynamic model, it is first necessary to refer all the appendage information to the attachment point and then transfer them from the appendage reference frame to Body reference frame by using a transformation matrix $\boldsymbol{T}_{B\leftarrow A_i}$.

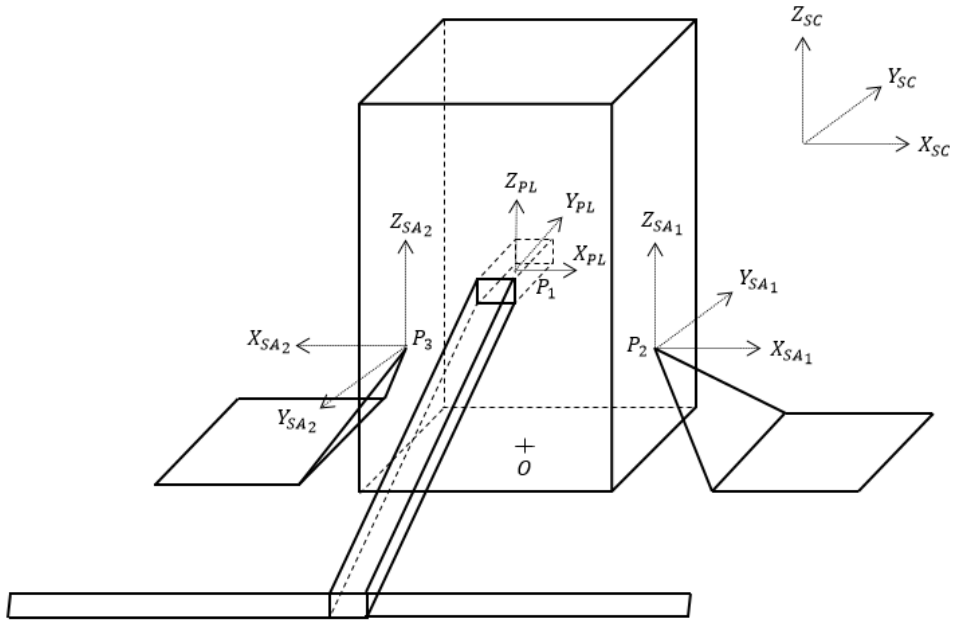

Fig. 3-2: S/C and Appendage reference frames visualization

3.1.2 KINEMATICS

The kinematic parameters of a body, or a system of bodies, are variables whose time variation quantitatively describes the motion of the object [4]. A kinematic model is composed of a set of equations, based on such parameters, defining the position and orientation in space of each elemental part of the bodies. Defining a kinematic model is preliminary both to write the dynamics of a system and to

formally state the attitude and control problem, as it allows to mathematically describe the target motion for such an object. The objective is to obtain analytical expressions for position, velocity and acceleration of an arbitrarily located point on the body.

Compared to a rigid body, the definition of the kinematics for a flexible body is complemented by adding a set of deformation functions to the rigid displacement. In the hypothesis of small elastic displacement with respect to undeformed configuration, the motion of a generic point P of an object is given by the superposition of a rigid motion plus a set of elastic displacements [4]. As for that, the vector representing the position of the point P in an inertial, Earth-centred, reference frame is

$$ {}^{I}X_{P} = {}^{I}X_{0} + \boldsymbol{T}_{I\leftarrow B}\left(r + x\right) = {}^{I}X_{0} + \boldsymbol{T}_{I\leftarrow B}\left(r + \sum_{k=1}^{N_m}\eta_k(t)\varphi_k(r)\right) \tag{3.5} $$

where ${}^{I}X_{O}$ represents the position vector of a generic body reference point in the inertial frame, r is the rigid component associated to the position of point P in the Body frame, x is the flexible component associated to the position of point P, φ_k are the first N_m-set of the structure eigenvectors and η_k their relevant modal amplitudes. The matrix $\boldsymbol{T}_{I\leftarrow B} = \boldsymbol{T}_{B\leftarrow I}^{T}$ describes the rotation from the body-axes to the ECI reference frame. In detail, the transformation $\boldsymbol{T}_{B\leftarrow I}$ can be accomplished in three steps, as described by

$$ \boldsymbol{T}_{B\leftarrow I} = \boldsymbol{T}_{B\leftarrow LVLH}(\phi,\theta,\varphi)\boldsymbol{T}_{LVLH\leftarrow LORF}(\alpha,\beta)\boldsymbol{T}_{LORF\leftarrow I}(\Omega,\mathrm{i},\varpi) \tag{3.6} $$

First, we move from Inertial to the LORF reference frame by using the 3-1-3 rotation matrix $\boldsymbol{T}_{LORF\leftarrow I}$. Such a matrix is expressed in terms of Euler's angles introduced in Par. 3.1.1.2. To refer to the generally used Local Vertical Local Horizon (LVLH) reference system the rotation matrix $\boldsymbol{T}_{LVLH\leftarrow LORF}$ is needed, performing a 3-2 rotation $(\alpha = -\pi/2,\ \beta = \pi/2)$. According to this approach, the Z-axis points in the nadir direction (negative position vector of the satellite along the orbit), the Y-axis in the negative orbit normal and the X-axis forms a right-handed coordinate system (parallel to the satellite velocity vector if the orbit is circular). Finally, the attitude of the satellite with respect to the LVLH reference frame is expressed by using yaw, pitch and roll angles (ϕ,θ,φ) reported in the 3-2-1 rotation matrix $\boldsymbol{T}_{B\leftarrow LVLH}(\phi,\theta,\varphi)$.

By time derivation, it is possible to obtain the velocity of the point P of the

spacecraft as

$$ {}^{I}\dot{X}_{P} = {}^{I}\dot{X}_{0} + \dot{\boldsymbol{T}}_{I\leftarrow B}\left(r + \sum_{k=1}^{N_m}\eta_k(t)\varphi_k(r)\right) + \boldsymbol{T}_{I\leftarrow B}\left(\sum_{k=1}^{N_m}\dot{\eta}_k(t)\varphi_k(r)\right) \tag{3.7} $$

where the term $\dot{\boldsymbol{T}}_{I\leftarrow B}$ may be rewritten as

$$ \dot{\boldsymbol{T}}_{I\leftarrow B} = \boldsymbol{T}_{I\leftarrow B}\mathbf{H}(\omega) \tag{3.8} $$

with $\mathbf{H}(\omega)$ antisymmetric matrix containing the components of the angular rates ω of the spacecraft with respect to the Inertial frame written in the Body reference frame

$$ \mathbf{H}(\omega) = \begin{bmatrix} 0 & -\omega_z & \omega_y \\ \omega_z & 0 & -\omega_x \\ -\omega_y & \omega_x & 0 \end{bmatrix} \tag{3.9} $$

Consequently, one may write

$$ {}^{I}\dot{X}_{P} = {}^{I}\dot{X}_{0} + \boldsymbol{T}_{I\leftarrow B}\mathbf{H}(\omega)r + \boldsymbol{T}_{I\leftarrow B}\mathbf{H}(\omega)\sum_{k=1}^{N_m}\eta_k(t)\varphi_k(r) + \boldsymbol{T}_{I\leftarrow B}\sum_{k=1}^{N_m}\dot{\eta}_k(t)\varphi_k(r) \tag{3.10} $$

3.1.3 KINETIC ENERGY

The expression of the kinetic energy of the system can be computed as

$$ K = \frac{1}{2}\int_{\mathcal{B}} {}^{I}\dot{X}_{P}^{T}\,{}^{I}\dot{X}_{P}\rho(r)d\mathcal{B} \tag{3.11} $$

where $\rho(r)$ is the density distribution in the reference configuration. By substituting eq. (3.10) into eq. (3.11), the energy may be rewritten as

$$ K = \frac{1}{2}v^{T}\boldsymbol{M}v + \tilde{p}^{T}\left(v\times\omega\right) + v^{T}L_k\dot{\eta}_k + \frac{1}{2}\omega^{T}\tilde{\boldsymbol{J}}\omega + \omega^{T}\tilde{S}_k\dot{\eta}_k + \frac{1}{2}\dot{\eta}_k\boldsymbol{M}_F\dot{\eta}_k \tag{3.12} $$

where $\boldsymbol{M} = m\boldsymbol{I}$ is the mass matrix of the system, $v = T_{B\leftarrow I}\,{}^{I}\dot{X}_{0}$ is the translational velocity of the origin in the Body reference frame, ω is the angular velocity in the Body reference frame. The other terms are related to the flexibility of the specific body. The modal participation factors with respect to translation L_k and to rotation S_k indicate the coupling between the rigid motion (translation and rotation) and the k-th elastic mode and can be expressed as

$$ L_k = \int_{\mathcal{B}}\varphi_k\rho d\mathcal{B} \tag{3.13} $$

$$S_k = \int_{\mathcal{B}} r \times \varphi_k \rho d\mathcal{B} \tag{3.14}$$

where φ_k is the eigenvector associated to the k-th elastic mode. Therefore, the modified static moment can be written as

$$\tilde{p} = \int_{\mathcal{B}} r \rho d\mathcal{B} + L_k \eta_k = p + L_k \eta_k \tag{3.15}$$

where p is computed by using the formulation of the static moment for a rigid body. The eigenvectors φ_k may be rearranged in the matrix $\boldsymbol{\Phi} = [\varphi_1, \varphi_2, ..., \varphi_N]$, to obtain an expression for the modal mass matrix

$$\boldsymbol{M}_F = \int_{\mathcal{B}} \boldsymbol{\Phi}^T \boldsymbol{\Phi} \ \rho d\mathcal{B} \tag{3.16}$$

In case of eigenvectors normalized with respect to mass, the matrix $\boldsymbol{M}_F$ becomes an identity matrix and the coupling factor P_{kt} between k-th and t-th modes can be defined as

$$P_{kt} = \int_{\mathcal{B}} \varphi_k \times \varphi_t \ \rho d\mathcal{B} \tag{3.17}$$

which is used in the definition of the elastic variation of the rotation modal participation factor as

$$\tilde{S}_k = S_k + P_{kt} \eta_k \tag{3.18}$$

For a flexible body, the inertia tensor should be defined as

$$\tilde{\boldsymbol{J}} = \boldsymbol{J}_0 + \sum_{k=1}^{N_m} \boldsymbol{J}_1^k \eta_k + \sum_{k=1}^{N_m} \sum_{t=1}^{N_m} \boldsymbol{J}_2^{kt} \eta_k \eta_t \tag{3.19}$$

where

- $\boldsymbol{J}_0$ is the inertia tensor used in the classical equations describing the dynamics of a rigid body, defined as

$$J_{0_{sm}} = \int_{\mathcal{B}} \delta_{st} r_j r_j - r_s r_m \ \rho d\mathcal{B} \tag{3.20}$$

- $\boldsymbol{J}_1^k$ is the matrix representing the first variation of the inertia tensor related to the k-th elastic mode, defined as

$$J_{1\ sm}^k = \int_{\mathcal{B}} 2\delta_{sm} r_j \varphi_j^k - r_s \varphi_m^k - r_m \varphi_s^k \ \rho d\mathcal{B} \tag{3.21}$$

- $\boldsymbol{J}_2^{kt}$ is the matrix representing the second variation of the inertia tensor related to the k-th and t-th elastic mode, defined as

$$J_{2\ sm}^{kt} = \int_{\mathcal{B}} \delta_{sm}\varphi_j^k\varphi_j^t - \varphi_s^k\varphi_m^t \ \rho d\mathcal{B} \tag{3.22}$$

It is worth noting the off-diagonal components of $\boldsymbol{J}_2^{kt}$ matrix are the projection of the s-th components (in terms of coordinated axes) of the k-th mode on the m-th component of the t-th mode: in general, they are not symmetric. In addition, one may define the term

$$\tilde{\boldsymbol{J}}_1^k = \boldsymbol{J}_1^k + 2\sum_{k=1}^{N_m} \boldsymbol{J}_2^{kt}\eta_k \tag{3.23}$$

which will later be used. More details on how to derived the invariants $\boldsymbol{J}_1^k$ and $\boldsymbol{J}_2^{kt}$ can be found in the work of Santini and Gasbarri [4][5]. Different studies have been conducted to study the influence of such quantities on the overall system dynamics [7][8]. Such investigations agree that the Euclidean norm of the term $\boldsymbol{J}_1^k$ is typically smaller than the norm of $\boldsymbol{J}_0$ and, consequently, the variables $\boldsymbol{J}_2^{kt}$ and P_{kt} (which are generally even much lower than $\boldsymbol{J}_1^k$ in terms of norm) may be almost always neglected.

3.1.4 POTENTIAL ENERGY FUNCTIONALS

In this section, the potential energy functionals for a piezoelectric material and for gravitational field are introduced, to be further used when deriving the equations motion for the flexible spacecraft equipped with piezoelectric material.

3.1.4.1 PIEZO-ELECTRIC POTENTIAL ENERGY FUNCTIONAL

Concerning the potential energy functional, we consider both the elastic and piezoelectric contributions. By recurring to the Finite Element Method (FEM) theory, we can assume that the piezo constitutive equations can be written for the j-th finite element under the form [9][10]

$$\begin{aligned} T &= \boldsymbol{c}^{\boldsymbol{E}} S - \boldsymbol{e}^{\boldsymbol{T}} E_F \\ D &= \boldsymbol{e}\ S + \boldsymbol{\varepsilon}^{\boldsymbol{S}} E_F \end{aligned} \tag{3.24}$$

where T is the stress vector, S the strain vector, E_F the electric field, D the electric displacement, $\boldsymbol{c}^E$ the elastic coefficient at constant electric field, $\boldsymbol{e}$ the piezoelectric coupling term and $\boldsymbol{\varepsilon}^s$ the dielectric coefficients at constant strain. According to linear piezoelectricity theory [10], the electrical enthalpy H is defined as

$$H = \frac{1}{2}\left[S^T T - {E_F}^T Q\right] \tag{3.25}$$

The potential functional can be written as

$$\Pi_I^j = \frac{1}{2}\int_B \left[S^T T - {E_F}^T Q\right]\rho dB \tag{3.26}$$

Then, we can assume that the elastic displacement u and the electric potential ψ over an element can be related to their corresponding u_i and ψ_i values in specific point of the discretizes continuum, called nodes, by means of some shape functions N_u, N_ψ for both displacement and voltages

$$\begin{aligned} u &= \mathrm{N}_u u_i \\ \psi &= \mathrm{N}_\psi \psi_i \end{aligned} \tag{3.27}$$

Consequently, the strain vector and the electric field in eq. (3.26) can be written as

$$\begin{aligned} S &= D\,u = D\,\mathrm{N}_u\,u_i = B_u u_i \\ E_F &= -\nabla\psi = -\nabla \mathrm{N}_\psi \psi_i = -B_\psi \psi_i \end{aligned} \tag{3.28}$$

where ∇ is the gradient operator and D contains the derivatives

$$D = \begin{bmatrix} \partial_x & 0 & 0 & 0 & \partial_z & \partial_y \\ 0 & \partial_y & 0 & \partial_z & 0 & \partial_x \\ 0 & 0 & \partial_z & \partial_y & \partial_x & 0 \end{bmatrix}^T \tag{3.29}$$

The matrices B_u and B_ψ are considered shape functions derivatives. Based on eq. (3.26), the potential energy functional for a finite element can be then rewritten as

$$\Pi_I^j = \frac{1}{2} u_i^T \boldsymbol{K}_{UU} u_i + u_i^T \boldsymbol{K}_{U\psi} \psi_i - \psi_i^T \boldsymbol{K}_{\psi\psi} \psi_i \tag{3.30}$$

where u_i elastic displacement, $\boldsymbol{K}_{UU}$ stiffness matrix of the system, $\boldsymbol{K}_{U\psi}$ electro-mechanical coupling matrix, $\boldsymbol{K}_{\psi\psi}$ dielectric properties matrix, ψ electric potential

$$\boldsymbol{K}_{UU} = \int_B B_u^T c^E B_u \rho dB \tag{3.31}$$

$$\boldsymbol{K}_{U\psi} = \int_B B_u{}^T e^E B_\psi \rho dB \tag{3.32}$$

$$\boldsymbol{K}_{\psi\psi} = \int_B B_\psi{}^T \varepsilon^S B_\psi \rho dB \tag{3.33}$$

However, each j-th finite element of the continuum is connected to other elements via global nodes. Therefore, the degrees of freedom of each finite element have to be related to global degrees of freedom of the discretized body by means of mapping functions expressed as matrices L_u, L_ψ

$$\begin{aligned} u_i^k &= \boldsymbol{L}_u^k x \\ \psi_i^k &= \boldsymbol{L}_u^k \psi \end{aligned} \tag{3.34}$$

The potential functional for the assembled system can finally be written as

$$\Pi_I = \frac{1}{2} x^T \sum_j L_u^j{}^T \boldsymbol{K}_{UU}^j L_u^j x + x^T \sum_j L_u^j{}^T \boldsymbol{K}_{U\psi}^j L_\psi^j \psi - \psi^T \sum_j L_\psi^j{}^T \boldsymbol{K}_{\psi\psi}^j L_\psi^j \psi \tag{3.35}$$

where

$$\boldsymbol{K}_{UU}^G = \sum_k L_u^j{}^T \boldsymbol{K}_{UU}^k L_u^j \tag{3.36}$$

$$\boldsymbol{K}_{U\psi}^G = \sum_k L_u^j{}^T \boldsymbol{K}_{U\psi}^j L_\psi^j \tag{3.37}$$

$$\boldsymbol{K}_{\psi\psi}^G = \sum_k L_\psi^j{}^T \boldsymbol{K}_{\psi\psi}^j L_\psi^j \tag{3.38}$$

are the *global* stiffness, electro-mechanical coupling and electric properties matrices.

3.1.4.2 GRAVITATIONAL POTENTIAL

In this section, the conservative external actions contribution to the flexible body dynamics is considered in terms of gravitational central field interaction. Such an effect is particularly relevant when studying the motion of a body in a Low Earth Orbit (LEO) environment, where the effects of the gravity attraction are surely not negligible. In detail, the unit mass Earth's gravitational potential [3] may be expressed as

$$\Pi_E = -\frac{\mu_\oplus}{\left|{}^I X_P\right|}\left\{1 - \sum_{k=2}^{\infty} J_k \left(\frac{R_e}{\left|{}^I X_P\right|}\right) P_k \sin(\mathrm{M}) + \sum_{k=2}^{\infty}\sum_{j=2}^{\infty} J_{k,j} P_k^j \sin(\mathrm{M}) \cos\left[m\left(L - L_{k,j}\right)\right]\right\} \tag{3.39}$$

where $\mu_{\oplus} = 398600.4 km^3/s^2$ is the Earth standard gravitational parameter, ${}^I X_P$ is the vector indicating the position of a generic point P of the body with respect to the center of the earth in the Inertial reference frame, R_e is the Earth's radius, M and L are the body longitude and latitude in the Earth Centered Earth Fixed (ECEF) reference frame.

By considering the Earth as a perfect sphere, the contribution of the higher order terms may be neglected and the potential becomes

$$\Pi_E = -\frac{\mu_{\oplus}}{\left|{}^I X_P\right|} \tag{3.40}$$

The vector ${}^I X_P$ may be written as in eq. (3.5) as

$${}^I X_P = {}^I X_0 + \boldsymbol{T}_{I \leftarrow B}\left(r + \sum_{k=1}^{N_m} \eta_k(t)\varphi_k(r)\right) = {}^I X_0 + \boldsymbol{T}_{I \leftarrow B}(\xi) \tag{3.41}$$

By applying a Taylor expansion to the term $1/{}^I X_P$ up to the second order

$$\frac{1}{\left|{}^I X_P\right|} = \frac{1}{\left|{}^I X_0\right|}\left(1 - \hat{k}^T \frac{\xi}{\left|{}^I X_0\right|} - \frac{1}{2}\frac{\xi^T\xi}{\left|{}^I X_0\right|^2} + \frac{3}{2}\frac{\left(\hat{k}^T\xi\right)^2}{\left|{}^I X_0\right|^2}\right) \tag{3.42}$$

where $\hat{k} = \boldsymbol{T}_{B \leftarrow I}\, {}^I X_0 \big/ \left|{}^I X_0\right|$ is the unit vector of the anti-direction of the central gravity field expressed in Body reference frame. Substituting eq. (3.42) into eq. (3.40) and integrating over the volume of the body we obtain

$$\Pi_E = -\mu_{\oplus}\int_{\mathcal{B}} \frac{1}{\left|{}^I X_0\right|}\left(1 - \hat{k}^T \frac{\xi}{\left|{}^I X_0\right|} - \frac{1}{2}\frac{\xi^T\xi}{\left|{}^I X_0\right|^2} + \frac{3}{2}\frac{\left(\hat{k}^T\xi\right)^2}{\left|{}^I X_0\right|^2}\right)\rho(r)d\mathcal{B} \tag{3.43}$$

that becomes

$$\Pi_E = -\frac{\mu_{\oplus} m}{\left|{}^I X_0\right|} + \frac{\mu_{\oplus}\hat{k}^T\tilde{p}}{\left|{}^I X_0\right|^2} + \frac{3}{2}\frac{\mu_{\oplus}\hat{k}^T\tilde{\boldsymbol{J}}k}{\left|{}^I X_0\right|^3} - \frac{1}{2}\frac{\mu_{\oplus} tr\left(\tilde{\boldsymbol{J}}\right)}{\left|{}^I X_0\right|^3} \tag{3.44}$$

By deriving with respect to the Lagrangian variables [3][4], the expressions of the gravitational forces, torques and k-th elastic forces in Body frame can be described as reported in eq. (3.45). It should be noticed the term c_g represents the so-called *gravity gradient* torque, which is composed also by an additional term, depending on the static moment of the structure, as the dynamic equations are not referred to

the body CoM, but are written with respect to a generic point P.

$$
\begin{aligned}
f_g &= -\frac{m\boldsymbol{I}\mu_{\oplus}\hat{k}}{\left|{}^{I}X_0\right|^2} - \frac{\mu_{\oplus}\tilde{p}}{\left|{}^{I}X_0\right|^3} + \frac{3\mu_{\oplus}\hat{k}\left(\hat{k}^T\tilde{p}\right)}{\left|{}^{I}X_0\right|^3} - \frac{3\mu_{\oplus}\tilde{\boldsymbol{J}}\hat{k}}{\left|{}^{I}X_0\right|^4} + \frac{15\mu_{\oplus}\hat{k}\left(\hat{k}^T\tilde{\boldsymbol{J}}\hat{k}\right)}{2\left|{}^{I}X_0\right|^4} - \frac{3\mu_{\oplus}\hat{k}tr\left(\tilde{\boldsymbol{J}}\right)}{2\left|{}^{I}X_0\right|^4} \\
c_g &= -\frac{\mu_{\oplus}\hat{k}}{\left|{}^{I}X_0\right|^2}\left(\tilde{p}\wedge\hat{k}\right) + \frac{3\mu_{\oplus}}{\left|{}^{I}X_0\right|^3}(\hat{k}\wedge\tilde{\boldsymbol{J}}\hat{k}) \\
\tilde{f}_{g,k} &= -\frac{\mu_{\oplus}}{\left|{}^{I}X_0\right|^2}\left(\hat{k}^T L_k\right) - \frac{3\mu_{\oplus}}{2\left|{}^{I}X_0\right|^3}\left(\hat{k}^T\tilde{\boldsymbol{J}}_1^k\hat{k}\right) + \frac{\mu_{\oplus}}{2\left|{}^{I}X_0\right|^3}tr\left(\tilde{\boldsymbol{J}}_1^k\right)
\end{aligned}
\tag{3.45}
$$

3.1.5 GOVERNING EQUATIONS

Now we can split eq. (3.3), written in the Inertial reference frame, in

$$
\begin{cases}
\dfrac{d}{dt}\left[\dfrac{\partial K}{\partial {}^{I}\dot{X}_0} - \dfrac{\partial \Pi_I}{\partial {}^{I}\dot{X}_0}\right] - \left[\dfrac{\partial K}{\partial {}^{I}X_0} - \dfrac{\partial \Pi_I}{\partial {}^{I}X_0}\right] + \dfrac{\partial \mathcal{F}}{\partial {}^{I}\dot{X}_0} = -\dfrac{\partial \Pi_E}{\partial {}^{I}X_0} + F^{nc} \\
\dfrac{d}{dt}\left[\dfrac{\partial K}{\partial \dot{\Theta}} - \dfrac{\partial \Pi_I}{\partial \dot{\Theta}}\right] - \left[\dfrac{\partial K}{\partial \Theta} - \dfrac{\partial \Pi_I}{\partial \Theta}\right] + \dfrac{\partial \mathcal{F}}{\partial \dot{\Theta}} = -\dfrac{\partial \Pi_E}{\partial \Theta} + C^{nc} \\
\dfrac{d}{dt}\left[\dfrac{\partial K}{\partial \dot{\eta}} - \dfrac{\partial \Pi_I}{\partial \dot{\eta}}\right] - \left[\dfrac{\partial K}{\partial \eta} - \dfrac{\partial \Pi_I}{\partial \eta}\right] + \dfrac{\partial \mathcal{F}}{\partial \dot{\eta}} = -\dfrac{\partial \Pi_E}{\partial \eta} + Q_A{}^{nc}
\end{cases}
\tag{3.46}
$$

However, being $\Pi_I = \Pi_I(A), \Pi_E = \Pi_E(S)$ and $\mathcal{F} = \mathcal{F}\left(A, \dot{A}\right)$ (Π_I and $\mathcal{F}$ are quadratic positive semi definite functions in their arguments), eq. (3.46) may be rewritten as

$$
\begin{cases}
\dfrac{d}{dt}\dfrac{\partial K}{\partial {}^{I}\dot{X}_0} = -\dfrac{\partial \Pi_E}{\partial {}^{I}X_0} + F^{nc} \\
\dfrac{d}{dt}\dfrac{\partial K}{\partial \dot{\Theta}} = -\dfrac{\partial \Pi_E}{\partial \Theta} + C^{nc} \\
\dfrac{d}{dt}\dfrac{\partial K}{\partial \dot{\eta}} - \dfrac{\partial K}{\partial \eta} + \dfrac{\partial \Pi_I}{\partial \eta} + \dfrac{\partial \mathcal{F}}{\partial \dot{\eta}} = -\dfrac{\partial \Pi_E}{\partial \eta} + Q_A{}^{nc}
\end{cases}
\tag{3.47}
$$

By referring to the chain derivation rule, and recalling that $v = T_{B\leftarrow I}\,{}^{I}\dot{X}_0$, the first of eq. (3.47), can be written in the Body reference frame as

$$
\frac{d}{dt}\frac{\partial K}{\partial v} + \boldsymbol{H}(\omega)\frac{\partial K}{\partial v} = \boldsymbol{T}_{B\leftarrow I}\left(-\frac{\partial \Pi_E}{\partial {}^{I}X_0} + F^{nc}\right) = f_g + f^{nc}
\tag{3.48}
$$

where $\boldsymbol{H}(\omega)$ is the anti-symmetric matrix introduced in eq. (3.8).

By substituting the expression of kinetic energy in eq. (3.12) into eq. (3.48) and computing the corresponding time derivatives, we may obtain

$$\boldsymbol{M}\, a+\omega\wedge\left(\omega\wedge\tilde{p}\right)+\dot{\omega}\wedge\tilde{p}+2\omega\wedge\sum_{k=1}^{N_m}L_k\dot{\eta}_k+\sum_{k=1}^{N_m}L_k\ddot{\eta}_k=f_G+F^{nc} \tag{3.49}$$

with $a=\dot{v}+\omega\times v$ the acceleration in the Body reference frame. By assuming the rotational rate depends linearly on the derivatives of the three Lagrangian parameters Θ (i.e. Euler's angles), $\partial\dot{\Theta}=\partial\omega$, and by adding and subtracting the term $\partial K/\partial\Theta$ to the second relation of eq. (3.47) it can be obtained

$$\frac{d}{dt}\left(\frac{\partial\omega}{\partial\dot{\Theta}}\frac{\partial K}{\partial\omega}\right)-\frac{\partial\omega}{\partial\Theta}\frac{\partial K}{\partial\omega}+\frac{\partial v}{\partial\Theta}\frac{\partial K}{\partial v}=\boldsymbol{T}_{B\leftarrow I}\left(-\frac{\partial\Pi_E}{\partial\Theta}+C^{nc}\right)=c_g+c^{nc} \tag{3.50}$$

So that one may write

$$\frac{d}{dt}\frac{\partial K}{\partial\omega}+\boldsymbol{H}(\omega)\frac{\partial K}{\partial\omega}+\boldsymbol{H}(v)\frac{\partial K}{\partial v}=c_g+c^{nc} \tag{3.51}$$

where $\boldsymbol{H}(v)$ is the anti-symmetric matrix of the translational velocity in the Body reference frame. By substituting the expression of kinetic energy in eq. (3.12) into eq. (3.51)

$$\tilde{\boldsymbol{J}}\dot{\omega}+\omega\wedge\tilde{\boldsymbol{J}}\omega+\tilde{p}\wedge a+\sum_{k=1}^{N_m}\sum_{t=1}^{N_m}P^{kt}\dot{\eta}_t\dot{\eta}_k+\sum_{k=1}^{N_m}\tilde{S}_k\ddot{\eta}_k+\omega\wedge\sum_{k=1}^{N_m}\tilde{S}_k\dot{\eta}_k+\sum_{k=1}^{N_m}\tilde{\boldsymbol{J}}_1^k\dot{\eta}_k\omega=c_g+c^{nc} \tag{3.52}$$

To write the equation of flexible dynamics we have to consider both the internal potential Π_I and the dissipation function $\mathcal{F}$

$$\frac{d}{dt}\frac{\partial K}{\partial\dot{\eta}}-\frac{\partial K}{\partial\eta}+\frac{\partial\Pi_I}{\partial\eta}+\frac{\partial\mathcal{F}}{\partial\dot{\eta}}=-\frac{\partial\Pi_E}{\partial\eta}+Q_A{}^{nc} \tag{3.53}$$

By assuming a classic linear elastic and dissipative model, we have

$$\Pi_I=\frac{1}{2}x^T\boldsymbol{K}_{UU}^G x+x^T\boldsymbol{K}_{U\psi}^G\psi-\psi^T\boldsymbol{K}_{\psi\psi}^G\psi \tag{3.54}$$

$$\mathcal{F}=\dot{x}^T\boldsymbol{C}_D\dot{x} \tag{3.55}$$

where $\boldsymbol{C}_D$ represents the damping matrix. By assuming that a linear transformation exists as $\eta=\boldsymbol{\Phi}x$, eq.s (3.54) and (3.55) may be projected on modal basis, assuming the form

$$\Pi_I=\frac{1}{2}\eta^T\tilde{\boldsymbol{K}}_{UU}^G\eta+\eta^T\tilde{\boldsymbol{K}}_{U\psi}^G\psi-\psi^T\boldsymbol{K}_{\psi\psi}^G\psi \tag{3.56}$$

$$\mathcal{F}=\dot{\eta}^T\tilde{\boldsymbol{C}}_D\dot{\eta} \tag{3.57}$$

where

$$\tilde{\boldsymbol{K}}_{UU}^{G} = \boldsymbol{\Phi}^{T} \boldsymbol{K}_{UU}^{G} \boldsymbol{\Phi} \tag{3.58}$$

$$\tilde{\boldsymbol{K}}_{U\psi}^{G} = \boldsymbol{\Phi}^{T} \boldsymbol{K}_{U\psi}^{G} \tag{3.59}$$

$$\tilde{\boldsymbol{C}}_{D} = \boldsymbol{\Phi}^{T} \boldsymbol{C}_{D} \boldsymbol{\Phi} \tag{3.60}$$

with $\boldsymbol{\Phi}$ matrix containing the elastic modes of the flexible structure. In detail, the matrix $\tilde{\boldsymbol{K}}_{UU}^{G}$ is assumed equivalent to $\boldsymbol{\Omega}^{2}$, which is a diagonal matrix listing all squared angular frequencies of the appendages as cantilevered to satellite. Concerning the damping model, we may assume $\boldsymbol{C}_{D} = \alpha \boldsymbol{K}_{UU}^{G}$ (i.e. damping proportional to the stiffness of the structure) so to have $\tilde{\boldsymbol{C}}_{D} = \boldsymbol{\Phi}^{T} \alpha \boldsymbol{K}_{UU}^{G} \boldsymbol{\Phi} = \alpha \boldsymbol{\Omega}^{2}$ with some coefficient α guaranteeing the existence of a real modal matrix. In particular, one may consider $\tilde{\boldsymbol{C}}_{D} = 2\boldsymbol{\Sigma}\boldsymbol{\Omega}$, where $\boldsymbol{\Sigma}$ is a diagonal matrix containing the k-th damping factor ξ_k of the corresponding elastic mode.

By substituting the expression of kinetic energy of eq. (3.12), internal potential energy of eq. (3.56), dissipative functional of (3.57) into eq. (3.53), and by computing relevant time derivatives, the final expression of the flexible dynamics equation for the k-th mode will be

$$L_k^T a + \tilde{S}_k^T \dot{\omega} + \ddot{\eta}_k + \Omega_k^2 \eta_k + 2\xi_k \Omega_k \eta_k - \frac{1}{2} \omega^T \boldsymbol{J}_1^k \omega + 2\omega^T \sum_{m=1}^{N_m} P^{km} \dot{\eta}_m + \tilde{\boldsymbol{K}}_{U\psi} \psi_k = \tilde{f}_{g,k} + \tilde{Q}_{\eta}^{nc} \tag{3.61}$$

3.1.5.1 FINAL SYSTEM OF EQUATIONS

The final equations of motion can now be written. It should be noticed, however, that the terms appearing in the kinematics equation in eq. (3.5) have different order of magnitudes. Indeed, the position of the origin of Body reference frame ${}^{I}X_0$ is of the same order of the Earth's radius, the vector r defining the location of a generic point P in the body reference frame is generally of the order of meters, while the elastic displacement x may be considered as a fraction of a characteristic length of the spacecraft. Hence, the study of the orbital dynamics and of the displacement of the body with respect to the Body reference frame would produce few significant results. Conversely, investigating the attitude dynamics in the Inertial reference frame, being such dynamics focussed on the rotation of the body around its reference point, would make difficult to estimate the Euler's angles with respect to the orbital frame. Therefore, one may express the first

equation (translation) with respect to the Inertial reference frame, by multiplying for the transformation matrix $\boldsymbol{T}_{I\leftarrow B}$, while the second one (rotation) with respect to the Body reference frame, as follows

$$M\,{}^{I}\ddot{X}_0 + \boldsymbol{T}_{I\leftarrow B}\left[\omega\wedge\left(\omega\wedge\tilde{p}\right)+\dot{\omega}\wedge\tilde{p}+2\omega\wedge\sum_{k=1}^{N_m}L_k\dot{\eta}_k+\sum_{k=1}^{\tilde{N}_m}L_k\ddot{\eta}_k\right]=\boldsymbol{T}_{I\leftarrow B}f_g+\boldsymbol{T}_{I\leftarrow B}f^{nc} \quad (3.62)$$

$$\tilde{\boldsymbol{J}}\dot{\omega}+\omega\wedge\tilde{\boldsymbol{J}}\omega+\tilde{p}\wedge a+\sum_{k=1}^{N_m}\sum_{t=1}^{N_m}P^{kt}\dot{\eta}_t\dot{\eta}_k+\sum_{k=1}^{N_m}\tilde{S}_k\ddot{\eta}_k+\omega\wedge\sum_{k=1}^{N_m}\tilde{S}_k\dot{\eta}_k+\sum_{k=1}^{N_m}\tilde{\boldsymbol{J}}_1^k\dot{\eta}_k\omega=c_g+c^{nc} \quad (3.63)$$

$$L_k^T a+\tilde{S}_k^T\dot{\omega}+\ddot{\eta}_k+\Omega_k^2\eta_k+2\xi_k\Omega_k\eta_k-\frac{1}{2}\omega^T\boldsymbol{J}_1^k\omega+2\omega^T\sum_{m=1}^{N_m}P^{km}\dot{\eta}_m=-\tilde{\boldsymbol{K}}_{U\psi}\psi_k+\tilde{f}_{g,k}+\tilde{Q}_\eta^{\,nc} \quad (3.64)$$

The system of equations may be rewritten in a more compact form as

$$\boldsymbol{M}\ddot{S}+\boldsymbol{C}\dot{S}+\boldsymbol{K}S+N_L=F \quad (3.65)$$

where S is the vector of Lagrangian parameters already presented at the beginning of this chapter. The matrix $\boldsymbol{M}$ may be defined as

$$\boldsymbol{M}=\begin{bmatrix} m\boldsymbol{I} & \boldsymbol{T}_{I\leftarrow B}\tilde{\boldsymbol{p}}^{\times} & \boldsymbol{T}_{I\leftarrow B}\boldsymbol{L} \\ \left(\tilde{\boldsymbol{p}}^{\times}\right)^T\boldsymbol{T}_{I\leftarrow B}^T & \tilde{\boldsymbol{J}} & \tilde{\boldsymbol{S}} \\ \boldsymbol{L}^T\boldsymbol{T}_{I\leftarrow B}^T & \tilde{\boldsymbol{S}}^T & \boldsymbol{M}_F \end{bmatrix} \quad (3.66)$$

where $\tilde{\boldsymbol{p}}^{\times}$ is the anti-symmetric matrix of the static moment vector, defined as

$$\tilde{\boldsymbol{p}}^{\times}=\begin{bmatrix} 0 & \tilde{p}_3 & -\tilde{p}_2 \\ -\tilde{p}_3 & 0 & \tilde{p}_1 \\ \tilde{p}_2 & -\tilde{p}_1 & 0 \end{bmatrix} \quad (3.67)$$

Furthermore, the matrices $\boldsymbol{C}$ and $\boldsymbol{K}$ are

$$\boldsymbol{K}=\begin{bmatrix} \boldsymbol{0} & \boldsymbol{0} & \boldsymbol{0} \\ \boldsymbol{0} & \boldsymbol{0} & \boldsymbol{0} \\ \boldsymbol{0} & \boldsymbol{0} & \boldsymbol{\Omega^2} \end{bmatrix} \qquad \boldsymbol{C}=\begin{bmatrix} \boldsymbol{0} & \boldsymbol{0} & \boldsymbol{0} \\ \boldsymbol{0} & \boldsymbol{0} & \boldsymbol{0} \\ \boldsymbol{0} & \boldsymbol{0} & 2\Sigma\boldsymbol{\Omega} \end{bmatrix} \quad (3.68)$$

The vector of the non-linear terms N_L is

$$N_L=\begin{bmatrix} \boldsymbol{T}_{I\leftarrow B}\left[\omega\wedge\left(\omega\wedge\tilde{p}\right)+2\omega\wedge\sum_{k=1}^{N_m}L_k\dot{\eta}_k\right] \\ \omega\wedge\tilde{\boldsymbol{J}}\omega+\sum_{k=1}^{N_m}\sum_{t=1}^{N_m}P^{kt}\dot{\eta}_t\dot{\eta}_k+\omega\wedge\sum_{k=1}^{N_m}\tilde{S}_k\dot{A}_k+\sum_{k=1}^{N_m}\tilde{\boldsymbol{J}}_1^k\eta_k\omega \\ -\frac{1}{2}\omega^T\boldsymbol{J}_1^k\omega+2\omega^T\sum_{m=1}^{N_m}P^{km}\dot{\eta}_m \end{bmatrix} \quad (3.69)$$

The term containing the generalized forces acting on the system is

$$F = \begin{bmatrix} \boldsymbol{T}_{I\leftarrow B} f_g + \boldsymbol{T}_{I\leftarrow B} f^{nc} \\ c_g + c^{nc} \\ -\tilde{\boldsymbol{K}}_{U\psi}\psi_k + \tilde{f}_{g,k} + \tilde{Q}_\eta^{\,nc} \end{bmatrix} \tag{3.70}$$

The system of equations reported in eq. (3.65) can be applied to the problem of a flexible appendage attached to a central platform.

3.2 ASSEMBLY OF MULTIPLE FLEXIBLE APPENDAGES

The spacecraft is hereby considered as a central rigid bus equipped with flexible appendages complemented with active vibration suppression devices. The proposed formulation allows a generic approach for assembling different FEMs and rigid models. In general, we distinguish the following common features of almost all satellites:

1. A rigid main body (also called box/hub/platform in the space industry) to which the rest of the substructures will be connected. The term "rigid" is an approximation meaning that the flexible modes are too far away from the low frequency modes, by at least one order of magnitudes;

2. Substructures clamped to the rigid body, which could be deployable appendages, as solar panels, booms, trusses, antennas and masts.

In the next sections, a multibody approach will be used to derive the non-linear dynamics for a spacecraft equipped with such different flexible appendages.

3.2.1 FROM APPENDAGES MODEL TO DYNAMIC EQUATIONS

Typically, for general tri-dimensional geometries, the flexible substructures are designed by using commercial software implementing the theory of finite elements (as Nastran, Ansys, etc.). The data retrieved from such tools may be then imported in a programming environment to develop the tri-dimensional full dynamic model of the system.

In this case, both rigid body characteristics (as mass, inertia, static moment) and couplings between flexible and rigid dynamics, namely the modal participation factors, are defined in a specific Appendage reference frame A_i, with $i = 1,...,L$, being L the total number of appendages equipped to the spacecraft, which can be translated and generally oriented with respect to the satellite platform (see Fig. 3-3).

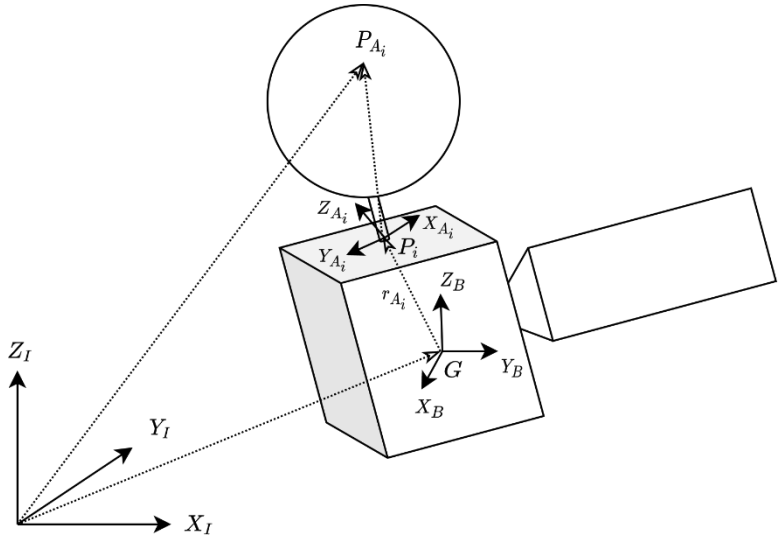

Fig. 3-3: Satellite with flexible appendages

As already anticipated in Par. 3.1.1.6, it is necessary to transform the information of each appendage to the Body reference frame by using a transformation matrix $\boldsymbol{T}_{B\leftarrow A_i}$. To this purpose, the integrals of inertial properties and rigid/flexible couplings should be transformed as well, by considering that the kinematics is modified as follows

$$ {}^{I}X_{P_{A_i}} = {}^{I}X_{G} + \boldsymbol{T}_{I\leftarrow B}\left(r_{A_i} + \boldsymbol{T}_{B\leftarrow A_i} r + \sum_{k=1}^{N_m} \boldsymbol{T}_{B\leftarrow A_i} \eta_k(t)\varphi_k(r) \right) \tag{3.71} $$

Where G is the origin of the Body reference frame, $r_{A_i} = P_i G$ is the vector indicating the position of the attachment point in the Body reference frame, while the vector $P_{A_i}P_i = r + \sum_{k=1}^{N} \eta_k(t)\varphi_k(r)$ represents the location of a generic point P_{A_i} of the appendage with respect to the attachment point, in the Appendage reference frame. By following the same procedure illustrated in Par. 3.1.3, the main integrals of inertial properties should be now computed in the appendage domain $r \in V_A$ and referred to the origin of the Body reference frame as follows

$$m_{A_i} = \int_{V_{A_i}} \rho_{A_i} dV_{A_i} \tag{3.72}$$

$${}^{B}p_G^{A_i} = \int_{V_{A_i}} \left(\boldsymbol{T}_{B\leftarrow A_i} r + r_{A_i} \right) \rho_{A_i} dV_{A_i} = \boldsymbol{T}_{B\leftarrow A_i} \, {}^{A_i}p_{P_i}^{A_i} + m_{A_i} r_{A_i} \tag{3.73}$$

$${}^{B}L_k^{A_i} = \int_{V_A} \left(\boldsymbol{T}_{B\leftarrow A_i} \varphi_k(r) \right) \rho_A dV_A = \boldsymbol{T}_{B\leftarrow A_i} \, {}^{A_i}L_k^{A_i} \tag{3.74}$$

$${}^{B}S_k^{A_i} = \int_{V_{A_i}} \left(\boldsymbol{T}_{B\leftarrow A_i} r + r_{A_i} \right) \times \left(\boldsymbol{T}_{B\leftarrow A_i} \varphi_k(r) \right) \rho_{A_i} dV_{A_i} = \boldsymbol{T}_{B\leftarrow A_i} \, {}^{A_i}S_k^{A_i} + r_{A_i} \times \boldsymbol{T}_{B\leftarrow A_i} \, {}^{A_i}L_k^{A_i} \tag{3.75}$$

$$\begin{aligned} {}^{B}\boldsymbol{J}_G^{A_i} &= \int_{V_A} \left(\boldsymbol{T}_{B\leftarrow A_i} r + r_{A_i} \right)^T \left(\boldsymbol{T}_{B\leftarrow A_i} r + r_{A_i} \right) - \left(\boldsymbol{T}_{B\leftarrow A_i} r + r_{A_i} \right) \left(\boldsymbol{T}_{B\leftarrow A_i} r + r_{A_i} \right)^T \rho_A dV_A = \\ & \boldsymbol{T}_{A_i\leftarrow B} \, {}^{A_i}\boldsymbol{J}_{P_i}^{A_i} \boldsymbol{T}_{A_i\leftarrow B} - m_{A_i} \left(r_{A_i}{}^T r_{A_i} - r_{A_i} r_{A_i}{}^T \right) + {}^{B}p_{A_i}^{P_i T} r_{A_i} - {}^{B}p_{A_i}^{P_i} r_{A_i}{}^T + r_{A_i}{}^T \, {}^{B}p_{A_i}^{P_i} - r_{A_i} \, {}^{B}p_{A_i}^{P_i T} \end{aligned} \tag{3.76}$$

In the presented notation, the left superscript indicates the reference frame in which the term is written, the right superscript the body to which the term is referred (bus or appendages) and the right subscript the point with respect to the term is computed. In detail, ${}^{B}p_G^{A_i}$ is the static moment of the appendage transported to the bus CoG G in the Body reference frame, ${}^{B}L_k^{A_i}$ and ${}^{B}S_k^{A_i}$ are the modal participation factors rotated and transported to the bus CoM, ${}^{B}\boldsymbol{J}_G^{A_i}$ is the inertia tensor of the appendage transferred to the bus CoM in the Body reference frame. Alternatively, if we compute the inertia tensor ${}^{A_i}\boldsymbol{J}_{G_{A_i}}^{A_i}$ with respect to the CoM G_{A_i} of the appendage itself (i.e. the origin of the Appendage reference frame is the CoM of the substructure and ${}^{B}p_{P_i}^{A_i} = 0$), we may directly apply the Huygens theorem and obtain the classical expression

$$\begin{aligned} {}^{B}\boldsymbol{J}_G^{A_i} &= \int_{V_A} \left(\boldsymbol{T}_{B\leftarrow A_i} r + r_{A_i} \right)^T \left(\boldsymbol{T}_{B\leftarrow A_i} r + r_{A_i} \right) - \left(\boldsymbol{T}_{B\leftarrow A_i} r + r_{A_i} \right) \left(\boldsymbol{T}_{B\leftarrow A_i} r + r_{A_i} \right)^T \rho_A dV_A = \\ & \boldsymbol{T}_{A_i\leftarrow B} \, {}^{A_i}\boldsymbol{J}_{G_{A_i}}^{A_i} \boldsymbol{T}_{A_i\leftarrow B} - m_{A_i} \left(r_{A_i}{}^2 \right) \end{aligned} \tag{3.77}$$

Furthermore, we have

$${}^{B}P_{kt}^{A_i} = \int_{V_{A_i}} \left(\boldsymbol{T}_{B\leftarrow A_i} \varphi_k \times \boldsymbol{T}_{B\leftarrow A_i} \varphi_t \right) \rho_{A_i} dV_{A_i} \tag{3.78}$$

$${}^{B}\tilde{S}_k^{A_i} = {}^{B}S_k^{A_i} + {}^{B}P_{kt}\eta_k \tag{3.79}$$

$${}^{B}\boldsymbol{J}_1^{A_i,k}{}_{sm} = \int_{V_{A_i}} \begin{matrix} 2\delta_{sm} \left(\boldsymbol{T}_{B\leftarrow A_i} r + r_{A_i} \right)_j \boldsymbol{T}_{B\leftarrow A_i} \varphi_j^k - \left(\boldsymbol{T}_{B\leftarrow A_i} r + r_{A_i} \right)_s \boldsymbol{T}_{B\leftarrow A_i} \varphi_m^k - \\ - \left(\boldsymbol{T}_{B\leftarrow A_i} r + r_{A_i} \right)_m \boldsymbol{T}_{B\leftarrow A_i} \varphi_s^k \end{matrix} \rho_{A_i} dV_{A_i} \tag{3.80}$$

$$ {}^{B}J_{2}^{A_i,kt}{}_{sm} = \int_{V_{A_i}} \delta_{sm} \boldsymbol{T}_{B\leftarrow A_i} \varphi_j^k \boldsymbol{T}_{B\leftarrow A_i} \varphi_j^t - \boldsymbol{T}_{B\leftarrow A_i} \varphi_s^k \boldsymbol{T}_{B\leftarrow A_i} \varphi_m^t \, \rho_{A_i} dV_{A_i} \tag{3.81} $$

$$ {}^{B}\tilde{\boldsymbol{J}}_{1}^{A_i,k} = {}^{B}\boldsymbol{J}_{1}^{A_i,k} + 2\sum_{k=1}^{N} {}^{B}\boldsymbol{J}_{2}^{A_i,kt} \eta_k \tag{3.82} $$

Finally, the equations (3.62), (3.63) and (3.64) may be easily rewritten by substituting the new expressions of the inertial terms to obtain their expression with respect to the satellite CoG G, as it will be presented in the next section.

3.2.2 MULTIBODY APPROACH

The study of large space structures composed of different flexible appendages has been a major concern in the last decades in both mechanics and control applications. Several approaches were used to describe flexible models composed of more than one appendage in tree-type, star-like or chain-like configurations [11][12][13]. Among them, one of the most referenced method in literature is Kane's approach [14], used in several fields as space robotic dynamics, in-orbit servicing, flexible spacecraft dynamics with sloshing propellant. Moreover, techniques to build the overall dynamics of an assembled system based on *substructuring* approaches have been investigated as well for designing, optimizing and controlling large systems. Such a philosophy consists in the macrodiscretization of those systems into a set of subsystems known as substructures. Indeed, each substructure can be modelled independently from the others (via analytical models in easier cases or finite element, or F.E., techniques for more complex bodies) in order to recover the behaviour of the system for different boundaries conditions. To properly incorporate F.E. data in a dynamic model, two main procedures were followed: Transfer Matrix (TM) and Component Modes Synthesis (CMS). The original TM method was proposed in [15] and then complemented with F.E. theory in [16]. However, the TM technique has some limitations due to the inversion of matrices which are dependent on boundary conditions [17]. As a matter of fact, the most common approach in engineering practice is the CMS, as introduced in [18][19]. In this field, methods based on the relation between forces and accelerations at the attachment point of the appendage on the main body, known as mass/inertia approach, have been developed in [20] and adopted by Alazard et al. [21].

In this thesis, a general multibody approach based on mass/inertia approach complemented with piezoelectric distributed element is illustrated: the equations for each of the M bodies to be connected to a central hub are written in each Body reference frame (with the corresponding implemented smart devices), then the forces exchanged between each couple of bodies at interconnection points are equated and equations for the complete assembly written. By assuming a central rigid body, we may write the equations for the satellite platform for a generic point P_b as

$$\begin{bmatrix} m_b \boldsymbol{I} & {}^B\boldsymbol{p}_{P_b}^{b\times} \\ {}^B\boldsymbol{p}_{P_b}^{b\times T} & {}^B\boldsymbol{J}_{P_b}^{b} \end{bmatrix} \begin{bmatrix} {}^B a_{P_b}^{b} \\ {}^B\dot{\omega}^{B|I} \end{bmatrix} = \begin{bmatrix} F_{P_b}^{b} \\ C_{P_b}^{b} \end{bmatrix} - \begin{bmatrix} {}^B\omega^{B|I} \times {}^B\omega^{B|I} \times {}^B p_{P_b}^{b} \\ {}^B\omega^{B|I} \times {}^B\boldsymbol{J}_{P_b}^{b}\, {}^B\omega^{B|I} \end{bmatrix} \tag{3.83}$$

which is the system of equations we obtain from eq.s (3.49) and (3.52) without considering the flexibility of the system. In detail, ${}^B\omega^{B|I}$ is the angular rate of the body with respect to the Inertial reference frame, written in the Body reference frame, ${}^B a_{P_b}^{b}$ is the acceleration of the point P_b in Body frame, associated at the bus of the spacecraft (indicated by the letter b), $F_{P_b}^{b}$ and $C_{P_b}^{b}$ are forces and torques exerted on the body at point P_b. To simplify the following notation, the angular velocity ${}^B\omega^{B|I}$ is simply indicated as ω_b. If we assume to integrate the equations with respect to the platform CoG G, the static moment ${}^B\boldsymbol{p}_b$ will be zero and we obtain

$$\begin{bmatrix} m_b & 0 \\ 0 & {}^B\boldsymbol{J}_G^{b} \end{bmatrix} \begin{bmatrix} {}^B a_G^{b} \\ \dot{\omega}_b \end{bmatrix} = \begin{bmatrix} F_G^{b} \\ C_G^{b} \end{bmatrix} - \begin{bmatrix} 0 \\ \omega_b \times {}^B\boldsymbol{J}_G^{b}\omega_b \end{bmatrix} \tag{3.84}$$

If other forces are exerted to the spacecraft at points different from G, they can easily be transported to G by using the following relation

$$\begin{bmatrix} F_G^{b} \\ C_G^{b} \end{bmatrix} = \begin{bmatrix} \boldsymbol{I} & \boldsymbol{0} \\ \boldsymbol{GP}^{\times} & \boldsymbol{I} \end{bmatrix} \begin{bmatrix} F_{P_b}^{b} \\ C_{P_b}^{b} \end{bmatrix} = \boldsymbol{\tau}_{GP} \begin{bmatrix} F_{P_b}^{b} \\ C_{P_b}^{b} \end{bmatrix} \tag{3.85}$$

The operator $(\bullet)^{\times}$ indicates an anti-symmetric matrix. Therefore, we may write

$$\begin{bmatrix} m_b & 0 \\ 0 & {}^B\boldsymbol{J}_G^{b} \end{bmatrix} \begin{bmatrix} {}^B a_G^{b} \\ \dot{\omega}_b \end{bmatrix} = \begin{bmatrix} F_G^{b} \\ C_G^{b} \end{bmatrix} + \begin{bmatrix} \sum_{i=1}^{n} F_{P_i}^{b} \\ \sum_{i=1}^{n} C_{P_i}^{b} + \boldsymbol{GP_i}^{\times} F_{P_i}^{b} \end{bmatrix} - \begin{bmatrix} 0 \\ \omega_b \times {}^B\boldsymbol{J}_G^{b}\omega_b \end{bmatrix} \tag{3.86}$$

The complete dynamics of the system is deduced by assembling the effect of each flexible appendage on the main bus through the connection points P_i. Indeed, one

may write the relation reported in eq. (3.87), where the unknown forces exchanged by the two bodies at the attachment point are equal but opposite in sign

$$\begin{bmatrix} F_{P_i}^{b} \\ C_{P_i}^{b} \\ 0 \end{bmatrix} = -\begin{bmatrix} F_{P_i}^{A_i} \\ C_{P_i}^{A_i} \\ \tilde{Q}_{\eta}^{nc} \end{bmatrix} \tag{3.87}$$

Concerning the flexible body, the equations of dynamics may be written with respect to the bus CoM as introduced in Par. 3.2.1

$$\begin{bmatrix} m_{A_i}\boldsymbol{I} & {}^{B}\tilde{\boldsymbol{p}}_{G}^{A_i\times} & {}^{B}\boldsymbol{L}_{k}^{A_i} \\ \left({}^{B}\tilde{\boldsymbol{p}}_{G}^{A_i\times}\right)^{T} & {}^{B}\tilde{\boldsymbol{J}}_{G}^{A_i} & {}^{B}\tilde{\boldsymbol{S}}_{k}^{A_i} \\ {}^{B}\boldsymbol{L}_{k}^{A_i T} & {}^{B}\tilde{\boldsymbol{S}}_{k}^{A_i T} & \boldsymbol{I} \end{bmatrix} \begin{bmatrix} {}^{B}a_{G}^{A_i} \\ \dot{\omega}_{A_i} \\ \ddot{\eta}_{A_i} \end{bmatrix} + \begin{bmatrix} \boldsymbol{0} & \boldsymbol{0} & \boldsymbol{0} \\ \boldsymbol{0} & \boldsymbol{0} & \boldsymbol{0} \\ \boldsymbol{0} & \boldsymbol{0} & 2\Sigma\boldsymbol{\Omega} \end{bmatrix} \begin{bmatrix} {}^{B}v_{G}^{A_i} \\ \omega_{A_i} \\ \dot{\eta}_{A_i} \end{bmatrix} + \begin{bmatrix} \boldsymbol{0} & \boldsymbol{0} & \boldsymbol{0} \\ \boldsymbol{0} & \boldsymbol{0} & \boldsymbol{0} \\ \boldsymbol{0} & \boldsymbol{0} & \boldsymbol{\Omega}^{2} \end{bmatrix} \begin{bmatrix} {}^{B}x_{G}^{A_i} \\ \theta_{A_i} \\ \eta_{A_i} \end{bmatrix} +$$
$$+ {}^{B}N_{L}^{G} = \begin{bmatrix} {}^{B}f_{g} + {}^{B}f_{G}^{nc} \\ {}^{B}c_{g} + {}^{B}c_{G}^{nc} \\ -\tilde{\boldsymbol{K}}_{U\psi}\psi_{k} + \tilde{f}_{G,k} \end{bmatrix} - \boldsymbol{\tau}_{GP} \begin{bmatrix} \sum_{i=1}^{n} {}^{B}F_{P_i}^{b} \\ \sum_{i=1}^{n} {}^{B}C_{P_i}^{b} \\ 0 \end{bmatrix} \tag{3.88}$$

where

$${}^{B}N_{L}^{G} = \begin{bmatrix} \omega \wedge \left(\omega \wedge {}^{G}\tilde{p}_{G}^{A_i}\right) + 2\omega \wedge \sum_{k=1}^{N} {}^{B}L_{k}^{A_i}\dot{\eta}_{k} \\ \omega \wedge {}^{B}\tilde{\boldsymbol{J}}_{G}^{A_i}\omega + \sum_{k=1}^{N}\sum_{t=1}^{N} {}^{B}P^{kt}\dot{\eta}_{t}\dot{\eta}_{k} + \omega \wedge \sum_{k=1}^{N} {}^{B}\tilde{S}_{k}^{A_i}\dot{A}_{k} + \sum_{k=1}^{N} {}^{B}\tilde{\boldsymbol{J}}_{1}^{A_i,k}\eta_{k}\omega \\ -\frac{1}{2}\omega^{T}\,{}^{B}\tilde{\boldsymbol{J}}_{1}^{A_i,k}\omega + 2\omega^{T}\sum_{m=1}^{N} {}^{B}P_{km}^{A_i}\dot{\eta}_{m} \end{bmatrix} \tag{3.89}$$

$$\begin{aligned} {}^{B}f_{G} &= -\frac{m\boldsymbol{I}\mu_{\oplus}\hat{k}}{\left|{}^{I}X_{0}\right|^{2}} - \frac{\mu_{\oplus}\,{}^{B}\tilde{p}_{G}^{A_i}}{\left|{}^{I}X_{0}\right|^{3}} + \frac{3\mu_{\oplus}\hat{k}\left(\hat{k}^{T}\,{}^{B}\tilde{p}_{G}^{A_i}\right)}{\left|{}^{I}X_{0}\right|^{3}} - \frac{3\mu_{\oplus}\,{}^{B}\tilde{\boldsymbol{J}}_{G}^{A_i}\hat{k}}{\left|{}^{I}X_{0}\right|^{4}} + \\ &\quad + \frac{15\mu_{\oplus}\hat{k}\left(\hat{k}^{T}\,{}^{B}\tilde{\boldsymbol{J}}_{G}^{A_i}\hat{k}\right)}{2\left|{}^{I}X_{0}\right|^{4}} - \frac{3\mu_{\oplus}\hat{k}tr\left({}^{B}\tilde{\boldsymbol{J}}_{G}^{A_i}\right)}{2\left|{}^{I}X_{0}\right|^{4}} \\ {}^{B}c_{G} &= -\frac{\mu_{\oplus}\hat{k}}{\left|{}^{I}X_{0}\right|^{2}}\left({}^{B}\tilde{p}_{G}^{A_i} \wedge \hat{k}\right) + \frac{3\mu_{\oplus}}{\left|{}^{I}X_{0}\right|^{3}}\left(\hat{k} \wedge {}^{B}\tilde{\boldsymbol{J}}_{G}^{A_i}\hat{k}\right) \\ \tilde{f}_{G,k} &= -\frac{\mu_{\oplus}}{\left|{}^{I}X_{0}\right|^{2}}\left(\hat{k}^{T}\,{}^{B}L_{k}^{A_i}\right) - \frac{3\mu_{\oplus}}{2\left|{}^{I}X_{0}\right|^{3}}\left(\hat{k}^{T}\,{}^{B}\tilde{\boldsymbol{J}}_{1}^{k}\hat{k}\right) + \frac{\mu_{\oplus}}{2\left|{}^{I}X_{0}\right|^{3}}tr\left({}^{B}\tilde{\boldsymbol{J}}_{1}^{k}\right) \end{aligned} \tag{3.90}$$

The last term on the right side of eq. (3.88) may be substituted referring to eq. (3.86)

as follows

$$\boldsymbol{\tau}_{GP}\begin{bmatrix}\sum_{i=1}^{n}F_{P_i}^{b}\\ \sum_{i=1}^{n}C_{P_i}^{b}\\ 0\end{bmatrix}=\begin{bmatrix}\sum_{i=1}^{n}F_{P_i}^{b}\\ \sum_{i=1}^{n}C_{P_i}^{b}+\boldsymbol{GP_i}^{\times}F_{P_i}^{b}\\ 0\end{bmatrix}=\begin{bmatrix}m_b\boldsymbol{I} & 0 & 0\\ 0 & {}^{B}\boldsymbol{J}_{P_b}^{b} & 0\\ 0 & 0 & 0\end{bmatrix}\begin{bmatrix}{}^{B}a_G^{b}\\ \dot{\omega}_b\\ \ddot{\eta}_{A_i}\end{bmatrix}+\begin{bmatrix}0\\ \omega_b\times{}^{B}\boldsymbol{J}_{P_b}^{b}\omega_b\\ 0\end{bmatrix}-\begin{bmatrix}F_G^{b}\\ C_G^{b}\\ 0\end{bmatrix} \quad (3.91)$$

By imposing that there is no relative motion between the two appendages in the attachment point, so that

$$\begin{aligned}{}^{B}a_G^{A_i}&={}^{B}a_G^{b}\\ {}^{B}v_G^{A_i}&={}^{B}v_G^{b}\\ {}^{B}x_G^{A_i}&={}^{B}x_G^{b}\end{aligned} \quad (3.92)$$

One may now write the equations of the assembled system with respect to the bus CoG as reported below

$$\begin{bmatrix}\left(m_{A_i}+m_b\right)\boldsymbol{I} & \boldsymbol{T}_{I\leftarrow B}\,{}^{B}\tilde{\boldsymbol{p}}_G^{A_i\times} & \boldsymbol{T}_{I\leftarrow B}\,{}^{B}\boldsymbol{L}_k^{A_i}\\ \left(\boldsymbol{T}_{I\leftarrow B}\,{}^{B}\tilde{\boldsymbol{p}}_G^{A_i\times}\right)^{T} & {}^{B}\tilde{\boldsymbol{J}}_{G,TOT}^{A_i} & {}^{B}\tilde{\boldsymbol{S}}_k^{A_i}\\ {}^{B}\boldsymbol{L}_k^{A_i T}\boldsymbol{T}_{I\leftarrow B}^{T} & {}^{B}\tilde{\boldsymbol{S}}_k^{A_i T} & \boldsymbol{I}\end{bmatrix}\begin{bmatrix}{}^{B}a_G^{A_i}\\ \dot{\omega}_{A_i}\\ \ddot{\eta}_{A_i}\end{bmatrix}+\begin{bmatrix}\boldsymbol{0} & \boldsymbol{0} & \boldsymbol{0}\\ \boldsymbol{0} & \boldsymbol{0} & \boldsymbol{0}\\ \boldsymbol{0} & \boldsymbol{0} & 2\Sigma\boldsymbol{\Omega}\end{bmatrix}\begin{bmatrix}{}^{B}v_G^{A_i}\\ \omega_{A_i}\\ \dot{\eta}_{A_i}\end{bmatrix}+\begin{bmatrix}\boldsymbol{0} & \boldsymbol{0} & \boldsymbol{0}\\ \boldsymbol{0} & \boldsymbol{0} & \boldsymbol{0}\\ \boldsymbol{0} & \boldsymbol{0} & \boldsymbol{\Omega}^{2}\end{bmatrix}\begin{bmatrix}{}^{B}x_G^{A_i}\\ \theta_{A_i}\\ \eta_{A_i}\end{bmatrix}+$$
$$+\begin{bmatrix}\boldsymbol{T}_{I\leftarrow B}\left[\omega\wedge\left(\omega\wedge{}^{B}\tilde{p}_G^{A_i}\right)+2\omega\wedge\sum_{k=1}^{N}L_k\dot{\eta}_k\right]\\ \omega\wedge{}^{B}\tilde{\boldsymbol{J}}_{G,TOT}^{A_i}\omega+\sum_{k=1}^{N}\sum_{t=1}^{N}{}^{B}P_{tk}^{A_i}\dot{\eta}_t\dot{\eta}_k+\omega\wedge\sum_{k=1}^{N}{}^{B}\tilde{S}_k\dot{\eta}_k+\sum_{k=1}^{N}{}^{B}\tilde{\boldsymbol{J}}_1^{A_i,k}\eta_k\omega\\ -\frac{1}{2}\omega^{T}\,{}^{B}\tilde{\boldsymbol{J}}_1^{A_i,k}\omega+2\omega^{T}\sum_{m=1}^{N}{}^{B}P^{km}\dot{\eta}_m\end{bmatrix}=\begin{bmatrix}\boldsymbol{T}_{I\leftarrow B}\left({}^{B}f_g+{}^{B}f_G^{nc}\right)\\ {}^{B}c_g+{}^{B}c_G^{nc}\\ -\tilde{\boldsymbol{K}}_{U\psi}\psi_k+\tilde{f}_{g,k}+\tilde{f}_G^{nc}\end{bmatrix} \quad (3.93)$$

where ${}^{B}\tilde{\boldsymbol{J}}_{G,TOT}^{A_i}={}^{B}\tilde{\boldsymbol{J}}_G^{A_i}+{}^{B}\boldsymbol{J}_G^{b}$ is the total inertia of the spacecraft system. This procedure is also equivalent to apply to eq.s (3.49), (3.52) and (3.61) the following acceleration transport between two points G and P

$$\begin{bmatrix}a_P\\ \omega\end{bmatrix}=\begin{bmatrix}\boldsymbol{I} & \boldsymbol{r}_{A_i}^{\times}\\ \boldsymbol{0} & \boldsymbol{I}\end{bmatrix}\begin{bmatrix}a_G\\ \omega\end{bmatrix}+\begin{bmatrix}\omega\times\omega\times r_{A_i}\\ 0\end{bmatrix} \quad (3.94)$$

Such a procedure will be used in the next section to derive the linearized dynamics for the assembled spacecraft, by neglecting the second order term in the angular rate.

If more than one appendage is attached to the platform, the inertial properties

(namely mass, inertia and static moment) should be summed to obtain the contribution of all the substructures, while the modal participation factors add a new column in the mass matrix in eq. (3.93). The dynamic equations finally become

$$\boldsymbol{M}_{TOT}^{G}\ddot{S}+\boldsymbol{C}_{TOT}\dot{S}+K_{TOT}S+N_{L,TOT}=F_{TOT}^{G} \tag{3.95}$$

with

$$\boldsymbol{M}_{TOT}^{G}=\begin{bmatrix} \left(m_b+\sum_{i=1}^{L}m_{A_i}\right)\boldsymbol{I} & \boldsymbol{T}_{I\leftarrow B}\sum_{i=1}^{L}{}^{B}\tilde{\boldsymbol{p}}_{G}^{A_i\times} & \boldsymbol{T}_{I\leftarrow B}\,{}^{B}\boldsymbol{L}_{k}^{A_1} & \cdots & \boldsymbol{T}_{I\leftarrow B}\,{}^{B}\boldsymbol{L}_{k}^{A_L} \\ \left(\boldsymbol{T}_{I\leftarrow B}\sum_{i=1}^{L}{}^{B}\tilde{\boldsymbol{p}}_{G}^{A_i\times}\right)^{T} & {}^{B}\boldsymbol{J}_{b}^{G}+\sum_{i=1}^{L}{}^{B}\tilde{\boldsymbol{J}}_{G}^{A_i} & {}^{B}\tilde{\boldsymbol{S}}_{k}^{A_1} & \cdots & {}^{B}\tilde{\boldsymbol{S}}_{k}^{A_L} \\ {}^{B}\boldsymbol{L}_{k}^{A_1T}\boldsymbol{T}_{I\leftarrow B}^{T} & {}^{B}\tilde{\boldsymbol{S}}_{k}^{A_1T} & \boldsymbol{I}_{A_1} & \boldsymbol{0} & \boldsymbol{0} \\ \vdots & \vdots & \boldsymbol{0} & \ddots & \boldsymbol{0} \\ {}^{B}\boldsymbol{L}_{k}^{A_LT}\boldsymbol{T}_{I\leftarrow B}^{T} & {}^{B}\tilde{\boldsymbol{S}}_{k}^{A_LT} & \boldsymbol{0} & \boldsymbol{0} & \boldsymbol{I}_{A_L} \end{bmatrix} \tag{3.96}$$

$$\boldsymbol{K}_{TOT}=\begin{bmatrix} \boldsymbol{0} & \boldsymbol{0} & \boldsymbol{0} & \cdots & \boldsymbol{0} \\ \boldsymbol{0} & \boldsymbol{0} & \boldsymbol{0} & \cdots & \boldsymbol{0} \\ \boldsymbol{0} & \boldsymbol{0} & \Omega_{A_1}^{2} & \boldsymbol{0} & \boldsymbol{0} \\ \vdots & \vdots & \boldsymbol{0} & \ddots & \boldsymbol{0} \\ \boldsymbol{0} & \boldsymbol{0} & \boldsymbol{0} & \boldsymbol{0} & \Omega_{A_L}^{2} \end{bmatrix} \tag{3.97}$$

$$\boldsymbol{C}_{TOT}=\begin{bmatrix} \boldsymbol{0} & \boldsymbol{0} & \boldsymbol{0} & \cdots & \boldsymbol{0} \\ \boldsymbol{0} & \boldsymbol{0} & \boldsymbol{0} & \cdots & \boldsymbol{0} \\ \boldsymbol{0} & \boldsymbol{0} & 2\Sigma\Omega_{A_1} & \boldsymbol{0} & \boldsymbol{0} \\ \vdots & \vdots & \boldsymbol{0} & \ddots & \boldsymbol{0} \\ \boldsymbol{0} & \boldsymbol{0} & \boldsymbol{0} & \boldsymbol{0} & 2\Sigma\Omega_{A_L} \end{bmatrix} \tag{3.98}$$

That is equivalent to substitute in the dynamics for a single appendage reported in eq. (3.93), the following quantities

$$\begin{aligned} {}^{B}\boldsymbol{L}_{k}^{A_i} &\rightarrow \begin{bmatrix} {}^{B}\boldsymbol{L}_{k}^{A_1} & \cdots & {}^{B}\boldsymbol{L}_{k}^{A_L} \end{bmatrix} \\ {}^{B}\tilde{\boldsymbol{S}}_{k}^{A_i} &\rightarrow \begin{bmatrix} {}^{B}\tilde{\boldsymbol{S}}_{k}^{A_1} & \cdots & {}^{B}\tilde{\boldsymbol{S}}_{k}^{A_L} \end{bmatrix} \\ {}^{B}\tilde{\boldsymbol{J}}_{G,TOT}^{A_i} &\rightarrow {}^{B}\boldsymbol{J}_{G}^{b}+\sum_{i=1}^{L}{}^{B}\tilde{\boldsymbol{J}}_{G}^{A_i} \\ {}^{B}\tilde{\boldsymbol{p}}_{G}^{A_i\times} &\rightarrow \sum_{i=1}^{L}{}^{B}\tilde{\boldsymbol{p}}_{G}^{A_i\times} \end{aligned} \tag{3.99}$$

The presented non-linear model should be implemented when developing high-fidelity simulators aiming at investigating the dynamics of in-orbit flexible structures subjected both to forces from the platform control system, gravitational effects and distributed active control.

3.3 LINEARIZED STATE-SPACE MODEL FOR CONTROL SYNTHESIS

In order to simplify the control synthesis task for the assembled spacecraft system, the dynamic model in eq. (3.95) should be linearized around a reference trajectory. The choice of such trajectory is highly dependent on the specific application and mission [3]. In this thesis, to develop a linear model for a flexible spacecraft with multiple appendages, a formulation is introduced based on a well-known and used procedure from Alazar et al. [21][23]. However, for research purposes, it has been necessary to complement the available theory by implementing a way to observe and interact in some structure's critical points. Indeed, by enabling distributed control it is possible to further exploit the controllability and observability of the entire spacecraft as a whole and not as a matter of the central platform.

Let us re-introduce the dynamics of a rigid body, referred to its CoM G, by considering also possible forces and torques applied to P_i generic points, which may be assumed as attachment points without losing generality, as follows

$$\begin{bmatrix} m_b & 0 \\ 0 & {}^{B}\boldsymbol{J}_G^b \end{bmatrix} \begin{bmatrix} {}^{B}a_G^b \\ \dot{\omega}_b \end{bmatrix} = \begin{bmatrix} F_G^b + \sum_{i=1}^{n} F_{P_i}^b \\ C_G^{b,T} \end{bmatrix} - \begin{bmatrix} 0 \\ \omega_b \times {}^{B}\boldsymbol{J}_G^b \omega_b \end{bmatrix} \tag{3.100}$$

where $C_b^{G,T} = C_b^{G,} + \sum_{i=1}^{n} \left(C_b^{P_i} + \boldsymbol{GP_i}^{\times} F_b^{P_i} \right)$. By recalling that the accelerations and angular rate variations experienced at the spacecraft's CoG, G, can be transported to another point in the rigid main body by the following relationship in linear form (neglecting second order terms with angular rate):

$$\begin{bmatrix} {}^{B}a_{P_b}^b \\ \dot{\omega}_b \end{bmatrix} = \begin{bmatrix} \boldsymbol{I} & \boldsymbol{PG}^{\times} \\ \boldsymbol{0} & \boldsymbol{I} \end{bmatrix} \begin{bmatrix} {}^{B}a_G^b \\ \dot{\omega}_b \end{bmatrix} = \boldsymbol{\tau}_{PG} \begin{bmatrix} {}^{B}a_G^b \\ \dot{\omega}_b \end{bmatrix} \tag{3.101}$$

Concerning a flexible appendage, for control synthesis purposes, it is usually extremely useful to obtain its equations of motion condensed at the attachment point P_i. To derive a linear model for eq. (3.100) around a general operating point ω_{oi}, being the angular velocity of orbital reference system with respect to the Inertial frame $\omega_{oi} = [0, -\omega_0, 0]^T$, a Taylor expansion around such operating point may be carried out [24]. The angular rate of the body with respect to the Inertial reference frame, written in Body reference frame, may be written as

$$\omega = \omega_b = \omega_{bo} + \omega_{oi} \tag{3.102}$$

where ω_{bo} is the angular rate of the body with respect to the orbital reference frame. Considering that the non-linear attitude relation in eq. (3.100) depends only on two variables, namely ω_b and $C_b^{G,T}$, one may write

$$ {}^{B}\boldsymbol{J}_b^G\dot{\omega} = {}^{B}\boldsymbol{J}_b^G\dot{\omega}_{oi} + \left.\frac{\partial^B \boldsymbol{J}_b^G\dot{\omega}}{\partial\omega}\right|_{\omega=\omega_{oi}}\left(\omega-\omega_{oi}\right) + \left.\frac{\partial^B C_b^{G,T}}{\partial\omega}\right|_{\omega=\omega_{oi}}\left(C_b^{G,T}-C_{b,oi}^{G,T}\right) \tag{3.103} $$

where $C_{b,oi}^{G,T}=0$. The second Jacobian appearing in eq. (3.103) is an identity matrix, while the first one may be written as

$$ \boldsymbol{H}_{jac} = \left.\frac{\partial^B \boldsymbol{J}_b^G\dot{\omega}}{\partial\omega}\right|_{\omega=\omega_{oi}} = \left.\frac{\partial\left(C_b^{G,T}-\omega\times\boldsymbol{J}_b^G\omega\right)}{\partial\omega}\right|_{\omega=\omega_{oi}} = 0 - \left.\frac{\partial\left(\omega\times\boldsymbol{J}_b^G\omega\right)}{\partial\omega}\right|_{\omega=\omega_{oi}} = \tag{3.104} $$
$$ = (\boldsymbol{\omega}^{\times})_{|\omega=\omega_{0i}}\,{}^{B}\boldsymbol{J}_b^G - ({}^{B}\boldsymbol{J}_b^G\omega_b)^{\times}{}_{|\omega=\omega_{0i}} $$

Finally, we obtain

$$ \begin{bmatrix} m_b & 0 \\ 0 & {}^{B}\boldsymbol{J}_b^G \end{bmatrix}\begin{bmatrix} a_G \\ \dot{\omega}_b \end{bmatrix} + \begin{bmatrix} 0 & 0 \\ 0 & \boldsymbol{H}_{jac} \end{bmatrix}\begin{bmatrix} v_G \\ \omega_b \end{bmatrix} = \begin{bmatrix} F_b^G + \sum_{i=1}^{n} F_b^{P_i} \\ C_b^G + \sum_{i=1}^{n}\left(C_b^{P_i} + \boldsymbol{GP_i}^{\times}F_b^{P_i}\right) \end{bmatrix} \tag{3.105} $$

Regarding the kinematics, we may describe the non-linear evolution of the attitude motion of the body reference frame with respect to the reference frame by using either Euler's angles, as the 3-2-1 rotation matrix below

$$ \begin{bmatrix} \dot{\theta}_x \\ \dot{\theta}_y \\ \dot{\theta}_z \end{bmatrix} = \frac{1}{\cos(\theta_y)}\begin{bmatrix} \cos(\theta_y) & \sin(\theta_x)\sin(\theta_y) & \cos(\theta_x)\sin(\theta_y) \\ 0 & \cos(\theta_x)\cos(\theta_y) & -\sin(\theta_x)\cos(\theta_y) \\ 0 & \sin(\theta_x) & \cos(\theta_x) \end{bmatrix}\omega_{bo} = \boldsymbol{Q}^{\theta}(\theta_{bo})\omega_{bo} \tag{3.106} $$

or by referring to quaternions $q = q_{bo}$

$$ \dot{q} = \frac{1}{2}\begin{bmatrix} 0 & -\omega_x & -\omega_y & -\omega_z \\ \omega_x & 0 & \omega_z & -\omega_y \\ \omega_y & -\omega_z & 0 & \omega_x \\ \omega_z & \omega_y & -\omega_x & 0 \end{bmatrix} q = \frac{1}{2}\boldsymbol{Q}^{q}(\omega_{bo})q \tag{3.107} $$

By expanding by using a Taylor's series we may write

$$ \dot{\theta} = \dot{\theta}_{oi} + \left.\frac{\partial\dot{\theta}}{\partial\theta}\right|_{\theta=\theta_{oi},\,\omega=\omega_{oi}}\left(\theta-\theta_{oi}\right) + \left.\frac{\partial\dot{\theta}}{\partial\omega}\right|_{\theta=\theta_{oi},\,\omega=\omega_{oi}}\left(\omega-\omega_{oi}\right) \tag{3.108} $$

where the operating point is $\theta_{oi} = \left[0, \theta_o, 0\right]^T$.

We would have then

$$\dot{\theta} = \left.\frac{\partial \mathbf{Q}^{\theta}(\theta)\omega}{\partial\theta}\right|_{\theta=\theta_{oi},\ \omega=\omega_{oi}} \theta + \left.\frac{\partial \mathbf{Q}^{\theta}(\theta)\omega}{\partial\omega}\right|_{\theta=\theta_{oi},\ \omega=\omega_{oi}} \left(\omega-\omega_{oi}\right) = \\ = \left.\frac{\partial \mathbf{Q}^{\theta}(\theta)}{\partial\theta}\right|_{\theta=\theta_{oi},\ \omega=\omega_{oi}} \omega_{oi}\theta + \mathbf{Q}^{\theta}(\theta_{oi})\left(\omega-\omega_{oi}\right) \tag{3.109}$$

However, some considerations have to be reported: the orbital dynamics are assumed to have a negligible effect when the orbital frequency is very low with respect to the controller bandwidth [3][24] (i.e. when the duration of the manoeuvre is short with respect to the orbital period). Furthermore, this is the case in most space applications, where the angular rates are not high enough in order to retain the gyroscopic stiffness term.

In such conditions, which often constitute the standard situation for a satellite orbiting the Earth, the velocity ω_{oi} and the operating point θ_{oi} may be assumed equal to zero [24]. According to this approach, one may further assume

$$\boldsymbol{H}_{jac} = (\boldsymbol{\omega}^{\times})_{|\omega=0}\,{}^{B}\boldsymbol{J}_{b}^{G} - ({}^{B}\boldsymbol{J}_{b}^{G}\omega)^{\times}_{|\omega=0} = \boldsymbol{0} - \boldsymbol{0} = \boldsymbol{0} \\ \dot{\theta} = \left.\frac{\partial \mathbf{Q}^{\theta}(\theta)}{\partial\theta}\right|_{\theta=\theta_{oi},\ \omega=\omega_{oi}} \omega_{oi}\theta + \mathbf{Q}^{\theta}(\theta_{oi})\left(\omega-\omega_{oi}\right) = \boldsymbol{0}\,\theta + \boldsymbol{I}\,\omega = \boldsymbol{I}\,\omega \tag{3.110}$$

where $\boldsymbol{I}$ is the identity matrix.

3.3.1 FLEXIBLE APPENDAGE: CONDENSED EQUATIONS OF MOTION

For control purposes, the size of the system is generally unacceptably high (i.e. it could easily reach more than a thousand of degrees of freedom for a flexible appendage). Therefore, by considering the modal coordinates introduced in Par. 3.1.2, some alternative representations can be produced. For a formulation in which the inverse and direct dynamics of the substructure can be extracted without losing the flexible and rigid motion behaviour. This philosophy implies a formulation of the equations of motion that allows establishing the correct relation between applied forces and accelerations to the substructure under study [25].

Since it is generally assumed the existence of damping does not cause coupling of the undamped natural modes of vibration [18], the linearized dynamics of the

flexible part may be initially written as

$$\boldsymbol{M}\ddot{q} + \boldsymbol{K}q = F \tag{3.111}$$

where the vector q contains the degrees of freedom, or DOFs, for all the nodes of the substructure. As the flexible appendages are assumed connected to the central bus by using a single attachment point, the condensation approach that will be used in this thesis is based on Imbert's method [26], a simplification of the well-known Craig-Bampton theory [27]. Indeed, the set q may be partitioned in two sub-groups, namely fixed boundary or interfaced DOFs q_r and internal elastic DOFs q_j. One may then rewrite eq. (3.111) as

$$\begin{bmatrix} \boldsymbol{M}_{rr} & \boldsymbol{M}_{rj} \\ \boldsymbol{M}_{jr} & \boldsymbol{M}_{jj} \end{bmatrix} \begin{bmatrix} \ddot{q}_r \\ \ddot{q}_j \end{bmatrix} + \begin{bmatrix} \boldsymbol{K}_{rr} & \boldsymbol{K}_{rj} \\ \boldsymbol{K}_{jr} & \boldsymbol{K}_{jj} \end{bmatrix} \begin{bmatrix} q_r \\ q_j \end{bmatrix} = \begin{bmatrix} F_r \\ F_j \end{bmatrix} \tag{3.112}$$

It should be noticed the coordinates q_r are the nodes of freedom of the condensation or attachment point P_i. The set of physical coordinates q may further be converted in a hybrid set containing physical variables at the interface nodes q_r and modal coordinates η_k in the internal part of the structure, by using the following transformation

$$q = \begin{bmatrix} q_r \\ q_i \end{bmatrix} = \begin{bmatrix} \boldsymbol{I} & \boldsymbol{0} \\ \boldsymbol{\Phi}_{rk} & \boldsymbol{\Phi}_{jk} \end{bmatrix} \begin{bmatrix} q_r \\ \eta_k \end{bmatrix} = \boldsymbol{\Psi}_I \begin{bmatrix} q_r \\ \eta_k \end{bmatrix} \tag{3.113}$$

where $\boldsymbol{\Psi}_I$ is the simplified Craig-Bampton's or Imbert's transformation matrix, $\boldsymbol{\Phi}_{rk}$ is the matrix of Static Constrained Modes, which describes the static response of the substructure to excitation coming from neighbouring substructures through the interface degrees of freedom, while $\boldsymbol{\Phi}_{jk}$ is the Fixed Base Modes matrix, containing modes obtained by constraining the interface nodes and with no forces applied on the internal nodes . In detail, the columns of the matrix $\boldsymbol{\Phi}_{rk}$ are rigid body displacements at the j-th degrees of freedom due to a unit motion at one of the r-th degrees of freedom. Hence, the matrix $\boldsymbol{\Phi}_{rk}$ can be obtained as

$$\boldsymbol{\Phi}_{rk} = -K_{jj}^{-1} K_{jr} \tag{3.114}$$

However, for a substructure with an isostatic interface (exactly 6 degrees of freedom, i.e. the node representing the attachment point P_i) the Craig-Bampton's Static Constraint Modes Matrix will lapse into the rigid modes matrix at the interface point. In this case, rigid body modes can be easily computed from the locations and orientations of the degrees of freedom, as reported in eq. (3.115).

$$\boldsymbol{\Phi}_{rk} = \begin{bmatrix} \boldsymbol{\phi}_{Tk} \\ \boldsymbol{\phi}_{Rk} \end{bmatrix} = \begin{bmatrix} 1 & 0 & 0 & 0 & \Delta z & -\Delta y \\ 0 & 1 & 0 & -\Delta z & 0 & \Delta x \\ \vdots & 0 & 1 & \Delta y & -\Delta x & 0 \\ \vdots & \vdots & 0 & 1 & 0 & 0 \\ \vdots & \vdots & \vdots & 0 & 1 & 0 \\ 0 & 0 & 0 & 0 & 0 & 1 \end{bmatrix} \tag{3.115}$$

In detail, $\Delta x = (x_b - x_a), \Delta y = (y_b - y_a), \Delta z = (z_b - z_a)$ are the coordinates of some arbitrary point B with respect to an interface point A. Conversely, the Fixed Base Modes can be obtained by solving the equation for the ω_o^2 structure eigenvalues

$$\left[\boldsymbol{K}_{jj} - \omega_o^2 \boldsymbol{M}_{jj} \right] \boldsymbol{\Phi}_j = 0 \tag{3.116}$$

It is worth noting that

$$q_j = \boldsymbol{\Phi}_{rk} q_r + \boldsymbol{\Phi}_{jk} \eta_{jk} \tag{3.117}$$

where $\boldsymbol{\Phi}_{rk} q_r$ indicates the rigid body displacements of the j-th degrees of freedom due to the r-th boundary degrees of freedom and $\boldsymbol{\Phi}_{jk} \eta_{jk}$ are the elastic displacements of the internal nodes relative to the displaced base [27].

By pre- and post-multiplying eq. (3.111) for the transformation matrix $\boldsymbol{\Psi}_I$, and by adding also a damping matrix proportional to the velocity of each point in the displacement set, we obtain

$$\begin{bmatrix} \tilde{\mathbf{M}}_{rr} & \tilde{\mathbf{M}}_{rj} \\ \tilde{\mathbf{M}}_{jr} & \tilde{\mathbf{M}}_{jj} \end{bmatrix} \begin{bmatrix} \ddot{q}_r \\ \ddot{\eta}_j \end{bmatrix} + \begin{bmatrix} \mathbf{0} & \mathbf{0} \\ \mathbf{0} & \tilde{\mathbf{D}}_{jj} \end{bmatrix} \begin{bmatrix} \dot{q}_r \\ \dot{\eta}_j \end{bmatrix} + \begin{bmatrix} \tilde{\boldsymbol{K}}_{rr} & \mathbf{0} \\ \mathbf{0} & \tilde{\mathbf{K}}_{jj} \end{bmatrix} \begin{bmatrix} q_r \\ \eta_j \end{bmatrix} = \begin{bmatrix} \mathbf{I}_r & \boldsymbol{\phi}_{rm} \\ \mathbf{0} & \boldsymbol{\phi}_{jm} \end{bmatrix} \begin{bmatrix} F_r \\ F_j \end{bmatrix} \tag{3.118}$$

where $\tilde{\mathbf{M}}_{rr}$ is the is the structural mass matrix reduced to the boundary nodes (as in Guyan transformation), $\tilde{\mathbf{M}}_{rj} = \tilde{\mathbf{M}}_{rj}^{\,T}$ contains the modal participation factors of the model in the rigid body motion, $\tilde{\mathbf{M}}_{jj}$ is the generalized mass and it is usually set to identity for mass-normalized modes, so that $\tilde{\mathbf{M}}_{jj} = \boldsymbol{I}_{jj}$, $\tilde{\mathbf{D}}_{jj}$ is the damping matrix which can be described as $\tilde{\mathbf{D}}_{jj} = 2\boldsymbol{\Sigma\Omega}_{jj}$, $\tilde{\mathbf{K}}_{jj} = \boldsymbol{\Omega}_{jj}^{\,2}$ is the stiffness matrix in the modal base, $\tilde{\boldsymbol{K}}_{rr}$ is usually zero when the boundary is statically determinant (i.e. is null since the work done by a self-equilibrating force system on a rigid-body displacement is zero [18]).

We can now write the linear equations with respect to the appendage attachment

point P_i as

$$\begin{bmatrix} m_{A_i}\boldsymbol{I} & {}^{B}\tilde{\boldsymbol{p}}_{P_i}^{A_i\times} & {}^{B}\boldsymbol{L}_{k}^{A_i} \\ \left({}^{B}\tilde{\boldsymbol{p}}_{P_i}^{A_i\times}\right)^{T} & {}^{B}\tilde{\boldsymbol{J}}_{G}^{P_i} & {}^{B}\tilde{\boldsymbol{S}}_{k}^{A_i,P_i} \\ {}^{B}\boldsymbol{L}_{k}^{A_i T} & \left({}^{B}\tilde{\boldsymbol{S}}_{k}^{A_i,P_i}\right)^{T} & \boldsymbol{I} \end{bmatrix} \begin{bmatrix} {}^{B}a_{P_i}^{A_i} \\ \dot{\omega}_{A_i} \\ \ddot{\eta}_{A_i} \end{bmatrix} + \begin{bmatrix} \boldsymbol{0} & \boldsymbol{0} & \boldsymbol{0} \\ \boldsymbol{0} & \boldsymbol{0} & \boldsymbol{0} \\ \boldsymbol{0} & \boldsymbol{0} & 2\Sigma\boldsymbol{\Omega} \end{bmatrix} \begin{bmatrix} {}^{B}v_{P_i}^{A_i} \\ \omega_{A_i} \\ \dot{\eta}_{A_i} \end{bmatrix} + \begin{bmatrix} \boldsymbol{0} & \boldsymbol{0} & \boldsymbol{0} \\ \boldsymbol{0} & \boldsymbol{0} & \boldsymbol{0} \\ \boldsymbol{0} & \boldsymbol{0} & \boldsymbol{\Omega^2} \end{bmatrix} \begin{bmatrix} {}^{B}x_{P_i}^{A_i} \\ \theta_{A_i} \\ \eta_{A_i} \end{bmatrix} = \tag{3.119}$$
$$= \begin{bmatrix} \mathbf{I}_r & \mathbf{0} & \boldsymbol{\phi}_{Tk} \\ \mathbf{0} & \mathbf{I}_r & \boldsymbol{\phi}_{Rk} \\ \mathbf{0} & \mathbf{0} & \boldsymbol{\phi}_{jk} \end{bmatrix} \begin{bmatrix} F_r \\ C_r \\ F_{jk} \end{bmatrix}$$

where $F_{jk} = F_j^{PZT} + F_j^G = \tilde{\boldsymbol{K}}_{U\psi}\psi_k + F_j^G$. For simplifying the assembly, the gyroscopic terms coming from the appendage's root will be neglected, hypothesis which is in line with spacecraft's common angular rates, as already explained in the precedent paragraph.

3.3.2 MULTIBODY APPROACH: LINEARIZED

The equilibrium trough the main body at the connection points of the appendage gives (in the linearized form) can be obtained by transporting the information of the rigid hub in eq. (3.100) to the attachment point, also by using the transformation in eq. (3.101)

$$\begin{bmatrix} F_{P_i}^{A_i} \\ C_{A_i}^{A_i} \\ \tilde{Q}_{\eta} \end{bmatrix} = \begin{bmatrix} -F_{P_i}^{b} \\ -C_{P_i}^{b} \\ 0 \end{bmatrix} = \begin{bmatrix} -m_b\mathbf{I} & \mathbf{0} & \mathbf{0} \\ m_b\left(\mathbf{GP}_i^{\times}\right) & -{}^{B}\boldsymbol{J}_b^{G} & \mathbf{0} \\ \mathbf{0} & \mathbf{0} & \mathbf{0} \end{bmatrix} \begin{bmatrix} {}^{B}a_{P_i}^{b} \\ \dot{\omega}_b \\ \ddot{\eta}_k^{A_i} \end{bmatrix} + \begin{bmatrix} \mathbf{0} & \mathbf{0} & \mathbf{0} \\ \mathbf{0} & \mathbf{H}_{jac} & \mathbf{0} \\ \mathbf{0} & \mathbf{0} & \mathbf{0} \end{bmatrix} \begin{bmatrix} {}^{B}v_{P_i}^{b} \\ \omega_b \\ \dot{\eta}_k^{A_i} \end{bmatrix} +$$
$$+ \begin{bmatrix} \mathbf{I}_3 & \mathbf{0} & \mathbf{0} \\ -\left(\mathbf{GP}_i^{\times}\right) & \mathbf{I}_3 & \mathbf{0} \\ \mathbf{0} & \mathbf{0} & \mathbf{I}_k \end{bmatrix} \begin{bmatrix} F_G^b \\ C_G^b \\ F_k^{A_i} \end{bmatrix} \tag{3.120}$$

To proceed, eq. (3.119) may be reported to the CoG of the bus by using

$$\begin{bmatrix} {}^{B}a_{P_i}^{b} \\ \dot{\omega}_b \\ \ddot{\eta}_k \end{bmatrix} = \begin{bmatrix} \boldsymbol{I} & \boldsymbol{P_iG}^{\times} & \boldsymbol{0} \\ \boldsymbol{0} & \boldsymbol{I} & \boldsymbol{0} \\ \boldsymbol{0} & \boldsymbol{0} & \boldsymbol{I} \end{bmatrix} \begin{bmatrix} {}^{B}a_{G}^{b} \\ \dot{\omega}_b \\ \ddot{\eta}_k \end{bmatrix} \tag{3.121}$$

Then, after some passages which are omitted for simplicity's sake, one may further write the following equations

$$\begin{bmatrix} m_{A_i}\boldsymbol{I} & {}^{B}\tilde{\boldsymbol{p}}_{P_i}^{A_i\times} - m_{A_i}\boldsymbol{G}\boldsymbol{P}_i^{\times} & {}^{B}\boldsymbol{L}_k^{A_i} \\ \left({}^{B}\tilde{\boldsymbol{p}}_{P_i}^{A_i\times} - m_{A_i}\boldsymbol{G}\boldsymbol{P}_i^{\times}\right)^T & {}^{B}\tilde{\boldsymbol{J}}_{G_{A_i}}^{A_i} - m_{A_i}\boldsymbol{G}_{A_i}\boldsymbol{G}^2 & {}^{B}\tilde{\boldsymbol{S}}_k^{A_i,G} \\ {}^{B}\boldsymbol{L}_k^{A_i T} & \left({}^{B}\tilde{\boldsymbol{S}}_k^{A_i,G}\right)^T & \boldsymbol{I} \end{bmatrix} \begin{bmatrix} {}^{B}a_G^{A_i} \\ \dot{\omega}_{A_i} \\ \ddot{\eta}_{A_i} \end{bmatrix} + \begin{bmatrix} \boldsymbol{0} & \boldsymbol{0} & \boldsymbol{0} \\ \boldsymbol{0} & \boldsymbol{0} & \boldsymbol{0} \\ \boldsymbol{0} & \boldsymbol{0} & 2\Sigma\boldsymbol{\Omega}_{A_i} \end{bmatrix} \begin{bmatrix} {}^{B}v_G^{A_i} \\ \omega_{A_i} \\ \dot{\eta}_{A_i} \end{bmatrix} +$$
$$+ \begin{bmatrix} \boldsymbol{0} & \boldsymbol{0} & \boldsymbol{0} \\ \boldsymbol{0} & \boldsymbol{0} & \boldsymbol{0} \\ \boldsymbol{0} & \boldsymbol{0} & \boldsymbol{\Omega}_{A_i}{}^2 \end{bmatrix} \begin{bmatrix} {}^{B}x_G^{A_i} \\ \theta_{A_i} \\ \eta_{A_i} \end{bmatrix} = \begin{bmatrix} \boldsymbol{I} & \boldsymbol{P}_i\boldsymbol{G}^{\times} & \boldsymbol{0} \\ \boldsymbol{0} & \boldsymbol{I} & \boldsymbol{0} \\ \boldsymbol{0} & \boldsymbol{0} & \boldsymbol{I} \end{bmatrix} \begin{bmatrix} \mathbf{I}_r & \mathbf{0} & \boldsymbol{\phi}_{Tk} \\ \mathbf{0} & \mathbf{I}_r & \boldsymbol{\phi}_{Rk} \\ \mathbf{0} & \mathbf{0} & \boldsymbol{\phi}_{jk} \end{bmatrix} \left\{ \begin{bmatrix} -m_b\mathbf{I} & \mathbf{0} & \mathbf{0} \\ m_b\left(\mathbf{G}\mathbf{P}_i^{\times}\right) & -{}^{B}\boldsymbol{J}_G^b & \mathbf{0} \\ \mathbf{0} & \mathbf{0} & \mathbf{0} \end{bmatrix} \begin{bmatrix} {}^{B}a_{P_i}^b \\ \dot{\omega}_b \\ \ddot{\eta}_k^{A_i} \end{bmatrix} + \right. \tag{3.122}$$
$$\left. + \begin{bmatrix} \mathbf{0} & \mathbf{0} & \mathbf{0} \\ \mathbf{0} & \mathbf{H}_{jac} & \mathbf{0} \\ \mathbf{0} & \mathbf{0} & \mathbf{0} \end{bmatrix} \begin{bmatrix} v_{P_i}^b \\ \omega_b \\ \dot{\eta}_k^{A_i} \end{bmatrix} + \begin{bmatrix} \mathbf{I}_3 & \mathbf{0} & \mathbf{0} \\ -\left(\mathbf{G}\mathbf{P}_i^{\times}\right) & \mathbf{I}_3 & \mathbf{0} \\ \mathbf{0} & \mathbf{0} & \mathbf{I}_k \end{bmatrix} \begin{bmatrix} F_G^b \\ C_G^b \\ 0 \end{bmatrix} + \begin{bmatrix} 0 \\ 0 \\ -\tilde{\boldsymbol{K}}_{U\psi}\psi_k + \tilde{f}_k^{ext} \end{bmatrix} \right\}$$

where ${}^{B}\tilde{\boldsymbol{S}}_k^{A_i,G} = {}^{B}\tilde{\boldsymbol{S}}_k^{A_i,P_i} + \boldsymbol{G}\boldsymbol{P}_i^{\times}\,{}^{B}\boldsymbol{L}_k^{A_i}$. By transferring the bus mass matrix terms at the left of eq. (3.122), and by recalling eq. (3.92), we finally obtain the equation of motion of the system composed by the main hub and the flexible appendage

$$\begin{bmatrix} \left(m_{A_i}+m_b\right)\boldsymbol{I} & {}^{B}\tilde{\boldsymbol{p}}_{P_i}^{A_i\times} - m_{A_i}\boldsymbol{G}\boldsymbol{P}_i^{\times} & {}^{B}\boldsymbol{L}_k^{A_i} \\ \left({}^{B}\tilde{\boldsymbol{p}}_{P_i}^{A_i\times} - m_{A_i}\boldsymbol{G}\boldsymbol{P}_i^{\times}\right)^T & {}^{B}\tilde{\boldsymbol{J}}_G^b + {}^{B}\tilde{\boldsymbol{J}}_{G_{A_i}}^{A_i} - m_{A_i}\boldsymbol{G}_{A_i}\boldsymbol{G}^2 & {}^{B}\tilde{\boldsymbol{S}}_k^{A_i,G} \\ {}^{B}\boldsymbol{L}_k^{A_i T} & \left({}^{B}\tilde{\boldsymbol{S}}_k^{A_i,G}\right)^T & \boldsymbol{I} \end{bmatrix} \begin{bmatrix} {}^{B}a_G^b \\ \dot{\omega}_{A_i} \\ \ddot{\eta}_{A_i} \end{bmatrix} +$$
$$\begin{bmatrix} \boldsymbol{0} & \boldsymbol{0} & \boldsymbol{0} \\ \boldsymbol{0} & \boldsymbol{0} & \boldsymbol{0} \\ \boldsymbol{0} & \boldsymbol{0} & 2\Sigma\boldsymbol{\Omega}_{A_i} \end{bmatrix} \begin{bmatrix} {}^{B}v_G^b \\ \omega_{A_i} \\ \dot{\eta}_{A_i} \end{bmatrix} + + \begin{bmatrix} \boldsymbol{0} & \boldsymbol{0} & \boldsymbol{0} \\ \boldsymbol{0} & \boldsymbol{0} & \boldsymbol{0} \\ \boldsymbol{0} & \boldsymbol{0} & \boldsymbol{\Omega}_{A_i}{}^2 \end{bmatrix} \begin{bmatrix} {}^{B}x_G^b \\ \theta_{A_i} \\ \eta_{A_i} \end{bmatrix} = \boldsymbol{\Gamma}_i \left\{ \begin{bmatrix} F_G^b \\ C_G^b \\ 0 \end{bmatrix} + \begin{bmatrix} 0 \\ 0 \\ f_k^{A_i} \end{bmatrix} \right\} \tag{3.123}$$

where F_b^G and C_b^G are the forces and torques acting on the assembled system at the bus CoM, $f_k^{A_i}$ is the vector of the physical forces acting on the flexible dynamics and $\boldsymbol{\Gamma}_i$ is the generalized forces projection matrix as

$$\boldsymbol{\Gamma}_i = \begin{bmatrix} \boldsymbol{I} & \boldsymbol{0} & \boldsymbol{\phi}_{Tk} \\ \boldsymbol{0} & \boldsymbol{I} & \boldsymbol{\phi}_{Rk} + \mathbf{G}\mathbf{P}_i^{\times}\boldsymbol{\phi}_{Tk} \\ \boldsymbol{0} & \boldsymbol{0} & \boldsymbol{\phi}_{Jk} \end{bmatrix} \tag{3.124}$$

Generalizing to $\boldsymbol{L}$ appendages, the mass, damping, stiffness and input matrices will be assembled according to the logic reported in eq. (3.125).

$$\boldsymbol{M}=\begin{bmatrix}\left(\sum_{i=1}^{L} m_{A_i}+m_b\right)\boldsymbol{I} & \tilde{p}^{TOT} & {}^{B}\boldsymbol{L}_k^{A_1} & \cdots & {}^{B}\boldsymbol{L}_k^{A_L}\\ \left(\tilde{p}^{TOT}\right)^T & {}^{B}\tilde{\boldsymbol{J}}_G^{TOT} & {}^{B}\tilde{\boldsymbol{S}}_k^{A_1,G} & \cdots & {}^{B}\tilde{\boldsymbol{S}}_k^{A_L,G}\\ \left({}^{B}\boldsymbol{L}_k^{A_1}\right)^T & \left({}^{B}\tilde{\boldsymbol{S}}_k^{A_1,G}\right)^T & \boldsymbol{I}_k{}^{A_1} & \boldsymbol{0} & \boldsymbol{0}\\ \vdots & \vdots & \boldsymbol{0} & \ddots & \boldsymbol{0}\\ \left({}^{B}\boldsymbol{L}_k^{A_L}\right)^T & \left({}^{B}\tilde{\boldsymbol{S}}_k^{A_L,G}\right) & \boldsymbol{0} & \boldsymbol{0} & \boldsymbol{I}_k{}^{A_L}\end{bmatrix} \tag{3.125}$$

In the matrix $\boldsymbol{M}$ the following terms are considered

$$\begin{aligned}\tilde{p}^{TOT} &= \sum_{i=1}^{L} {}^{B}\tilde{\boldsymbol{p}}_{A_i}^{P_i\times} - m_{A_i}\boldsymbol{G}\boldsymbol{P}_i^{\times}\\ {}^{B}\tilde{\boldsymbol{J}}_G^{TOT} &= {}^{B}\tilde{\boldsymbol{J}}_G^{b} + \sum_{i=1}^{L} {}^{B}\tilde{\boldsymbol{J}}_{G_{A_i}}^{A_i} - m_{A_i}\boldsymbol{G}_{A_i}\boldsymbol{G}^2\\ {}^{B}\tilde{\boldsymbol{S}}_k^{A_1,G} &= {}^{B}\tilde{\boldsymbol{S}}_k^{A_1,P_1} + \boldsymbol{G}\boldsymbol{P}_i^{\times}\,{}^{B}\boldsymbol{L}_k^{A_1}\end{aligned} \tag{3.126}$$

and

$$\boldsymbol{K}=\begin{bmatrix}\boldsymbol{0} & \boldsymbol{0} & \boldsymbol{0} & \cdots & \boldsymbol{0}\\ \boldsymbol{0} & \boldsymbol{0} & \boldsymbol{0} & \cdots & \boldsymbol{0}\\ \boldsymbol{0} & \boldsymbol{0} & \boldsymbol{\Omega}_{A_1}{}^{2} & \boldsymbol{0} & \boldsymbol{0}\\ \vdots & \vdots & \boldsymbol{0} & \ddots & \boldsymbol{0}\\ \boldsymbol{0} & \boldsymbol{0} & \boldsymbol{0} & \boldsymbol{0} & \boldsymbol{\Omega}_{A_L}{}^{2}\end{bmatrix} \tag{3.127}$$

$$\boldsymbol{C}=\begin{bmatrix}\boldsymbol{0} & \boldsymbol{0} & \boldsymbol{0} & \cdots & \boldsymbol{0}\\ \boldsymbol{0} & \boldsymbol{0} & \boldsymbol{0} & \cdots & \boldsymbol{0}\\ \boldsymbol{0} & \boldsymbol{0} & 2\boldsymbol{\Sigma}_{A_1}\boldsymbol{\Omega}_{A_1} & \boldsymbol{0} & \boldsymbol{0}\\ \vdots & \vdots & \boldsymbol{0} & \ddots & \boldsymbol{0}\\ \boldsymbol{0} & \boldsymbol{0} & \boldsymbol{0} & \boldsymbol{0} & 2\boldsymbol{\Sigma}_{A_L}\boldsymbol{\Omega}_{A_L}\end{bmatrix} \tag{3.128}$$

where $\boldsymbol{\Omega}_{A_i}$ is the diagonal matrix containing the natural frequencies of the appendage A_i and $\boldsymbol{\Sigma}_{A_L}$ is the diagonal matrix containing the damping ratios of the appendage A_i. Also, the generalized forces projection matrix becomes

$$\boldsymbol{\Gamma}=\begin{bmatrix}\boldsymbol{I} & \boldsymbol{0} & \boldsymbol{\phi}_{Tk}^{A_1} & \cdots & \boldsymbol{\phi}_{Tk}^{A_L}\\ \boldsymbol{0} & \boldsymbol{I} & \boldsymbol{\phi}_{Rk}^{A_1}+\mathbf{GP}_1^{\times}\boldsymbol{\phi}_{Tk}^{A_1} & \cdots & \boldsymbol{\phi}_{Rk}^{A_L}+\mathbf{GP}_L{}^{\times}\boldsymbol{\phi}_{Tk}^{A_L}\\ \boldsymbol{0} & \boldsymbol{0} & \boldsymbol{\phi}_{Jk}^{A_1} & \boldsymbol{0} & \boldsymbol{0}\\ \vdots & \vdots & \boldsymbol{0} & \ddots & \boldsymbol{0}\\ \boldsymbol{0} & \boldsymbol{0} & \boldsymbol{0} & \boldsymbol{0} & \boldsymbol{\phi}_{Jk}^{A_L}\end{bmatrix} \tag{3.129}$$

Finally, the second order dynamic equations for the assembled system with multiple appendages may be written as

$$\boldsymbol{M}\ddot{X} + \boldsymbol{C}\dot{X} + \boldsymbol{K}X = \boldsymbol{\Gamma}F \tag{3.130}$$

where $X = \left[{}^{B}x_{G}^{A_i} \quad {}^{B}\theta^{B|I} \quad \eta_{A_1} \cdots \eta_{A_L} \right]$, with $x_{A_i}^{G}$ position of the main body CoG in Body reference frame, ${}^{B}\theta^{B|I}$ attitude of the main body with respect to the Inertial frame written in Body reference frame and η_{A_i} vector of modal amplitudes for the i-th flexible appendage.

3.4 TRANSFER TO STATE-SPACE MODEL

Once the assembled matrices describing the equations of motion of the system have been derived, the conversion to state-space form for control analysis is straightforward using the following relations

$$x = \begin{bmatrix} X \\ \dot{X} \end{bmatrix} = \begin{bmatrix} {}^{B}x_{G}^{A_i} \\ {}^{B}\theta^{B|I} \\ \eta_{A_i} \\ {}^{B}v_{G}^{A_i} \\ {}^{B}\omega^{B|I} \\ \dot{\eta}_{A_i} \end{bmatrix} \tag{3.131}$$

Then the state-space form can be expressed by

$$\begin{aligned} \dot{x} &= \boldsymbol{A}x + \boldsymbol{B}u \\ y &= \boldsymbol{C}x + \boldsymbol{D}_u u \end{aligned} \tag{3.132}$$

with

$$\boldsymbol{A} = \begin{bmatrix} \boldsymbol{0} & \boldsymbol{I} \\ -\boldsymbol{M}^{-1}\boldsymbol{K} & -\boldsymbol{M}^{-1}\boldsymbol{D} \end{bmatrix}, \quad \boldsymbol{B} = \begin{bmatrix} \boldsymbol{0} \\ \boldsymbol{M}^{-1}\boldsymbol{\Gamma} \end{bmatrix}, \quad \boldsymbol{C} = \begin{bmatrix} \boldsymbol{C}_{oq} & \boldsymbol{C}_{ov} \end{bmatrix} \tag{3.133}$$

and $\boldsymbol{D}_u$ direct transition, or feedthrough, matrix of the system, $u = \left[F_G, C_G, f_k \right]$ vector of the inputs to the system. In detail, $\boldsymbol{A}$ is a $2(6+N \times 6+N)$ matrix (where N is the sum of the number of modal amplitudes for each appendage), $\boldsymbol{B}$ is $2(6+N) \times 6+S$ (where S is the number of inputs for all the appendages) and $\boldsymbol{C}$ is $6+R \times 2(6+N)$ (where R is the number of outputs for all the appendages). We may also define the

Input matrix as $\boldsymbol{I}_M = \boldsymbol{M}^{-1}\boldsymbol{\Gamma}$. As far as the output matrix is concerned, we have

$$\mathbf{C} = \begin{bmatrix} \mathbf{O}_B^{Pos} & \mathbf{0} \\ \mathbf{0} & \mathbf{O}_B^{Vel} \end{bmatrix} \tag{3.134}$$

where

$$\mathbf{O}_B^{Pos} = \mathbf{O}_B^{Vel} = \begin{bmatrix} \boldsymbol{I} & \boldsymbol{0} & \boldsymbol{0} & \cdots & \boldsymbol{0} \\ \boldsymbol{0} & \boldsymbol{I} & \boldsymbol{0} & \cdots & \boldsymbol{0} \\ \boldsymbol{\phi}_{Tk}^{A_1} & \boldsymbol{\phi}_{Rk}^{A_1} + \mathbf{GP}_1^{\times}\boldsymbol{\phi}_{Tk}^{A_1} & \boldsymbol{\phi}_{Jk}^{A_1} & \boldsymbol{0} & \boldsymbol{0} \\ \vdots & \vdots & \boldsymbol{0} & \ddots & \boldsymbol{0} \\ \boldsymbol{\phi}_{Tk}^{A_L} & \boldsymbol{\phi}_{Rk}^{A_L} + \mathbf{GP}_L^{\times}\boldsymbol{\phi}_{Tk}^{A_L} & \boldsymbol{0} & \boldsymbol{0} & \boldsymbol{\phi}_{Jk}^{A_L} \end{bmatrix} \tag{3.135}$$

3.4.1 Nodes of Interest (NOIs)

For control purposes, it often convenient to retain in the dynamic model the elastic modes computed at specific locations of the flexible structure. Such points are generally chosen in a way both to obtain sufficient information on the dynamic behaviour the system and to verify if the performance requirements are fulfilled during spacecraft operations. In detail, these locations are identified with specific nodes in the FEM model of the flexible appendage, namely Nodes of Interest (NOIs). In this thesis, two sets of NOIs are proposed: a first group of nodes aimed at monitoring if the system requirements are satisfied during an attitude manoeuvre, called Requirements NOIs (R-NOIs), and a second sub-set including those nodes where the active vibration control distributed system exerts its control actions, named Distributed-control NOIs (D-NOIs), as illustrated in Fig. 3-4.

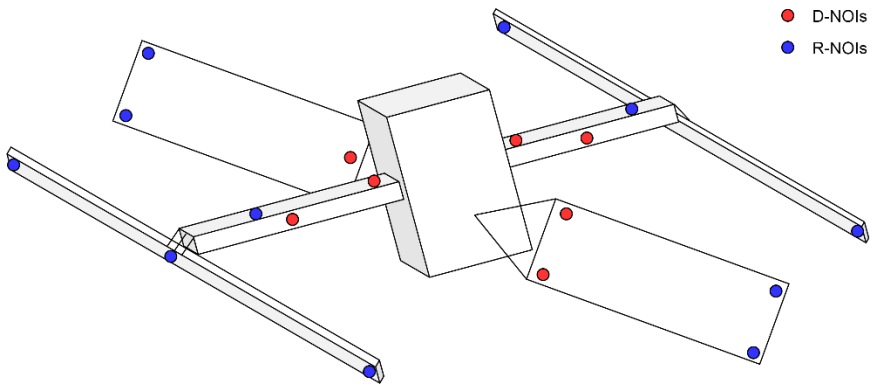

Fig. 3-4: Nodes of Interest for distributed control and requirements verification

The input matrix may be partitioned/modified accordingly

$$\bar{\boldsymbol{\Gamma}} = \begin{bmatrix} \boldsymbol{I} & \boldsymbol{0} & {}^{D}\boldsymbol{\phi}_{Tk}^{A_1} & {}^{R}\boldsymbol{\phi}_{Tk}^{A_1} & \cdots & {}^{D}\boldsymbol{\phi}_{Tk}^{A_L} & {}^{R}\boldsymbol{\phi}_{Tk}^{A_L} \\ \boldsymbol{0} & \boldsymbol{I} & {}^{D}\bar{\boldsymbol{\phi}}_{Rk}^{A_1} & {}^{R}\bar{\boldsymbol{\phi}}_{Rk}^{A_1} & \cdots & {}^{D}\bar{\boldsymbol{\phi}}_{Rk}^{A_L} & {}^{R}\bar{\boldsymbol{\phi}}_{Rk}^{A_L} \\ \boldsymbol{0} & \boldsymbol{0} & {}^{D}\boldsymbol{\phi}_{Jk}^{A_1} & \boldsymbol{0} & \boldsymbol{0} & \boldsymbol{0} & \boldsymbol{0} \\ \vdots & \vdots & \boldsymbol{0} & {}^{R}\boldsymbol{\phi}_{Jk}^{A_1} & \boldsymbol{0} & \vdots & \vdots \\ \vdots & \vdots & \vdots & \boldsymbol{0} & \ddots & \boldsymbol{0} & \vdots \\ \vdots & \vdots & \vdots & \vdots & \boldsymbol{0} & {}^{D}\boldsymbol{\phi}_{Jk}^{A_L} & \boldsymbol{0} \\ \boldsymbol{0} & \boldsymbol{0} & \boldsymbol{0} & \boldsymbol{0} & \boldsymbol{0} & \boldsymbol{0} & {}^{R}\boldsymbol{\phi}_{Jk}^{A_L} \end{bmatrix} \tag{3.136}$$

where $\bar{\boldsymbol{\phi}}_{Rk}^{A_i} = \boldsymbol{\phi}_{Rk}^{A_i} + \mathbf{GP}_i^{\times}\boldsymbol{\phi}_{Tk}^{A_i}$. The left subscript D indicates that the rigid and fixed interfaced modes are referred to the nodes used for carrying out distributed control (i.e. D-NOIs), while the left subscript R points out the modes are considered in the nodes employed for calculations of requirements performance (i.e. R-NOIs).

The matrix $\bar{\boldsymbol{\Gamma}}$ has then to be multiplied by the vector of the generalized forces acting on the spacecraft system. In particular, the D-NOIs, will be subjected to the forces originated by the distributed control system. In the case of piezoelectric materials, an electro-mechanical coupling matrix $\boldsymbol{K}_{U\psi}$ has been already defined in Par. 3.1.4.1 to indicate the conversion of a commanded input voltage to a generalized physical force to be applied to specific nodes of the structure. In detail, the final modal forces acting on the flexible dynamic equation will be given by $\tilde{\boldsymbol{K}}_{U\psi} = {}^{D}\boldsymbol{\phi}_{Jk}^{A_i}\boldsymbol{K}_{U\psi}$. Hence, an auxiliary matrix may be introduced to project the distributed physical forces on the modal base

$$\bar{\boldsymbol{P}} = \begin{bmatrix} \boldsymbol{I} & \boldsymbol{0} & \boldsymbol{0} & \boldsymbol{0} & \cdots & \cdots & \boldsymbol{0} \\ \boldsymbol{0} & \boldsymbol{I} & \boldsymbol{0} & \boldsymbol{0} & \cdots & \cdots & \boldsymbol{0} \\ \boldsymbol{0} & \boldsymbol{0} & \boldsymbol{K}_{U\psi}^{A_1} & \boldsymbol{0} & \boldsymbol{0} & \boldsymbol{0} & \boldsymbol{0} \\ \vdots & \vdots & \boldsymbol{0} & {}^{R}\boldsymbol{I}^{A_1} & \boldsymbol{0} & \vdots & \vdots \\ \vdots & \vdots & \vdots & \boldsymbol{0} & \ddots & \boldsymbol{0} & \vdots \\ \vdots & \vdots & \vdots & \vdots & \boldsymbol{0} & \boldsymbol{K}_{U\psi}^{A_L} & \boldsymbol{0} \\ \boldsymbol{0} & \boldsymbol{0} & \boldsymbol{0} & \boldsymbol{0} & \boldsymbol{0} & \boldsymbol{0} & {}^{R}\boldsymbol{I}^{A_L} \end{bmatrix} \tag{3.137}$$

So that the input matrix becomes $\boldsymbol{I}_M = \boldsymbol{M}^{-1}\bar{\boldsymbol{\Gamma}}\bar{\boldsymbol{P}}$. An analogous procedure may be applied also for the output matrix $\mathbf{C}$, which can be derived by pre-multiplying the transpose of the input matrix (assuming to have a fully observable state at this

step, and selecting relevant observations further in the thesis) by a matrix $\bar{\boldsymbol{P}}_T$, as indicated below

$$\mathbf{C} = \bar{\boldsymbol{P}}_T \begin{bmatrix} \bar{\mathbf{O}}_B^{Pos} & \mathbf{0} \\ \mathbf{0} & \bar{\mathbf{O}}_B^{Vel} \end{bmatrix} \tag{3.138}$$

with

$$\bar{\mathbf{O}}_B^{Pos} = \bar{\mathbf{O}}_B^{Vel} = \bar{\boldsymbol{\Gamma}}^T \tag{3.139}$$

and, in case of collocated distributed control system, one may assume

$$\bar{\boldsymbol{P}}_T = \begin{bmatrix} \boldsymbol{I} & \boldsymbol{0} & \boldsymbol{0} & \boldsymbol{0} & \cdots & \cdots & \boldsymbol{0} \\ \boldsymbol{0} & \boldsymbol{I} & \boldsymbol{0} & \boldsymbol{0} & \cdots & \cdots & \boldsymbol{0} \\ \boldsymbol{0} & \boldsymbol{0} & \left(\boldsymbol{K}_{U\psi}^{A_1}\right)^T & \boldsymbol{0} & \boldsymbol{0} & \boldsymbol{0} & \boldsymbol{0} \\ \vdots & \vdots & \boldsymbol{0} & {}^R\boldsymbol{I}^{A_1} & \boldsymbol{0} & \vdots & \vdots \\ \vdots & \vdots & \vdots & \boldsymbol{0} & \ddots & \boldsymbol{0} & \vdots \\ \vdots & \vdots & \vdots & \vdots & \boldsymbol{0} & \left(\boldsymbol{K}_{U\psi}^{A_L}\right)^T & \boldsymbol{0} \\ \boldsymbol{0} & \boldsymbol{0} & \boldsymbol{0} & \boldsymbol{0} & \boldsymbol{0} & \boldsymbol{0} & {}^R\boldsymbol{I}^{A_L} \end{bmatrix} \tag{3.140}$$

Once the mathematical foundations have been laid, the next two chapters will be devoted to the development of approaches to optimally place smart actuators and sensors on flexible space structures.

BIBLIOGRAPHY

[1] G.L. Ketner, *Survey of historical incidents with Control-Structures Interaction and recommended technology improve-ments needed to put hardware in space*, prepared for Control Structures Interaction Office, NASA, Langley Research Center, Washington, 1989;

[2] M. J. Sidi, *Spacecraft Dynamics and Control*, Cambridge University Press, 1997.

[3] L. Mazzini, *The Dynamics of the Flexible Satellite*. In: Flexible Spacecraft Dynamics, Control and Guidance. Springer Aerospace Technology. Springer, Cham., 2016;

[4] P. Santini, P. Gasbarri, *Dynamics of multibody systems in space environment; Lagrangian vs. Eulerian approach*, Acta Astronautica, Volume 54, Issue 1, January 2004, Pages 1-24;

[5] P. Santini, *Stability of Flexible Spacecraft*, ACTA Astronautica, Vol. 3 1976.

[6] P.W.Likins, R.E.Roberson, J. Wittenburg, *Dynamics of Flexible Spacecraft*, Department of General Mechanics, Course held in Dubrovnik, Published by Springer and Verlag, 1972;

[7] W. Witteveen, F. Pichler, *On the relevance of inertia related terms in the equations of motion of a flexible body in the floating frame of reference formulation*, Multibody System Dynamics, Vol. 46, pp 77-105, 2019;

[8] P. Gasbarri et al., *Effects of uncertainties and flexible dynamic contributions on the control of a spacecraft full-coupled model*, Acta Astronautica, Vol. 94, Issue 1, January–February 2014, Pages 515-526;

[9] A. Preumont, *Vibration Control of Active Structures: An Introduction*, 3rd ed. Springer Netherlands, 2011

[10] V. Piefort, *Finite Element Modelling of Piezoelectric Active Structures*, Doctor of Applied Sciences, Universitè Libre de Bruxelles, Active Structures Laboratory Department of Mechanical Engineering and Robotics, 2001

[11] M. Pascal, *Dynamics analysis of a system of hinged-connected flexible bodies*, Celest. Mech., Vol. 41, 253-274, 1988;

[12] J. Ho, *Direct path method for flexible multibody spacecraft dynamics*, Journal of Spacecr. Rockets 14(2), 102–110, 1977;

[13] V. Modi, A. Suleman, Y. Morita, *An approach to dynamics and control of orbiting flexible structures*, Int. J. Numer. Methods Eng. 32(8), 1727–1748, 1991;

[14] T. R. Kane, R. Ryan, A. Banerjee, Dynamics of a cantilever beam attached to a moving base., J. Guid. Control Dyn. 10(2), 139–151, 1987;

[15] F. Leckie, E. Pestel, *Transfer Matrix Fundamentals*, Int. J. Mech. Sci., Vol. 2, pp 137-167, 1960;

[16] M. A. Dokainish, *A new approach for plate vibrations: combination of transfer matrix and finite element technique*, J. Eng. Ind. 94(2), pp 526-530, 1972;

[17] T. Tan et al., *A modified finite element transfer matrix for control design of space structures*, Comp. Struct. Vol. 36, Issue 1, pp- 47-55, 1990;

[18] W. Hurty, *Dynamic Analysis of Structural Systems Using Component Modes*, AIAA J., Vol. 3, Issue 4, pp 678-685, 1965;

[19] R. R. Jr. Craig, *A brief tutorial on substructure analysis and testing,* International Modal Analysis Conference (IMAC), San Antonio, TX, USA, Feb 7-10, Vol. 1, pp 899-908;

[20] R. R. Craig, C. J. Chang, *Substructure coupling for dynamic analysis and testing*, NASA contractor report, National Aeronautics and Space Administration, 1977;

[21] D. Alazar, C. Cumer, K. H.M. Tantawi, *Linear Dynamic Modeling of Spacecraft with Various Flexible Appendages and On-board Angular Momentums*, 7th International ESA Conference on Guidance, Navigation & Control Systems (GNC 2008), 2 June 2008 - 5 June 2008 (Tralee, Ireland)

[22] N. Guy, D. Alazard, C. Cumer and C. Charbonnel, *Dynamic modeling and analysis of spacecraft with variable tilt of flexible appendage*, Journal of Dyamic Systems Measurements and Control, Vol. 136, Issue 2, 2014;

[23] J. Chebbi et al., *Linear Dynamics of flexible multibody systems: a system-based approach,* Multibody Syst. Dyn., Vol. 41, pp 75-100, 2017;

[24] F. Ankersen, *Guidance, Navigation, Control and Relative Dynamics for Spacecraft Proximity Maneuvers*, Doctoral thesis, Aalbord University, December 2015;

[25] J. A. Perez Gonzalez, *Commande Robuste Structurée: Application Co-Design Mécanique / Contrôle d'Attitude d'un Satellite Flexible*. Physique de l'espace, Institut Superieur De l'Aeronatique et de L'Espace (ISAE), 2016.

[26] J.F. Imbert, *Analyse des Structures par Elements Finis*. ENSTA. CEPAD, cepaudes edition, 1979. 15, 48, 54, 72, 200 ;

[27] Craig R, Bampton M , *Coupling of substructures for dynamic analysis*. AIAA J 6(7):1313–1319 , 1968;

Chapter 4
AVC: A CLOSED-LOOP APPROACH

In this chapter, the logic behind the design of a distributed network of actuators and sensors for collocated Active Vibration Control (AVC) of space structures is presented. In detail, focus is addressed to investigate the optimal placement of smart devices on a truss structure by following a closed loop philosophy. In-cascade optimization algorithms are used and results presented, also by verifying the system response to modifications of structural properties and actuators characteristics.

The selection of an appropriate criterion to find the most convenient locations for distributed actuators and sensors is an issue of the utmost importance for the optimal design of a vibration suppression system. Generally, such a choice depends on how to translate system physical requirements into a proper mathematical form. To this purpose, two different philosophies may be contemplated for the search of optimal positions: a *closed-loop* approach, when a closed-loop performance metric must be minimized, or an *open-loop* approach, when the relative controllability and observability of the dominant system modes are increased from a controls perspective [1].

4.1 PROBLEM STATEMENT

In the design of actively controlled structures, the determination of the actuator/sensor locations is an issue of paramount importance to address. In fact, properly chosen actuator/sensor locations result in effectively working control actions and in certain cases are a requirement for the stability of the system. In

Gupta et al. [2] an overview of the optimization criteria (such as maximizing modal forces/moments or deflection of the host structures, maximizing dissipative energy, minimizing control effort, maximizing degree of controllability and observability, minimizing spill-over in residual modes) for optimal placement of piezoelectric sensor and actuator on a smart structure is given. However, many of the proposed methods have mostly targeted only simple case studies such as beams and plates structures, while studies on more complex structures is still lacking in literature.

In general, given a large set of actuators or sensors, the placement problem consists of determining the locations of a reduced subset of devices such that their effect on a flexible structure is maximized while keeping at minimum the required number of devices. One approach is based on an *open-loop* strategy, which often traduces in a combinatory optimization problem as the set of the possible location combinations is discrete [3]. In literature, measures of controllability and observability are often adopted to compare the different combinations of actuator and sensor locations. Among them, the most rigorous quantitative measures are provided by the controllability and observability Gramians (see Chapter 5). Such quantities allows to compute optimal placement indexes to be used for placement of actuators and sensors on flexible structures, as in [1][4][5][6][7]. Other strategies may be adopted, as iterative methods to find the optimal combination [8], solving the discrete problem is a continuous domain by using statistical analysis [9], recurring to search techniques, as genetic algorithms [10], measures of singular value decompositions (SVD) of a configuration such as the minimum singular value, the maximum singular value, the condition number, the relative gain array [11]. However, these methods do not decrease the computational cost inherent to high-dimensional problems, typical for closed-loop placement strategies. Conversely, methods based on effectiveness indices are intuitive and can achieve remarkable results, while minimizing computational efforts. Examples are approaches based on the aforementioned gramians, the modal strain energy (MSE) [12] and eigen-sensitivity [13]. In general, the benefits of employing an open-loop approach to the placement problem are the independence from the type of control architecture to be designed for the problem and a straightforward and computationally efficient procedure.

One alternative philosophy is based on measuring a *closed-loop* performance of the system. Conversely to the open-loop approach, the placement here takes

benefit from already achieving a desired control objective, which is directly included in the placement algorithm. However, for a large number of locations of sensors/actuators these search methods present a high computational effort and not necessary converge to a global optimum. Very different schemes can be developed according to the specific adopted controller. However, in general, to perform a closed-loop optimization two steps are necessary: the definition of a *performance criterion*, so that the locations of actuators/sensors maximize a selected performance metric of the Active Vibration Control (AVC) scheme, and the selection of a proper *optimization algorithm,* to carry out the search for desired locations. The outcome of the process can be considered as the optimal spatial configuration of the distributed devices. Concerning the performance criterion, in literature several methods are contemplated. To cite some of them, space-time integral of some error metrics [14], optimization of the movement of the transmission zeros of the system into the left half plane LQG and LQR performance metric based on the root mean square contribution of each sensor output is considered [15][16], $\boldsymbol{H_2}$-based cost index [17], pole placement techniques are considered [18]. With regard to optimization algorithms, several options are currently available. An overview of the state-of-the-art of current optimization methods is reported in Fig. 4-1.

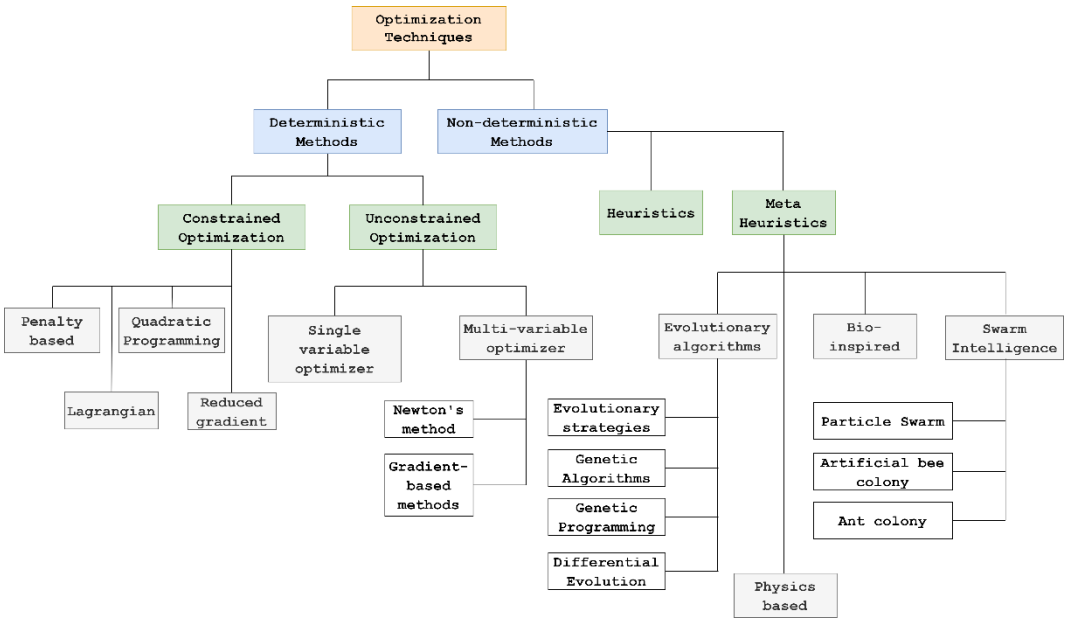

Fig. 4-1: Broad classification of optimization algorithms

It should be noticed that for large-order flexible structures, non-deterministic

methods should be considered, as they are more suitable to solve high dimensional problems. However, they may not always lead to a global optimal solution. To improve the achievable results, such algorithms may be used in series with deterministic gradient-based techniques. In this chapter, a performance criterion based on a pole placement philosophy is considered, while different optimization algorithms are used to minimize the selected objective function.

4.2 Optimal Design of a network of smart devices

In this chapter, an investigation on the best positioning of active on a mesh antenna supporting structure by a closed-loop method is carried out. In particular, the adopted optimization strategy aims at finding the optimal set of Direct Velocity Feedback (DVF) gains that minimizes the control effort. Moreover, the same results are used to carry out the best placement of the actuators in the structure, by switching-off the actuators driven by the lowest gains.

First, some considerations about closed-loop systems have to be introduced. When using a DVF strategy, the control inputs are directly obtained by multiplying the velocity measurements from the sensors by a constant gain matrix. In this chapter, an approach is proposed to optimize such a matrix. Historically, the DVF controller was applied to Large Space Structures from 1989 by M.J. Balas [18]. Conversely to other LSS control systems, where a low number of critical vibration modes was controlled and spillover into the residual modes could lead to instability if not using compensation, the DVF method guarantees that all vibration modes remain stable. In the research work carried out by M. Ikeda [19], the direct feedback of velocity and displacement (DVDFB) is considered for large space structures (LSS) with collocated sensors and actuators. Indeed, it has been demonstrated that, if the rigid modes of LSS are controllable and observable, and the gain matrices are positive definite, then the closed-loop system is stable under any perturbations in mass, damping, and stiffness. The stability condition is derived based on the fact that the transfer function matrix of the collocated system is symmetric. Since the symmetry is always satisfied from the fundamental mechanical law, the stability of the closed-loop system is preserved under the parameter perturbation of LSS and gains of DVDFB. Thus, both DVDFB and DVF belongs to a robust stabilizing control law class. In detail, such scheme was tested on the dynamic model of the Engineering Test Satellite VI equipped with solar panels. A more recent work by I. Nakic [20] proposed a novel approach to the

problem of Direct Velocity Feedback (DVF) optimization of vibrational structures, which treats simultaneously small as well as large gains, by using both Lyapunov equation and quadratic eigenvalue problem.

Therefore, given the properties of such control scheme, a DVF controller was chosen to be implemented in the proposed closed-loop architecture. By referring to the state-space formulation presented in Par. 3.4, and by assuming a network of collocated actuators/sensors is mounted on the structure, which implies the condition $\boldsymbol{C} = \boldsymbol{B}^T$ is satisfied, one may write

$$y = \boldsymbol{C}x = \boldsymbol{B}^T x = \begin{bmatrix} \boldsymbol{C}_{oq} & \boldsymbol{C}_{ov} \end{bmatrix} x = \begin{bmatrix} \boldsymbol{0} & \boldsymbol{B}_{ov}{}^T \end{bmatrix} x \tag{4.1}$$

The control input can be defined as follows

$$u = -\boldsymbol{K}_{DVF} y \tag{4.2}$$

and the closed-loop system represented by the following expression

$$\dot{x} = \boldsymbol{A}x - \boldsymbol{B}\boldsymbol{K}_{DVF}\boldsymbol{B}^T x \tag{4.3}$$

Consequently, the closed-loop matrix becomes $\boldsymbol{A}_{cl} = \boldsymbol{A} - \boldsymbol{B}\boldsymbol{K}_{DVF}\boldsymbol{B}^T$ and the closed-loop state space is described by

$$\boldsymbol{A}_{cl} = \begin{bmatrix} \boldsymbol{0} & \boldsymbol{I} \\ -\boldsymbol{M}^{-1}\boldsymbol{K} & -\boldsymbol{M}^{-1}\left(\boldsymbol{D} + \boldsymbol{B}\boldsymbol{K}_{DVF}\boldsymbol{B}^T\right) \end{bmatrix}, \quad \boldsymbol{B} = \begin{bmatrix} \boldsymbol{0} \\ \boldsymbol{B}_{ov} \end{bmatrix}, \quad \boldsymbol{C} = \begin{bmatrix} \boldsymbol{0} & \boldsymbol{C}_{ov} \end{bmatrix} \tag{4.4}$$

4.2.1 TEST CASE DESCRIPTION

In this chapter, a distributed vibration control system on a spacecraft equipped with a mesh reflector is investigated[1] [22]. In detail, as closed-loop methods are used, a simplified model of the tri-dimensional structure has been derived to test the proposed architecture. Indeed, this study is focused on the impact of pitch manoeuvres (along Z_B axis in Fig. 4-2) on the antenna supporting structure. The retained system configuration is still comprised of the main system components: a central rigid satellite, a flexible boom and a flexible large antenna mesh structure (respectively indicated with numbers 1, 2 and 3 in Fig. 4-2) have been chosen to

[1] Part of this chapter was published by the thesis author in F. Angeletti et al., *Optimal design and robust analysis of a net of active devices for micro-vibration control of an on-orbit large space antenna*, Acta Astronautica, Vol. 164, Nov. 2019, pp. 241-253, [22];

validate an active distributed control solution based on piezoelectric devices.

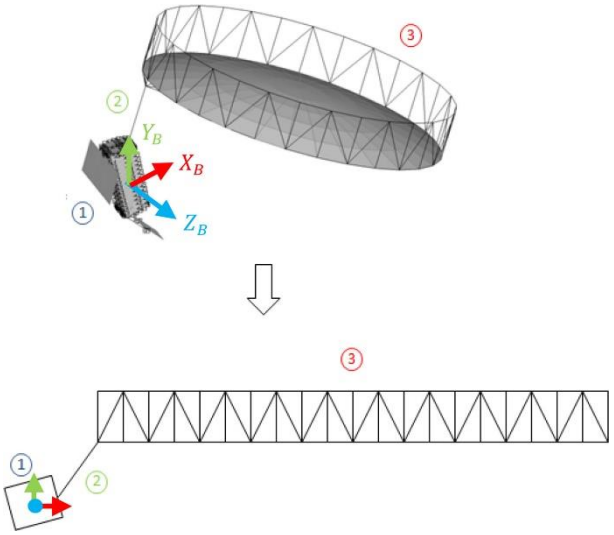

Fig. 4-2: Planar supporting structure [22]

The analysed antenna model is a planar structure composed both of passive and active elements, in a way to reproduce the reticular system that supports the reflector in the actual tri-dimensional case. It is composed of 251 elements with a total amount of 633 DOFs. Each structural part has a length of 1 meter, for a total length of 20 meters. The spacecraft appendage is composed of a deployed boom and the antenna supporting truss structure, both realized in composite material, with different section areas. The main mechanical properties are presented in Table 4-1.

Table 4-1: Properties of the substructures

Substructures	Boom	Antenna
Inertia properties		
Length (m)	4	20
Mass (kg)	152.3	57.95
Total inertia (kg m²)	1650	8590
FEM properties		
F.E. number	8	243
Area (m²)	0.0236	3.92e-4
Young Modulus (GPa)	150	200

A modal analysis has been performed to assess the first frequencies and modal shapes of the appendage in the case the boom is clamped at its end. The first five frequencies are reported in Table 4-2. For convenience's sake, the corresponding

modal shapes obtained by using the Matlab FEM code are presented too. By projecting the equations of motion on a modal basis, the damping coefficient $\xi = 0.02$ has been added. The eigenvalues observed in the case of passive structural damping are reported as complex conjugated couples $\eta = -\lambda \pm j\upsilon$ in Table 4-3.

Table 4-2: Appendage frequencies

N°	Frequency (Hz)	Modal Shape
1	1.92	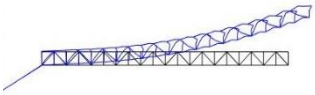
2	9.80	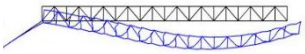
3	20.26	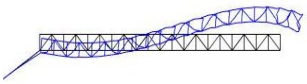
4	43.04	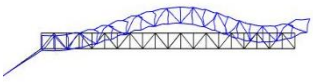
5	51.11	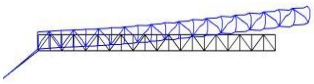

Table 4-3: Eigenvalues: passive structure

N°	Eigenvalues
1-2	-0.24 ± 12.09j
3-4	-1.23 ± 61.59j
5-6	-2.55 ± 127.27j
7-8	-5.41 ± 270.42j
9-10	-6.52 ± 326.10j

As the interest is focused on truss-like structures of a mesh reflector, a scheme composed of an embedded piezoelectric stack actuator/sensor frame into a structural element in assumed, as indicated in Fig. 4-3. More details on the presented model are also given in Appendix A.

Therefore, according to a DVF closed loop logic, the contribution of the piezo elements to the system dynamics can be schematized considering modifying the mass and stiffness matrices and by adding a new damping matrix in the equations

$$\boldsymbol{M}_{FLEX}\ddot{x} + (\boldsymbol{C}_S + \boldsymbol{C}_{pz})\dot{x} + \boldsymbol{K}_{FLEX}x = F \tag{4.5}$$

where $\boldsymbol{C}_S$ models the structure passive damping. It is demonstrated [21][22] that

the active damping matrix for a single element of truss structure can be formulated for each element as

$$\boldsymbol{C}_{\boldsymbol{pz}_k} = g_k 2\frac{E_{pz}A_{pz}G}{L_{pz}\delta_{pz}}\begin{bmatrix} 1 & -1 \\ -1 & 1 \end{bmatrix} \tag{4.6}$$

where g_k is the gain of the k-th element (and it is associated to the power consumption necessary to introduce an active damping in the adaptive-truss), G is a coefficient dependent on the piezo-device physics properties (Young module E_{pz}, area A_{pz}, length L_{pz}, electrical resistance, electromechanical coupling coefficient), δ_{pz} is an non-dimensional parameter referring to the piezo-electric device length. The global matrix can be obtained by following standard finite element assembling methods. In view of the above, if considering the active devices as positioned in the middle of each beam (as highlighted in red in Fig. 4-3-(a)), the design variables to be determined are the gains g_k, $k = 1,...,81$, one for each potentially active beam of the supporting structure.

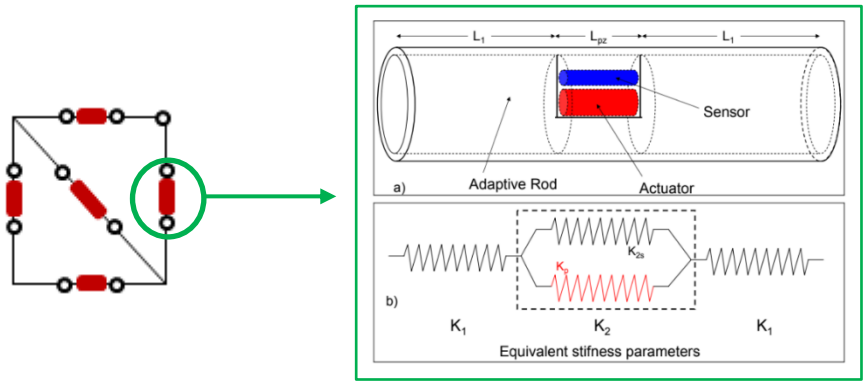

(a) (b)

Fig. 4-3: (a) Possible positions of actuators in a bay; (b) overview of an embedded piezo element

Finally, by projecting eq. (4.14) on the modal basis we obtain

$$\ddot{A} + \boldsymbol{\Omega}^2 A + \left(2\xi\boldsymbol{\Omega} + \boldsymbol{\Phi}^T\boldsymbol{C}_{pz}\boldsymbol{\Phi}\right)\dot{A} = \boldsymbol{\Phi}^T F \tag{4.7}$$

that is the reference equation to perform the pole placement by computing for each set of gains new values of the eigenvalues when the external forces are null.

The focus of this analysis is related to suppress the vibrations of the flexible substructure, which is influenced by both the platform and elastic parts. However, it has been verified that in this case the boom and related mechanical interfaces with the antenna supporting structure are so rigid that the flexible modes of the

antenna are in practice decoupled from the rest of the satellite (as it can be deduced from the modal shapes reported in Table 4-2). Therefore, to perform the optimization procedure only the flexible substructure composed of the boom and the antenna supporting structure has been considered. Because of this the rigid motion of the spacecraft is initially neglected and the relevant dynamic equations reduce to the ones of its flexible parts. The results of the optimization are then validated by simulating the actual dynamic behaviour of the orbiting spacecraft when performing an attitude maneuver (see Par. 4.3).

4.2.2 IN-CASCADE OPTIMIZATION PROCEDURES

The optimal placement and gain selection for a velocity feedback scheme is investigated by the means of in-cascade optimization procedures. The adopted strategy employs a genetic algorithm and a reinforcement learning methodology, both coupled with a gradient-based approach. The aim of the procedure is to make a comparison among the results obtained by using the two algorithms (namely genetic and reinforcement learning) when applied to this problem. More thoroughly, the optimization problem is solved first by genetic and reinforcement learning methods, that independently produced as intermediate optimum solution a set of variables (i.e. the velocity feedback gains). Then, the process is continued in both cases with the deterministic gradient-based method: the first time by using as initial guess the result from genetic algorithm, the second time the result from reinforcement learning. The resulting optimal gains are then tested on a flexible spacecraft performing an attitude manouvre.

4.2.2.1 POLE PLACEMENT VIA GENETIC ALGORITHM

The pole placement procedure aims at individuating the minimum gain distribution such that the real parts of a selected number S of eigenvalues from the homogeneous eq. (4.7) have an assigned value higher than the respective eigenvalues resulting from passive structural damping, as indicated below

$$\lambda_i > \alpha\lambda_{0i} = \lambda^*_i, \quad i = 1,...,S \tag{4.8}$$

with $\alpha > 1$, λ_i real part of the eigenvalues of the active structure and λ_{0i} real part

of the eigenvalues due only to the passive damping. The problem may be formulated as a constrained optimization procedure in the following terms:

Find the gains vector g *to minimize the function* $\Lambda(g)$ *subjected to the constraints*

$$\lambda_i \geq \lambda^*_i \text{, with } (i = 1,...,N_c) \text{ and } g_l \leq g_k \leq g_u$$

where N_C is the number of constraints, $\Lambda(g)$ is the objective function defined as

$$\Lambda(g) = \sum_{k=1}^{N_a} g_k \tag{4.9}$$

N_a is the number of active elements and λ_i^* the assigned constrained value on the real part of the eigenvalue η obtained from the equations

$$\left| \boldsymbol{G} - \eta(\underline{g})\boldsymbol{H} \right| = 0 \tag{4.10}$$

being

$$\boldsymbol{G} = \begin{bmatrix} 0 & -\boldsymbol{I} \\ \boldsymbol{\Omega}^2 & 2\xi\boldsymbol{\Omega} + \boldsymbol{\Phi}^T \boldsymbol{C}_{pz}(\boldsymbol{g})\boldsymbol{\Phi} \end{bmatrix} \quad \boldsymbol{H} = -\begin{bmatrix} \boldsymbol{I} & 0 \\ 0 & \boldsymbol{I} \end{bmatrix} \tag{4.11}$$

where the generic eigenvalue is defined by

$$\eta = -\lambda \pm j\upsilon \tag{4.12}$$

In this case study, the first five modes are simultaneously controlled. The imposed constraints guarantee an increase on the real part of the controlled eigenvalue greater than at least the 30% of the respective passive structure, i.e.

$$\lambda_i > (1 + 0.3)\lambda_{0i} = \lambda^*_i, \quad i = 1,...,5 \tag{4.13}$$

The optimization algorithm is here performed through a Genetic Algorithm (GA) technique based on Augmented Lagrangian Genetic Algorithm (ALGA), in order to solve the optimization problem subjected to non-linear constraints. The algorithm converged to an optimal solution in the gains range [0 100].

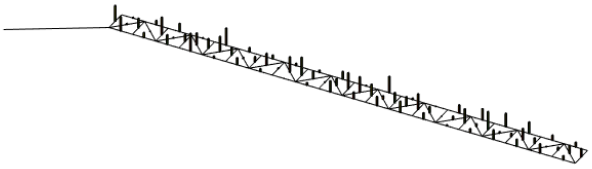

Fig. 4-4: Non-dimensional gain distribution

The non-dimensional gains distribution is presented in Fig. 4-4, where the gains have been normalized with respect to the maximum value found in the interval. A good enhancement of the damping properties of the system can be observed, due to the piezo-electric devices contribution. The new values of the first five structural eigenvalues are listed in Table 4-4.

Table 4-4: Eigenvalues after GA optimization

N°	Eigenvalues
1-2	-0.33 ± 12.09i
3-4	-3.26 ± 62.02i
5-6	-9.34 ± 130.27i
7-8	-20.12 ± 287.42i
9-10	-24.66± 358.10i

The total sum of the network gains can be assumed as a quality parameter giving information about the power consumption: the less the sum, the less the power consumption. In the present analysis, the total sum is equal to 1603.5.

4.2.2.2 POLE PLACEMENT VIA REINFORCEMENT LEARNING ALGORITHM

An alternative method to find an optimal distribution of derivative gains is to adopt a Reinforcement Learning (RL) algorithm. Roughly speaking, the RL agent wants to learn how to select the controller gains in order to maximize a given reward signal [23]. The aim here is to estimate an action-value function and consequently to optimize a policy $\boldsymbol{Q}(s,a)$, i.e. to estimate the best decisional policy $\boldsymbol{Q}^*(s,a)$ for a set of states s and actions a by improving the initial one until the condition $\boldsymbol{Q}(s,a) \approx \boldsymbol{Q}^*(s,a)$ is achieved. This leads to a mapping of the actions (i.e. the gains) the agent can select to optimally control the first five modes of the flexible system, according to its initial state.

The choice of states and actions is of paramount importance for a successful RL method. According to the objective of this Chapter, the actions are chosen as the actuators gains itself. The agent can decide if assign to the net of active device an equally spaced finite value included in the interval [0-100]. The states variables are referred to the real part λ_1 of the eigenvalues with respect to the desired increased value λ_i^*. Indeed, the state variables are five, one for each mode to be controlled. They can assume a single value between the numbers [-0.5, 0, 0.5],

respectively if the real part of the eigenvalue is lower, equal or higher than the corresponding λ_i^*. This leads to a total amount of 3^5 possible states combination. If considering 51 possible actions values, each Q-table will be composed of 243 rows and 51 columns, for a total of 81 Q-tables of 12393 elements each (i.e. one Q-table per actuator).

The reward function is needed to define the desired goal in the RL problem. This operation associates a combination of state-action with a numerical signal which indicated the "goodness" of that state-action pair. In this perspective, the RL agent search to maximize the absolute value of the real part of the first five eigenvalues to reduce undesired vibrations. Since the goal of the agent is to increase the damping capability of the structure while maintaining minimum the sum of the gains, the reward signal is here defined as:

$$R_S = \left(\delta d_1^2 - \gamma d_2^{\,3}\right) \quad with$$
$$d_1 = \sum_{i=1}^{5} \chi_i \left|\lambda_i - \lambda_i^*\right| \qquad d_2 = sum(g) \tag{4.14}$$

where γ is a variable gain and δ is a scaling coefficient introduced to match the orders of magnitude of the two rewarding terms. The variable χ_i is a weighting coefficient different for each eigenvalue, here adopted to give more emphasis to the damping of the first fundamental frequency in the perspective of CSI issue mitigation. The adopted algorithm is named SARSA (State Action Reward State Action), whose updating rule involves the current state and action and the reward corresponding to the transition into the next state by selecting one of the next available actions.

Table 4-5: Algorithm overview

SARSA Algorithm – Control Optimization Problem
Initialize randomly the gains in the Q-table *Q(s,a)*
Goal: enhance of the 30% the real part of the first five eigenvalues
Initialize the state *s* Choose an action *a* from *s* by using the ε-greedy policy
Repeat for each step of the episode (different combination of gains) Take an action a, observe r and choose s' Choose a' from s' by using the ε-greedy policy $Q(s,a) \leftarrow Q(s,a) + \alpha\left[r + \gamma Q(s',a') - Q(s,a)\right]$ $s \leftarrow s'$ $a \leftarrow a'$
Until *s* is terminal

In particular, the change to the policy after an agent's interaction with the environment influence future decisions. At the end of the procedure, we can obtain a set of gains to be implemented in the control scheme. The relevant gain distribution is reported in Fig. 4-5. The new values of system eigenvalues are reported in Table 4-6. We can notice the first ones agree with those individuated by using the GA algorithm.

Table 4-6: Eigenvalues after RL optimization

N°	Eigenvalues
1-2	-0.32 ± 12.09i
3-4	-3.34 ± 61.98i
5-6	-7.99 ± 129.87i
7-8	-17.68 ± 286.43i
9-10	-21.25 ± 357.20i

In particular, Fig. 4-6 depicts the progression of the reward signal through iterations. The convergence of the learning process is reached after few iterations and the fitted learning curve is reported in red.

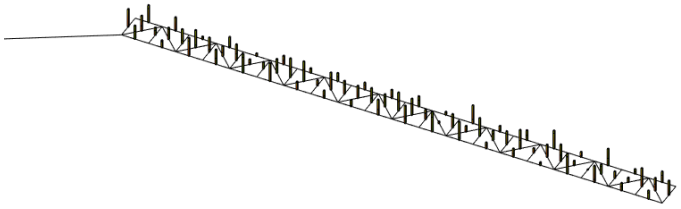

Fig. 4-5: Non-dimensional gains distribution

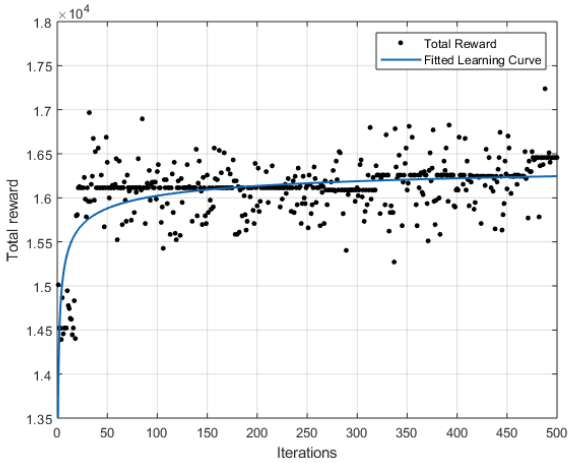

Fig. 4-6: Total reward through iterations

The total sum $\Lambda(g)$ is equal to 1476.7. In this case, we can notice a good enhancement of the damping properties of the system with lower gains than the previous case.

4.2.2.3 POLE PLACEMENT REFINEMENT VIA GRADIENT-BASED OPTIMIZATION

To further improve the efficiency of the control system, two new set of gains have been identified by supplying the results of the GA and RL procedures as the initial best guess of a gradient-based optimization algorithm. The minimization problem has been set in this case as described in Par. 4.2.2.1, as both the objective function and the constraints are those employed in the Genetic Algorithm. As far as this study case is concerned, the initial guess provided by the RL optimization procedure has identified the best minimum.

The convergence of the objective function through iterations is reported in Fig. 4-7 and Fig. 4-8. It is worth noting that the gradient-based algorithm can refine the pole placement by significantly reducing the objective function of about one third. Furthermore, the gains distribution is depicted in Fig. 4-9 and Fig. 4-10. It is possible to observe that the maximum gains are distributed more regularly than the GA and RL solutions and gather near the boom. A decreasing trend in the gain values can be noticed moving towards the free end of the antenna supporting structure (see Fig. 4-10).

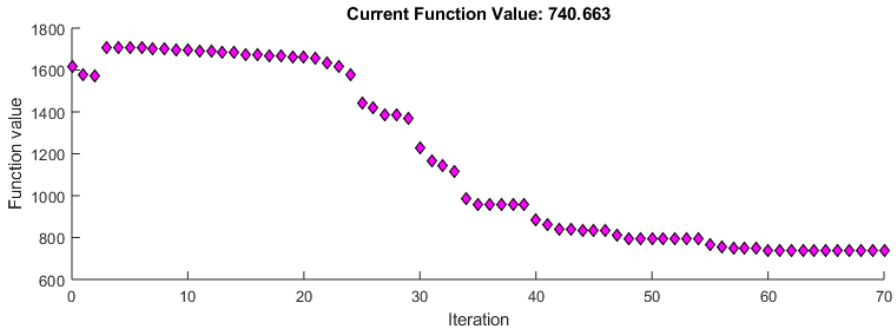

Fig. 4-7: Gradient-based after GA: Objective function values through iterations

Therefore, the two cascade solutions have been compared. It has been observed that, by choosing a proper formulation of the rewarding function in the reinforcement learning algorithm, the results deriving from the latter method gave a minor value of the sum of gains with respect to the one obtained when using the

genetic method. Finally, the RL/gradient-based procedure proved to find the lowest value of the objective function.

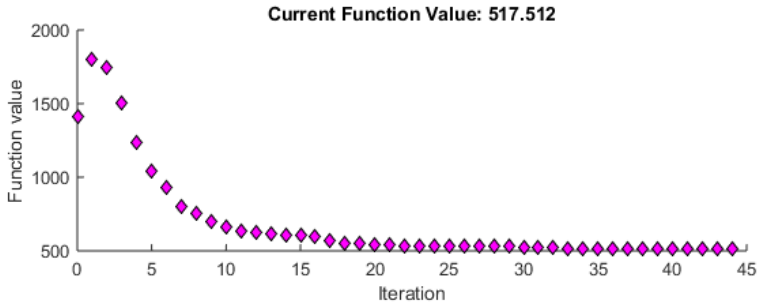

Fig. 4-8: Gradient-based after GA: Objective function values through iterations

Fig. 4-9: Final non-dimensional gains distribution

Fig. 4-10: Final non-dimensional gains distribution: lateral view

4.2.2.4 PLACEMENT BY USING OPTIMIZED GAINS

An interesting result is that the same gains identified via in-cascade optimization procedures can be used to locate the smart devices in the structure. Indeed, no significant change in the damping capability of the system has been identified when omitting those actuators driven by a gain lower than an assigned threshold, in this case equal to:

$$T_S = 10\%\ g_{\max} \tag{4.15}$$

where $g_{\max}$ is the upper bound of the interval [0-100] in which the gains are

searched (see Fig. 4-11).

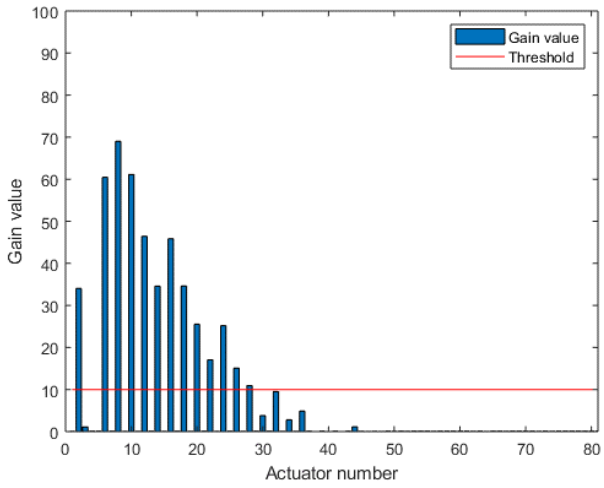

Fig. 4-11: Gain value vs actuator number

Therefore, only thirteen actuators are left in the system, while the others do not further contribute to the damping. A comparison between the eigenvalues when all the actuators are driven by the optimized gains and those resulting from the reduced number of devices is reported in Table 4-7.

Table 4-7: Eigenvalues after G-B optimization

N°	All actuators	13 Actuators
1-2	-0.313 ± 12.09i	-0.311 ± 12.09i
3-4	-3.28 ± 62.10i	-3.21 ± 62.10i
5-6	-8.78 ± 127.87i	-8.34 ± 127.87i
7-8	-17.75 ± 288.63i	-15.56 ± 288.63i
9-10	-19.83 ± 359.90i	-16.29 ± 359.90i

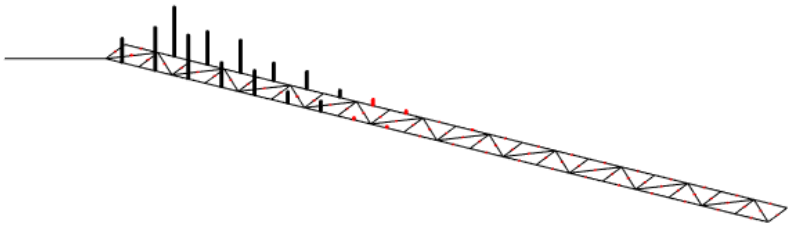

Fig. 4-12: Omitted actuators in red

In Fig. 4-12, the omitted devices are reported in red for clarity's sake. The total sum

$\Lambda(g)$ is finally equal to 517.51. The obtained gains will be also used to define the control strategy described in the next sections.

4.3 VIBRATION CONTROL VIA CLOSED-LOOP OPTIMIZED DVF

Many control strategies have been developed for solving the issue of control/structure interaction. As already mentioned in Chapter 1, the objective of this research is to study a different approach, consisting in facing the problem from the structural point of view, trying to actively damp the vibrations induced by the attitude control system and the orbital perturbations, by using smart material stack devices. To this purpose, the thirteen actuators identified after the optimization methods are driven by the gains derived from the RL and G-B optimization procedures to validate the control scheme for a typical spacecraft manoeuvre. It must be noticed that the optimization process is not aimed at finding the optimal gains for a specific manoeuvre, but it is intended as a general pole placement to guarantee a proper damping in various scenarios.

The actuation voltages are proportional to the first derivative with respect to time of the vector of the modal amplitudes

$$\phi = \beta \dot{A} \tag{4.16}$$

By comparing the two formulations in eq. (3.64) and eq. (4.7) (without considering the non-linear terms) the gains for the control law can be evaluated as follows:

$$\boldsymbol{\Phi}^T \boldsymbol{K}_{X\phi} \phi = \boldsymbol{\Phi}^T \boldsymbol{C}_{pz}(g) \boldsymbol{\Phi} \dot{A} \tag{4.17}$$

Finally, by substituting the control law and simplifying we obtain:

$$\boldsymbol{C}_{pz} \boldsymbol{\Phi} = \boldsymbol{K}_{X\phi} \boldsymbol{\beta} \quad \rightarrow \quad \boldsymbol{\beta} = \boldsymbol{K}_{X\phi}^{+} \left(\boldsymbol{C}_{pz}(g) \boldsymbol{\Phi} \right) \tag{4.18}$$

where $\boldsymbol{K}_{X\phi}^{+}$ represents the Moore-Penrose inverse of the electro-mechanical coupling matrix. According to this approach, the results coming from the optimization procedure can be directly used in the control scheme.

4.3.1 SIMULATIONS

The truss frame is equipped with smart actuators whose properties are listed in Table 4-8. A platform of cubic shape (mass assumed equal to 500kg and size to 2 m) is selected for this test case. To consider a real case, the chosen orbit is similar to the one adopted for the SMAP (Soil Moisture Active Passive) mission, which is currently equipping a mesh reflector. The chosen parameters are presented in Table 4-9.

Table 4-8: Actuators physical properties

	Smart device
Area (m^2)	5.92e-5
Young Modulus (GPa)	130
Density (kg/m^3)	7000
Electro-mechanical coupling coefficient d_{33} (V/m)	400e-12
Resistance R (Ohm)	2000

Table 4-9: Orbit data

	Symbol	Value
Eccentricity	e	0
Orbital radius (km)	R	7078
Initial position on the orbit (deg)	β	25
Initial orientation w.r.t. the local vertical (deg)	φ	5
Orbital period (min)	T_o	98.77

An attitude manoeuvre has been simulated to study the performance of the active control in damping out the vibrations. A simple bang-bang manoeuvre is considered. The resulting displacements at the tip of the antenna supporting structure is presented in Fig. 4-13. To evaluate the effective enhancement in the damping capability of the system the value of the logarithmic decrement for the tip displacement time history has been computed as

$$\delta = \frac{1}{m} \ln\left(\frac{x_i^{TIP}}{x_{i+m}^{TIP}} \right) \tag{4.19}$$

where x_i^{TIP} and x_{i+m}^{TIP} are two peaks identified in the time history and m is the number of peaks between them. In the case of passive structural damping the logarithmic decrement value is $\delta_{PASSIVE} = 0.0581$. On the contrary, when using the thirteen actuators the value increases to $\delta_{NOM} = 0.0721$. A good enhancement of the structural

damping capability can be clearly noticed when using the piezo actuators devices.

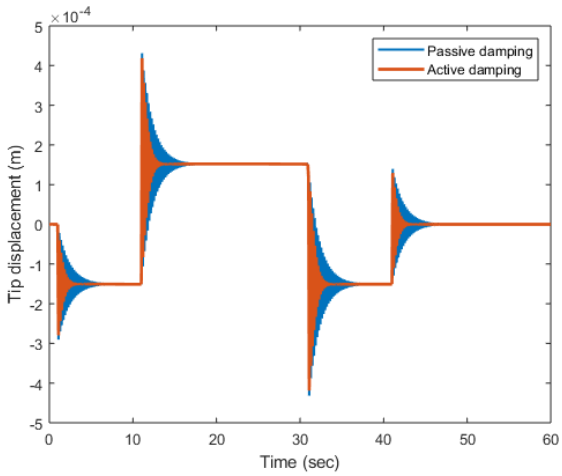

Fig. 4-13: Tip displacement with and without active control

The time histories of two actuators input voltages are also reported in Fig. 4-14 and Fig. 4-15. To avoid the actuators, undergo a higher input voltage than their physical limit (dielectric breakdown), saturation blocks are added to the control scheme. A factor of safety is introduced to additionally lower the maximum allowable value and enhance the reliability of the system.

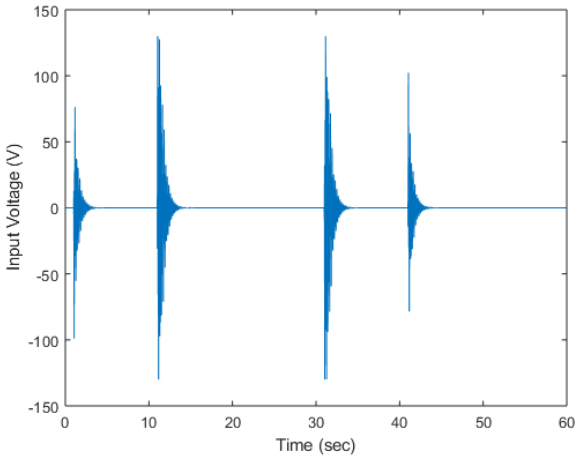

Fig. 4-14: Input voltage time history (not saturated actuator) – Optimized DVF control – Actuator n°6

It is worth noting the actuators with a higher derivative gain (corresponding to the one obtained from the optimization procedure) reach the saturation condition (as shown in Fig. 4-15).

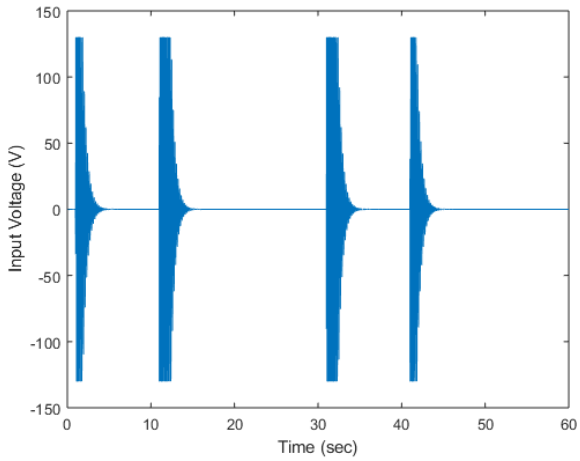

Fig. 4-15: Input voltage time history (saturated actuator) – Optimized DVF control – Actuator n°2

As for that, the control channel is saturated for a few seconds, but this event still does not compromise the effective damping capability of the active system. To evaluate the power consumption required by the active devices network, the mean power absorbed by each actuator has been computed as

$$\overline{P}_i = \frac{1}{T_F}\int_0^T P_i(t)dt = \frac{1}{T_F}\int_0^T C_P \phi_i^2(t)dt \tag{4.20}$$

where the i-th index indicates the actuator number, T_F is the total manoeuvre time, C_P the electrical capacitance (as reported in Table 4-8) and ϕ_i the voltage supplied to each device. The average power consumption $\overline{P}_i$, referred to each actuator, is showed in Fig. 4-16.

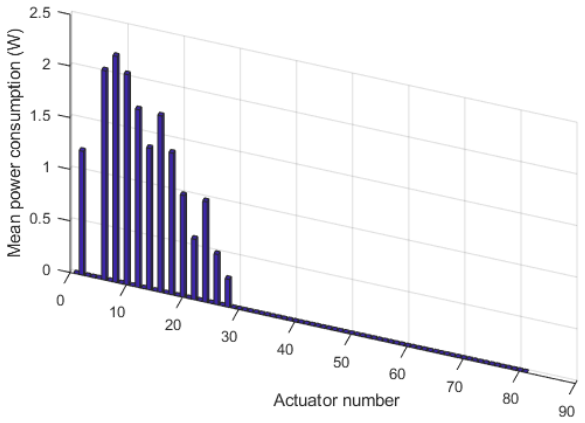

Fig. 4-16: Average power consumption in Watts

It can be noticed the actuators requiring most of the power are those placed near the boom. This result is expected if considering that the antenna frame structure receives the perturbation originated by the satellite motion through the boom itself. The total mean power consumption is computed as

$$\overline{P} = \sum_{i=1}^{13} \overline{P}_i \tag{4.21}$$

and it's equal to 16.86 W. According to the available data about SMAP spacecraft accoutred with the patented Astromesh reflector, its solar panels can generate 1500 W of electric power [24]. As for that, the power amount reserved to the active damping system seems to be affordable for the mission.

According to the results of the closed loop simulations, the actuators should be able to impress an elongation equal to

$$\Delta L = n\, d_{33}\, \phi \tag{4.22}$$

In both cases, the maximum elongation does not exceed 30 μm, thus allowing the network to be composed of most of the actuators available in the market at present.

In the following sections, additional investigations concerning the robustness of the proposed control scheme will be carried out by referring to the first control strategy.

4.4 ROBUSTNESS OF THE CONTROL SYSTEM

To investigate the controller behaviour under different operative conditions further analyses have been carried out via Monte Carlo campaigns [22]. In particular, a change in both the mechanical and electrical properties of piezo actuators has been simulated by varying gains associated to the faulty devices. Then, the properties of the passive structures are considered as uncertain as well to study the impact of such a modification of the system dynamic behaviour.

4.4.1 DAMAGED ACTUATORS

In this section the robustness of the actuators network in damping the vibration when one or more devices are in a "damaged" condition will be

analysed. The decrease of the piezoelectric physical and electromechanical properties is modelled as a gain reduction of the 50% on randomly chosen actuators. As a first investigation, a number $N_D = 5$ of actuators has been randomly considered as "damaged" in the manoeuvre simulation. A campaign of 400 simulations has been performed to study the controller behaviour. The number of simulated scenarios has been selected based on the trend of both mean and standard deviation of the collected samples. The network system proved to guarantee good damping performance even in conditions other than the nominal case.

As a performance index, the value of the logarithmic decrement has been computed for each scenario. Furthermore, the collected data have been processed by the means of the MATLAB Distribution Fitting Toolbox. Their mean value μ and standard deviation σ have been computed as

$$\mu = \frac{1}{N_V}\sum_{i=1}^{N_V} x_i^{TIP} \qquad \sigma = \sqrt{\frac{1}{N_V - 1}\sum_{i=1}^{N_V}\left|x_i^{TIP} - \mu\right|^2} \tag{4.23}$$

where N_V is the number of element of x_i^{TIP} vector.

In this case, the mean value is μ=0.0708 and the corresponding standard deviation σ=3.87e-4. According to those results, no significant impact has been detected on the controller, since the standard deviation of δ is two orders of magnitude less than its mean value, as indicated in Fig. 4-17. In particular, the values of the logarithmic decrement in the case of active control are reported as blue circles, while the value of δ when considering only passive structural damping is depicted as a black line.

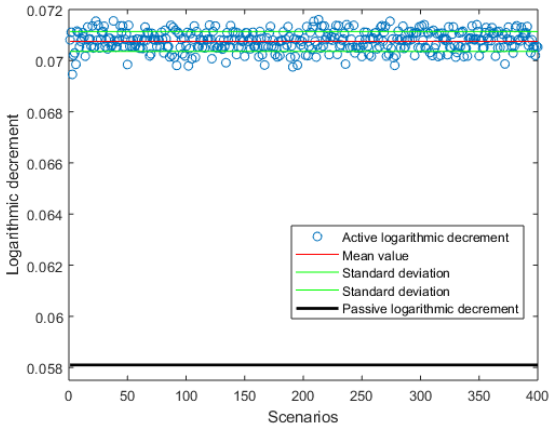

Fig. 4-17: Logarithmic decrement: μ=0.0708 σ=3.87e-4

Even in the worst damping condition (δ=0.0695) identified in Fig. 4-17, the capability of the system is not particularly affected by the damages, as indicated by the time histories of the tip displacement in Fig. 4-18. In addition, the damaged actuators are highlighted in red in Fig. 4-19 and the total mean power consumption is $\overline{P} = 15.08W$.

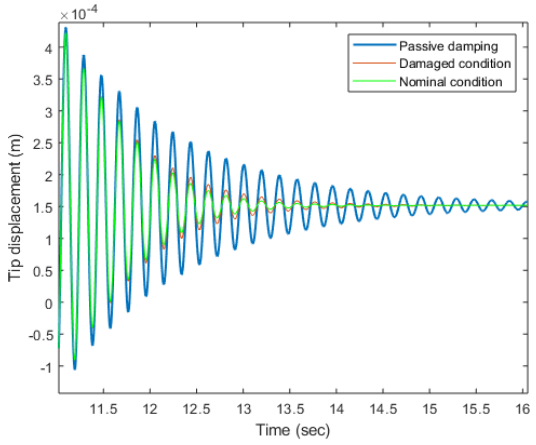

Fig. 4-18: Comparison of tip displacement – damaged condition δ=0.0695

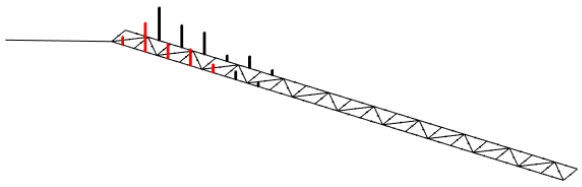

Fig. 4-19: Damaged actuators distribution in red: δ=0.0695

A second study case has been performed by randomly switching off five actuators. More thoroughly, 400 simulations have been repeated to study the change in the control system damping behaviour. To make a comparison with the previous case study, both the trend of logarithmic decrement is presented in Fig. 4-20. In particular, the mean value is μ=0.0699 and the corresponding standard deviation σ=0.0012.

As expected, the standard deviation of the logarithmic decrement is higher, and the mean power consumption is lower than the previous case. However, only very few scenarios out of 400 simulations resulted in a reduction of δ higher than the 10% of the nominal case value. The worst-case condition is found if the same actuators individuated in the previous analysis (those missing in Fig. 4-22) are

switched off and the related logarithmic decrement is δ=0.0642.

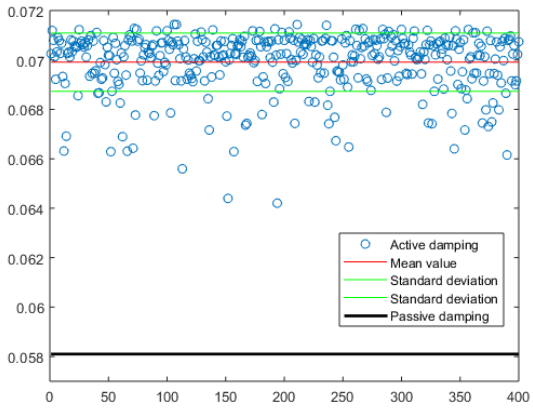

Fig. 4-20: Logarithmic decrement: μ=0.0699 σ=0.0012

The time history of the tip displacement in such a scenario is compared to the trends deriving from passive structural damping and controller nominal condition in Fig. 4-21. A significant reduction in the damping of the vibration is noticeable, even if the event of those five actuators switched-off at the same time can be considered as unlikely to happen.

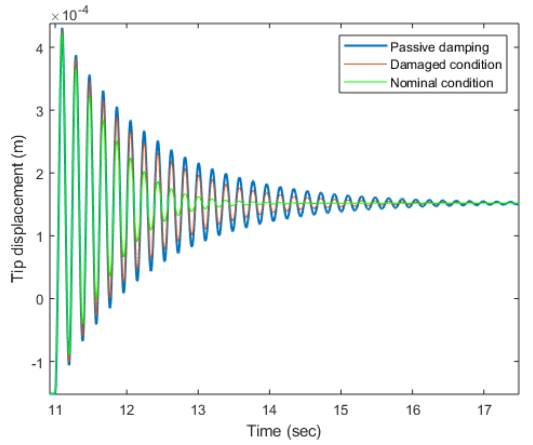

Fig. 4-21: Comparison of tip displacement – damaged condition: δ=0.00642

It is worth noting that in the second case study the damping performance is lower than the other cases. This reduction in the control system capability can be expected if considering that the damaged actuators are those driven by the higher gains.

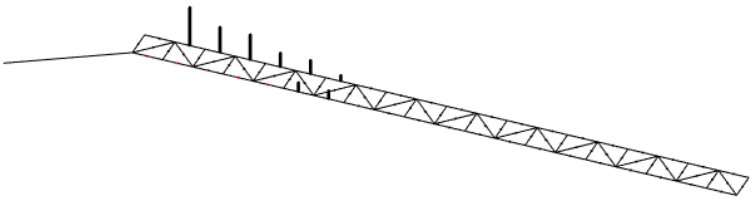

Fig. 4-22: Switched-off actuators: δ=0.00642

4.4.2 ROBUSTNESS ANALYSIS

In this case, as the controller gains have been optimized for a specific passive structure, the properties of the supporting structure are assumed as uncertain to simulate a possible change in the mechanical characteristics after launch or due to in-orbit aging. Affected features are: Young modulus E_{stru}, area A_{stru}, bending stiffness I_{stru}. The properties are assumed to be known with $\pm 10\%$ of uncertainty.

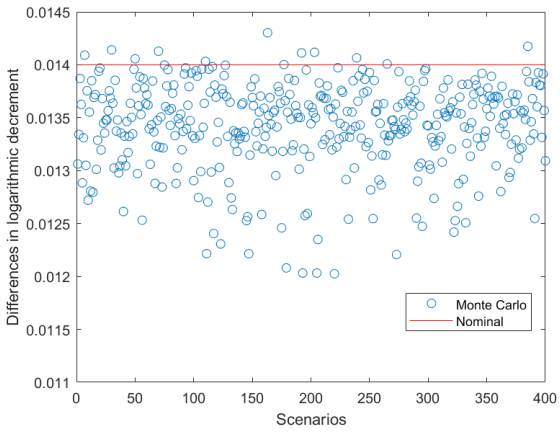

Fig. 4-23: Differences in active and passive logarithmic decrements

The controller robustness has been assessed by adding uncertainties to the aforementioned parameters. In Fig. 4-23, the difference in the logarithmic decrement between passive and active damping, computed on the tip displacement as

$$\Lambda = \delta_{active} - \delta_{passive} \tag{4.24}$$

It is worth noting that, by introducing uncertainties on structural parameters the differences in the logarithmic decrement are similar to the value in the nominal

case. In some scenarios the value of this parameters exceeds even the nominal one. This is related to the fact that by changing the mechanical properties of the passive structure the damping capability of the control system could actually increase due to new favourable conditions. It is worth noting that the passive structural damping varies accordingly with the new properties of the structure in each scenario.

In conclusion, the gains associated to different numbers of devices have been reduced by 50%. The net demonstrated to guarantee a satisfactory damping performance even if five actuators out of thirteen are considered as "damaged". Then, the effects of a reduced number of actuators have been presented. The system seemed to be affected by the switched-off actuators if the number is equal to near the half of the total. Considering that space systems can vary their characteristics as a result of both launch campaign and in-orbit aging processes, Monte Carlo simulations campaigns have been carried out to evaluate the performance of the controller (which has been designed for the nominal case). Results have confirmed that the adopted velocity feedback controller is robust even to significant variations in the passive structure physical properties.

BIBLIOGRAPHY

[1] W. K. Gawronski, *Advanced Structural Dynamics and Active Control of Structures*, Mechanical Engineering Series, Springer, New York, 2004;

[2] V. Gupta, M. Sharma and N. Thakur, *Optimization Criteria for Optimal Placement of Piezoelectric Sensors and Actuators on a Smart Structure: A Technical Review*, Journal Of Intelligent Material Systems And Structures, Vol. 21—August 2010;

[3] M. Zapateiro, F. Pozo, *Advances on Analysis and Control of Vibrations: Theory and Applications*, InTech Edition, 2012

[4] K. B. Lim, *Method for optimal actuator and sensor placement for large flexible structures*, AIAA J. Guidance, Dynamics, Contr,, vol. 15, pp. 49–57, 1992.

[5] R. W. Longman and K. T. Alfriend, *Energy optimal degree of controllability and observability for regulator and maneuver problems*, Proc. 16th Annu. Conf. Inform. Sci. Syst., Princeton, N.J., Mar. 1982.

[6] Y. Kim and J. L. Junkins, *A measure of controllability for actuator placement*, AIAA J. Guidance, Dynamics, Contr., vol. 14, no. 5, pp. 895–902, Sept.–Oct. 1991.

[7] K. B. Lim, *Disturbance rejection approach to actuator and sensor placement*, AIAA J. Guidance, Dynamics, Contr., vol. 20, no. 1, pp. 203–204, 1997.

[8] R. T. Haftka, H. M. Adelman, *Selection of Actuator Locations for Static Shape Control of Large Space Structures by Heuristic Integer Programming*, Computers and Structures , 20: 575–582, 1985;

[9] R. A. Burdisso, R. T. Haftka, *Statistical analysis of static shape control in space structures,* AIAA Journal, 28:1504-1508, 1990;

[10] S. S. Rao, T. S. Pan, V. B. Venkayya, *Optimal Placement of Actuators in Actively Controlled Structures Using Genetic Algorithms*, AIAA Journal, 29: 942–943, 1991;

[11] M. Guney, E. Eskinat, *Optimal actuator and sensor placement in flexible structures using closed-loop criteria*, Journal of Sound and Vibration 312 (2008) 210–233;

[12] A. Preumont A, J. P. Dufour, C. Malekian, *Active damping by a local force feedback with piezoelectric actuators*, Journal of Guidance, Control and Dynamics 15:390-395, 1992;

[13] A. Bilbao, R. Avilés, J. Aguirrebeitia, I. F. Bustos, *Eigensensitivity-based optimal damper location in variable geometry trusses,* AIAA Journal, 47 : 576-590, 2009;

[14] W. H. Chen and J. H. Seinfeld, *Optimal location of process measurements*, Int. J. Contr., vol. 21, no. 6, pp. 1003–1014, 1975.

[15] R. E. Skelton and M. L. DeLorenzo, *Selection of noisy actuators and sensors for linear stochastic systems*, J. Large-Scale Syst., Theory, Applicat., vol. 4, pp. 109–136, Apr. 1983.

[16] J. N. Juang and G. Rodriguez, *Formulation and applications of large structure actuator and sensor placements*, VPI/AIAA Symp. Dynamics Contr. Large Flexible Structures, 1979, pp. 247–262.

[17] G. J. Balas, P. M. Young, *Sensor Selection via Closed-Loop Control Objectives*, IEEE Transactions On Control Systems Technology, Vol. 7, No. 6, November 1999

[18] M.J. Balas, *Direct Velocity Feedback Control of Large Space Structures*, Journal of Guidance, Control, and Dynamics, Vol. 2, No. 3 (1979), pp. 252-253;

[19] M. lkeda, K. Koujitani and T. Kida, *Optimality Of Direct Velocity And Displacement Feedback For Large Space Structures With Collocated Sensors And Actuators*, IFAC 12th Triennial World Congress, Sydney, Australia, 1993;

[20] I. Nakic et al., *Optimal Direct Velocity Feedback*, Applied Mathematics and Computation 225 (2013) 590–600;

[21] F. di Scioscio, P. Gasbarri, C. Marianetti, and C. Toglia, *Control of Vibrations of the International Space Station with Piezoelectric Actuators*, in Proceedings of the International Astronautical Federation, Fukoka, Japan, 2005, vol. 6, pp. 16–21.

[22] F. Angeletti, P. Gasbarri, M. Sabatini, *Optimal design and robust analysis of a net of active devices for micro-vibration control of an on-orbit large space antenna*, Acta Astronautica, Vol. 164, Nov. 2019, pp. 241-253;

[23] N.R. Ravishankar et al., *Reinforcement Learning Algorithms: Survey and Classification*, in Indian Journal of Science & Technology, India, 2017, vol. 10, Issue 1.

[24] Thomson, *AstroMesh deployable reflectors for Ku- and Ka-band commercial satellites*, in: 20th AIAA International Communication Satellite Systems Conference and Exhibit, 2002, AIAA 2002-2032.

Chapter 5
PLACEMENT: AN OPEN-LOOP APPROACH

In this chapter, a general procedure to perform a straightforward and computationally efficient placement for high-dimensional structures is proposed and tested on different study cases. The procedure applies two optimization strategies, one based on the concepts of controllability and observability gramians and the other on the examination of the modal strain energy and singular values of the flexible structure equipped with collocated actuators and sensors.

In this section, a placement process aimed at finding the best location to place collocated actuators/sensors for active vibration purposes is proposed. To obtain results independent from the adopted control system, an open loop placement is considered. As mentioned in Chapter 4, such a procedure is generally based on the notions of system controllability and observability, which will be presented hereafter.

5.1 CONTROLLABILITY AND OBSERVABILITY

The concepts of controllability and observability may be described in a heuristic way by referring to the ability of moving and observing the states of a system [1]. Indeed, if the input to a system can move all the states in an arbitrary direction, the system can be considered as fully controllable. On the other hand, if all the states of the system cannot be observed at the output, the system is not defined as fully observable. Gawronski [2] declined such definitions for a flexible structure. Indeed, a structure can be considered controllable if the installed

actuators excite all its structural modes. Moreover, it is assumed observable if the implemented sensors can potentially detect the motions associated to all the modes. Canonically, for linear systems, information in terms of interaction between inputs/outputs and the states may be derived by referring to the matrices of the state-space representation $(\boldsymbol{A},\boldsymbol{B},\boldsymbol{C})$. Indeed, a system, or the pair $(\boldsymbol{A},\boldsymbol{B})$ is controllable if it is possible to find a continuous input $u(t), t \in [t_0, t_1]$ such that the system is moved from the initial state $x(t_0)$ to the state $x(t_1)$ at a finite time $t_1 > t_0$, for all initial instant t_0 and initial states. Moreover, a system, or the pair $(\boldsymbol{A},\boldsymbol{C})$ is observable at t_0 if the state $x(t_0)$ can be detected from the output $y(t)$ for $t \in [t_0, t_1]$ and $t_1 > t_0$, for all states and initial time instants. In conclusions, there are several criteria to verify the controllability and observability of a system, some of them are reported hereafter.

According to the *Kalman* rank condition definition, a linear system with s inputs is controllable if and only if the matrix $\boldsymbol{C}$ of dimensions $N \times sN$

$$\boldsymbol{C} = \begin{bmatrix} \boldsymbol{B} & \boldsymbol{AB} & \boldsymbol{A}^2\boldsymbol{B} & \cdots & \boldsymbol{A}^{N-1}\boldsymbol{B} \end{bmatrix} \tag{5.1}$$

has rank equal to N. Conversely, a system with r outputs is observable if the matrix of dimensions $rN \times N$

$$\boldsymbol{O} = \begin{bmatrix} \boldsymbol{C} & \boldsymbol{CA} & \boldsymbol{CA}^2 & \cdots & \boldsymbol{CA}^{N-1} \end{bmatrix}^T \tag{5.2}$$

has rank equal to N. However, these definitions have two relevant drawbacks. First, they determine the controllability and observability of the system as overall properties. Indeed, they verify their existence or the non-existence, without providing any information about degrees of controllability. Second, they can be practically implemented only for systems of small dimensions, as they depend on powers of the state matrix up to $N-1$.

An alternative test, avoiding the numerical difficulties of the previous method, involves the concepts of *controllability and observability gramians*, $\boldsymbol{W}_C$ and $\boldsymbol{W}_O$ respectively, being

$$\boldsymbol{W}_C = \int_0^t e^{A\tau} B B^T e^{A^T\tau} d\tau, \qquad \boldsymbol{W}_O = \int_0^t e^{A^T\tau} C^T C e^{A\tau} d\tau \tag{5.3}$$

In such cases, a system is defined controllable (observable) if the related gramian has full rank, thus is it is definite positive. An interesting property of such matrices

can be noticed in the case they are diagonal and equal. In detail, the diagonality property implies an independent measure of controllability (observability) can be associated to each. Such a measure is the diagonal value of the gramians. On the other hand, the equality property indicates that each state is equally controllable and observable. In particular, the diagonality of gramians is a very useful tool to separately evaluate each state. Therefore, the concept of balanced realization can be introduced: a system $(\boldsymbol{A},\boldsymbol{B},\boldsymbol{C})$ is open-loop balanced if its controllability and observability gramians are equal and diagonal

$$\begin{aligned} &\boldsymbol{W}_C = \boldsymbol{W}_O = \boldsymbol{\Upsilon} \\ &\boldsymbol{\Upsilon} = diag(\gamma_1,...,\gamma_N) \quad \gamma_i > 0,\ i = 1,...,N \end{aligned} \tag{5.4}$$

The matrix $\boldsymbol{\Upsilon}$ is diagonal and the values γ_i are the Hankel singular values of the system (which are usually defined as the eigenvalues of the product of controllability and observability gramians).

Concerning flexible structures, according to Gawronski [2], in case of small damping ($\xi \ll 1$, which is often the standard for spacecraft flexible appendages), the balanced and modal representation of flexible structures are closely related. Indeed, the balanced gramians are equal and diagonal; likewise, the gramians in modal coordinates are diagonally dominant, and by using proper scaling, they are approximately equal. Therefore, a closed form gramians for flexible structures can be defined as

$$\boldsymbol{W}_C \simeq diag(w_{ci}\boldsymbol{I}_2) \qquad \boldsymbol{W}_O \simeq diag(w_{oi}\boldsymbol{I}_2) \tag{5.5}$$

$$w_{ci} = \frac{\|B_{mi}\|_2^2}{4\xi_i\omega_i}, \qquad w_{oi} = \frac{\|C_{mi}\|_2^2}{4\xi_i\omega_i} \tag{5.6}$$

where w_{ci} and w_{oi} are the controllability and observability factors and the Hankel singular value are obtained in approximation as $\gamma_i = \sqrt{w_{ci}w_{oi}}$. In the frequency domain the gramians can be rewritten as

$$\boldsymbol{W}_C = \frac{1}{2\pi}\int_{-\infty}^{\infty} H(v)BB^T H^*(v)dv, \qquad \boldsymbol{W}_O = \frac{1}{2\pi}\int_{-\infty}^{\infty} H^*(v)C^T CH(v)dv \tag{5.7}$$

where $H(v)$ is the Fourier transform of the term e^{Ar}

$$H(v) = \left(jvI - A\right)^{-1} \tag{5.8}$$

and $H^*(v)$ is the complex conjugate transpose of $H(v)$.

5.2 OPEN LOOP PLACEMENT

In this section, the placement process aimed at finding the best location to place collocated actuators/sensors for active vibration purposes is presented. To obtain results independent from the adopted control system, an open loop placement is considered. Considering a generic satellite composed of a rigid hub and attached flexible structures, the placement can lie on the fact the assembled satellite's modes are a combination of the modes of the single appendages. Therefore, the positioning procedure may be performed on each flexible substructure. According to this approach, the best location of the devices is found to optimally control the modes of the appendages, thus automatically allowing also controlling the modes of the satellite. Information on how the actuators action interacts on modes of different appendages may be obtained afterward by directly inspecting the input matrix. However, even if the action of one actuator also affects another substructure, it results to be more reliable to use actuators/sensors implemented on one appendage to perform active vibration on that very structure, rather than considering the interaction with the devices mounted on a different appendage (while, of course, it could guarantee a certain level of redundancy).

In detail, two straightforward and computationally efficient methodologies are presented and compared to carry out the placement of a set of actuators and sensors on a flexible structure:

- the *Norm-based placement* method makes use of the controllability and observability gramians of the system and attempt to optimize the sensor and actuator locations to increase, from a control perspective, the relative controllability and observability of the important system mode;

- the *MSE and SVD-based placement* method is based on the extraction of the modal strain energy (MSE) from a commercial finite element tool and the computation of Singular Values Decomposition (SVD) of the modal input matrix of the system to evaluate the effect of positioning collocated actuators/sensors on flexible structures.

5.3 NORM-BASED PLACEMENT

The first method relies on the definition of system norms, based on controllability and observability gramians, to investigate the placement of co-located pairs of actuators/sensors on large flexible structures. A placement index grading the effects of an actuator/sensor on a specific mode is defined and considered to perform the placement process. Here the positioning of actuators and sensors is based on the work of Gawronsky [2] and adapted to exploit the properties of observability and controllability gramians to bypass complex search methods, enabling favorable scaling for high-dimensional systems. As opposed to standard search procedures, which could be overwhelming and time consuming for large numbers of locations of actuators/sensors, such a method consists in a non-search strategy based on the controllability/observability of the system. In detail, it aims at grading the participation of actuators/sensors in the norm of the system, i.e. how effective is the actuator/sensor pair when addressing selected modes of the structures.

In particular, the gramian-based approach involves a combinatorial optimization problem, different from a continuous optimization problem. Indeed, according to T. Summers et al. [3], sensor and actuator placement can be formulated as set function optimization problems. For a given finite set V = {1,..., M}, a set function $f : 2V \rightarrow R$ assigns a real number to each subset of V. In our setting, the elements of V represent potential locations for the placement of sensors or actuators in a dynamical system, and the function f is a metric for how controllable or observable the system is for a given set of placements, which is to be maximized. We consider set function optimization problems of the form

$$\underset{S \subseteq V, |S|=k}{\text{maximize}} \quad f(S) \tag{5.9}$$

where the problem is to select a *k*-element subset of V that maximizes f . This is a finite combinatorial optimization problem, so the solution simply consists in enumerating all possible subsets of size *k*, evaluate f , and pick the best subset. Furthermore, by using a parallel between sub-modularity (for combinatorial optimization problems) and convexity (for continuous optimization problems), Summers demonstrated how controllability and observability Gramians yield modular set functions and are therefore efficiently globally optimized.

Of course, as it is not possible to find optimal locations for actuators/sensors

for all modes simultaneously, the final configuration will depend on some weighting coefficients introduced to give importance to some modes over the others. According to this, by varying such constants, the final resulting configuration will be not unique.

In detail, to carry out the placement procedure, some steps are necessary:

1. Definition of the Controllability and Observability gramians of the system, as presented in Par. 5.1;
2. Computation of the norm of the flexible structure, which may be considered as a sum (the max) of the norms of the structure if using H_2 norm (H_∞ norm);
3. Computation of the norm of a mode, which is assumed to be the sum of the norms of actuators/sensors that are implemented on the structure (both for H_2 and H_∞ norms);
4. Grading of the effects of an actuator/sensor on a specific mode based on its participation in the system norm by computing placement indices;
5. Selection of a subset of reduced locations (corresponding to higher placement indices) where pairs of co-located actuators/sensors may be optimally placed.

5.3.1 SYSTEM NORMS

A measure of the intensity of a system response to external excitations, as unit impulse, may be provided by the system norms [2][4]. Concerning flexible structures, three norms can be considered, namely H_2, H_∞ and Hankel norms. In detail, H_2 norm can be defined as a root-mean-square sum of the norms of individual modes, while H_∞ and Hankel norms are determined as the largest corresponding modal norm (as later described in this section). Each of the three norms of a mode with multiple inputs or outputs can be decomposed into the sum of norms of a single input (or output), thus allowing for efficient strategies for model reduction and actuator/sensor placement.

In particular, if $[\boldsymbol{A},\boldsymbol{B},\boldsymbol{C}]$ is the representation of a space-state system and $\boldsymbol{G}(\omega)=\boldsymbol{C}\left(j\omega I-\boldsymbol{A}\right)^{-1}\boldsymbol{B}$ is the corresponding transfer function, the H_2 norm can be defined as

$$\|\boldsymbol{G}\|_2^2=\frac{1}{2\pi}\int_{-\infty}^{\infty} tr\left(\boldsymbol{G}^*(\omega)\boldsymbol{G}(\omega)\right)d\omega \tag{5.10}$$

where the operator $tr(\bullet)$ indicates the sum of the squared magnitudes of all the elements of $\boldsymbol{G}(\omega)$. Furthermore, it follows from eq. (5.7) that the H_2 norm may be conveniently expressed as below

$$\|\boldsymbol{G}\|_2 = \sqrt{tr\left(\boldsymbol{C}^T\boldsymbol{C}\boldsymbol{W}_C\right)} = \sqrt{tr\left(\boldsymbol{B}\boldsymbol{B}^T\boldsymbol{W}_O\right)} \tag{5.11}$$

where $\boldsymbol{W}_C$ and $\boldsymbol{W}_O$ are the controllability and observability gramians respectively. Conversely, the H_∞ is computed as

$$\|\boldsymbol{G}\|_\infty = \max_{\omega} \sigma_{\max}(\boldsymbol{G}(\omega)) \tag{5.12}$$

where $\sigma_{\max}$ is the maximum singular value of the transfer function $\boldsymbol{G}$.

5.3.1.1 NORM OF A MODE AND NORM OF A STRUCTURE

Let n_d be the number of the degrees of freedom of the system, while *R* be the number of outputs and *S* the number of inputs, as presented in Chapter 3, the equations of motion of a structure can be expressed as

$$\begin{aligned} &\boldsymbol{M}\ddot{q} + \boldsymbol{D}\dot{q} + \boldsymbol{K}q = \boldsymbol{B}u \\ &y = \boldsymbol{C}_{\boldsymbol{oq}}q + \boldsymbol{C}_{\boldsymbol{ov}}\dot{q} \end{aligned} \tag{5.13}$$

where q is the $n_d \times 1$ nodal displacement vector, $\dot{q}$ is the $n_d \times 1$ nodal velocity vector u is the $S \times 1$ input command, y is the $R \times 1$ output of the system, $\boldsymbol{B}$ is the $n_d \times S$ input matrix, $\boldsymbol{C}_{\boldsymbol{oq}}$ is the $R \times n_d$ displacement output matrix, while $\boldsymbol{C}_{\boldsymbol{ov}}$ is the $R \times n_d$ velocity output matrix. By projecting eq. (5.13) on a modal basis represented by the modal matrix Φ, one can write

$$\begin{aligned} &\Phi^T\boldsymbol{M}\Phi\ddot{q}_m + \Phi^T\boldsymbol{D}\Phi\dot{q}_m + \Phi^T\boldsymbol{K}\Phi q_m = \Phi^T\boldsymbol{B}_o u \\ &y = \boldsymbol{C}_{\boldsymbol{oq}}\Phi q_m + \boldsymbol{C}_{\boldsymbol{ov}}\Phi\dot{q}_m \end{aligned} \tag{5.14}$$

Then, if modal displacements and velocities are assumed as state variables, so that $x_1 = q_m$ and $x_2 = \dot{q}_m$, the equations of motion can be presented as first-order differential equations as

$$\boldsymbol{A} = \begin{bmatrix} \boldsymbol{0} & \boldsymbol{I} \\ -\boldsymbol{\Omega}^2 & -2\boldsymbol{Z}\boldsymbol{\Omega} \end{bmatrix}, \quad \boldsymbol{B} = \begin{bmatrix} \boldsymbol{0} \\ \boldsymbol{B}_m \end{bmatrix}, \quad \boldsymbol{C} = \begin{bmatrix} \boldsymbol{C}_{mq} & \boldsymbol{C}_{mv} \end{bmatrix} \tag{5.15}$$

where the matrices can be further decomposed in sub-matrices, each for the *i*-th considered mode ($i = 1,...,n$ with n number of modes)

$$\boldsymbol{A}_{mi} = \begin{bmatrix} 0 & 1 \\ -\omega_i^2 & -2\xi_i\omega_i \end{bmatrix}, \quad \boldsymbol{B}_{mi} = \begin{bmatrix} 0 \\ b_{mi} \end{bmatrix}, \quad \boldsymbol{C}_{mi} = \begin{bmatrix} c_{mqi} & c_{mvi} \end{bmatrix} \tag{5.16}$$

Assuming to represent structural dynamics via modal approach, each mode of a structure is considered independent from others. According to [5][1], the norms of a single mode are independent as well. If $G_i(\omega) = C_{mi}\left(j\omega I - A_{mi}\right)^{-1} B_{mi}$ is the transfer function of the i-th mode, the H_2 norm of a mode can be computed as

$$\left\|G_i\right\|_2 \simeq \frac{\left\|\boldsymbol{B}_{mi}\right\|_2 \left\|\boldsymbol{C}_{mi}\right\|_2}{2\sqrt{\xi_i\omega_i}} \tag{5.17}$$

Indeed, by considering the definition of the H_2 norm in eq. (5.11) and the closed-form gramians expressions in eq.(5.6), one may prove

$$\left\|G_i\right\|_2 \simeq \sqrt{tr\left(\boldsymbol{C}_{mi}^T \boldsymbol{C}_{mi} \boldsymbol{W}_{ci}\right)} = \left(\left\|\boldsymbol{B}_{mi}\right\|_2 \left\|\boldsymbol{C}_{mi}\right\|_2\right) \Big/ 2\sqrt{\xi_i\omega}_i \tag{5.18}$$

It can be noticed $\left\|G_i\right\|_2$ results to be also the modal cost of Skelton and Hughes [6]. Furthermore, the H_∞ norm of a single mode may be estimated as

$$\left\|G_i\right\|_\infty \simeq \frac{\left\|\boldsymbol{B}_{mi}\right\|_2 \left\|\boldsymbol{C}_{mi}\right\|_2}{2\xi_i\omega_i} \tag{5.19}$$

A proof to justify the approximation is reported in [2], together with a visual representation of the difference between balanced and modal representations. In detail, the two norms may be related through the following expression

$$\left\|G_i\right\|_\infty \cong \sqrt{\xi_i\omega_i}\left\|G_i\right\|_2 \tag{5.20}$$

A structure may be in turn expressed in terms of the norms of its modes.

The H_2 norm of a structure is defined approximately as the root-mean square sum of the modal norms as below

$$\left\|\boldsymbol{G}\right\|_2 \simeq \sqrt{\sum_{i=1}^{N}\left\|G_i\right\|_2^2} \tag{5.21}$$

Indeed, one can write

$$\|\boldsymbol{G}\|_2^2 \cong tr\left(\boldsymbol{C}_m^T \boldsymbol{C}_m \boldsymbol{W}_C\right) \cong \sum_{i=1}^{n} tr\left(\boldsymbol{C}_{mi}^T \boldsymbol{C}_{mi} \boldsymbol{W}_{Ci}\right) = \sum_{i=1}^{n} \|G_i\|_2^2 \tag{5.22}$$

While the H_∞ may be expressed as the largest among the norms of the modes

$$\|\boldsymbol{G}\|_\infty \simeq \max_i \|G_i\|_\infty, \qquad i = 1,...,n \tag{5.23}$$

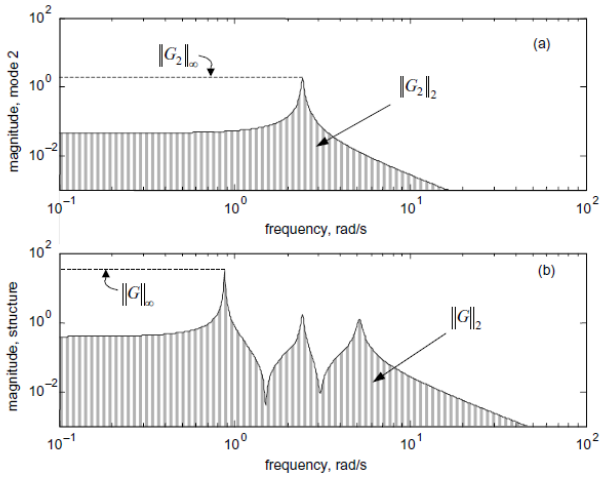

Fig. 5-1: $\boldsymbol{H_2}$ and $\boldsymbol{H}_\infty$ norm of the second mode (top) and of the structure (bottom) [2]

5.3.1.2 NORM OF A STRUCTURE WITH ACTUATORS AND SENSORS

Now, let us consider a flexible structure on which a set of *S* actuators and a set of *R* sensors have been implemented. The modal input matrix $\boldsymbol{B}_m$ presented in Par. 5.3.1.1 is composed of *N* row-wise blocks of size $2 \times S$ as

$$\boldsymbol{B}_m = \begin{bmatrix} \boldsymbol{B}_{m1} \\ \boldsymbol{B}_{m2} \\ \vdots \\ \boldsymbol{B}_{mN} \end{bmatrix} \quad \text{where} \quad \boldsymbol{B}_{mi} = \begin{bmatrix} \boldsymbol{B}_{mi1} & \boldsymbol{B}_{mi2} & \cdots & \boldsymbol{B}_{miS} \end{bmatrix} \tag{5.24}$$

Each row B_{mi} corresponds to the *i*-th mode of the structure. The elements B_{mij} of the matrix $\boldsymbol{B}_m$ represent the effect of the j-th actuator on the *i*-th mode. The same approach may be applied to the modal output matrix $\boldsymbol{C}_m$

$$\boldsymbol{C}_m = \begin{bmatrix} \boldsymbol{C}_{m1} & \boldsymbol{C}_{m2} & \cdots & \boldsymbol{C}_{mN} \end{bmatrix} \quad \text{where} \quad \boldsymbol{C}_{mi} = \begin{bmatrix} \boldsymbol{C}_{mi1} \\ \boldsymbol{C}_{mi2} \\ \vdots \\ \boldsymbol{C}_{miR} \end{bmatrix} \tag{5.25}$$

where each element C_{mij} of the matrix $\boldsymbol{C}_m$ allows to compute the *j*-th output in correspondence of the i-th mode.

At this point, an interesting property of both the H_2 and H_∞ norms may be applied: the norm of the *i*-th mode of a structure with a set of S actuators is the root-mean square sum of the norms of a structure with all the actuators from the set

$$\|G_i\|_2 \cong \sqrt{\sum_{j=1}^{S} \|G_{ij}\|_2^2}, \qquad i = 1,...,N \tag{5.26}$$

In addition, from eq. (5.17), the norm of the *i*-th mode with the j-th actuator is

$$\|G_{ij}\|_2 \cong \frac{\|\boldsymbol{B}_{mij}\|_2 \|\boldsymbol{C}_{mi}\|_2}{2\sqrt{\xi_i \omega_i}} \tag{5.27}$$

Likewise, the norm of the *i*-th mode of a structure in eq. (5.26) can be computed also in terms of H_∞ norm as

$$\|G_i\|_\infty \cong \sqrt{\sum_{j=1}^{S} \|G_{ij}\|_\infty^2}, \qquad i = 1,...,N \tag{5.28}$$

$$\|G_{ij}\|_\infty \cong \frac{\|\boldsymbol{B}_{mij}\|_2 \|\boldsymbol{C}_{mi}\|_2}{2\xi_i \omega_i} \tag{5.29}$$

Similarly, the eq.s from (5.26) to (5.29) may be rewritten to address the case of computing the norm of the i-th mode of a structure with a set of *R* sensors as

$$\|G_i\|_2 \cong \sqrt{\sum_{k=1}^{R} \|G_{ik}\|_2^2}, \quad i = 1,...,N \qquad \|G_{ik}\|_2 \cong \frac{\|\boldsymbol{B}_{mi}\|_2 \|\boldsymbol{C}_{mki}\|_2}{2\sqrt{\xi_i \omega_i}} \tag{5.30}$$

and in terms of H_∞ norm as

$$\|G_i\|_\infty \cong \sqrt{\sum_{k=1}^{R} \|G_{ik}\|_\infty^2}, \quad i = 1,...,N \qquad \|G_{ik}\|_\infty \cong \frac{\|\boldsymbol{B}_{mi}\|_2 \|\boldsymbol{C}_{mki}\|_2}{2\xi_i \omega_i} \tag{5.31}$$

Finally, by exploiting the additive properties of modal norms, the norm of a structure can be computed as follows in case of a set of *S* actuators

$$\|G\|_2 \cong \sqrt{\sum_{j=1}^{S}\|G_i\|_2^2} = \sqrt{\sum_{j=1}^{S}\left(\sum_{i=1}^{N}\|G_{ij}\|_2^2\right)} = \sqrt{\sum_{j=1}^{S}\|G_j\|_2^2} \tag{5.32}$$

Accordingly,

$$\|G\|_\infty \cong \sqrt{\sum_{j=1}^{S}\|G_j\|_\infty^2} \tag{5.33}$$

The same result can be obtained when referring to the set of R sensors

$$\|G\|_2 \cong \sqrt{\sum_{j=1}^{R}\|G_j\|_2^2} \qquad \|G\|_\infty \cong \sqrt{\sum_{k=1}^{R}\|G_k\|_\infty^2} \tag{5.34}$$

To conclude, the norm of a mode is the sum of the norms of actuators or sensors for that mode, as described in Par. 5.3.1.1. An explanatory scheme of the presented logic is reported in Fig. 5-2.

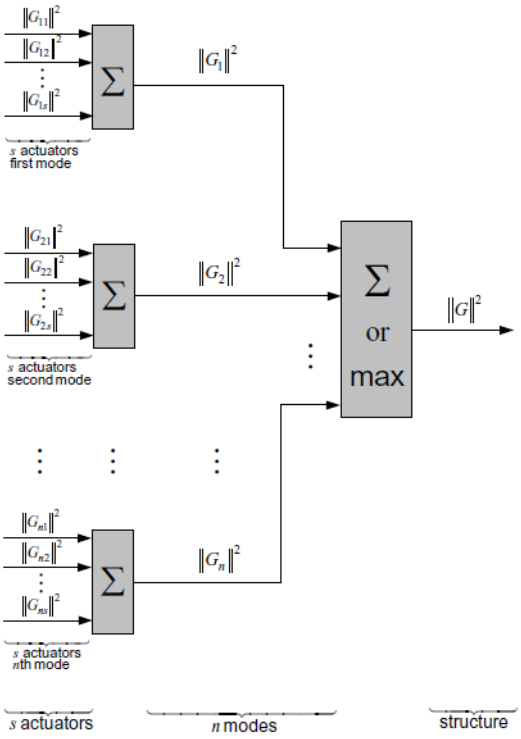

Fig. 5-2: Combination of modal and actuators norms into the norm of a structure [2]

Furthermore, it has been shown that the norm of a structure may be computed from the norms of modes, either using the H_2 (root-mean square sum of the norms) or the H_∞ norm (selection of the largest norm). Such a decomposition proves to be

very useful in the analysis of structural properties, as will be illustrated in the next sections.

5.3.2 PLACEMENT INDICES AND MATRIX

The placement of actuators and sensors may be conducted independently from each other, yet being the two procedures very similar. A simplification of this method is obtained in presence of collocated actuators/sensors; in this case only one index is enough to evaluate the best position for the transducers. Let us consider two large sets of possible actuators and sensors locations as $\mathcal{S}$ and $\mathcal{R}$ respectively. In detail, these two groups contain all the allowable locations of the devices of populations R and S respectively (usually being $R < \mathcal{R}$ and $S < \mathcal{S}$, as the same actuator/sensor may be implemented on the structure in the same location but with different orientations). The objective is to achieve the optimal placement of a number $s < S$ of actuators (or sensors) within the given set $\mathcal{S}$.

A placement index may be defined by considering the ratio between the transfer function of the i-th mode and k-th actuator $\|G_{ki}\|_2$ (as in eq. (5.27)) and the transfer function of the structure with all the actuators candidates $\|G\|_2$. Furthermore, weights $w_{ki} \geq 0$ can be included to selectively give more importance to a specific actuator or mode in practical applications. The placement index is then defined as

$$\sigma_{2ki} = w_{ki} \frac{\|G_{ki}\|_2}{\|G\|_2}, \qquad k = 1,...,S, \quad i = 1,...,n \tag{5.35}$$

The indices σ_{2ki} may be conveniently rearranged to visualize the importance of different actuators acting on all the considered modes by assembling the placement matrix Λ_2 as

$$\Lambda_2 = \begin{bmatrix} \sigma_{211} & \sigma_{212} & \cdots & \sigma_{21k} & \cdots & \sigma_{21S} \\ \sigma_{221} & \sigma_{222} & \cdots & \sigma_{22k} & \cdots & \sigma_{22S} \\ \cdots & \cdots & \cdots & \cdots & \cdots & \cdots \\ \sigma_{2i1} & \sigma_{2i2} & \cdots & \sigma_{2ik} & \cdots & \sigma_{2iS} \\ \cdots & \cdots & \cdots & \cdots & \cdots & \cdots \\ \sigma_{2n1} & \sigma_{2n2} & \cdots & \sigma_{2nk} & \cdots & \sigma_{2nS} \end{bmatrix} \begin{matrix} \\ \\ \\ \leftarrow \\ \\ \\ \end{matrix} \begin{matrix} \\ \\ \\ i\text{-th mode} \\ \\ \\ \end{matrix} \qquad \begin{matrix} k\text{-th actuator} \\ \downarrow \end{matrix} \tag{5.36}$$

As it can be deduced by directly inspecting eq. (5.36), the *k*-th column of the matrix lists the indices evaluating the effect of the *k*-th actuators on all the modes of the structure. Conversely, the i-th row of the matrix regroups the indices of the i-th mode for all the considered actuators.

In the case of the H_2 norm, a vector comprising the actuators placement indices can be defined as $\sigma_a = [\sigma_{a1} \quad \sigma_{a2} \quad \cdots \quad \sigma_{aS}]$, where each *k*-th element is the root-mean square of the k-th indices over all the modes, as in

$$\sigma_{ak} = \sqrt{\sum_{i=1}^{n} \sigma_{ik}^2}, \qquad k = 1,...,S \tag{5.37}$$

Conversely, if considering the H_∞ norm, the *k*-th component of the vector σ_a is considered equal to the largest actuator index over all the modes

$$\sigma_{ak} = \max_i (\sigma_{ik}), \qquad i = 1,...,n, \quad k = 1,...,S \tag{5.38}$$

The vector σ_a provides the designer with an important information: it quantifies the weighted contribution of the *k*-th actuator at all the (selected) modes to the norm of the flexible structure. With this in mind, the actuators with small σ_{ak} may be removed being the least significant ones.

$$\sigma_{OPT} = \max_k (\sigma_a) \qquad k = 1,...,S \tag{5.39}$$

By placing the actuator and sensor at the locations of the maximum index values, the vibration of the *i*-th mode can be controlled by an actuator input signal of minimal energy and measured by a sensor with maximum output energy.

5.3.2.1 CORRELATION OF PLACEMENT INDICES

When addressing the placement problem on very large structures (i.e. long masts, antennas or wide solar panels) a relevant number of admissible locations is generally to be considered. In this case, a further step to conclude the procedure might be actually required. If a particular actuator/sensor location is associated to a high value of the placement index, in general so the adjacent locations are. However, not always they represent the best choice, as a proper modification of

the gain for the device (actuator or sensor) located in the original position may compensate the difference. For instance, if we consider an actuator A to be in the best position n° 1 and an actuator B in best position n° 2 very close to A, the actuator B could become as much effective as (and even more effective than) A if considering a proper gain increase for actuating B when implementing a closed loop controller. If the objective is to find optimal locations that cannot be compensated from gain adjustment, a correlation index of each actuator/sensor norms is to be computed.

$$g_k = \begin{bmatrix} \|G_{k1}\|^2 \\ \|G_{k2}\|^2 \\ \vdots \\ \|G_{kn}\|^2 \end{bmatrix} \tag{5.40}$$

Where $\|G_{ki}\|$ is the transfer function of the *k*-th actuator at the *i*-th mode. Then, the correlation index can be defined as

$$r_{ik} = \frac{g_i^T g_k}{\|g_i\|_2 \|g_k\|_2}, \qquad i = 1,...,r, \qquad k = i+1,...,R \tag{5.41}$$

By individuating a small number ε, varying accordingly to the application (assumed usually to be in the range [0.01-0.20]), a membership number $I(k)$ may be denoted as

$$I(k) = \begin{cases} 0 & r_{ik} > (1-\varepsilon), \quad \sigma_k \le \sigma_i \\ 1 & \text{elsewhere} \end{cases}, \qquad k = 1,...,R \tag{5.42}$$

If the index $I(k)$ is equal to one, the actuator location is accepted; otherwise, it is discarded as too similar to at least one of the already selected locations (the two locations *i* and *k* are highly correlated) or the *i*-th location has a higher performance index σ_i than σ_k .

5.4 MSE|SVD-BASED PLACEMENT

The placement of active elements in a flexible structure can be carried out from the inspection of the map of the Modal Strain Energy (MSE) in the finite element model. The element strain energy can be defined as the amount of elastic energy

stored in a finite element. The active parts should be placed where their authority over the modes to control is the largest. Indeed, according to [2], the control authority is proportional to the fraction of MSE in the element. The search procedure is greatly assisted by the fact the map of the fraction of MSE is directly available in commercial finite element packages (such as MSC Nastran).

Although mode shapes are relative quantities, relative strains, internal loads, and stresses developed when a structure deforms in a mode shape can be helpful in predicting qualitative responses or in isolating troublesome modal frequencies [7]. Therefore, they can be effectively used in the analysis/design process. Modal quantities can be selected to identify problem areas by indicating the more highly stressed elements. Indeed, elements that are consistently highly stressed across many or all modes will probably be highly stressed when dynamic loads are applied. In this context, Element Strain Energy is an extremely useful tool for determining which elements to modify the least, but have the greatest potential for impacting results. Indeed, elements with large values of strain energy in a mode indicate the location of large elastic deformation (energy). These elements are those which most directly affect the deformation in a mode. Therefore, by changing the properties of those elements with large strain energy, one should have more effect on the natural frequencies and mode shapes than if elements with low strain energy were changed. In the context of a normal modes solution, the modal element strain energy cannot be compared across modes. Within a mode, the modal strain energy can still provide useful relative information. If you find the same elements having a large amount of modal strain energy across several modes, these elements are good candidates for modification.

In detail [7], the MSE is computed as

$$ESE_e = \frac{1}{2} u_e^T \boldsymbol{K}_{ee} u_e \tag{5.43}$$

where u_e is the element displacement and $\boldsymbol{K}_{ee}$ is the elemental stiffness. The strain energies are provided by mode and also by element type (as BEAM, QUAD4, etc). Furthermore, useful additional quantities as strain energy percentage of the total for each element and also energy density (in terms of strain energy per unit volume, removing some bias related to the element size) can be computed by the software and extracted.

The map of modal strain energies is a powerful tool, but it does not provide

enough practical information on how to implement actuators on the structure. Indeed, some actuators could be mounted in different orientations on a same finite element (especially when referring to a piezo stack with offset on a truss structure). To consider also different orientations and generally to reduce the set of best locations where to place the actuator/sensor the following considerations may be introduced.

According to [8], the Singular Values (SVs) of input matrix can be used to optimize the actuator locations in order to reduce the control effort and suppress spillover. Lammering [9] used the trace of the input matrix as the objective function to minimize the control energy and spillover, while electric potentials (something like MSE) was introduced as an effectiveness index to get a subset of suitable locations. Therefore, the minimization of the maximal physical control force may be chosen as the criterion to drive the actuator placement [10]. The Singular Value Decomposition (SVD) of the input matrix $\boldsymbol{B}_m$ is used to measure the system controllability.

The SVD of the matrix $\boldsymbol{B}_m$ may be performed as illustrated below

$$\begin{aligned} \boldsymbol{B}_m &= \boldsymbol{U}\ \boldsymbol{S}_v\ \boldsymbol{Q} \\ \boldsymbol{S}_v &= \begin{bmatrix} \boldsymbol{\Sigma} & 0 \\ 0 & 0 \end{bmatrix}, \quad \boldsymbol{\Sigma} = diag\left[\sigma_1,...,\sigma_m\right] \end{aligned} \tag{5.44}$$

Where $\boldsymbol{U}^T\boldsymbol{U} = \boldsymbol{Q}^T\boldsymbol{Q} = \boldsymbol{I}$, where σ_i is the i-th singular value of $\boldsymbol{S}_v$. The system is assumed here controllable, so that both $\boldsymbol{B}_m$ and $\boldsymbol{S}_v$ are full rank, with $\boldsymbol{S}_v = \boldsymbol{\Sigma}$.

A new modal coordinate can be introduced to describe the system dynamics as

$$q = \boldsymbol{\Phi} U \eta^* = \boldsymbol{\Phi}^* \eta^* \tag{5.45}$$

where $\boldsymbol{\Phi}^*$ is still a modal matrix of the system which satisfies the orthogonality condition w.r.t the mass matrix of the system. The new variable η^* can be divided into controlled modes η^*_C and residual modes η^*_R. As the dynamic equation is decoupled in modal coordinates, the only part considered is

$$\ddot{\eta}^*_C + 2\xi\Omega\dot{\eta}^*_C + \Omega^2\eta^*_C = \boldsymbol{S}_v\boldsymbol{Q}^T u = \boldsymbol{S}_v u^* = f^*_C \tag{5.46}$$

As $\boldsymbol{Q}^T\boldsymbol{Q} = \boldsymbol{I}$, the inputs u and u^* can be considered to be equal and f^*_C is assumed to be the modal control force. The following relation between modal control force and physical input can be derived

$$u^* = \boldsymbol{S}_v^{-1} f_C^* = diag\left[\frac{1}{\sigma_1},...,\frac{1}{\sigma_n}\right] f_C^* \tag{5.47}$$

The relationship between i-th elements of the u^* and f_C^* is then

$$u_i^* = \frac{f_{Ci}^*}{\sigma_i} \tag{5.48}$$

The amplitude of the maximal elements in u_i^* depends both on the maximum value of the modal force (considered to vary in a fixed range) and the minimum singular value of the modal input matrix. Then, if the minimal singular value of a matrix $\boldsymbol{B}_m$ is larger, the maximal physical control force will be smaller. Finally, the optimization objective function can be defined as

$$\max\left[\sigma(\boldsymbol{B}_m)\big|_{\min}\right] \tag{5.49}$$

As the computational costs of considering all the possible combinations of collocated actuators/sensors to compose the modal input $\boldsymbol{B}_m$ is usually too high, a proper subset of possible location should be first defined.

5.4.1 PLACEMENT STRATEGY

The proposed placement approach may be described is some steps as follows:

1. *MSE-based sub-set of locations*: Denote an i-th group U_i, $i=1,...,N_m$, where N_m is the number of considered modes of the flexible structure. Such group is composed of e_j^i, $j=1,...,E_i$ elements, each of them representing one of the locations with the largest MSE for that specific i-th mode, for a total of E_i locations for each mode

$$U_i = \left[e_j^i,...,e_{E_i}^i\right] \tag{5.50}$$

This set is defined according to the data which may be extracted from a commercial tool as Nastran. For instance, if we suppose to control two modes $N_m = 2$ (i.e. $i=1,2$), we may assume to have two sets $U_{i=1,2}$ each of them with generic number of elements E_1, E_2. In this example, we may have

$$\begin{aligned} U_1 &= \begin{bmatrix} e_1^1 & e_2^1 & e_3^1 & e_4^1 \end{bmatrix} = \begin{bmatrix} a & b & c & d \end{bmatrix} \\ U_2 &= \begin{bmatrix} e_1^2 & e_2^2 & e_3^2 \end{bmatrix} = \begin{bmatrix} e & g & f & h & l \end{bmatrix} \end{aligned} \tag{5.51}$$

with $E_1 = 4,\ E_2 = 5$, where the letters a,b,c,d,e,f,g,h,l indicate the labels associated to as many locations on the structure.

2. *Non-repetitive combination of locations*: Since more than one actuator may be used to control a mode at the same time, a subset of $\varepsilon_i < E_i$ elements are chosen from each group U_i. For instance, if we suppose to control the first mode by using two actuators at the same time, we would have $\varepsilon_1 = 2$, while if we assume three actuators for the second mode $\varepsilon_2 = 3$. In order to randomly choose the two actuators, the combinations of all the actuators of the group U_i should be computed without repetitions, according to

$$c_1 = \frac{E_1!}{(E_1 - \varepsilon_1)!\ \varepsilon_1!} = 6 \qquad c_2 = \frac{E_2!}{(E_2 - \varepsilon_2)!\ \varepsilon_2!} = 10 \tag{5.52}$$

The combinations may then be re-organized in $\boldsymbol{C}_i$ matrices as follows

$$\begin{aligned} \boldsymbol{C}_1 &= \begin{bmatrix} a & a & a & b & b & c \\ b & c & d & c & d & d \end{bmatrix}^T \\ \boldsymbol{C}_2 &= \begin{bmatrix} e & e & e & e & e & e & f & f & f & g \\ f & f & f & g & g & h & g & g & h & h \\ g & h & l & h & l & l & h & l & l & l \end{bmatrix}^T \end{aligned} \tag{5.53}$$

Each matrix $\boldsymbol{C}_i$ contains all the possible combinations c_i of the elements of vector U_i, taken ε_i at a time, having dimensions $c_i \times \varepsilon_i$.

3. *Modal input matrix assembly*: When the total number of modes to be controlled is N_m (in the proposed example $N_m = 2$), the designer should consider also to combine locations from different U_i sets. In this case, when considering the other modes, the total number of combinations C_T and the number of combinations c_i for a single mode can be related as

$$C_T = \prod_{i=1}^{N} c_i \ , \text{ with} \qquad c_i = \frac{E_i!}{(E_i - \varepsilon_i)!\ \varepsilon_i!} \tag{5.54}$$

In particular, if considering $c_1 = 6,\ c_2 = 10$ we would have $C_T = 60$. Then, we are considering the C_T combinations as regrouped in a matrix $\boldsymbol{C}_F$,

whose dimensions are $C_T \times \left(\sum_i \varepsilon_i\right)$, as

$$\boldsymbol{C}_F = \left[\boldsymbol{C}_1 \quad \cdots \quad \boldsymbol{C}_{N_m}\right] \tag{5.55}$$

The modal input matrix $\boldsymbol{B}_m$ is built in a column-wise fashion, where each column corresponds to a particular actuator location (see Par. 5.3.1.2). Indeed, the modal input matrix may be described as

$$\boldsymbol{B}_m = \left[B_{m1} \quad \cdots \quad B_{ms} \quad \cdots \quad B_{mS}\right] \tag{5.56}$$

Where B_{ms}, with $s = 1,...,S$ is a vector describing the action of one actuator (in one location) on the structure and S is total number of actuators to be implemented on the structure.

Therefore, $\boldsymbol{B}_m$ may be assembled by considering a combinations of vectors B_{ms}, each corresponding to one actuator, and in particular associated to the elements contained in each row of the matrices $\boldsymbol{C}_F$, thus combining them as indicated in Fig. 5-3. Indeed, if we want to control N_m modes with ε_i actuators each, the matrix $\boldsymbol{B}_m$ will have dimension $N_m \times \sum_{i=1}^{N_m} \varepsilon_i$.

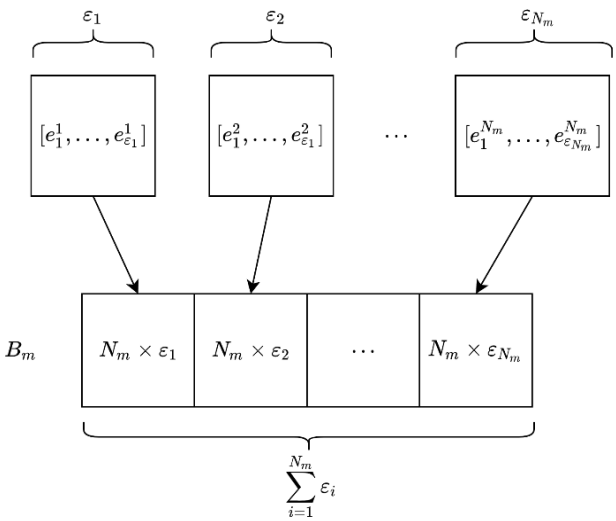

Fig. 5-3: Proposed logic to assemble the modal input $\boldsymbol{B}_m$

If considering again the previous example, where we wanted to control two modes $N_m = 2$, we would have the following modal input matrices as reported in eq. (5.57).

$$\begin{aligned} \boldsymbol{B}_m^1 &= \left[\bar{a} \;\; \bar{b} \;\middle|\; \bar{e} \;\; \bar{f} \;\; \bar{g} \right] \\ \boldsymbol{B}_m^2 &= \left[\bar{a} \;\; \bar{b} \;\middle|\; \bar{e} \;\; \bar{f} \;\; \bar{h} \right] \\ &\vdots \\ \boldsymbol{B}_m^{C_T} &= \left[\bar{c} \;\; \bar{d} \;\middle|\; \bar{g} \;\; \bar{h} \;\; \bar{l} \right] \end{aligned} \tag{5.57}$$

where the superscript $\bar{\cdot}$ indicates a column of the matrix $\boldsymbol{B}_m$, for instance, $\bar{a}$ indicates the column of the matrix $\boldsymbol{B}_m$ corresponding to the actuator with label *a*. Finally, one would have a total of C_T assembled modal input matrices to be used in the further step of the placement process.

However, the method can become computationally expensive by increasing the size of the initial set. For instance, let us consider two modes to be controlled by two elements each extracted from the subsets U_1 (of dimension $E_1 = 20$) and U_2 (of dimension $E_2 = 20$). Consequently, the number of combinations of actuators $\varepsilon_1 = 2, \varepsilon_2 = 3$ is $c_1 = 190,\ c_2 = 1140$. Thus, the total number of combinations will be $C_T = 2.16 \cdot 10^5$, reaching a total of C_T different matrices $\boldsymbol{B}_m$ whose SVs must be computed. Due to the possible existence of repeated elements in different U_1 sets, the actual number might be slightly less than C_T.

4. Calculate the SVs of the input matrix $\boldsymbol{B}_m$ of all the combinations, and the optimal combination should be the one that meet the objective function in eq. (5.49).

5.5 PROBLEM SET-UP

The two placement methods presented in previous paragraphs, namely Norm-based and MSE|SVD-based approaches, are inherently suitable to be implemented in a coding environment to automatize the placement operations for generically designed flexible structures. In this section, the logic behind the creation of an algorithm dedicated to the placement of actuators and sensors is illustrated. First, a set of possible types of actuators (and sensors) is presented according to their effect on the flexible structure. Then, a procedure for mapping their generalized forces on the degrees of freedom of the structure is proposed and finalized to be used for the placement process.

5.5.1 ACTUATORS TYPE AND EFFECT

Let us consider an element with two nodes m and n (three translations and three rotations each), the degrees of freedom to be considered will be

$$V_{nm} = \left[u_m, v_m, w_m, \alpha_m, \beta_m, \theta_m, u_n, v_n, w_n, \alpha_n, \beta_n, \theta_n\right] \tag{5.58}$$

where u, v, w indicate the translational degrees of freedom along the local X, Y and Z-axis in Fig. 5-4 respectively, while α, β, θ the rotational ones. The devices are considered to be implemented between two adjacent nodes of the structure (each node with six degrees of freedom), as illustrated in Fig. 5-4.

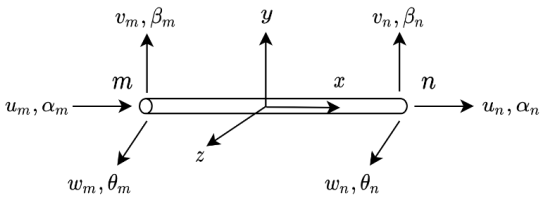

Fig. 5-4: 2-nodes FEM element

In particular, the possibility to place three types of actuators has been investigated in the algorithm. As the contemplated devices may act conversely as sensors, by using the direct piezoelectric effect, the same models are retained also to build the corresponding output matrices $\boldsymbol{C}_m$.

5.5.1.1 PIEZO-ELECTRIC STACK ACTUATORS (PSA)

A linear model of a piezo-electric stack actuator is proposed for placement purposes (based on the mathematical formulation reported in Par. 3.1.4.1). Indeed, the vector describing the action of the actuator on the two-nodes elements can be formulated in the element local reference system as

$$\boldsymbol{K}^e_{U\psi} = c_{PZ}\left[1,0,0,0,0,0,-1,0,0,0,0,0\right]^T \tag{5.59}$$

with

$$c_{PZ} = n\frac{d_{33}A_{PZ}E_{PZ}}{l_{PZ}} \tag{5.60}$$

where d_{33} is the piezoelectric material coefficient, n is the number of layers composing the piezo-stack, A_{PZ} , E_{PZ} and l_{PZ} are the area, the Young module and

the length of the device respectively. Such a formulation considers that the piezo device, constrained in the structural element, is exerting a bidirectional axial force on the structure equal to $F = c_{PZ}\psi_{ACT}$, where ψ_{ACT} is the piezo input voltage.

In case the local element reference frame and the global frame of the structure do not coincide, the vector has to be rotated and then assembled in the global structure reference frame to properly exert its action by means of a rotation matrix $\boldsymbol{T}_{g\leftarrow e}$, as in $\boldsymbol{K}^{G}_{U\psi} = \boldsymbol{T}_{g\leftarrow e}\boldsymbol{K}^{e}_{U\psi}$.

5.5.1.2 PIEZO-ELECTRIC STACK ACTUATORS WITH OFFSET (OPSA)

The case of a piezo-stack implemented on the structure by means of an external mechanical frame is considered, in order to observe the effects of applying both axial forces and bending moments to the structure. Indeed, such type of device was firstly proposed by Wei and Zhichun [12] with the aim to exploit the higher actuating power of piezo stacks with respect to piezo patches and to propose a simple yet efficient mechanical interface, by avoiding complex mechanisms and lever systems. In this investigation, the device is constrained in its mechanical frame and acts between two nodes of the structure by transmitting forces and moments to the host body, as illustrated in Fig. 5-5.

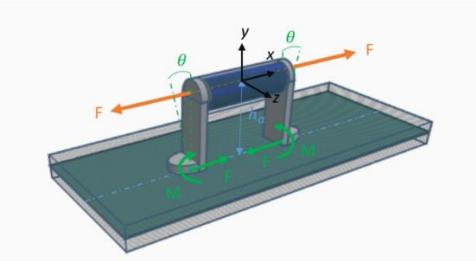

Fig. 5-5: Piezo-electric Stack with Offset (PPSA): concept design

Consequently, the electro-mechanical coupling relations for one smart actuator can be written in the element local element reference frame as

$$\boldsymbol{K}^{e}_{U\Psi} = c_{PZ}\left[1,0,0,0,0,-h_a,-1,0,0,0,0,h_a\right]^{T} \tag{5.61}$$

where h_a is the distance between the longitudinal axis of the actuator and the neutral plane of the passive structure and c_{PZ} is described in eq. (5.60). In such a formulation, the bending moment generated by the actuator about the local Z-axis can be described as reported in eq. (5.62).

$$M = Fh_a\psi_{ACT} = n\frac{d_{33}A_{PZ}E_{PZ}}{l_{PZ}}h_a\psi_{ACT} = c_{PZ}\ h_a\psi_{ACT} \tag{5.62}$$

In detail, ψ_{ACT} is the voltage needed to actuate the piezo device. Again, as usually the local reference frame and the global frame of the structure differ, the vector has to be rotated in the global structure reference frame by using a matrix $\boldsymbol{T}_{g\leftarrow e}$.

5.5.1.3 PIEZO-ELECTRIC PATCHES

According to [11], considering an electrode of constant width, a distributed laminar piezo-electric actuator is equivalent to adding concentrated moments at the boundaries of the device, as represented in Fig. 5-6. Therefore, the action of a piezo patch on the structure may be summarized as

$$M_P = d_{31}z_m b\,\psi_{ACT} = m_p\,\psi_{ACT} \tag{5.63}$$

where d_{31} is the piezo-electric material coefficient, z_m is the width of the lamina, b is the distance between the mid-plane of the beam and the mid-plane of the piezo strip. In particular, eq. (5.63) are based on the assumption that the thickness of the piezo strip is much smaller than that of the beam. The effect of the lamina to the flexible structure, according to beam theory, may be expressed as

$$\boldsymbol{K}^e_{u\Psi} = m_p\left[0,0,0,0,0,-1,0,0,0,0,0,1\right]^T \tag{5.64}$$

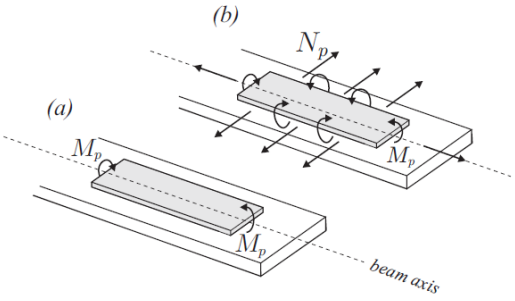

Fig. 5-6: Equivalent piezoelectric loads of a rectangular piezoelectric patch bonded on a beam: (a) beam theory, (b) laminate theory [11]

In case of referring to the laminate theory, the equivalent piezoelectric loads consist of an in-plane force N_P, normal to the contour of the electrode, and a constant moment M_P, acting along the contour of the electrode, as in Fig. 5-6, as

$$N_P = d_{31}\,\psi_{ACT} \tag{5.65}$$

where, by simplifying for the placement process's sake, one may assume

$$\boldsymbol{K}^{e}_{U\Psi} = d_{31}\left[0,0,1,0,z_m b,-z_m b,0,0,-1,0,-z_m b,z_m b\right]^T \tag{5.66}$$

In this thesis, as the structures to be controlled extends dominantly along one axis, and the structural response away from the actuator (e.g. tip displacement) are used to verify performance requirements, the piezoelectric loads of the beam theory are considered to be the dominant ones.

5.5.2 MAPPING OF GENERALIZED FORCES ON THE STRUCTURE

In this section, an overview on how the actions of actuators/sensors are implemented on the flexible structure is presented. As anticipated in Par. 5.5.1.1, a rotation matrix $\boldsymbol{T}_{g\leftarrow e}$ from local to global reference frame is needed to map out the actions of generalized forces exerted by the actuators on the structure, as follows

$$\begin{bmatrix} F_1 \\ M_1 \\ \hline F_2 \\ M_2 \end{bmatrix} = \begin{bmatrix} \boldsymbol{T}_{g\leftarrow e} & & & \\ & \boldsymbol{T}_{g\leftarrow e} & & \\ & & \boldsymbol{T}_{g\leftarrow e} & \\ & & & \boldsymbol{T}_{g\leftarrow e} \end{bmatrix} \begin{bmatrix} f_1 \\ m_1 \\ \hline f_2 \\ m_2 \end{bmatrix} \tag{5.67}$$

where $f_{PZ} = \left[\, f_1 \quad m_1 \,\middle|\, f_2 \quad m_2 \,\right]^T$ is the vector of the forces and moments generated by the actuator in its local reference frame in node 1 and node 2, $F_{PZ} = \left[\, F_1 \quad M_1 \,\middle|\, F_2 \quad M_2 \,\right]^T$ is the vector of the forces and moments exerted by the actuator in the structure global frame (in node 1 and node 2) and $\boldsymbol{T}_{g\leftarrow e}$ is the general rotation matrix for a two-node 3-D element defined as

$$\boldsymbol{T}_{g\leftarrow e} = \boldsymbol{R}_3\left(\theta_x\right)\boldsymbol{R}_2\left(\theta_y\right)\boldsymbol{R}_1\left(\theta_z\right) \tag{5.68}$$

where $\boldsymbol{T}_{g\leftarrow e}$ is the total rotation matrix composed of a first rotation $\boldsymbol{R}_1$ around the local Z-axis, a second rotation $\boldsymbol{R}_2$ around the local Y-axis and an additional rotation $\boldsymbol{R}_3$ around the longitudinal X-axis of the element (see Fig. 5-7).

In detail, the position of the element in the 3D space could be described by referring just to the first two rotations. The third angle θ_x is required when assuming that the element section may be oriented in different ways around the

longitudinal axis of the element. This approach has been used in the placement process to represent different orientations of the actuators.

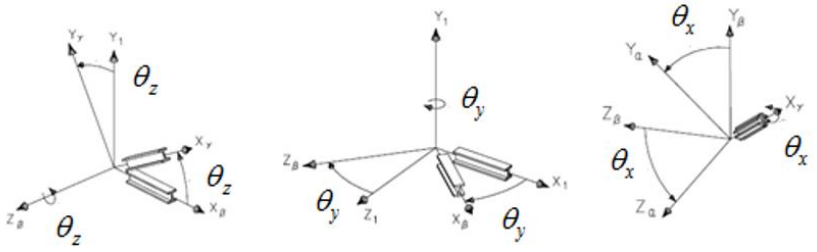

Fig. 5-7: From local to global reference frame: angles $\theta_z, \theta_y, \theta_x$

Indeed, in case of placing PPSA actuators, the generated bending moment may be generally oriented with respect to the three coordinated axes X, Y and Z. Their efficacy in suppressing vibrations depends not only on their actual location on the structure, but also on how the designer decides to orient them in the 3D space. Such an issue has been addressed in the placement procedure by allotting to each allowable position additional *virtual locations*, one for each orientation to be investigated by the algorithm. In Fig. 5-8, four possible orientations for a PPSA actuator on a truss structure are proposed: the actuator is represented in red, the longitudinal forces in green and the bending moment axes in blue. In particular, four θ_x angles have been chosen as $\theta_x = [0, \pi/4, \pi/2, 3\pi/4]$.

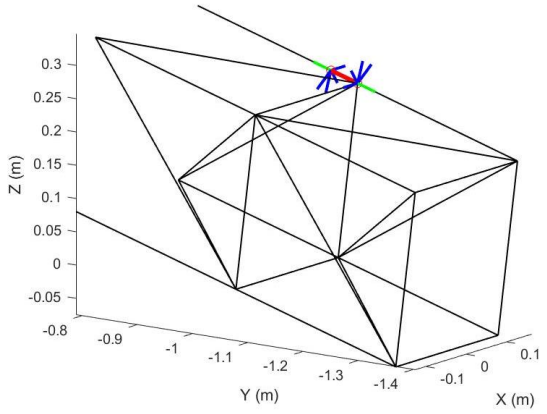

Fig. 5-8: Orientation for BEAM elements

A similar logic may be used when addressing the placement of piezoelectric stacks with offset on a shell structure composed of QUAD4 elements (four nodes each). In this case, six non-repetitive combinations of the four nodes may be selected and the actuator is assumed to exert its action on them (see Fig. 5-9, where

the actuators are in red, the axial forces in green and the bending moment axes in black).

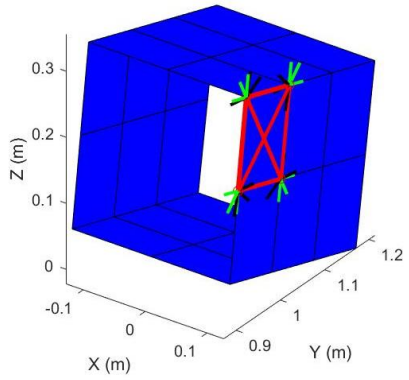

Fig. 5-9: Possible placement of PZT stacks on a QUAD4 element

Finally, a *location* s may be assumed not only as a virtual segment connecting two adjacent nodes, but also as an entity associated to a specific orientation in the 3D space. Hence, a location may be defined as $s=[ID|E_{ID}|N_{ID}|O_r]$, where ID is a label to identify the number of the location, E_{ID} is the identification number of the finite element where the active device is implemented, N_{ID} is a vector comprising the ID of the two considered nodes, while O_r indicates the orientation of the active devices.

The effect each actuator in a location s exerts on the structure can be described by the vector

$$\begin{aligned}\boldsymbol{K}^{d}_{U\Psi} = \boldsymbol{T}_{g\leftarrow e}\boldsymbol{K}^{e}_{U\Psi} = \eta_{PZT}[0,...,0,F^1_{PZ_X},F^1_{PZ_Y},F^1_{PZ_Z},F^1_{PZ_{MX}},F^1_{PZ_{MY}},F^1_{PZ_{MZ}},...\\ ...,0,...,0,F^2_{PZ_X},F^2_{PZ_Y},F^2_{PZ_Z},F^2_{PZ_{MX}},F^2_{PZ_{MY}},F^2_{PZ_{MZ}},...,0]^T\end{aligned} \tag{5.69}$$

Where η_{PZT} is the constant representing the electro-mechanical relations described in Par. 5.5.1 according to the type of actuator considered. The variables $\left[F^1_{PZ_X},...,F^2_{PZ_{MZ}}\right]$ indicate the components of both the forces (subscripts $_{PZ_X,PZ_Y,PZ_Z}$) and the moments (subscripts $_{PZ_{MX},PZ_{MY},PZ_{MZ}}$) applied on two nodes of the structures (superscript 1 for the first node and 2 for the second one), i.e. the quantities which will be multiplied by the input voltage. The vector has length equal to the number of the total degrees of freedom of the finite element system and the only non-zero elements are those corresponding to the translational and rotational degrees of freedom of the nodes where the actuator could be implemented.

Finally, the matrix $\boldsymbol{K}_{U\Psi}^{g}$ can be column-wise assembled by concatenating all the S vectors horizontally. Then, the modal input matrix of the space-state system in eq. (5.15) may be defined by pre-multiplying such matrix by the modes as in

$$\boldsymbol{B}_m = \Phi^T \boldsymbol{K}_{U\Psi}^{g} \tag{5.70}$$

and the placement may be carried out according to the theory presented in Par. 5.3 and Par. 5.4.

A synthesis of the placement procedure algorithm is reported in Fig. 5-10. A set of available data are extracted from a commercial finite element software or computed with in-house codes in case of simple geometries. Such information generally contains positions and ID of the nodes, Modal Strain Energy tables as well as Property Sets (PSETs) associated to different parts of the model, comprising characteristics as material association and dimensions of the component. In this context, two methods have been contemplated to automatically choose specific finite elements for placement purposes based on different inputs: the first approach identifies one or more volumes of interest and it may be used when only distinct zones of the flexible appendage are available to practically implement active vibration devices, the second one selects particular PSETs associated to precise features, as plates or beam elements, useful when investigating the placement of devices on an a structure composed of multiple types of finite elements. After having identified the elements of interest according to one of the two methods, one may want to further select a particular type of finite element to carry out the placement procedure. The accounted categories are five, namely CQUAD, CTRIA, CROD, CBAR and CBEAM elements, thus allowing to cover for a wide range of designs of flexible structures (see Chapter 2). Then, not all the elements falling into such groups have necessarily to be considered: a restricted sub-set may be again singled out.

Once defined the final set of finite elements to be taken into account, the characteristics of the actuator/sensor to be implemented may be selected, choosing among the types presented in Par. 5.5.1. At this point, the action of the device is mapped onto the structure as previously illustrated. The *full-assembled* Modal Input Matrix $\boldsymbol{B}_m$ is then computed: it contains all the possible locations selected so far for placement purposes. The two open-loop methods are then applied. The norm-based method will use the full-assembled $\boldsymbol{B}_m$ to compute norms of the structure equipped with such devices, evaluating placement indices to identify optimal locations and eventually correlation indices to further reduce the subset.

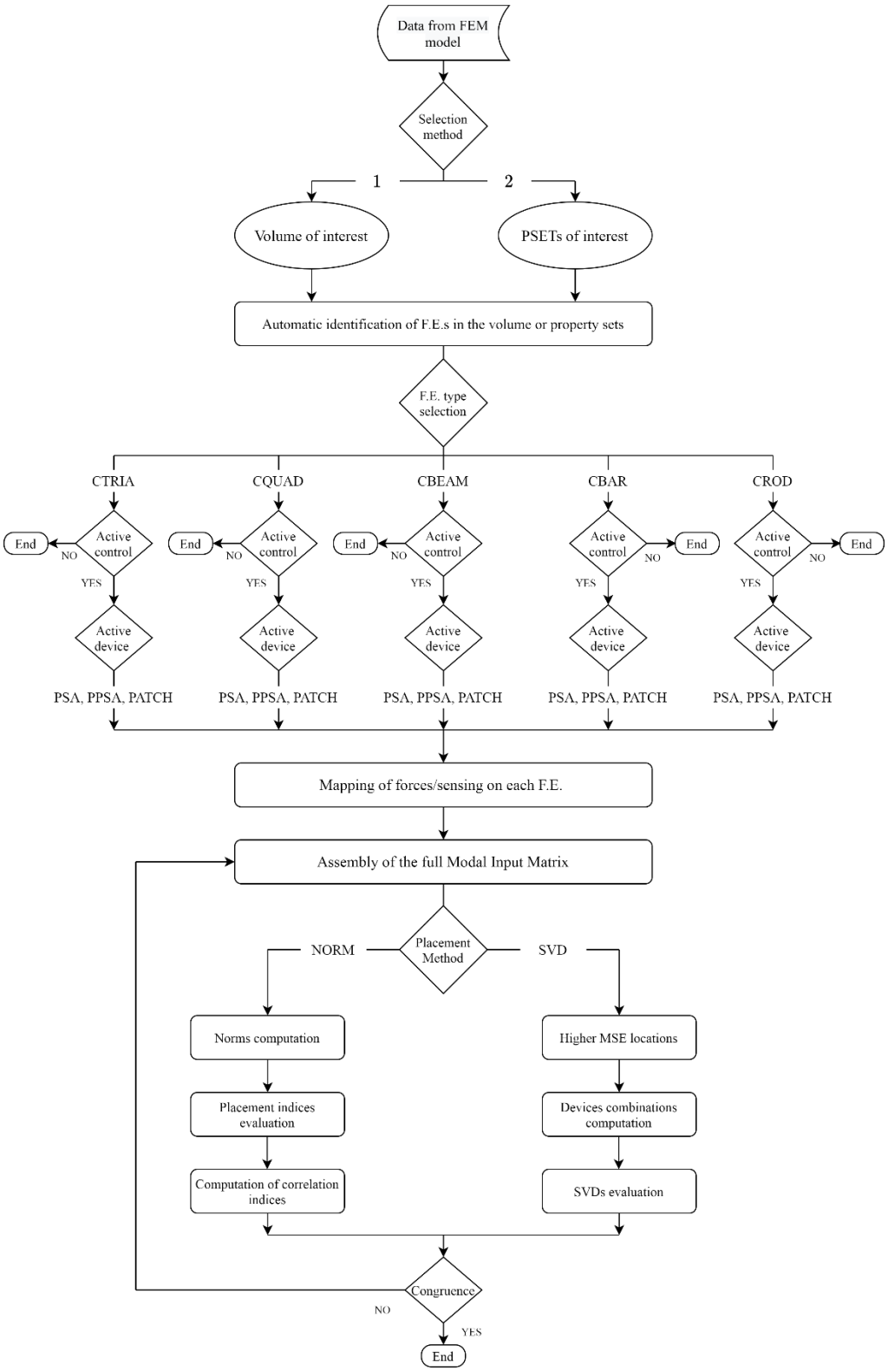

Fig. 5-10: Workflow logic of placement algorithm

The other approach makes use of MSE data extracted from the commercial finite element suite to reduce the full-assembled input matrix in a reduced matrix considering only the columns (i.e. the locations) associated with a higher MSE. Then, different combinations of such columns are computed as indicated in Par. 5.4.1. Finally, the results deriving from the two procedure are compared in terms of set of identified optimal locations to verify the output of the procedure. If the results differs for more than two locations, the placement process has to be repeated and/or different locations considered.

5.6 STUDY CASES

In this section, some applications of the proposed architecture are illustrated and relevant results reported. In particular, the analyzed flexible appendages fall into the most interesting categories identified in Par. 2.1.1. The following logic is adopted: first, an equivalent model of payloads of real space missions is designed and optimized in commercial finite element suites to obtain hints on their dynamic behaviour, then the model is modified to improve the performance of the instrument and finally a placement procedure is carried out to define a distributed active control solution.

5.6.1 STUDY CASE A: K-BAND INTERFEROMETER

The first study case involves the Surface Water and Ocean Topography (SWOT) mission, by CNES/NASA[2]. Such a structure has been chosen as it represents the last evolution of the wide-swath altimeter design and an increase in the size of such payload would imply an effective enhancement of the interferometric measurements [13][14]. An equivalent model for SWOT payload is derived, then, based on the insights obtained after the first investigation, a second extended model, improved from performance point of view, is designed for further analyses. The spacecraft equips two deployable booms, being two reflectors placed at the end point of such arms, connected to the satellite platform of the satellite. The distance between the antennas is 10 m. The total mass of KaRIn is 294kg. According to [15], the first vibration mode of KaRIn in free-free

[2] This section is part of a paper published by the thesis author in F. Angeletti et al., *Design and performance assessment of a distributed vibration suppression system of a large flexible antenna during attitude manoeuvres*, Acta Astronautica, Volume 176, November 2020, Pages 542-557

conditions is a bending mode of 7.20 Hz, thus meeting the construction requirements that call for a first mode frequency higher than 7 Hz. The second one is also a bending mode with frequency equal to 7.85 Hz, while the third one is a torsional mode of 8.69 Hz, as reported in Fig. 5-11.

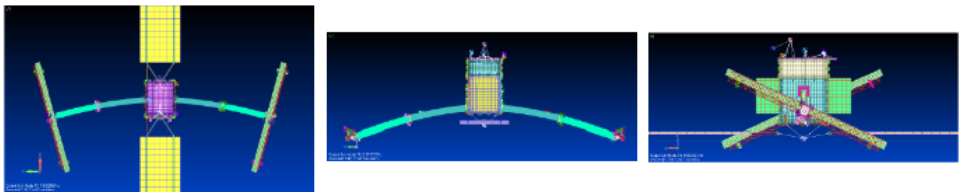

(a) (b) (c)

Fig. 5-11: SWOT first free-free modes: (a) first bending mode along Z-axis, (b) second bending mode along X-axis, (c) third torsional mode along Y-axis [15]

By referring to the available geometric and inertial data in [15], an equivalent Finite Element Method (FEM) model has been realized to reproduce the dynamic behaviour of a SWOT-like Payload Structure. The FEM model has been built in MSC Patran environment (pre- and post-processor of MSC Nastran software).

The structure is composed of both shell and beam elements [16],. The 2D elements are used to build the mast and the antenna surface, while the beam elements are implemented to replicate the backbone frames of the two reflectors. In particular, the elements of the FEM model have been organized in groups, each having different properties and materials, as shown in Table 5-1. Different mechanical and material properties have been assigned to each group to simulate the realistic behaviour of the main system components. The two booms have been modelled as one mast to reproduce their connection inside the platform.

Table 5-1: Groups from FEM model

Group		Visualization	Group		Visualization
1	Mast bulk	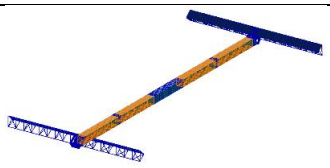	4	Reflector arrays	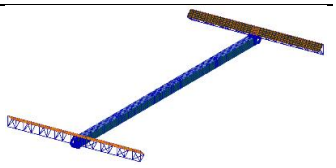
2	Central section		5	Reflector fixed to mast	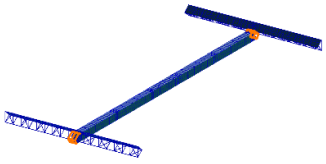

3	Mast joints sections	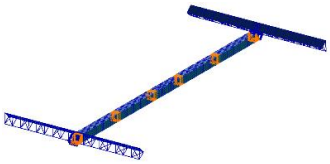	6	Reflector truss	

The orientation of the Payload with respect to a Local Vertical Local Horizon (LVLH, see Par. 3.1.1.3) reference frame is presented in Fig. 5-12.

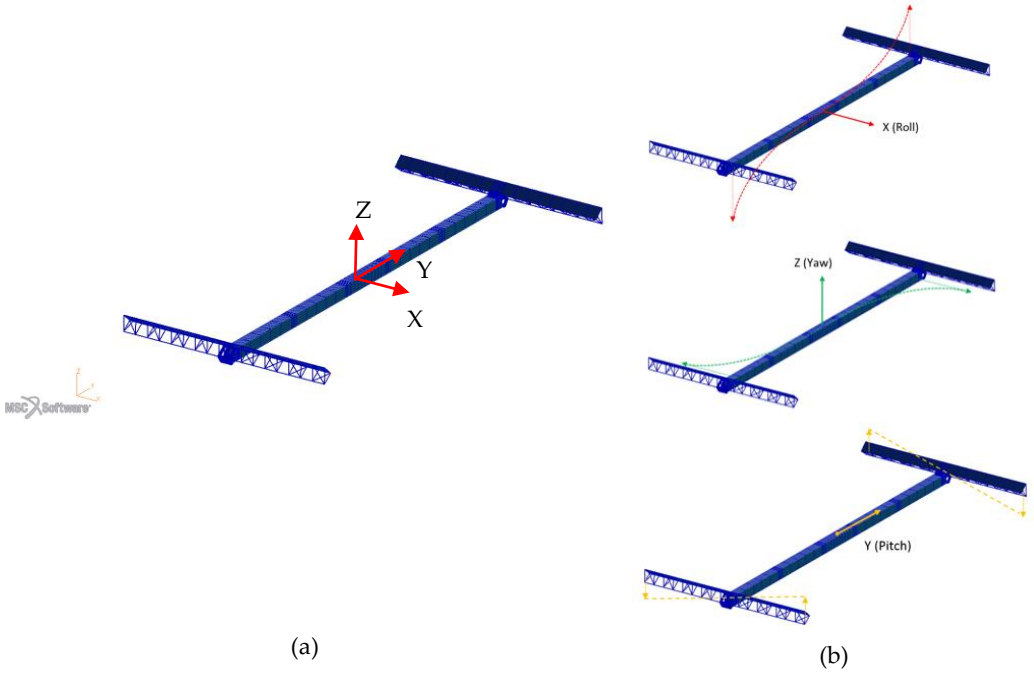

Fig. 5-12: (a) SWOT-like Payload in MSC Patran environment; (b) SWOT-like Payload axes of rotation (roll, pitch, yaw) and related anti-symmetric deformation modes

An optimization procedure has been set in order to match the values of the first frequencies reported in [15]. In this regard, a modal analysis is performed by constraining the structure in correspondence of its Centre of Mass (CoM). In particular, the optimization has been conducted by varying the value of the Young Modulus *E* for each group, the thickness of the shell elements and the radius of the beam elements. The objective function has been set by using the "DRESP2" entry together with the command "FUNC=MATCH" (functions used in MSC Nastran), that creates a response from the difference between analysis results r_j (associated with "DRESP1" entry, in this case the first three frequencies of the FEM model) and target values r_{jT} (the first three desired frequencies, that are input using "DTABLE" data). Therefore, a least squares minimization is performed

("METHOD=LS") where the function to minimize is

$$R = \sum_{j=1}^{3} \left(\frac{r_j - r_{jT}}{r_{jT}} \right)^2 \tag{5.71}$$

The Design Variables (DESVARs) deriving from the optimization are listed in Table 5-2. As an initial guess, all the variables are considered to be realized in equivalent aluminium-alloy material (70e9 N/m²) with a thickness/radius of 0.01 m. The final values of the Young Modulus of the DESVARs can be assumed as comparable with either aluminium or composite materials.

Table 5-2: Design Variables after the optimization process

N°	Name	DESVARs	Final value	N°	Name	DESVARs	Final value
1	E_{OM}	*E* of the bulk mast	7.1e10 N/m^2	7	R_{RABS}	Radius of reflector truss	0.005 m
2	E_{MJ}	*E* of the mast joint sections	7.2e10 N/m^2	8	R_{AMR}	Radius of mast-reflector attachment	0.02 m
3	E_{CM}	*E* of the mast central part	1.5e11 N/m^2	9	T_{OM}	Thickness of the outer mast	0.003 m
4	E_{RA}	*E* of the reflector array	7.4e10 N/m^2	10	T_{MJ}	Thickness of the mast joint sections	0.01 m
5	E_{RABS}	*E* of the reflector truss	1.91e11 N/m^2	11	T_{RA}	Thickness of the reflector array	0.03 m
6	E_{AMR}	*E* of the mast-reflector attachment	9.1e10 N/m^2	12	T_{CM}	Thickness of the mast central part	0.05 m

The total mass after the procedure is around 310 kg, in good accordance with the mass reported in [15] of 294 kg. The first mode is a Z-axis bending mode at 7.4 Hz, the second mode is X-axis bending mode at 8.41 Hz and the third mode is a Y-axis torsion mode at 9.11 Hz (see Fig. 5-13, Fig. 5-14 and Fig. 5-15). Such results are in good agreement with the available data.

The concept presented in this section will be further developed in next chapters to perform analysis of a distributed vibration control system.

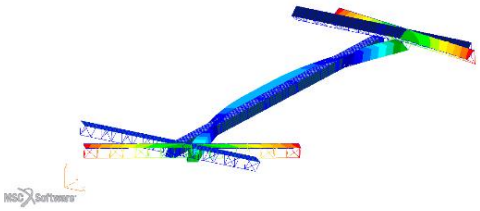

Fig. 5-13: First modal shape – matched FEM

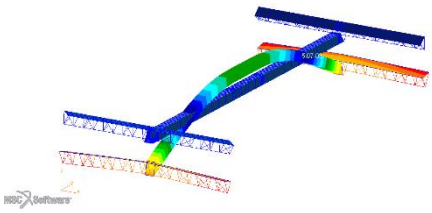

Fig. 5-14: Second modal shape – matched FEM

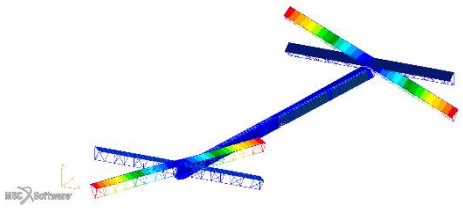

Fig. 5-15: Third modal shape – matched FEM

5.6.1.1 EXTENDED INTERFEROMETER AND PLACEMENT

A flexible structure representing a K-band Interferometer composed of a single long mast is considered in this section. In detail, with respect to the model presented in Par. 5.6.1, the concept has been improved from a performance point of view. Indeed, according to [13], the longer the mast is, the more precise the instrument and data acquisition will be. By increasing the baseline of the structure, the natural frequencies are expected to be lowered and the general dynamic behaviour affected accordingly. After increasing its size, an active control method may be actually required to guarantee a satisfactory pointing and deformation performance by avoiding classical stiffening methods. Therefore, a new payload model is created by increasing the distance between the two antennas from 10 to 25 m. A new modal analysis is performed by constraining the structure in correspondence of its Centre of Mass (CoM).

Though the payload characteristic dimension (along Y-axis) has been more than doubled, the mass of the new payload is increased only of around 30% (up to 413 kg). It is worth noting that the reverse engineering process (presented in Par. 5.6.1) provided valuable insights to proceed in the design of the new payload. In particular, the identified structural parts required to be more rigid are the mast itself, the attachment between the reflectors and the mast and the antenna backbone structure.

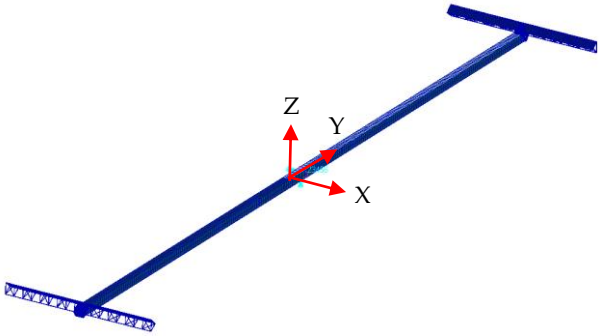

Fig. 5-16: Study case: extended SWOT-like model

Furthermore, the thickness and radius of main components are chosen to be similar to the ones obtained after the optimization process. Concerning the mass distribution, most of the mass is concentrated in the central part of the structure, where electronics and deployment devices are expected to be. The updated natural frequencies of the structure are significantly lower than the SWOT-like case, even if the order of the first three modal shapes (Z-axis bending, X-axis bending and Y-axis torsion) is maintained. The first five frequencies and modes are listed in Table 5-3.

Table 5-3: Modes representation

N°	Mode description	N°	Mode
1	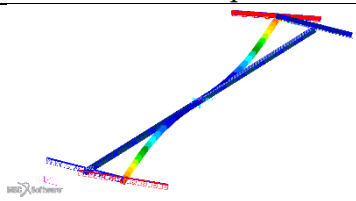 *Z-axis anti-symmetric mode*	4	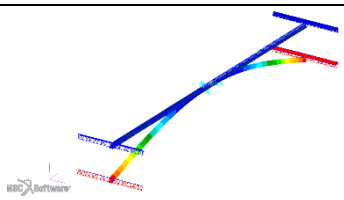 *X-axis symmetric mode*
2	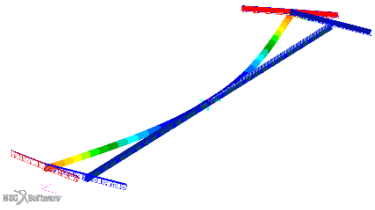 *Z-axis symmetric mode*	5	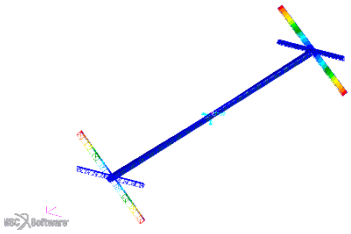 *Y-axis torsion mode*
3	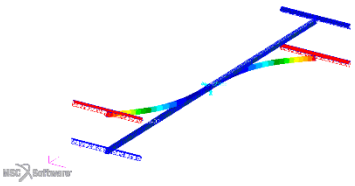 *X-axis anti-symmetric mode*		

To proceed with the assembly of the electromechanical coupling matrix in eq. (5.69), different locations suitable to place the actuators/sensors pairs are identified on the flexible structure. In this study, a triplet of collocated actuators/sensors (devices A, B and C) is considered to be potentially implemented on each half of the mast, so that six actuators have to be positioned on the structure. The set of actuators may be moved along the longitudinal direction of the mast (direction Y). Furthermore, the placement of two additional actuators on each reflector is here investigated to counteract its bending (devices D), for a total of four actuators dedicated to the reflector's backbone supporting structure. In particular, if considering a section of the mast, three actuators in P-PSA configuration could be mounted to damp undesired vibrations, as illustrated in Fig. 5-17. The piezoelectric devices are implemented on the structure so that two adjacent nodes are associated to a specific active element.

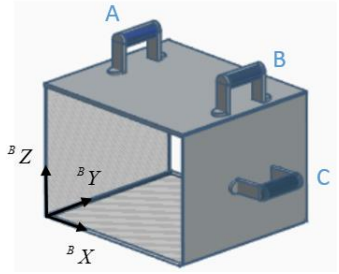

Fig. 5-17: Collocated actuators/sensors set-up

When the actuators A and B are connected/activated in-phase a deformation of pure bending about the ^{B}X axis arises; if connected out-of-phase pure twisting deformation about ^{B}Y axis is induced on the hosting structure. On account of this, in the first case we are able to control the third and fourth bending mode reported in Table 5-3, whereas in the second case we are able to control the fifth torsional mode. The presence of the actuator C, on the other hand, is required to counteract a bending around the ^{B}Z axis (mostly referred to the first and second modes of the mast in Table 5-3). Any combination of this actuation can be obtained by independently driving the actuator A, B and C.

To study the best placement of the considered ten devices, N_p spatial configurations of actuators/sensors have been retained. Let us suppose to have the actuators A and B acting on different elements along the Y-axis of the mast (red arrows in Fig. 5-18), likewise the actuator C is positioned by following the same

logic on the lateral faces of the mast (as indicated by the green arrows in Fig. 5-18). Furthermore, the yellow arrows in Fig. 5-18 indicate where the two couples of actuators D act along the X-axis on the two reflectors. The necessary information on the nodes position in the body reference frame and their corresponding elements are extracted from Nastran via a Matlab interface. The orientation of each element is reconstructed, and the bending axis of the actuator is established.

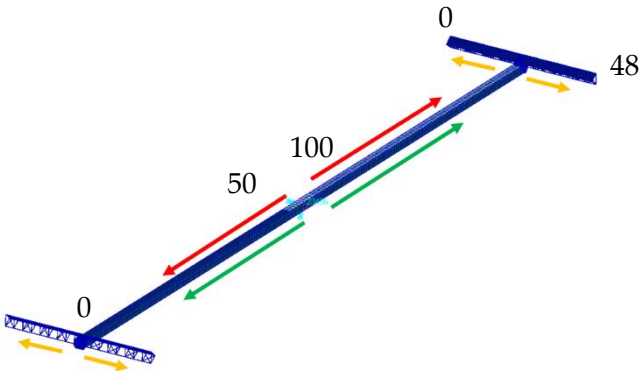

Fig. 5-18: Positioning of piezoelectric devices along the mast and the reflectors with associated active element number

Both the norm-based and MSE and SVD-based methods have been used to perform the placement process.

Let us now be supposed to control the third and fourth modes in Table 5-3 which are more relevant for a standard maneuver as a roll-tilt (about ${}^{B}X$ axis). Considering the elements located on the mast upper panel in the XY plane as the initial candidate set$S$, the optimal location for the sensor and the actuator of type A and B is near the root of the mast where we observe the maximum value of its curvature (see Fig. 5-19, where elements from 0 to 50 correspond to the –Y-axis half-mast and elements from 51 to 100 to the +Y-axis half-mast in the body reference frame). The same procedure (see Fig. 5-20) has been applied to identify sensor/actuator optimal position for the control of the first torsional modes (symmetric and asymmetric).

It is worth noting that, to maximize the efficiency of actuators both on bending and torsional modes, the optimal location for the considered configuration appears, once again, to be near the root of the mast. Furthermore, an investigation about the location of actuators on the antenna reflectors truss is carried out in Fig. 5-21 (where elements from 0 to 24 correspond to the –X-axis half-reflector and

elements from 25 to 48 to the +X-axis half-reflector in the body reference frame). The best placement for such actuators results to be near the connecting area with the mast, in agreement with the capacity of counteracting any bending modes of the reflectors induced by attitude manoeuvres. The obtained results are expected if looking at the modal shapes of the structure in Table 5-3.

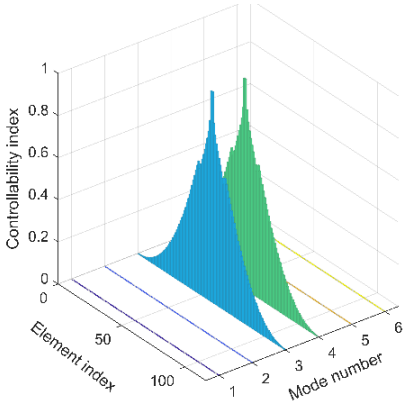

Fig. 5-19: Controllability indexes with weights $\boldsymbol{w_{k1256}} = \mathbf{0}$ and $\boldsymbol{w_{k34}} = \mathbf{1}$ (mast)

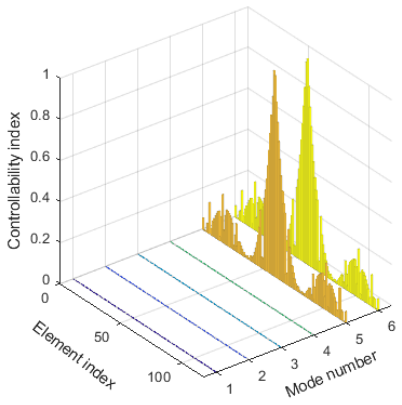

Fig. 5-20: Controllability indexes with weights $\boldsymbol{w_{k1234}} = \mathbf{0}$ and $\boldsymbol{w_{k56}} = \mathbf{1}$ (mast)

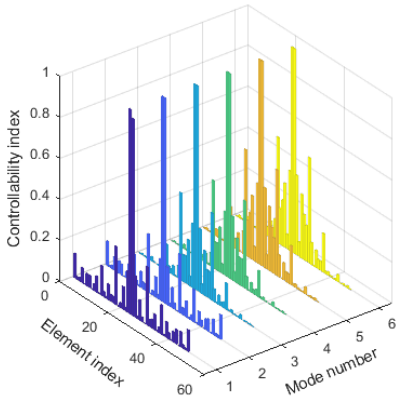

Fig. 5-21: Controllability indexes with weights $\boldsymbol{w_{k123456}} = \mathbf{1}$ (reflector)

To apply the MSE and SVD-based method, the modal strain energy data of the structural model are extracted from a finite element commercial tool, in this case MSC Nastran, and imported and visualized by using an interface in Matlab. By looking at the data illustrated in Fig. 5-22 to Fig. 5-26, a first correspondence may be noticed with the results deriving from the norm-based placement process. Indeed, the best locations to place active devices, according to such method, may be found in correspondence of the zones of the finite element model with a higher concentration of modal strain energy (in red in Fig. 5-22 to Fig. 5-26).

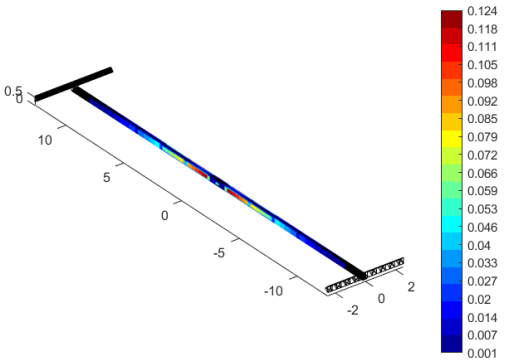

Fig. 5-22: MSE (percentage of total) of the first mode

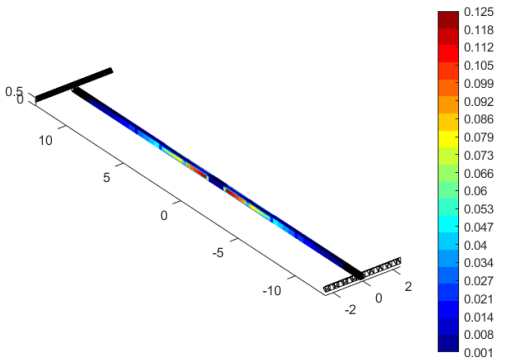

Fig. 5-23: MSE (percentage of total) of the second mode

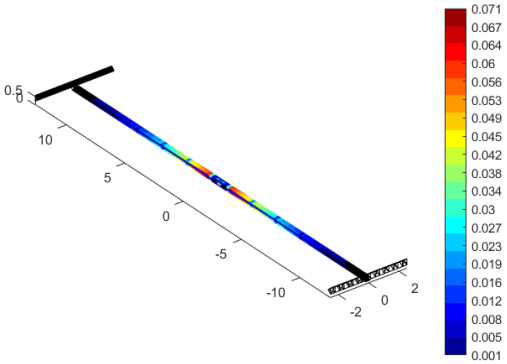

Fig. 5-24: MSE (percentage of total) of the third mode

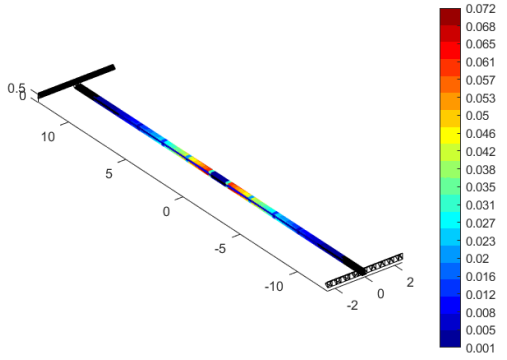

Fig. 5-25: MSE (percentage of total) of the fourth mode

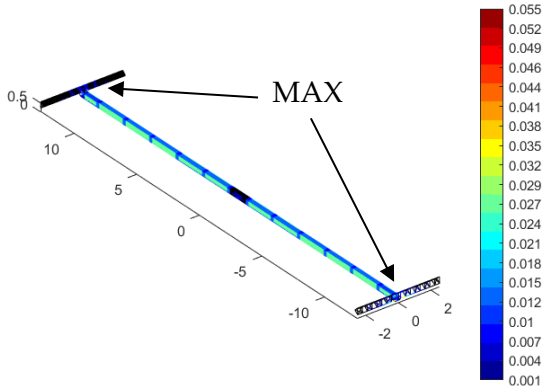

Fig. 5-26: MSE (percentage of total) of the fifth mode

Then, by selecting a restricted number of locations (in the red areas), their combination may be computed to derive the Singular Value Decomposition and related eigenvalues. It is found that the best locations according to the second placement method match the ones individuated by using the norm-based approach, thus cross-checking the obtained results.

Table 5-4: Comparison between Norm-based and MSE|SVD-based placement

Mode	Location s (Norm)	Mode	Location s (MSE|SVD)
1	(49,50) *mast*	1	(49,50) *mast*
2	(49,50) *mast*	2	(49,50) *mast*
3	(49,50) *mast*	3	(49,50) *mast*
4	(49,50) *mast*	4	(49,50) *mast*
5	(49,50) *mast*, (24,25) *reflector*	5	(49,50) *mast*, (24,25) *reflector*

The final set-up of actuators and sensors is shown in Fig. 5-27. In particular, the red patches indicate the actuators type A and B of Fig. 5-17, while the green ones the type C. Furthermore, the orange patches point out the position of the P-PSA devices mounted on the backbone truss of the antenna reflector.

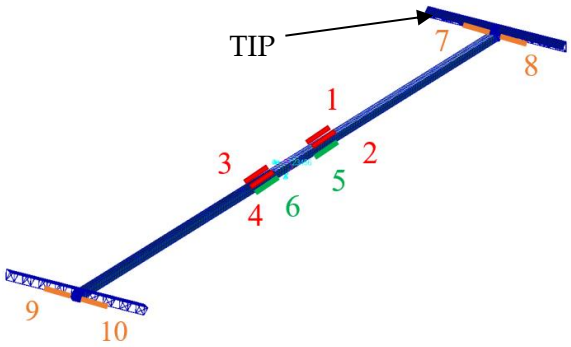

Fig. 5-27: Final position of actuators and sensors

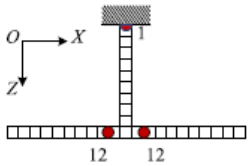

Fig. 5-28: Optimized configuration [17]

In this context, a recent research conducted by Y. Cao et al. [17] addressed the problem of actuators placement for a mono-dimensional single T-shaped structure by using a global mode method (GMM) and an energy criterion. The final configuration, reported in Fig. 5-28, resulted to be very similar to the one individuated in this thesis, thus further validating the proposed strategy.

5.6.2 Study Case B: Mesh Reflector

Similarly, a representative model for a mesh reflector dynamic behaviour is obtained. Indeed, based on available information [18][20], a replica of the 12-meters diameter Astromesh® reflector has been realized[3], as reported in Fig. 5-29,

[3] The results in this section were published by the thesis author in F. Angeletti et al., *Control-oriented modelling of an active suppression system for large space smart structures*, 71st International Astronautical Congress (IAC), Cyber Edition, October 12-14, 2020

in [19].

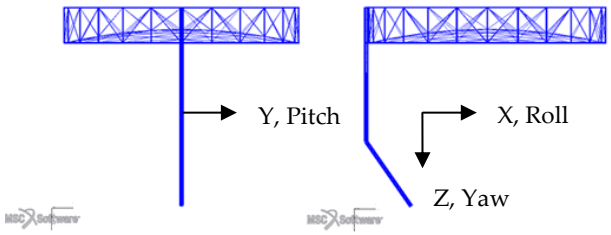

Fig. 5-29: Mesh reflector: (a) frontal view (b) lateral view

In detail, the truss or rim structure is composed of 30 parallelograms of 2.52 m height with a 1.26 m base, according to the data by Northrop Grumman [18]. An AstroMesh-like structure has been modelled in MSC Patran environment and the finite elements further organized in groups related to different parts of the structure. The groups are listed in Table 5-5.

Table 5-5: Groups from FEM model

Group		Visualization	Group		Visualization
1	Truss	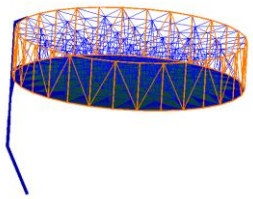	3	Cables	
2	Mesh	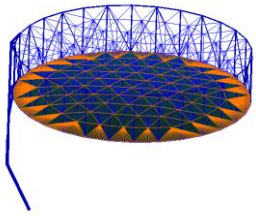	5	Boom	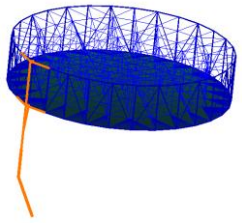

As the data concerning dimensions and material of each part of the instrument are not available, a reverse engineering procedure has been conducted by following the same logic presented in the previous paragraph to try to match the first frequency of the deployed instrument (without the boom). To this purpose, the Young modulus, density and geometric dimensions of the model have been considered as design variables to be varied in order to reproduce the desired dynamic behaviour. The final results are reported in Table 5-6, being in good agreement with the data reported in [20].

Table 5-6: Design Variables after the reverse engineering process

N°	Name	DESVARs	Final value	N°	Name	DESVARs	Final value
1	E_T	E of the truss	$125e9\ N/m^2$	4	D_T	Diameter of the truss elements	$0.020\ m$
2	E_M	E of the mesh	$7.2e10\ N/m^2$	5	T_M	Thickness of the mesh surface	$0.001\ m$
3	E_C	E of the cables	$125e9\ N/m^2$	6	A_C	Section area of the cables	$0.009\ m^2$

Table 5-7: Comparison between Astromesh® data and the designed replica

	Astromesh® data	Model Replica
Mass	Truss: 53 kg Mesh: 4.1 kg	Truss: 53.01 kg Mesh: 4.25 kg
	Total: 57.1 kg	Total: 57.26 kg
1st Mode	Truss only: 0.30 Hz Truss|Mesh: 0.80 Hz	Truss only: 0.30 Hz Truss|Mesh: 0.78 Hz

A visualization of the first flexible mode for the truss group clamped in correspondence of its attachment point is reported in Fig. 5-30 and Fig. 5-31. Both the first frequency of the antenna truss with and without internal cables and mesh is almost perfectly matched between the replica model and the AstroMesh® data.

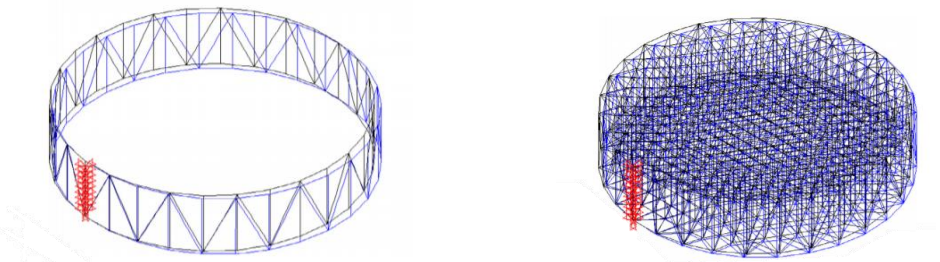

1st mode: 0.30 Hz

1st mode: 0.80 Hz

Fig. 5-30: (Left) First mode of the antenna truss; (Right) First mode of the antenna with mesh and cables [20]

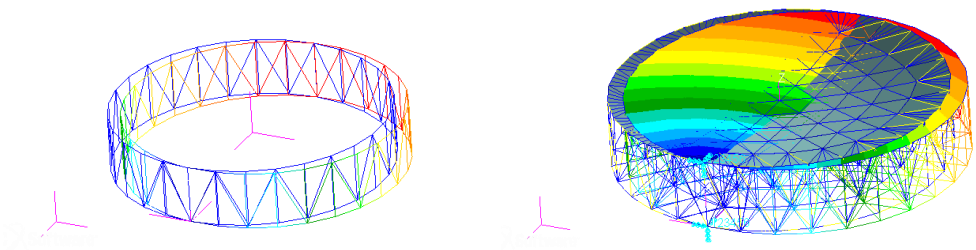

1st mode: 0.30 Hz 1st mode: 0.77 Hz

Fig. 5-31: (Left) First mode of the antenna truss; (Right) First mode of the antenna with mesh and cables

In the next section, the proposed model will be modified to obtain a reduced mass and lower natural frequencies, in order to verify the application of an active vibration control solution.

5.6.2.1 MODIFIED REFLECTOR AND PLACEMENT

A realistic representative model of the dynamic behaviour of a mesh reflector is developed as a study case to test the control strategy proposed in this thesis. Moreover, based on available information [18][17], a new design of the 12-meters diameter reflector is realized in a finite element simulation environment (namely MSC Nastran) and named Large Mesh Reflector Model (LMRM) [19]. Indeed, to exploit the advantages an active control system may induce on the system design, the model replica has been *further modified* to achieve a mass reduction of up to 30%. Indeed, a new LMRM has been derived by reducing the radius of truss structure and the density of the materials to obtain a lighter model, while still maintaining the same modal shapes and mass/stiffness distribution identified in the model replica. The comparison among the main dynamic features of the AstroMesh® antenna, the replica and the LMRM are reported in Table 5-8.

Table 5-8: Comparison between different models

	AstroMesh® data	Model Replica	LMRM
Mass (kg)	Truss: 53 Mesh: 4.1	Truss: 53.01 Mesh: 4.25	Truss: 38.34 Mesh: 4.25
	Total: 57.1	Total: 57.26	Total: 42.6
1st Mode (Hz)	Truss: 0.30 Truss+Mesh: 0.80	Truss: 0.30 Truss+Mesh: 0.78	Truss: 0.20 Truss+Mesh: 0.53

In detail, the truss structure is composed of 30 unit bays, while the parabolic surface (with an areal density of about 0.3 kg/m²) is thought to be supported by a net of rod elements representing the actual cable mesh of the reflector. Concerning the LMRM, the horizontal and vertical tubes of the truss are assumed to be 2.5 meters long (external radius 0.021m, internal radius 0.02m), while the diagonal ones 2.81 meters (external radius 0.01m, internal radius 0.009m). The material of the truss is Carbon Fiber Reinforced Polymer (CFRP), with density equal to 1550 kg/m³ and Young modulus 125 GPa. The cable mesh is represented by rod elements with area equal to 1 mm², in CFRP material.

To ensure a correct deployment of the reflector and to support the antenna when in-orbit, an extendable boom is generally implemented on the spacecraft platform. Therefore, an 8-meter long, 20 kg boom has been included in the structural model of the LMRM, which has been chosen as Study Case B. As specified in [18], the deployed payload, composed of boom and the reflector, has generally three distinct constrained mode, named yaw, pitch and roll modes. They correspond to torsion and bending with respect to the main coordinated axes, illustrated in Fig. 5-29 along with a complete model of the payload.

Usually, the yaw is the first fundamental mode, and it is often close to the pitch mode, while the roll one is larger than the others. Concerning the available data in [18], the order of the modes for the clamped system is yaw, pitch and roll, while the related frequencies are not available. Nevertheless, having compared the behaviour of the mesh reflector with the original AstroMesh® model, it is reasonable to assume the dynamics behaviour are similar. Indeed, the same order of natural modes can be found in Table 5-9 when referring to the Study case and its modal shapes.

In this study OPSA actuator are considered, as, compared to piezoelectric patches, contribute to exert a higher actuating force on the structure. However, the generated bending moment can be generally oriented with respect to the three coordinated. Therefore, in the placement procedure, each allowable physical position is allotted to additional virtual locations, one for each contemplated orientation (in black in Fig. 5-32, four orientations considered, in green the longitudinal forces, while in red the actual device). In detail, a location $s = [ID | E_{ID} | N_{ID} | O_r]$ is defined by a label ID, by the identification number E_{ID} of the finite element where the active device is implemented, by a vector N_{ID} listing the IDs of

the two considered nodes, and by a term O_r indicating the distinct orientation of the active device.

Table 5-9: Clamped modes and frequencies

Mode	AstroMesh®	LMRM replica
1st	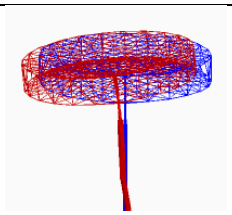	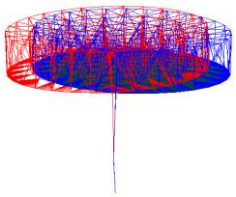
	Yaw mode: bending about Z axis Frequency: n.a. [18]	Yaw mode: bending about Zaxis Frequency: 0.41 Hz
2nd	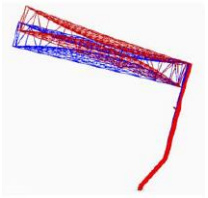	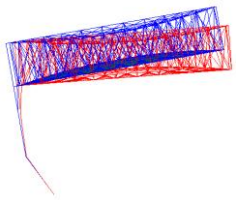
	Pitch mode: bending about Y axis Frequency: n.a. [18]	Pitch mode: bending about Y axis Frequency: 0.53 Hz
3rd	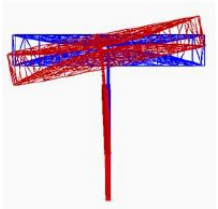	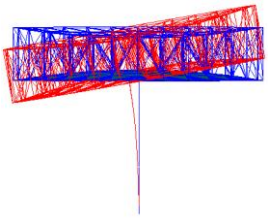
	Roll mode: torsion about X axis Frequency: n.a. [18]	Roll mode: torsion about X axis Frequency: 0.85 Hz

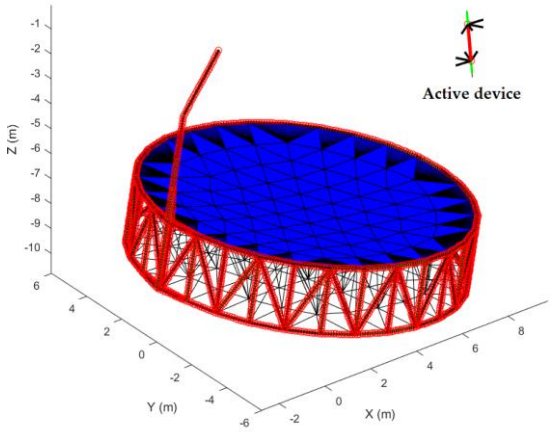

Fig. 5-32: Set of possible locations of smart devices

The plot of the placement matrices σ_{2ki} for the first, second, third and fourth mode are represented in Fig. 5-33 and Fig. 5-34, where the peaks of the placement indexes (both higher value and second higher peak) are circled in red. Indeed, frequencies up to 3 Hz have been considered for the placement, as it may interfere with the bandwidth of the controller and cause control/structure interaction issues. Higher frequencies have been discarded as it is less likely they may provoke performance deterioration.

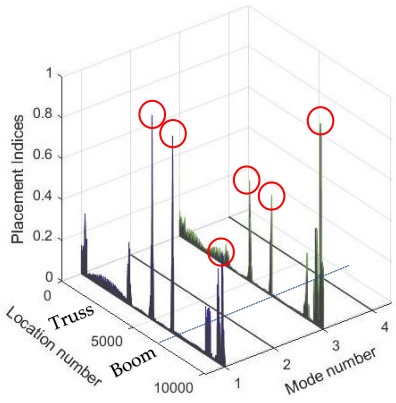

Fig. 5-33: Placement indices for i=1:4 with $w_{k1,3}=1$ and $w_{k2,4}=0$

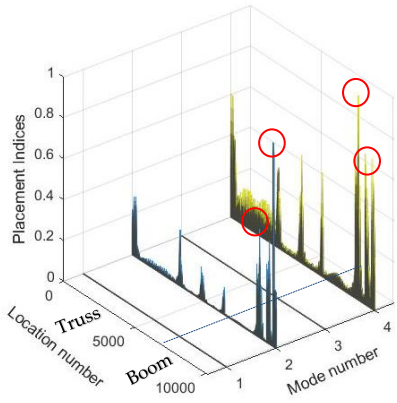

Fig. 5-34: Placement indices for i=1:4 with $w_{k2,4}=1$ and $w_{k1,3}=0$

Table 5-10: Norm-based placement outcome

Mode	Location ID	Forces direction: F. Force, M. Moment	Placement Index
1	(4975,6426)	F: ±Y, M: ±XZ	(1,0.98)
	(9927)	F: ±Z, M: ±X	(0.55)
2	(9925)	F: ±Z, M: ±Y	(1)
	(8977)	F: ±Z, M: ±Y	(0.58)
3	(9927)	F: ±Z, M: ±X	(1)
	(4924,6480)	F: ±Y, M: ±XZ	(0.57,0.58)
4	(8977)	F: ±Z, M: ±Y	(1)
	(9481)	F: ±Z, M: ±Y	(0.74)

It may be noticed how the axes of the bending moments exerted by the devices are oriented as expected with respect to the directions of the bending modes. Indeed, the first mode is composed mainly of a bending about the Z-axis and a minor bending about the X-axis. The second mode is a bending about the Y-axis, the third mode is a torsion of the reflector about the X-axis and consequent bending of the boom with respect to the same axis. The fourth mode is similar to the second, being

again a bending about the Y-axis, where the boom deflects as the second mode of a constrained-free beam.

As far as the second placement method is concerned, the MSE data are extracted from MSC.Nastran and imported in Matlab environment for further processing. The MSE in terms of energy density (weighted accordingly to the effective dimension of the finite element, for a more accurate information about the energy distribution) is reported in Fig. 5-35 to Fig. 5-38.

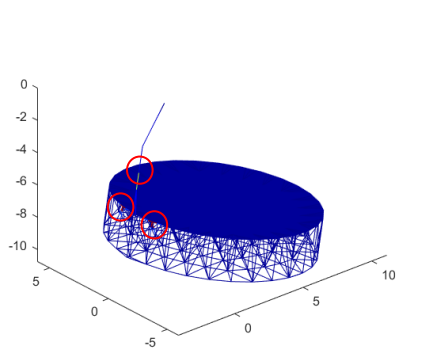

Fig. 5-35: MSE (element density) for the first mode

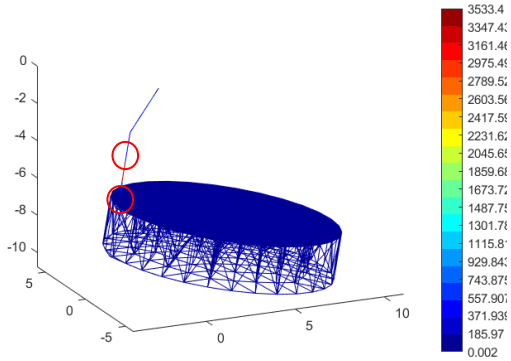

Fig. 5-36: MSE (element density) for the second mode

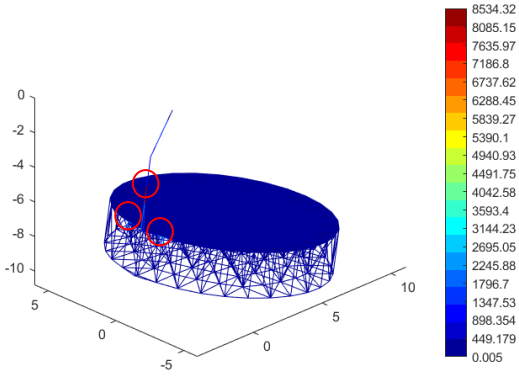

Fig. 5-37: MSE (element density) for the third mode

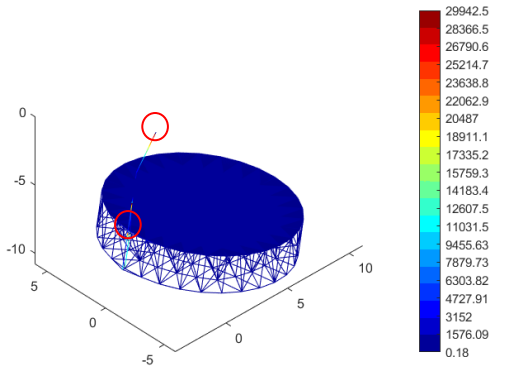

Fig. 5-38: MSE (element density) for the fourth mode

A good correspondence between elements with higher energy and results from the previous placement method can be noticed. After having identified elements in the subsets U_i, possible combinations are computed as indicated in Par. 5.4. The results are summarized in Table 5-11. In detail, combinations of two actuators for each

mode have been considered ($\varepsilon_i = 2$).

Table 5-11: MSE|SVD-based placement outcome

Mode	Locations ID	Normalized $\sigma(\boldsymbol{B}_m)\big\|_{\min}$
1-3	[4975,6426|9927, 8977]	(1)
	[4974,6426|9935, 8977]	(0.99)
2-4	[9925, 8977|8977, 9841]	(1)
	[9926, 8977|8977, 9841]	(0.97)

A good correspondence is evident when considering the results of the previous method. To conclude, the final configuration is presented based on such results in Table 5-12.

Table 5-12: Final configuration

Act/ Sens	Element ID	Mode			
		1	2	3	4
1	2907	++	-	+	-
2	3270	++	-	+	-
3	4077	-	++	-	+
4	4079	+	-	++	
5	3908	-	+	-	++

++ very effective, + effective,: not effective

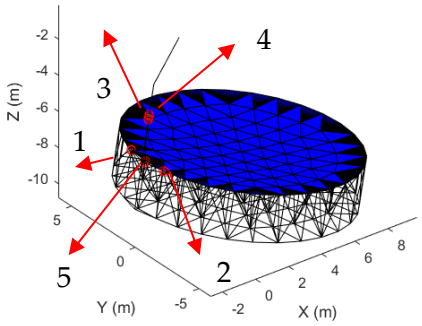

Fig. 5-39: Final configuration of co-located actuators/sensors

In the proposed configuration, a total of five actuators are placed on the flexible structure, in correspondence of the locations with higher placement indices and minimum SV for each considered mode. It is interesting to note that the devices are effective, in different amounts, on more than one mode at a time (see Table 5-12). The position and related number of the actuators is depicted in Fig. 5-39.

5.6.3 STUDY CASE C: GENERAL CONCEPT

In this section, the main results for the placement of co-located actuators/sensors on a general concept of a flexible radar interferometer are exposed. Indeed, the presented model has been developed in the frame of a research study funded by the European Space Agency (ESA), to take a possible evolution of the state-of-the-art of radar interferometers into account. Indeed, with respect to the case presented in Par. 5.6.1, the mast has been inclined of an angle α=15 deg with respect to Y-axes to further generalize the model while maintaining realistic payload requirements and adding more challenging ones (as the change of length of the baseline and the torsion on the reflector). The result is an "upside V-shaped" instrument, where the +Z-axis points in the nadir direction. With respect to a "downside V-shaped" instrument (where the "V" points in the zenith direction), such a configuration allows the swath to be more directive and avoids excessive loss of signal gain. The overall Payload FEM model, as imported in Matlab, is presented in Fig. 5-40.

To study a generic configuration, three structural sub-groups have been identified, corresponding to the two halves of the payload (beam and truss sides, Group A and B respectively), to perform a controllability and observability analysis and find the optimal configuration of the devices.

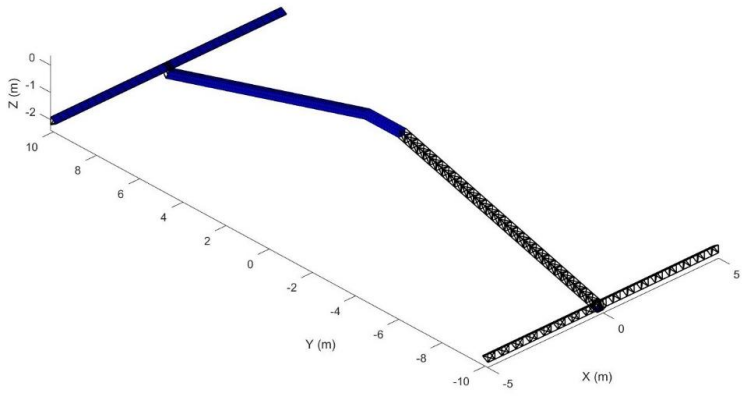

Fig. 5-40: Study Case C: FEM model imported in Matlab®

Indeed, as the central section of the antenna (inside the satellite platform) is supposed to host instrumentation and additional masses (bus hardware), such part is designed to be more rigid than the two masts. Therefore, the latter can be considered decoupled from each other, as it can be noticed from Table 5-13.

Table 5-13: Flexible modes (structure constrained in its CoM)

N°	Modal shape	N°	Modal shape
1	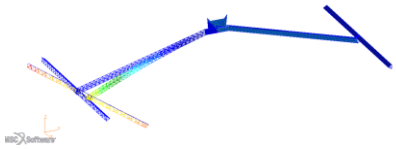 1.32 Hz	4	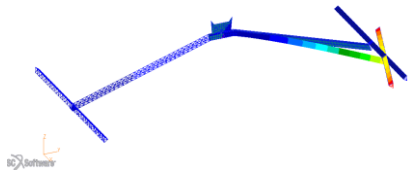 2.04 Hz
2	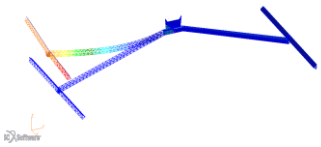 1.49 Hz	5	 2.24 Hz
3	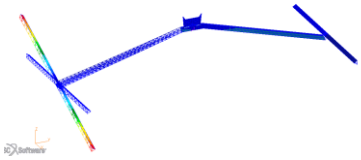 1.75 Hz	6	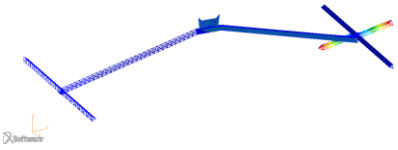 2.88 Hz

Concerning the inclination of the two reflectors, they have been designed taking the actual working principle of the KaRin instrument into account. As reported in [15], the interferometer is a dual-swath system, alternatively illuminating the left and right swaths on each side of the nadir track. These two swaths measure 50 km wide in a 1°-4° plan, as indicated in Fig. 5-41.

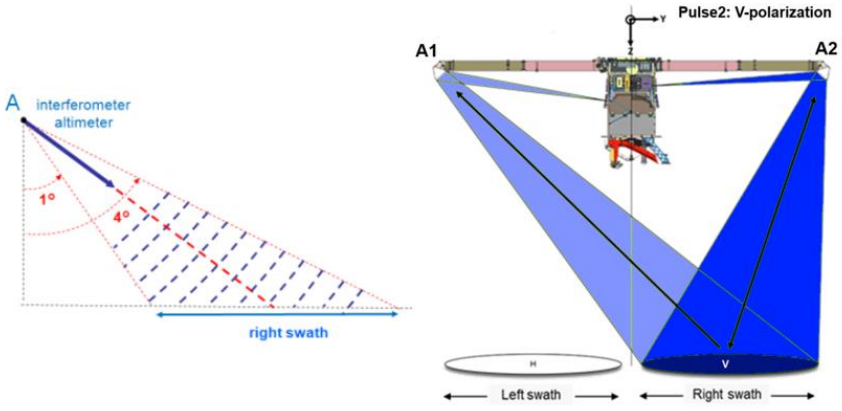

Fig. 5-41: KaRin off-nadir altimeter

The altimeter KaRIn operates in a "Non Ping-Pong mode", also called bi-static mode: one of the antennas transmits and both receive the radar echoes. In blue in

Fig. 5-41: the antenna A2 emits a pulse toward the right swath with a different polarization, "V". The two antennas (A1+A2) receive the backscattered signal in their respective direction. Therefore, by considering an inclination of the mast of $\alpha = 15°$ as already mentioned, the signal trajectory can be reconstructed starting by Fig. 5-41. Assumed the plan of the swath is $\gamma = 3°$ with $1° \leq \gamma \leq 4°$, some geometric considerations may be conducted as indicated in Fig. 5-42 to find the inclination θ the reflector.

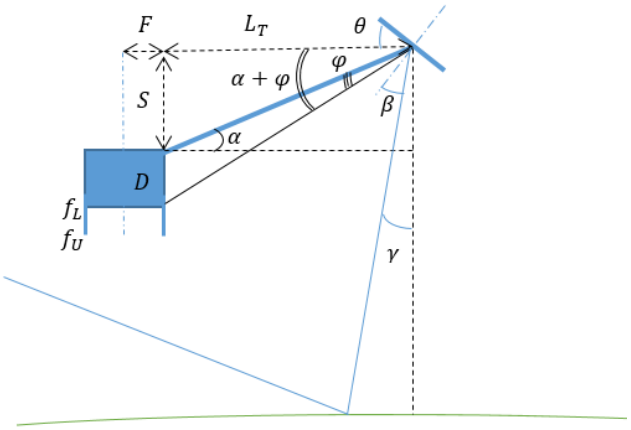

Fig. 5-42: Scheme to compute the reflector inclination

Given that half of the baseline can be described as

$$\frac{B}{2} = L_T + F = 10m \tag{5.72}$$

with $F = 0.66\ m$, the projection of the mast on horizontal direction is $L_T = 9.34\ m$. According to this consideration, the distance S can be defined as $S = L_T \tan(\alpha) \cong 2.5m$. By construction,

$$(S + D) = L_T \tan(\alpha + \varphi) \tag{5.73}$$

where $D = 0.73m$ indicates the position of the lower feed in the payload reference frame. Consequently, the angle φ between the mast and the line connecting the lower feed f_L and the phase center of the reflector is $\varphi \cong 16°$. Following by geometric considerations, assuming a symmetric reflection of the signal on the reflector surface, it is possible to write

$$\beta = \frac{1}{2}\left(\frac{\pi}{2} - \varphi - \alpha - \gamma\right) \cong 28° \tag{5.74}$$

$$\theta = \frac{\pi}{2} - \varphi - \alpha - \beta \cong 31° \tag{5.75}$$

By varying the plane of the swath γ in the allowed range, the final result varies of about ± 1 degrees maximum. The final value is assumed to be $\theta = 31°$. To validate the result, the same calculations have been repeated in the SWOT-like case (with $\alpha = 0°$). The corresponding inclination has been found to be in agreement with the available data for the current interferometer design.

5.6.3.1 PLACEMENT RESULTS

In this section, the outcomes related to the placement of elements on the mast are reported. In particular, as the beam side of the payload is very similar from a structural point of view to the Study Case A (and placement results are therefore comparable), in this paragraph only the findings concerning the truss side will be presented for brevity's sake. The data from the finite element commercial tool have been imported in Matlab environment to carry out the placement procedure, as reported in Fig. 5-43. In detail, the first three modes of the structure will be analyzed as they involve the truss half of the Payload, while the modes from four to six concern the beam side (as reported in Table 5-13). The normalized placement indices for the first three modes of the Payload are reported in Fig. 5-44.

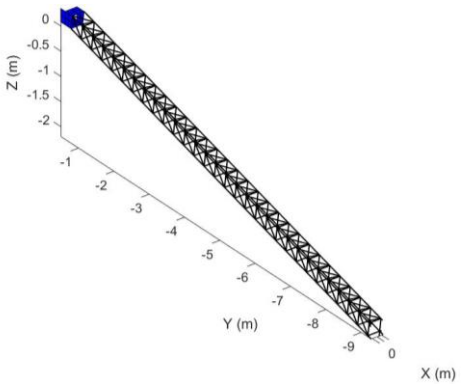

Fig. 5-43: Placement of co-located actuators/sensors on the truss side

By looking at the correlation indices in Fig. 5-44 (normalized with respect to their maximum value), it can be noticed the actuators near the root of the Payload give the higher contribution in terms of damping the first modes of the structure

(location number 0 is near the root).

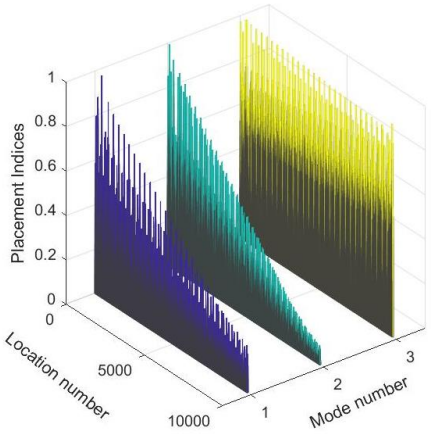

Fig. 5-44: Placement Indices Normalized: first three modes of the structure

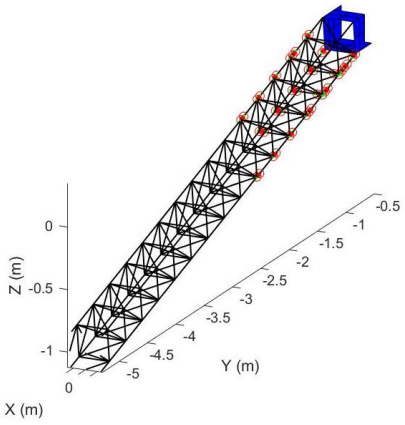

Fig. 5-45: Optimal position of actuator/sensor before correlation-based exclusion process

This result is expected, as, if considering the two sides of the antenna as clamped beams, the more efficient location of actuators would be at places where curve radius is important (i.e. at the fixed end of the beam) than where curve radius is small (i.e. at the free end of the beam). Concerning the third mode (mainly a torsion/bending of the reflector antenna) the difference among elements at the root and in the middle of the truss seems to be less relevant, therefore, devices devoted to control such modes will be also positioned in correspondence of the reflector (as illustrated later in this paragraph). Therefore, a preliminary distribution of actuators/sensors obtained without considering the correlation-based exclusion process presented in Par. 5.3.2.1 is depicted in Fig. 5-45. Again, the devices are condensed in the root area. The results can be obtained by using both piezoelectric OPSA and patches, however, OPSA have been preferred due to their higher efficiency.

After correlation-based exclusion process, the best locations to address the first mode of vibration are portrayed in Fig. 5-46 (where all the weights related to other modes are put to zero). Conversely, the optimal location to counteract the second mode of vibration is reported in Fig. 5-48. The obtained results prove to be in perfect agreement with the modal strain energy (MSE) distribution as extracted directly from Nastran tool (see Fig. 5-47 and Fig. 5-49, where the maximum MSE density is coloured in red).

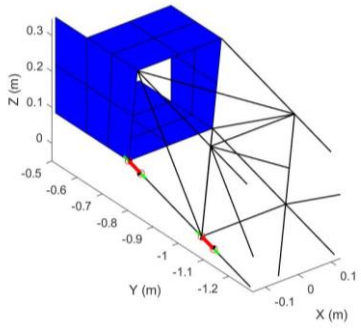

Fig. 5-46: Optimal position after correlation-based exclusion process (1st mode at 1.32 Hz): weights [1 0 0 0 0 0]

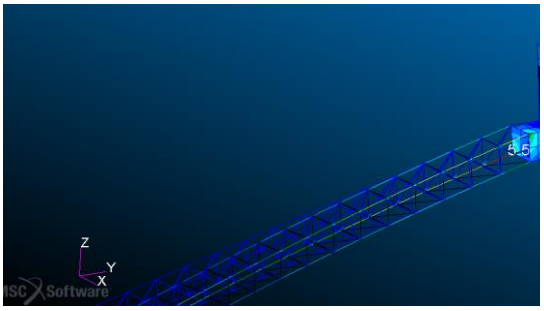

Fig. 5-47: Modal Energy Strain extracted from MSC Nastran (1st mode: 1.32 Hz)

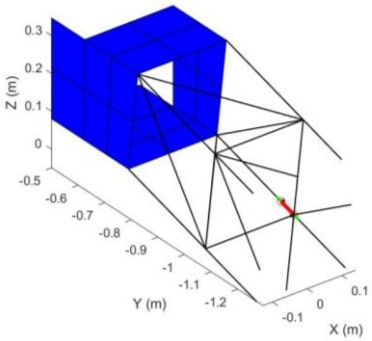

Fig. 5-48: Optimal position of after correlation-based exclusion process (2nd mode at 1.49 Hz): weights [0 1 0 0 0 0]

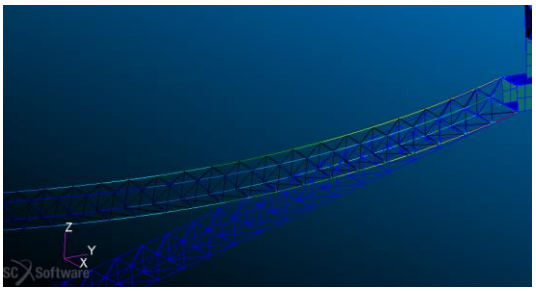

Fig. 5-49: Modal Energy Strain extracted from Nastran (2nd mode: 1.49 Hz)

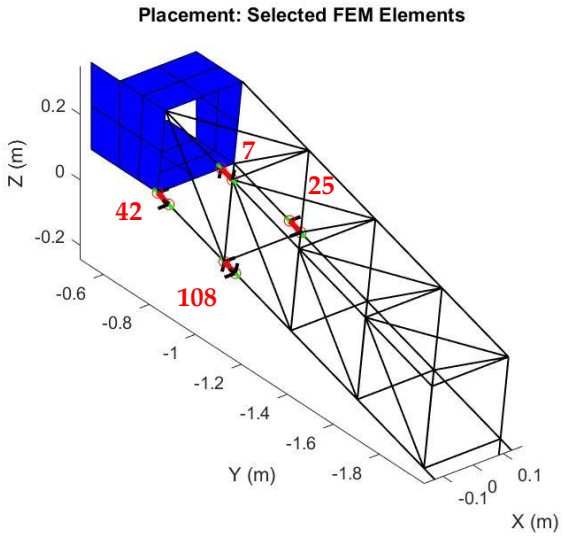

Fig. 5-50: Placement indices for the final beam configuration (combination to act on the coordinated axis X, Y and Z): weights [1 1 1 0 0 0]

By investigating the best combination to counteract the first, second and third modes of the Payload at the same time, four optimal location have been identified. These locations are in agreement with the modal strain energy distribution, but different combination may be considered if varying the orientation of their bending axes (see Fig. 5-50). In particular, two possible configurations have been identified, being the related placement index quite similar (see Table 5-14).

Table 5-14: Final configuration of co-located actuators/sensors on the truss structure

Actuator number	Element number	Placement Index σ_k	Bending Axis
1	42	1.248	±X
		1.138	±XZ
		1.174	±Z
2	108	1.143	±XZ
		1.092	±X
3	7	1.079	±X
4	25	1.198	±Z

Two possible configurations: conf. A highlighted in orange, actuators on elements 42 and 108, acting separately on axis X and Z, conf. B highlighted in green, actuators on elements 42 and 108 acting simultaneously on axis X and Z. A third actuator on element 25 can be added for counteracting the torsional mode.

Now, the placement on actuators/sensors on the antenna reflector is carried out. These actuators turn out to be useful when addressing the damping of the third and sixth modes of the Payload, which interests mainly the rotation of the antenna itself around the ±Y-axis. The optimal locations of the devices are shown in Fig. 5-51. The related correlation indices are reported in Fig. 5-52.

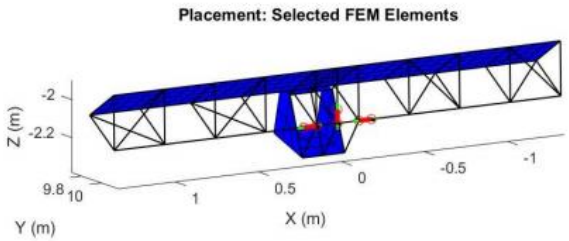

Fig. 5-51: Placement on the reflector

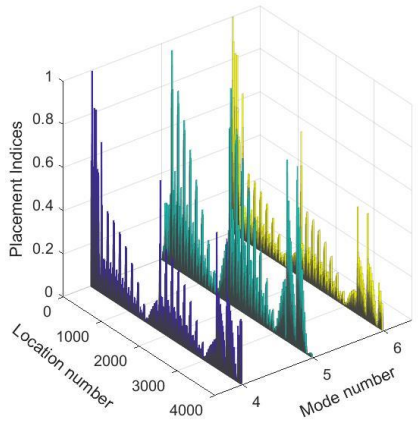

Fig. 5-52: Normalized placement indices

Note that the placement algorithm has determined not only the most appropriate location but also the orientation of devices: in this case, with a bending moment axis directed towards Y-axis for the two different types of actuators, both piezoelectric stacks with offset and patches.

5.6.4 Study Case D: Solar Array

In this section, a possible configuration of collocated actuators/sensors implemented on the solar panels is presented. In particular, the results of a rich mesh model generated in Nastran for placement purposes is imported in Matlab to carry out the placement process. The size of the solar panels is set equal to 3 x 8 m. The array is reinforced via a supporting structure in CFRP and a Yoke is added to reproduce the attachment of the panel to the platform. The modes of the structure are reported in Table 5-15.

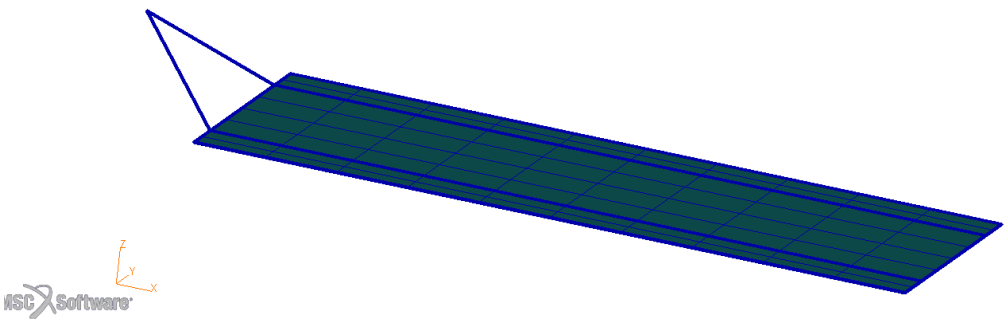

Fig. 5-53: Solar panel structure

Table 5-15: Modes of the clamped structure

N°	Modal shape	N°	Modal shape
1	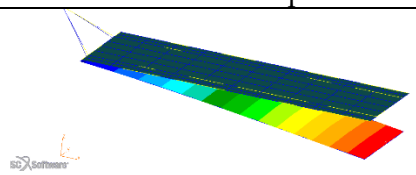 0.16 Hz	3	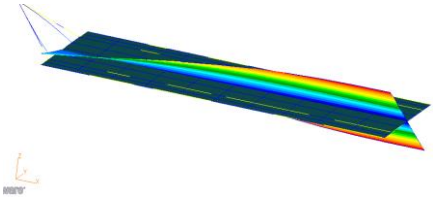 0.79 Hz
2	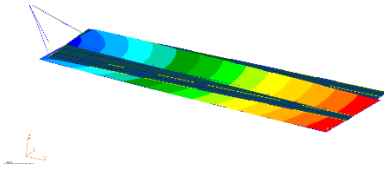 0.30 Hz		

As expected, the optimal location to control the first bending and torsional modes of the structure turns out to be near the attachment point (as indicated in Fig. 5-54). In detail the orientation of the beding axes of the actuators are oriented to have components along the ±XZ and ±ZY axes, to obtain controlling/sensing capabilities along the three coordinated axes. In Fig. 5-54, the normalized placement indices are illustrated. According to the geometry of the yoke, the actuators/sensors suitable to be used can be both piezo stack with offset and piezo patches.

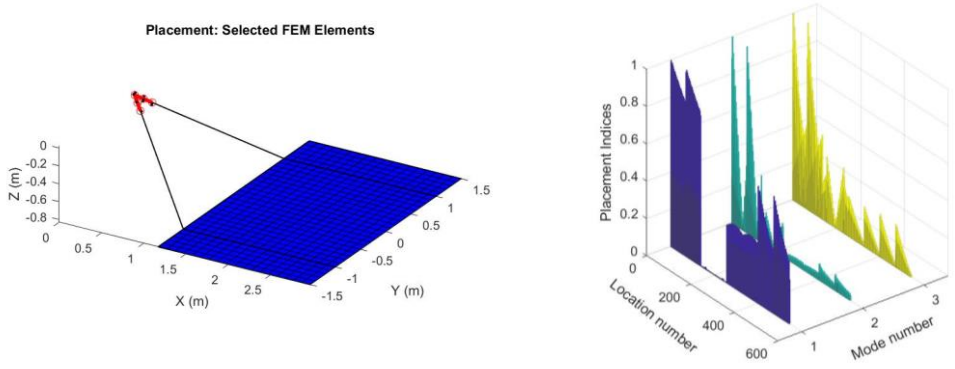

(a) (b)

Fig. 5-54: (a) Placement indices for the final configuration: weights [1 1 1 0 0 0]; (b) Normalized Placement Indices: first three modes

Such a conclusion is confirmed also by referring to the modal strain energy distribution as computed by Nastran tool (reported in Fig. 5-55, in red the maximum MSE).

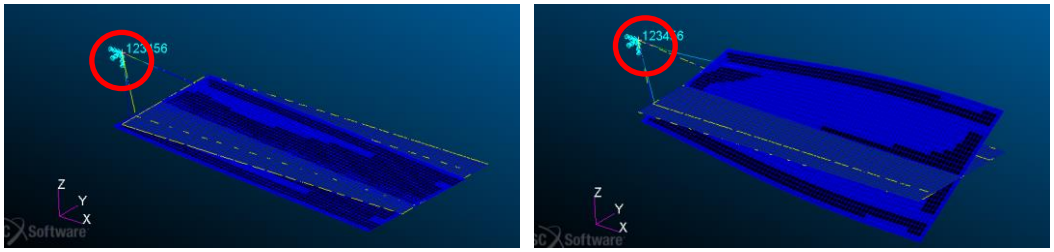

(a) (b)

Fig. 5-55: (a) Modal Energy Strain extracted from Nastran (1st mode); (b) Modal Energy Strain extracted from Nastran (3rd mode)

5.7 CONCLUSIONS

It should be noticed the proposed procedures (both gramian-based and MSE-based) indicate the same location and actuators orientation to perform active vibration control on the proposed flexible appendages. The benefit of the open-loop approach to the placement problem is its independence from the type of control design technique to be employed. Therefore, the designer has to evaluate the minimum number of actuators needed to meet the required performance when computing the closed-loop control system, based also on physical model and actual limits (as saturation, power consumption, mass, noise level, etc) of the considered devices. Spillover effects have not been examined at the moment but counteracting strategies for this problem can be in future addressed in the framework of large space structures control.

BIBLIOGRAPHY

[1] (2004) *Controllability and Observability*. In: Analysis and Control of Nonlinear Process Systems. Advanced Textbooks in Control and Signal Processing. Springer, London. https://doi.org/10.1007/1-85233-861-X_6

[2] W. K. Gawronski, *Advanced Structural Dynamics and Active Control of Structures*, Mechanical Engineering Series, Springer, New York, 2004;

[3] T. Summers, J. Lygeros, *Optimal Sensor and Actuator Placement in Complex Dynamical Networks,* Proceedings of the 19th World Congress The International Federation of Automatic Control Cape Town, South Africa. August 24-29, 2014

[4] T. Nestorovic, M. Trajkov, *Optimal actuator and sensor placement based on balanced reduced models,* Mechanical Systems and Signal Processing Volume 36, Issue 2, April 2013, Pages 271-289

[5] T. Kailath *Linear Systems*, Prentice Hall, Englewood Cliffs, NJ, 1980.

[6] R. E. Skelton and P.C. Hughes, *Modal Cost Analysis for Linear Matrix Second-Order Systems*, Journal of Dynamic Systems, Measurements and Control, vol. 102, 1980, pp. 151–158;

[7] MSC Software, *MSC Nastran Dynamics User's Guide*, pp. 120-121, 2019;

[8] H. Baruh H, L. Meirovitch, *On the placement of actuators in the control of distributed parameter systems*, AIAA paper 81-0638: 611-619, 1981;

[9] R. Lammering, J. H. Jia , C. A. Rogers, *Optimal placement of piezoelectric actuators in adaptive truss structures*, J. Sound Vib. 171: 67-85, 1994;

[10] K. Guo and J. Jiang, *Optimal Locations of Dampers/Actuators in Vibration Control of a Truss-Cored Sandwich Plate*, Advances on Analysis and Control of Vibrations: Theory and Applications, September 2012;

[11] A. Preumont, *Vibration Control of Active Structures*, Solid Mechanics and Its Applications, Third Edition, Springer Netherlands, 2011;

[12] W. Wei and Y. Zhichun, *A compact piezoelectric stack actuator and its simulation in vibration control*, Tsinghua Sci. Technol., 14 (N. S2) (2009), pp. 43-48;

[13] A. Ferretti, A. Monti-Guarnieri, C. Prati, F. Rocca, D. Massonnet, *InSAR Principles: Guidelines for SAR Interferometry Processing and Interpretation*, (TM-19, February 2007), ESA Publications, ESTEC;

[14] X. Sui, R. Zhang, F. Wu, Y. Li, X. Wan, *Sea surface height measuring using InSAR altimeter,* Geodesy and Geodynamics, Volume 8, Issue 4, 2017, Pages 278-284,

[15] G. Agnes, *ACT-10-0043 Precision Deployable mast for the Swot KARIN instrument*, October, 2014 (accessed 30.07.19);

[16] F. Angeletti, P. Gasbarri, M. Sabatini, P. Iannelli, *Design and performance assessment of a distributed vibration suppression system of a large flexible antenna during attitude manoeuvres*, Acta Astronautica, Volume 176, November 2020, Pages 542-557;

[17] Y. Cao, D. Cao, W. Huang, *Dynamic modeling and vibration control for a T-shaped bending and torsion structure*, International Journal of Mechanical Sciences 157–158 (2019) 773–786;

[18] Astro Aerospace, *AstroMesh™ deployable reflector data sheet DS-409 07/04*, Northrop Grumman Space Technology, 2004;

[19] F. Angeletti, P. Iannelli, P. Gasbarri, M. Sabatini, *Control-oriented modelling of an active suppression system for large space smart structures*, 71st International Astronautical Congress (IAC), Cyber Edition, October 12-14, 2020;

[20] S. Morterolle, B. Maurin, J.F. Dubé, J. Averseng, J. Quirant. *Modal behavior of a new large reflector conceptual design*, Aerospace Science and Technology, Elsevier, Vol. 42, pp.74-79, 2015;

Chapter 6
ADVANCED CONTROL STRATEGIES

*This chapter is devoted to design a general procedure to synthetize an integrated rigid/flexible control system, based on a **μ**-synthesis framework, for a large flexible spacecraft, once its flexible substructures are assembled and smart distributed actuators/sensors are placed on them, as indicated in the previous chapters. The resulting modelling and design strategy can be applied to a wide range of satellites equipping flexible appendages.*

The dynamics of in-orbit flexible structures is closely related to the behaviour of the platform they are connected to. Apart from standard control techniques, as Proportional-Derivative (PD), Proportional-Integral-Derivative (PID), also combined with filters to control a specific range of frequencies, advanced control techniques are currently researched to ensure pointing and maximum displacement requirements in case of coupled flexibility and rigid body motion. In this section, a general methodology used to address the problem of control design and synthesis, based on **μ**-synthesis, is presented to address the problem of vibration control for large spacecraft. In particular, the presence of a distributed active vibration control system is contemplated in the definition of the synthesis model to develop an integrated attitude/vibration controller.

6.1 ROBUST CONTROL

Robust control was introduced by Doyle and Glover [1], with the aim to design controllers that achieve a desired level of performance while coping with plant

uncertainties, disturbances and noise. In general, two types of problems can be identified [2]:

- Analysis problem: prove if the controller signal satisfies the desired performance over input disturbances, noise and model uncertainties;
- Synthesis problem: design a controller such that it automatically satisfies the required performance for the considered disturbance, noise and uncertainties.

In this chapter, the second problem will be tackled. In general, the objective of robust control of multivariable linear systems is to design a feedback controller that processes the measured variables and provides the control actions so that an appropriate metric of the transfer function from the exogenous signals to the error signals is minimized or made smaller than a prescribed value. In this thesis, an approach based on both loop-shaping and **μ**-synthesis is adopted to propose a general framework for deriving a robust controller for a flexible spacecraft.

6.1.1 LFT REPRESENTATION

When using robust control techniques, the unified framework under which the procedures are usually performed is called *Linear Fractional Transformation* (LFT). Indeed, a general feedback connection can be designed to include also uncertainties of the plant, as indicated in Fig. 6-1, where P is the generalized plant, K is the controller and Δ is the set of possible uncertainties.

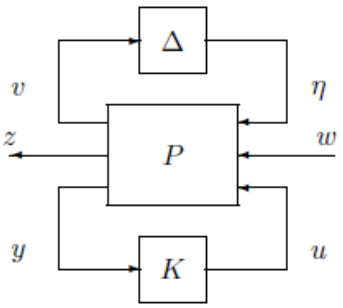

Fig. 6-1: LFT connections overview

The signals in the scheme can be described as: w includes noises, disturbances and reference signals, u is the controller output, y is the measurement, z includes the controlled signals and errors, η and υ define the connection between the matrix

P and the uncertainties block. The equation describing the interconnection is

$$\begin{bmatrix} \upsilon \\ z \\ y \end{bmatrix} = P \begin{bmatrix} \eta \\ \omega \\ u \end{bmatrix} \tag{6.1}$$

with $\eta = \Delta\upsilon$ and $u = Ky$. Then, the synthesis process reduces to find a controller such that closed loop is stable for all the admissible uncertainties Δ and the transfer matrix $T_{z\omega}$ from ω to z satisfies the relation

$$\|T_{z\omega}\|_\infty \le \gamma_p, \quad \gamma_p > 0 \tag{6.2}$$

where $\|T_{z\omega}\|_\infty$ is the H_∞ norm of the transfer function, which corresponds to minimize the norm of $T_{z\omega}$ according to the mission needs. An overview of the LFT generalized connection is presented in Fig. 6-2, where details on the exogenous signals w are reported, being d disturbances, r reference and n noise.

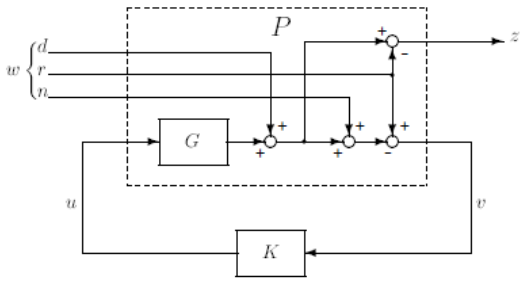

Fig. 6-2: Overview of the generalized connection (without uncertainties) [3]

To perform a loop shaping procedure, some definitions have to be made. In particular, an *input loop transfer matrix* L can be introduced as $\boldsymbol{L} = \boldsymbol{GK}$ to define the behaviour of the closed-loop system to specific inputs. Indeed, the *input sensitivity matrix* $\boldsymbol{S} = (\boldsymbol{I} + \boldsymbol{L})^{-1}$ is characterized as a good indicator of the closed-loop performance characteristics. When its magnitude is below 1 (i.e. $|S|<1$) then the disturbances are rejected, and the closed loop system is able to track the reference signals. In detail, the sensitivity function should be characterized by a low gain at low frequencies to ensure a good tracking performance and a moderate gain at high frequencies to limit the overshoot. Furthermore, an *input complementary sensitivity function* $\boldsymbol{T}$, specified as $\boldsymbol{T} = \boldsymbol{I} - \boldsymbol{S} = \boldsymbol{L}(\boldsymbol{I} + \boldsymbol{L})^{-1}$, is identified to study the system response to reference and sensor noise inputs. The frequency behaviour of the complementary sensitivity function generally has a gain near unity at low

frequencies for a good reference tracking and near zero at high frequencies to suppress the measurement noise effect. Finally, the *control signal transfer function*, defined as the transfer from the input signals to the generated command, is used to shape the frequency behaviour of the control signal in order to limit the control signal to guarantee compatibility with actuation capabilities (for example, to avoid actuator saturation due to bandwidth limitation).

6.2 General framework for Control Synthesis

In this section, the general procedure followed to carry out the synthesis process is presented. In detail, the procedure is performed in different steps:

1. *Derivation on an LFT representation of the dynamic system:* the model is reported in a form that is suitable to control synthesis by means of a general purpose Matlab code;

2. *Definition of requirements and weighting functions:* based on requirements to be respected, a set of weighting filters are derived in order to shape the dynamic behaviour of the controlled system;

3. *Construction of a multi-channel synthesis scheme*: following from the previous steps outcome, a synthesis scheme is built in Matlab/Simulink aimed at matching the feedback of a controller to be tuned, namely $K(s)$, with the corresponding inputs/outputs of the nominal system $G(s)$.

More details about each of the presented steps are reported in the next sections.

6.2.1 Automatic Assembly of an uncertain LFT plant

The derivation of a dynamic model tailored for an integrated GNC/vibration control architecture is an essential step in the control design process. Generally, in addition to the linearization of the plant (see Chapter 3), high-dimensional and complex structural models should be properly reduced, thus retaining the most representative properties to simulate the dynamic behaviour of the system.

Concerning flexible parts, only a subset of their flexible modes is included in the simplified model. The model reduction can be performed observing some properties of the system, as selecting the modes associated with higher modal effective mass or retaining the modes over a specified frequency range, being generally the low frequencies, which may interlap with the attitude control bandwidth. In addition, information regarding all the nodes of the structure is often not required, thus leading to the necessity of maintaining just some nodes (the NOIs presented in Par. 3.4.1).

In light of the above, a straightforward strategy to build a synthesis model taking into account such needs has been implemented, as illustrated in Fig. 6-3. In detail, a general-purpose code has been developed in Matlab as follows. The code is designed to read the results originated by modal analysis of flexible substructures (deriving from commercial suites, as MSC Nastran, or in-house codes) and to reconstruct an LFT form of the space-system model of the satellite, according to the control needs.

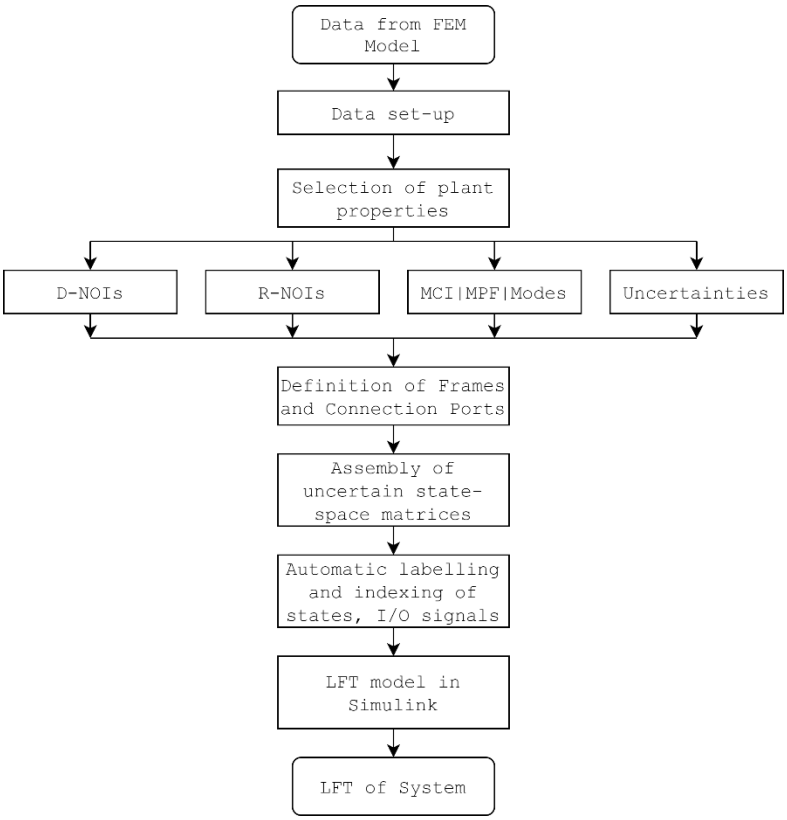

Fig. 6-3: Overview of automatic assembly code

By acquiring the structural outputs, the code reconstructs the mass, the damping

and the stiffness matrices of the analysed model. After the data set-up, the control designer is able to select the properties of the model, in particular the Nodes of Interest (NOIs) and the elastic modes related to each substructure to be considered in the dynamic equations. To this purpose, starting from data concerning flexible substructures or appendages of the spacecraft (as antennas and solar panels), the relevant matrices and vectors are built according to the mathematical formulation in Par. 3.2.2. Furthermore, the uncertain parameters of the model are defined and assigned to the relevant variables. Then, the rotation matrices and vector defining the orientation/position of attachment point and center of mass of the appendages are defined by referring to the input files. The creation of the assembled mass matrix is hence carried out by computing the total mass, inertia, and static moments of the system and by referring to the translational and rotational modal participation factors of each appendage. Consequently, the input and output matrix of the system as assembled as in Par. 3.3. Furthermore, the code is set to select the output channels after the assembling, so to have a higher flexibility in the design of the plant to be controlled.

To improve the traceability of I/O signals and of the states of the assembled system, automating naming rules and indexing have been added in the code, in order to assign specific labels to each state, input and output of the state-space model. Then, some preliminary dynamics assessments are performed, as the plot of pole-zero map of the system, the computation of the total inertia with respect to the satellite platform center of gravity G. Finally, the structure of the LFT model is reported in Fig. 6-4.

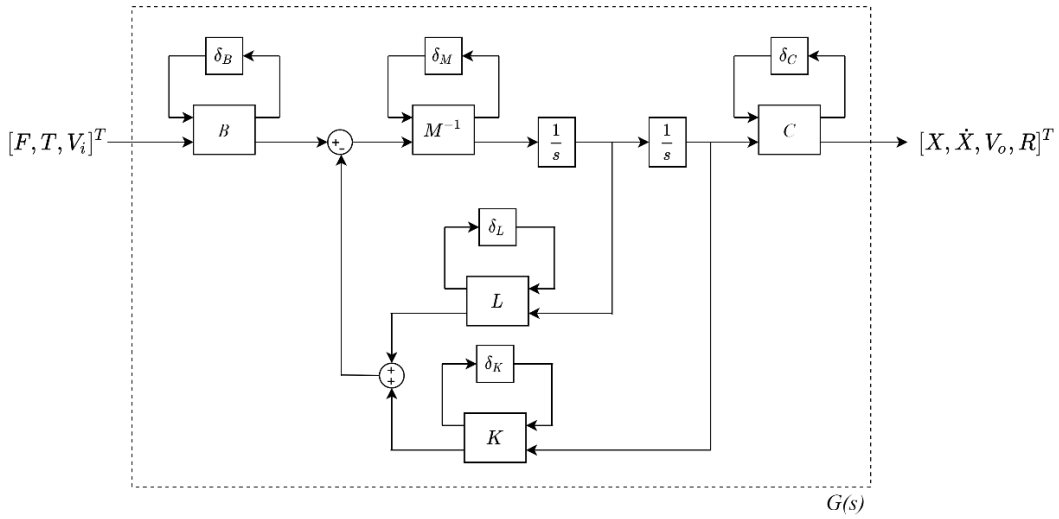

Fig. 6-4: LFT model of the uncertain flexible spacecraft

6.2.2 SYNTHESIS MODEL

In this thesis, an approach exploiting the advantages of both the loop-shaping method and the $\boldsymbol{\mu}$-synthesis strategy is applied to the problem of robust control design for a satellite equipped with flexible appendages. The control design can be assumed as a regulation problem, which implies the asymptotic tracking of prescribed reference signals and rejection of undesired disturbances [4]. Indeed, the synthesis procedure aims at compensating tracking errors due to uncertain dynamics and exogenous disturbances.

The control scheme map, in terms of plant input/output signals, is reported in Fig. 6-5. The correspondent mathematical formulation can be written as

$$\begin{bmatrix} \tilde{e} \\ \tilde{y} \\ \tilde{u} \end{bmatrix} = \begin{bmatrix} -\boldsymbol{N}_e\boldsymbol{S}\boldsymbol{G}\boldsymbol{N}_d & \boldsymbol{N}_e\boldsymbol{S}\boldsymbol{N}_r & -\boldsymbol{N}_e\boldsymbol{S}\boldsymbol{N}_n \\ \boldsymbol{N}_y\boldsymbol{S}\boldsymbol{G}\boldsymbol{N}_d & \boldsymbol{N}_e\boldsymbol{T}\boldsymbol{N}_r & -\boldsymbol{N}_y\boldsymbol{T}\boldsymbol{N}_n \\ -\boldsymbol{N}_u\boldsymbol{T}_0\boldsymbol{N}_d & \boldsymbol{N}_u\boldsymbol{S}_0\boldsymbol{K}\boldsymbol{N}_r & -\boldsymbol{N}_u\boldsymbol{S}_0\boldsymbol{K}\boldsymbol{N}_n \end{bmatrix} \begin{bmatrix} \tilde{d} \\ \tilde{r} \\ \tilde{n} \end{bmatrix} = \boldsymbol{M} \begin{bmatrix} \tilde{d} \\ \tilde{r} \\ \tilde{n} \end{bmatrix} \tag{6.3}$$

$$\begin{bmatrix} z_1 \\ z_2 \\ z_3 \end{bmatrix} = \begin{bmatrix} \boldsymbol{W}_S & 0 & 0 \\ 0 & \boldsymbol{W}_T & 0 \\ 0 & 0 & \boldsymbol{W}_U \end{bmatrix} \begin{bmatrix} \tilde{e} \\ \tilde{y} \\ \tilde{u} \end{bmatrix} = \boldsymbol{W} \begin{bmatrix} \tilde{e} \\ \tilde{y} \\ \tilde{u} \end{bmatrix} \tag{6.4}$$

where $\tilde{d}$ is the normalized external disturbances signal (generalized forces), $\tilde{r}$ is the normalized reference signal (including position, velocity, attitude, angular rate and references for the vibration control system), $\tilde{n}$ is the normalized measurement noise (in terms of position, velocity, attitude, rate and distributed control system). The outputs of the system are the normalized tracking error $\tilde{e}$ signal, $\tilde{y}$ the normalized output of the system and the normalized control signals $\tilde{u}$ (i.e. forces, torques and active vibration control commands). Indeed, by normalizing the input and the output of the closed loop, they are made independent from both magnitude and time units, so to guarantee a wide range of applicability. The variables z_1, z_2, z_3 are the performance outputs. The other terms in eq. (6.3) are filters used to carry out the loop shaping. In detail, they can be listed as

- The terms $\boldsymbol{G}, \boldsymbol{K}$ represent the dynamic system plant and the controller;
- Filters are introduced to identify the maximum expected behaviour, both in terms of magnitude and frequency, of the characteristics variable of the system: $\boldsymbol{N}_d$, $\boldsymbol{N}_r$ and $\boldsymbol{N}_n$ are the terms used to normalize the input signals, while $\boldsymbol{N}_y$, $\boldsymbol{N}_u$ and $\boldsymbol{N}_e$ are used for the output signals respectively;

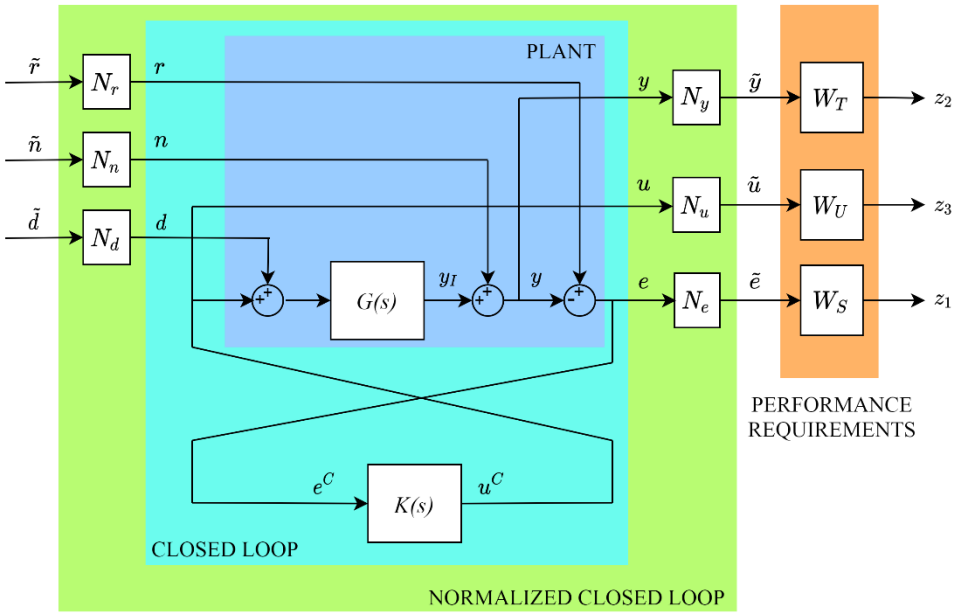

Fig. 6-5: Control synthesis scheme

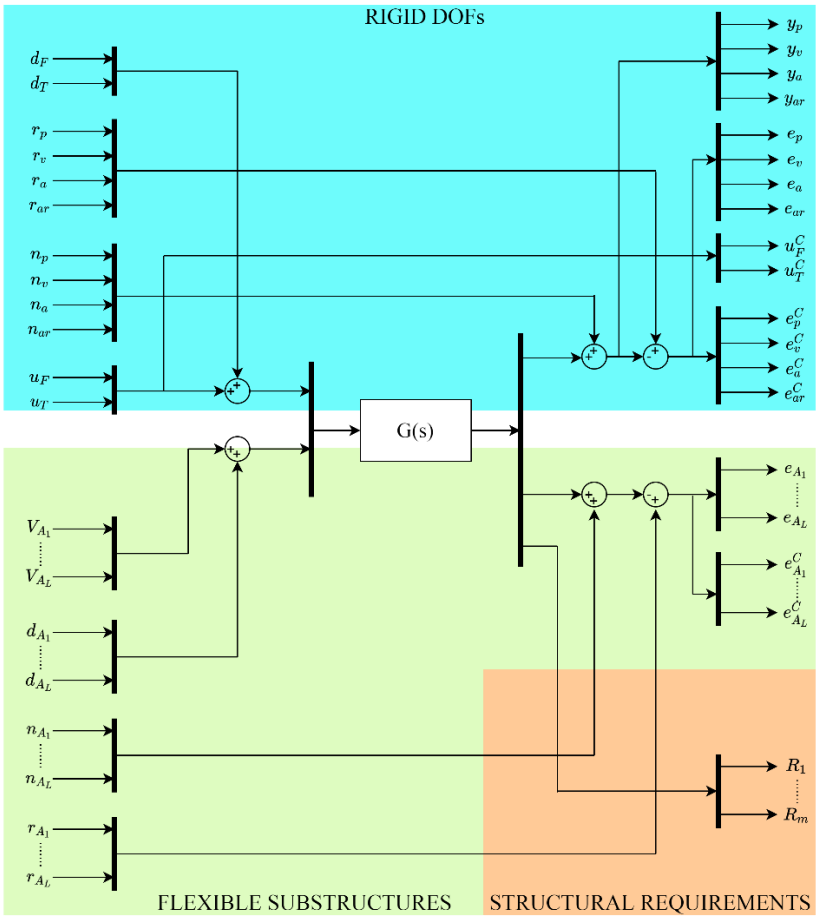

Fig. 6-6: I/O channels map of the Plant for synthetizing the integrated rigid/flexible controller

- The weighting functions $\boldsymbol{W}_S$, $\boldsymbol{W}_T$ and $\boldsymbol{W}_U$ define the requirements to be met at the end of the control design process, by shaping the sensitivity, the complementary sensitivity and the control signal sensitivity functions.

The closed loop is expanded in Fig. 6-6 to better illustrate the map of the control Input/Output channels. In particular, three zones can be identified: the I/O channels related to the rigid degrees of freedom (in blue), the ones referred to the flexible substructures (in green) and some structural requirements (in orange, as maximum displacements in specific nodes of the flexible structure).

6.2.3 MODEL TAILORING AND REQUIREMENTS DEFINITION

According to the specific study case, the map reported in Fig. 6-6 can be tailored by selecting only specific I/O channels. In this thesis, to test the synthesis process, as no orbital manoeuvre is to be performed, the input of the plants is retained as three-axis torque produced by the platform control system of the spacecraft and piezoelectric voltages, but the approach can be easily modulated for future analysis to include also the derivation of input forces. The outputs of the system are consequently reduced to the three-axis attitude, rate, output voltages from the piezoelectric sensors and information related to the specified requirements to be met (in this case, the displacement of some Nodes of Interest). The latter are auxiliary output channels to be constrained in order to fulfil the imposed requirements.

Now, some details will be given about the implementation of the filters and the weighting functions in the model closed loop. The filter $\boldsymbol{N}_d$ can be defined as a diagonal matrix with

$$\begin{cases} \boldsymbol{N}_d(s)_{ii} = H_i \\ \boldsymbol{N}_d(s)_{ij} = 0, \quad i \neq j \end{cases} \tag{6.5}$$

where $H_i = 0.01 Nm, i = 1,..,3$ is the maximum estimated value of the disturbance torque affecting the spacecraft. The filter $\boldsymbol{N}_n$ is used to characterize the measurement noise level as a power spectral density function. Therefore, it can be represented as a first-order transfer function as

$$\begin{cases} \boldsymbol{N}_d(s)_{ii} = \dfrac{\sigma\sqrt{\dfrac{\pi}{\omega_n}}}{\dfrac{s}{\omega_n}+1} \\ \boldsymbol{N}_d(s)_{ij} = 0, \quad i \neq j \end{cases} \tag{6.6}$$

where $\sigma = 10^{-3}$ is the noise standard deviation and $\omega_n = 0.3 rad/s$ is a characterizing frequency, usually equal to half the sampling measurement frequency. The filter $\boldsymbol{N}_r$ is used to specify the maximum expected change of the input signal to control. It can be defined analogously to the $\boldsymbol{N}_d$ filter as

$$\begin{cases} \boldsymbol{N}_r(s)_{ii} = N_i \\ \boldsymbol{N}_r(s)_{ij} = 0, \quad i \neq j \end{cases} \tag{6.7}$$

where $N_i, i = 1,..,3$ is the value of the input signal. Accordingly, the filters for the outputs of the system can be defined as

$$\begin{cases} \boldsymbol{N}_e(s)_{ii} = N_e \\ \boldsymbol{N}_e(s)_{ij} = 0, \quad i \neq j \end{cases} \tag{6.8}$$

$$\begin{cases} \boldsymbol{N}_u(s)_{ii} = H_{ui}^{-1} \\ \boldsymbol{N}_u(s)_{ij} = 0, \quad i \neq j \end{cases} \tag{6.9}$$

where $H_{ui}, i = 1,...,3$ is the maximum command level of the *i*-th channel. Finally, the filter weighting the control error is assumed to be equal to the one referring to the signals to be controlled

$$\boldsymbol{N}_y(s) = \boldsymbol{N}_e(s) \tag{6.10}$$

In addition, some weighting functions have been introduced to ensure the loop-shaping technique satisfies the considered requirements. There is not a general rule on how to set such functions. However, some guidelines may be found in [3]. The objective is to find a controller stabilizing the closed-loop system and minimizing the $\boldsymbol{H}_\infty$-norm of the Input/Output map, which corresponds to

$$\left\|\boldsymbol{W}(j\omega)\boldsymbol{M}(j\omega)\right\| < \gamma, \forall\omega \;\Leftrightarrow\; \left\|\boldsymbol{W}(j\omega)\right\| < \gamma\left\|\boldsymbol{M}(j\omega)^{-1}\right\|, \forall\omega, \quad \gamma < 1 \tag{6.11}$$

which means the weighting functions are used to represent the inverse of the desired frequency behaviour for the correspondent transfer function to be shaped, and can be defined as

$$\boldsymbol{W}_S^{\,ii}(s)=\left(\frac{\dfrac{s}{\sqrt[n_i]{M_S^{\,i}}}+\omega_S^{\,i}}{s+\omega_S^{\,i}\sqrt[n_i]{A_S^{\,i}}}\right)^{n_i},\qquad \boldsymbol{W}_T^{\,ii}(s)=\left(\frac{s+\omega_T^{\,i}\sqrt[n_i]{A_T^{\,i}}}{\dfrac{s}{\sqrt[n_i]{M_T^{\,i}}}+\omega_T^{\,i}}\right)^{n_i} \tag{6.12}$$

$$\boldsymbol{W}_U^{\,ii}(s)=\left(\frac{\dfrac{s}{\sqrt[n_i]{M_U^{\,i}}}+\omega_U^{\,i}}{\dfrac{s}{\sqrt[n_i]{A_U^{\,i}}}+\omega_U^{\,i}}\right)^{n_i} \tag{6.13}$$

where the parameters $M^i_{S,T,U}, A^i_{S,T,U}, \omega^i_{S,T,U}$ are parameters to be properly selected to the required closed loop behaviour. In particular, the weight $\boldsymbol{W}_S$, by shaping the sensitivity function, allows to define the following requirements:

- A minimum bandwidth of the closed loop system to satisfy minimum rise time requirements $(\omega_{cl} > \omega_S)$;
- A desired maximum overshoot of the response (generally below 30%) by constraining accordingly a value of the maximum peak of the sensitivity function via M_S. This parameter can be defined as

$$M_S = \|S\|_\infty = \|S(j\omega_{\max})\| = \frac{\alpha\sqrt{\alpha^2+4\xi^2}}{\sqrt{\left(1+\alpha^2\right)^2+4\xi^2\alpha^2}} \tag{6.14}$$

  where $\alpha=\sqrt{0.5+0.5\sqrt{1+8\xi^2}}$ and $\omega_{\max}=\alpha\omega_n$. In general, a typical value for M_S is 2 and $\xi \approx 0.3$
- Some desired steady state tracking error performance by constraining the lower frequency gain of the sensitivity function under A_S, where such a parameter is chosen to be equal to the ratio between the maximum steady state tracking error e_s and the maximum change of the signal to be controlled e_r

$$A_S = \frac{e_s}{e_r} \tag{6.15}$$

A similar reasoning is applied to select parameters for shaping the complementary sensitivity function through the weighting function $\boldsymbol{W}_T$, which is an indicator of the system response to reference and sensor noise inputs, and the weighting function $\boldsymbol{W}_U$, which is designed to shape the frequency behaviour of the control signal in order to limit the control signal to guarantee compatibility

with actuation capabilities (for example, to avoid actuator saturation due to bandwidth limitation).

6.3 SYNTHESIS PROCESS AND RESULTS

In this thesis, the $\boldsymbol{\mu}$-synthesis approach is chosen to carry out the synthesis process of a controller for a test-case uncertain model, representing a spacecraft equipped with a flexible appendage and a distributed vibration control system. In detail, such a method refers to the metrics $\boldsymbol{\mu}$, which is defined as the structured singular value of the transfer function from the exogenous signals to the error signals [2][3]. This procedure allows to consider structured uncertainties in the plant, which can represent both parametric uncertainties (as mass, inertia, frequencies, etc) and uncertain transfer function. Therefore, in general, designing a controller with a $\boldsymbol{\mu}$-synthesis approach guarantees higher performance than using a $\boldsymbol{H}_\infty$ controller (not considering the uncertainties) and then carry on a posteriori worst-case analysis (as a Monte Carlo) to assess the behaviour of the controller when uncertain parameters are considered. Two possible drawbacks are: it is more difficult with $\boldsymbol{\mu}$-synthesis to define the structure of the controller and the global convergence of the algorithm may not be guaranteed (but it provides satisfactory performance in practice, may converge to a local optimum and represents the state of the art of controllers for uncertain plants).

By assuming that the block Δ (representing the uncertainties of the system) is diagonal and belonging to the set

$$\Delta = \left\{ diag\left(\delta_1 \boldsymbol{I}_1, ..., \delta_n \boldsymbol{I}_n, \Delta_1, ..., \Delta_n\right) : \delta_i \in C, \Delta_j \in C^{mj \times mj} \right\} \tag{6.16}$$

with perturbation $\sigma(\Delta) \le 1$, then, given a matrix $\boldsymbol{M} \in C^{n \times n}$, the structured singular value can be defined as

$$\mu(\boldsymbol{M}) = \frac{1}{\min\left(\sigma(\Delta) : \Delta \in \bar{\Delta}, \det\left(I + \boldsymbol{M}\Delta\right) = 0\right)} \tag{6.17}$$

which means, $\mu(\boldsymbol{M})$ is the inverse of the smallest perturbation among all possible $\Delta \in \bar{\Delta}$. Therefore, the synthesis problem to be solved implies to find a controller $\boldsymbol{K}$ such that it minimizes the quantity

$$\inf_{K} \sup_{\omega} \mu\left(F_l\left(\boldsymbol{P},\boldsymbol{K}\right)\right) \tag{6.18}$$

where $F_l\left(\boldsymbol{P},\boldsymbol{K}\right)$ is the lower LFT of the closed loop of the generalized plant with the controller. In general, such problem has no analytical solution by directly optimizing $\boldsymbol{\mu}$. However, a solution can be found in an iterative way if $\boldsymbol{\mu}$ is replaced by its upper bound. The most common synthesis algorithm is the D-K Iteration, implementing a sequence of minimizations, and it is the method used in this thesis. Such a strategy includes two minimization: the first is performed as dynamic scaling (the so-called D-step), while the second one involves the controller (the K-step).

6.3.1 STUDY CASE

The developed synthesis framework is here applied to the case of a spacecraft hosting a flexible mesh reflector. In particular, an overview of the studied model is presented in Fig. 6-7, where the payload is the same as presented in Par. 5.6.2. The properties of the platform are presented in Table 6-1.

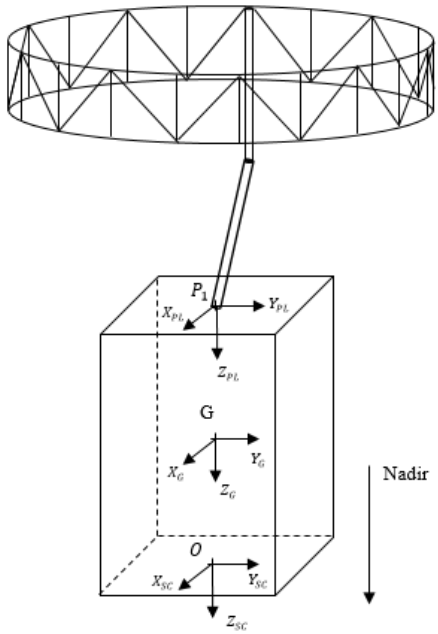

Fig. 6-7: Spacecraft model overview

Table 6-1: Platform Data

Properties		Platform					
Inertia properties							
Mass (kg)				1200			
Inertia wrt CoG (kg m²)		Ixx	Iyy	Izz	Ixy	Ixz	Iyz
		903.6	985.2	885.6	2	4	-7
CoG (m) (wrt S/C frame)				[0 ; 0 ; -2]			
Dimensions							
Width (m)				2			
Length (m)				2			
Height (m)				3			

In this analysis, the requirements matrix $\boldsymbol{W}$ is a 4×4 matrix as follows

- $\boldsymbol{W_S}^{(11)}$: X-axis spacecraft attitude constraint, defined as in eq. (6.12);
- $\boldsymbol{W_S}^{(22)}$: X-axis spacecraft attitude constraint, defined as in eq. (6.12);
- $\boldsymbol{W_S}^{(33)}$: X-axis spacecraft attitude constraint, defined as in eq. (6.12);
- $\boldsymbol{W_S}^{(44)}$: displacement of the tip of the antenna constraint, defined as a constant value to limit the displacement in all the bandwidth of interest, so to limit the peak of the displacement de facto.

Generally, some requirements can be defined in space missions concerning the Absolute Pointing Error (APE), which is the error between the commanded attitude and the actual one. In this thesis, a maximum APE < 0.05° is assumed to tune the parameters of the weighting functions. Also, a trade-off between the maximum overshoot for the spacecraft attitude rotation (expressed in terms of Euler's angles, to be below 30%) and the bandwidth of the manoeuvre (set to have a fast re-orientation) is carried out. The correspondent values of the sensitivity and complementary sensitivity functions are reported in Table 6-2.

Table 6-2: Requirements: Sensitivity and Complementary Sensitivity functions

		$\boldsymbol{A_S}$	$\boldsymbol{M_S}$	$\boldsymbol{\omega_S}$	$\boldsymbol{A_T}$	$\boldsymbol{M_T}$	$\boldsymbol{\omega_T}$
Spacecraft Rotation	X_B	0.01	2	0.02	0.5	200	0.4
	Y_B	0.01	2	0.02	0.5	200	0.4
	Z_B	0.01	2	0.02	0.5	200	0.4
Displacement	$\max(x_{TIP})$		0.005 m				

The parameters concerning the weighting functions to regulate the frequency behaviour of the control signal are listed in Table 6-3, set in a way the maximum

command does not exceed 50 Nm for the torques and 150V for the piezoelectric actuators (which is a limit generally found for commercially available stack actuators suitable also for space applications). Indeed, after a trade-off on different market options, a NOLIAC NAC2015-H100 type of stack actuator has been selected for this analysis.

Table 6-3: Requirements – Control signal transfer function (attitude and vibration)

		A_T	M_T	ω_T			A_P	M_P	ω_P
Spacecraft Rotation	X_B	60	20	10	Piezoelectric devices	1	100	15	15
	Y_B	60	20	10		2	100	15	15
	Z_B	60	20	10		3	100	15	15
						4	100	15	15
						5	100	15	15

Table 6-4: Uncertainties

	Uncertainty
Mass	3% of nominal value
Inertia	f(Mass)
Natural Frequencies (single appendage)	3% of nominal value
Piezo properties	8% of nominal value

The uncertainties considered in this study concerns both the inertial properties and frequencies of the model and the electro-mechanical properties of the piezoelectric devices. The selected values are reported in Table 6-4.

6.3.1.1 SYNTHESIS RESULTS

Once the synthesis framework and all the relevant parameters have been set according to the specific application, a D-K iterative algorithm can be adopted to find a local optimal solution to the problem of synthetizing a stable and robust controller. In this thesis, the Robust Control Toolbox [5] released in Matlab 2019b environment – state of the art for solving robust control problems also for space applications – has been used. In detail, Fig. 6-8 to Fig. 6-11 show the singular values of the sensitivity function (both referred to attitude and tip displacement of the payload constraints), the complementary sensitivity function and the control signal transfer function for the scaled closed loop system compared with the inverse of the corresponding weighting functions.

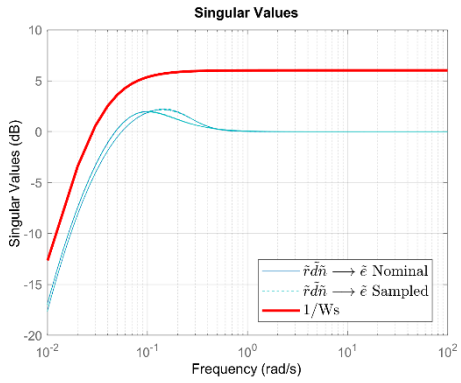

Fig. 6-8: Singular values of the sensitivity function $\tilde{r}\tilde{d}\tilde{n} \rightarrow \tilde{e}$ (attitude)

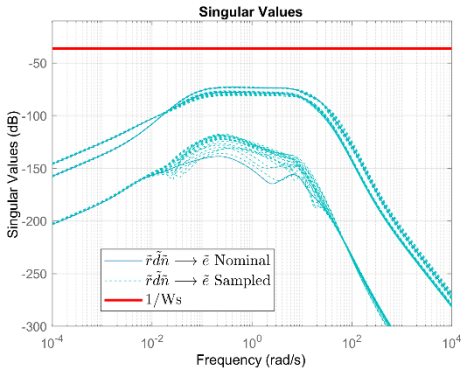

Fig. 6-9: Singular values of the sensitivity function $\tilde{r}\tilde{d}\tilde{n} \rightarrow \tilde{e}$ (displacement)

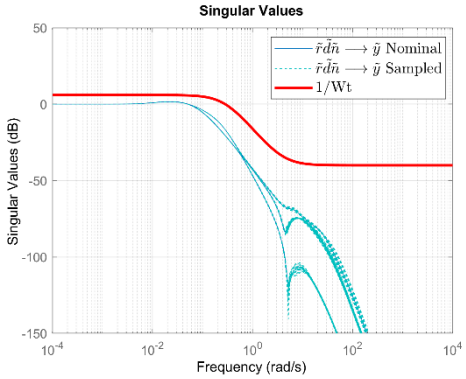

Fig. 6-10: Singular values of the complementary sensitivity function $\tilde{r}\tilde{d}\tilde{n} \rightarrow \tilde{y}$

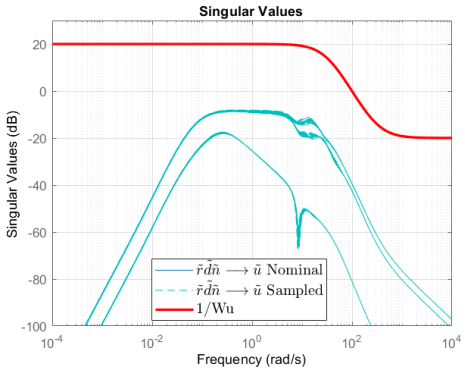

Fig. 6-11: Singular values of the control sensitivity function $\tilde{r}\tilde{d}\tilde{n} \rightarrow \tilde{u}$

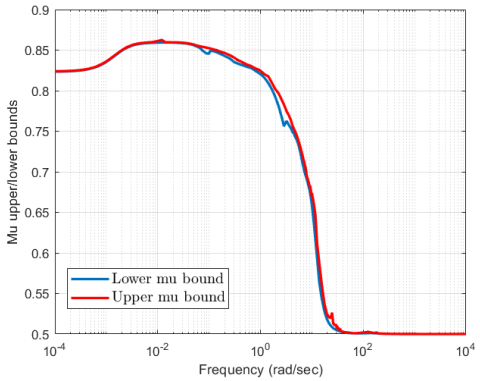

Fig. 6-12: Robust performance margins (mu upper and lower bounds)

Fig. 6-12 reports the upper and lower bounds on the structural singular value for the attitude controller obtained via μ-synthesis. It is shown that the system satisfies the performance requirements with a sufficient margin of value 0.863 obtained at a frequency of 0.013 rad/s. The controller is synthetized considering the first four modes of the spacecraft, which correspond to a bandwidth of interest of [0, 3] Hz.

6.3.1.2 SIMULATIONS: NON-LINEAR SPACECRAFT DYNAMICS

In this section, the controller is implemented in a spacecraft non-linear dynamics simulator. In detail, both a single pitch-axis manoeuvre and a three-axis manoeuvre have been performed. Despite the fact the controller was synthetized on four modes, the simulator was set-up considering up to ten modes (by neglecting the ones with modal effective mass lower than 3%). The trend of Euler's angles is depicted in Fig. 6-13 in case of a single axis rotation.

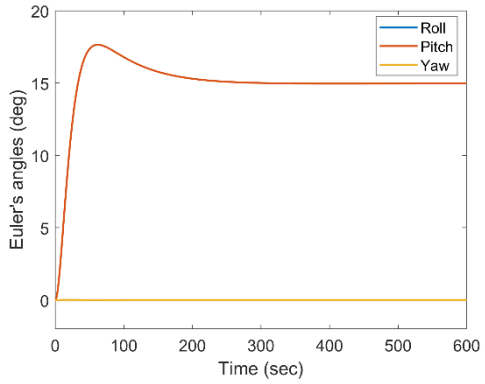

Fig. 6-13: Euler's angles

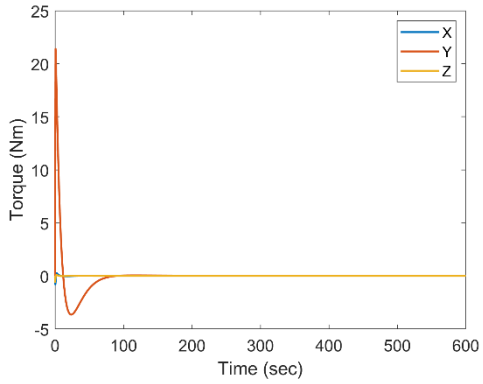

Fig. 6-14: Input torques

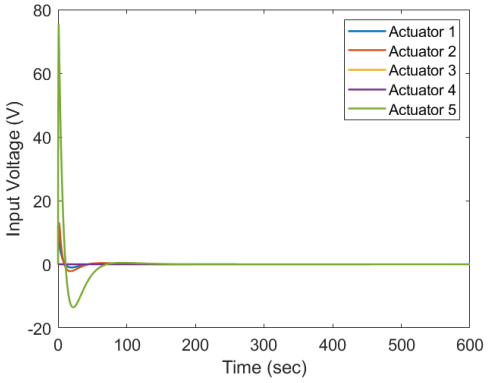

Fig. 6-15: Input voltages

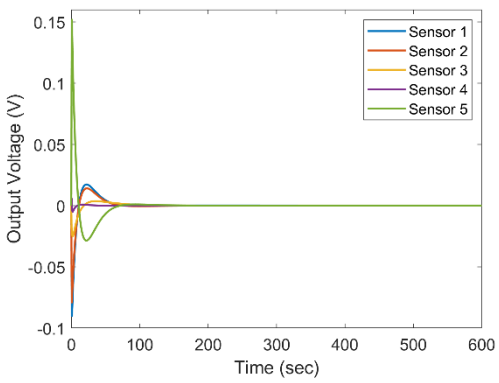

Fig. 6-16: Output voltages

An overshoot lower than the 30% of the desired angle can be noticed, thus

satisfying the imposed requirements. The constraint on maximum steady state error is respected too, being equal to 0.01 e_M at about 400 seconds, where e_M is the maximum expected error with respect to the reference. The commanded torques are illustrated in Fig. 6-14. The maximum torque is below the saturation constraint imposed to the robust controller during the synthesis process. Furthermore, both the results from sensing and actuation by using smart piezoelectric actuators and sensors are portrayed in Fig. 6-15 and Fig. 6-16. The values of voltages required to perform vibration suppression are both in the admissible range.

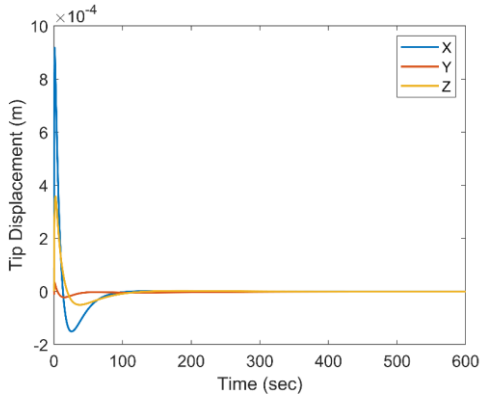

Fig. 6-17: Tip displacement

In Fig. 6-17, the displacement of the tip of the antenna with respect to time is reported. The vibration system ensures the maximum displacement is under the imposed constraint, thus being suitable to perform precision pointing operations.

Furthermore, the controller has been tested with a general three-axis manoeuvre, being the desired final angles equal to $[\varphi,\theta,\psi]=[10,15,15]\text{deg}$.

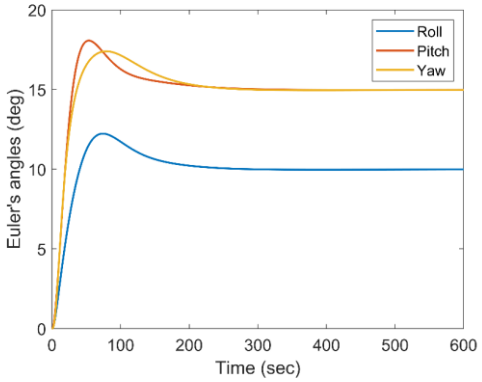

Fig. 6-18: Euler's angles

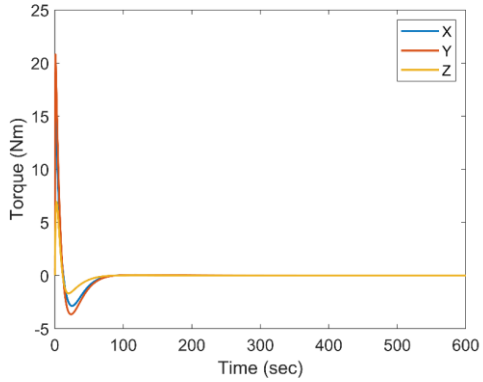

Fig. 6-19: Input torques

The time histories of the Euler's angles are reported in Fig. 6-18, while the commanded torques in Fig. 6-19. Both the outputs satisfy the imposed requirements. In Fig. 6-20 and Fig. 6-21, the actuated and sensed voltages as reported. Finally, the tip displacement is reported in Fig. 6-22.

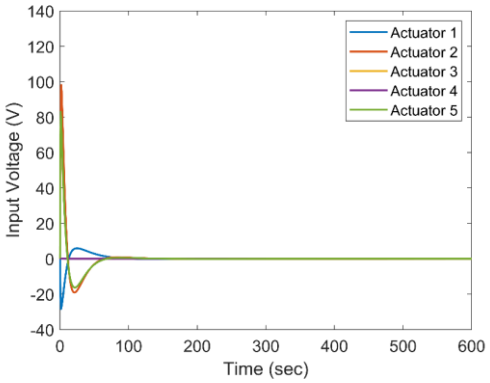

Fig. 6-20: Input voltages

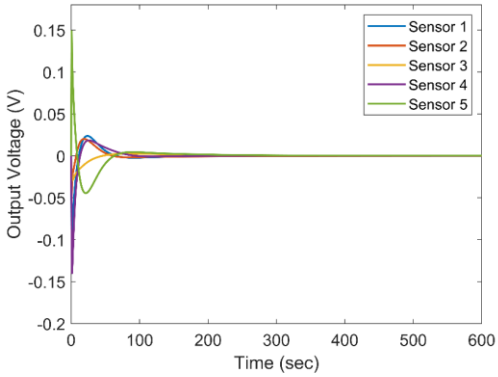

Fig. 6-21: Output voltages

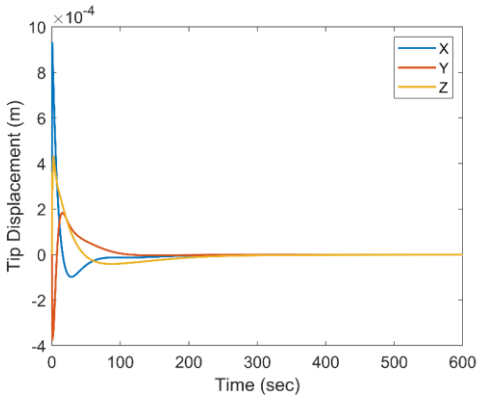

Fig. 6-22: Tip displacement

To conclude, the control system proved to be able to reach the desired set-point angles by keeping the maximum displacement of the tip of the reflector under the imposed constraint.

6.4 CONCLUSIONS

In this chapter, the synthesis of a robust unstructured controller for performing an integrated attitude and vibration control for a flexible spacecraft,

based on μ-synthesis metrics, is presented. The satellite synthesis model has been assembled by using the formulation introduced in Chapter 3, by using the data extracted from a commercial finite element suite (MSC Nastran), being the plant of the system considered uncertain. As this chapter is not devoted to the co-design of the system (in terms of modifying the parameters of both structure and control to reach an optimized space project, see Par. 2.2.3), but it is focussed on the synthesis of a controller for a spacecraft in an advanced design phase, the considered uncertainties are set only to represent possible changes in the inertial and piezoelectric properties after launch and in the orbital environment (assuming the distributed devices have been through a characterization/calibration process before launching). The results of the iterative process via D-K algorithm are presented and discussed and the synthetized controlled tested on a plant considering also the dynamic non-linear terms reported in eq. (3.69). The control system proved to be able to reach the desired set-point angles by satisfying the considered requirements concerning overshoot, steady-state error and maximum tip displacement. It should be noticed that, for simulation purposes, the controller was also sampled with a period of 0.1s, thus making the control law suitable for implementation on most modern satellites on-board computers. As future developments, the effect of more specific external disturbances (other than the system non-linearities) could be considered in the study, as well as the impact of the failures of some piezoelectric devices could be tested to verify the system efficacy in case of damages.

BIBLIOGRAPHY

[1] K. Glover and J. Doyle, *State-space formulae for all stabilizing controllers that satisfy an H∞-norm bound and relations to risk sensitivity*, Systems and Control Letters, vol. 11, pp. 167-172, 1988;

[2] K. Zhou, J. C. Doyle, *Essentials of Robust Control*, Prentice Hall, 1997.

[3] S. Skogestad, I. Ian Postlethwaite, *Multivariable Feedback Control: Analysis and Design*, 2nd Edition, Wiley, Nov. 2005;

[4] C. Scherer, *Theory of Robust Control*, Mechanical Engineering Systems and Control Group, Delft University of Technology, The Netherlands, April 2001.

[5] G. Balas, R. Chiang, A. Packard, M. Safonov, *Robust Control Toolbox™ User's Guide*, The MathWorks, Inc., Sept. 2020;

Chapter 7

IN-ORBIT FLEXIBLE SPACECRAFT SIMULATOR

In this chapter, a non-linear in-orbit simulator for a spacecraft equipped with flexible appendages based on the equations presented in Chapter 3 is presented. The tool is implemented in Simulink environment, to manage more easily the different blocks describing the dynamics of the system, including actuators and sensors both at platform and distributed level. Finally, simulations of spacecraft performing attitude manoeuvres with an enabled active vibration control are presented.

In this section, a tridimensional non-linear fully-coupled simulator for a flexible spacecraft, realized in MATLAB/SIMULINK environment, is introduced. The main purpose is to carry out dynamics simulations aiming at testing a distributed vibration control designed based on the placement results presented in Chapter 5. In detail, the equations describing the in-orbit spacecraft dynamics reported in Par. 3.2.2 are implemented in the simulator. The purpose of the tool is to allow for easily yet efficiently performing analysis of satellite behaviour and having a baseline for the implementation of future integrated advanced control techniques.

7.1 NON-LINEAR IN-ORBIT SIMULATOR

In this section, an overview of the proposed controller is presented. The simulator can be described according to different levels:

- *First-level blocks*, which comprehend the main areas of the dynamic system to be simulated;

- *Second-level blocks*, which implement equations presented in Par. 3.2.2;
- *Third-level block and utilities*, as in-house auxiliary functions and blocks.

The *first-level blocks* collect the secondary blocks used to perform the simulations of the dynamic system, as depicted in Fig. 7-1. In detail, the block *Dynamics & Environment* implements the non–linear equations describing the dynamics of a spacecraft composed of different flexible appendages in orbital environment (i.e. subjected to gravitational forces and torques). The output of such block - in terms of quaternion, angular rate and sensed charge on the piezoelectric electrodes - are fed to the *Sensors* block, where models of the selected sensors are implemented (see Par. 7.2.1.2 and Par. 7.2.2.2). The measured variables are then inputted into the *Control* block, which is used to compute the generalized forces and voltages to perform control at both platform and distributed structural level. Moreover, it is also used to produce a signal giving information on the operative mode of the actuators: two modes are considered in case of coarse or fine pointing. The block *Orbit Propagation* has a two-fold aim: it is demanded both to the propagation of the orbit given the position of the spacecraft and to the computation of the orientation matrices in the LVLH and Orbital reference frames, given the attitude of the satellite.

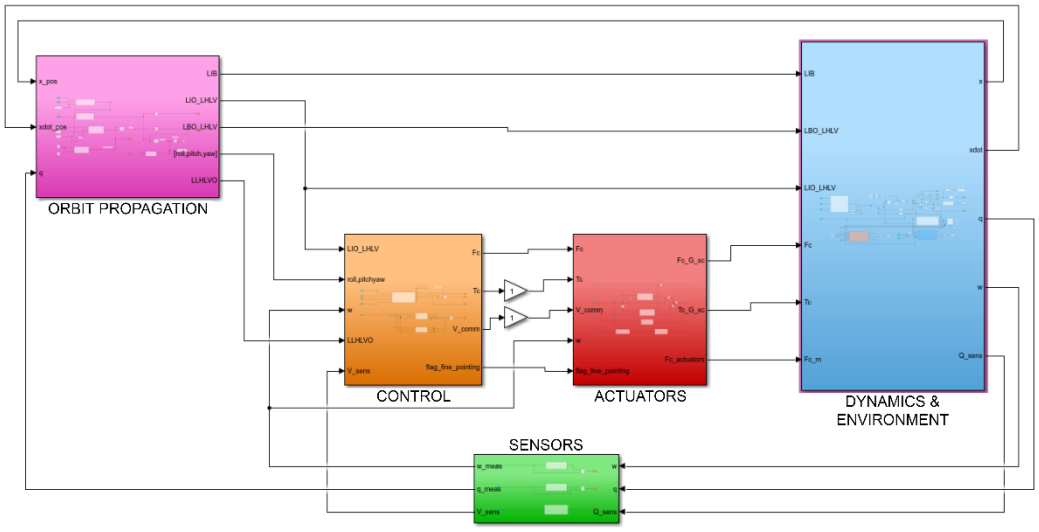

Fig. 7-1: First-level blocks overview (SIMULINK)

It should be noticed no GPS sensor is assumed in this work, as it is not the aim of the study to reproduce a high-fidelity orbit propagation algorithm, assumed that the simulated manoeuvres duration will be neglectable if compared to the orbital

period. Finally, the *Actuators* block implements the models of actuators at both platform and distributed control levels (see Par. 7.2.1.1 and 7.2.2.1).

Concerning the second-level blocks, an insight on the Dynamics & Environment unit is presented in Fig. 7-2. The spacecraft mass matrix is assembled in Simulink based on the data provided by the finite element analysis (see Chapter 3). The sub-blocks *Gravitational Forces* and *Non-linear Terms* simulate the non-linear behaviour of a flexible spacecraft subjected to the gravitational Earth field. The *B Matrix* block acts as a mapping matrix, distributing the applied forces, torques and piezoelectric contribution on the platform and on the flexible appendages.

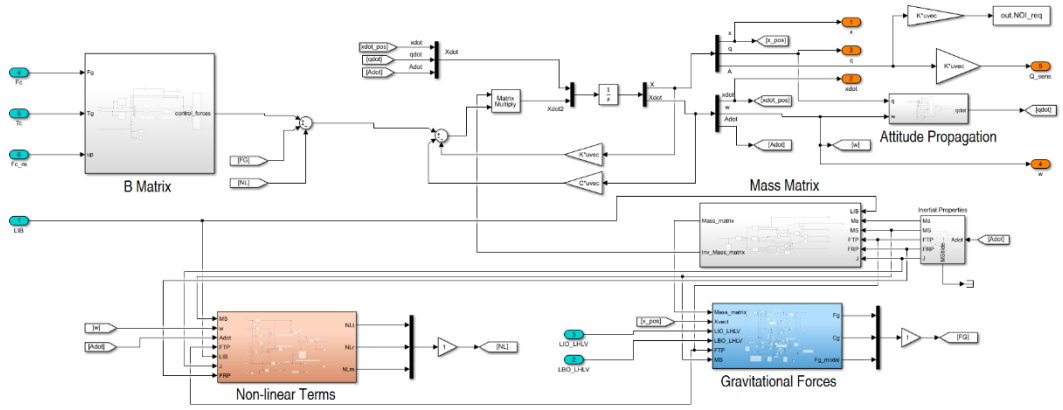

Fig. 7-2: Dynamics & Environment overview

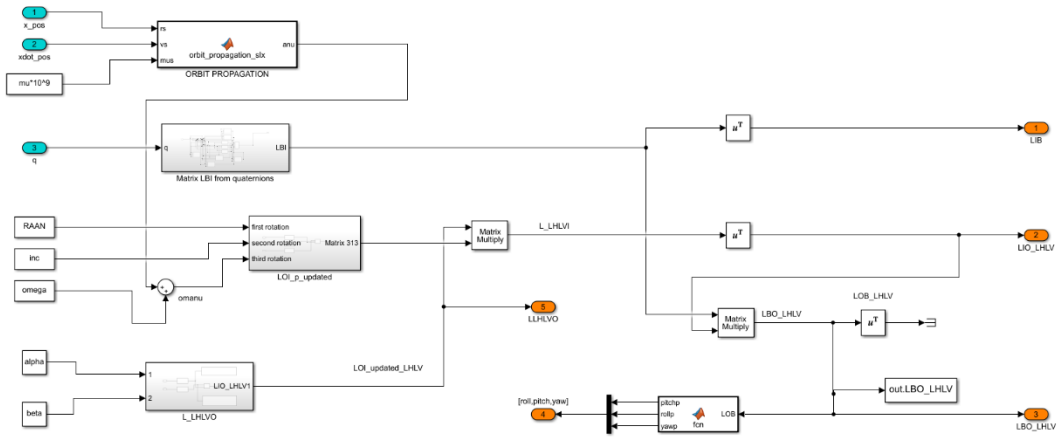

Fig. 7-3: Orbit Propagation overview

The *Orbit Propagation* block computes the evolution of the true anomaly based on the integration of Kepler's orbital equations, given the position and velocity of the spacecraft along the orbit (see Fig. 7-3). Such an information is used to retrace the

matrix $\boldsymbol{T}_{LORF\leftarrow I}(\Omega,\mathrm{i},\varpi)$ describing the attitude in the Local Orbital Reference Frame (LORF), as illustrated in Chapter 3. Also, by using the quaternion denoting the attitude of the body system with respect to the inertial reference frame, the matrix $\boldsymbol{T}_{B\leftarrow LVLH}(\phi,\theta,\varphi)$ - describing the attitude of the body with respect to the Local Vertical Local Horizon (LVLH) frame - is computed and the related Euler's angles derived. Then, the *Control* blocks implements the strategy to define the correspondent attitude and angular rate error, while computing the generalized forces required to perform the manoeuvre.

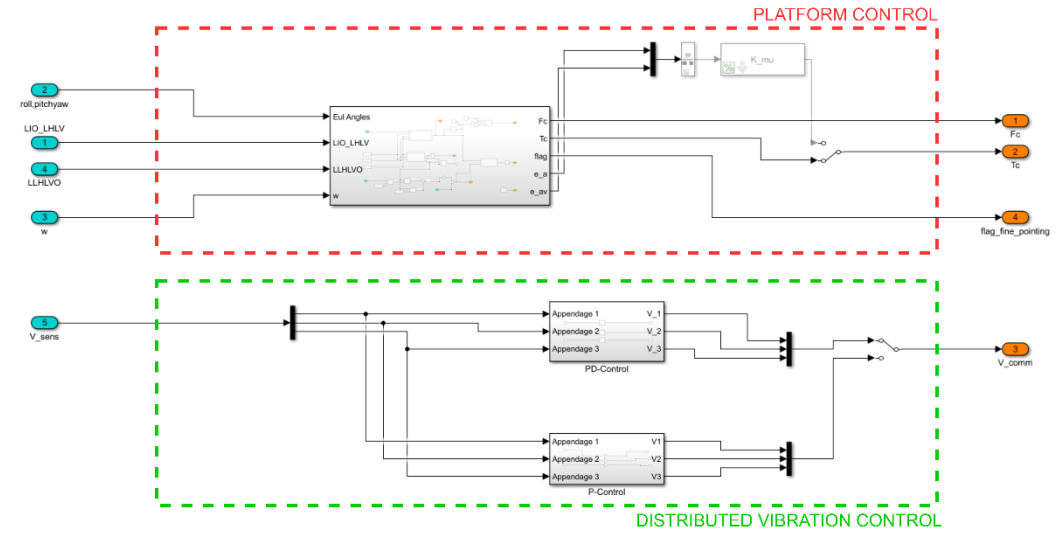

Fig. 7-4: Control overview

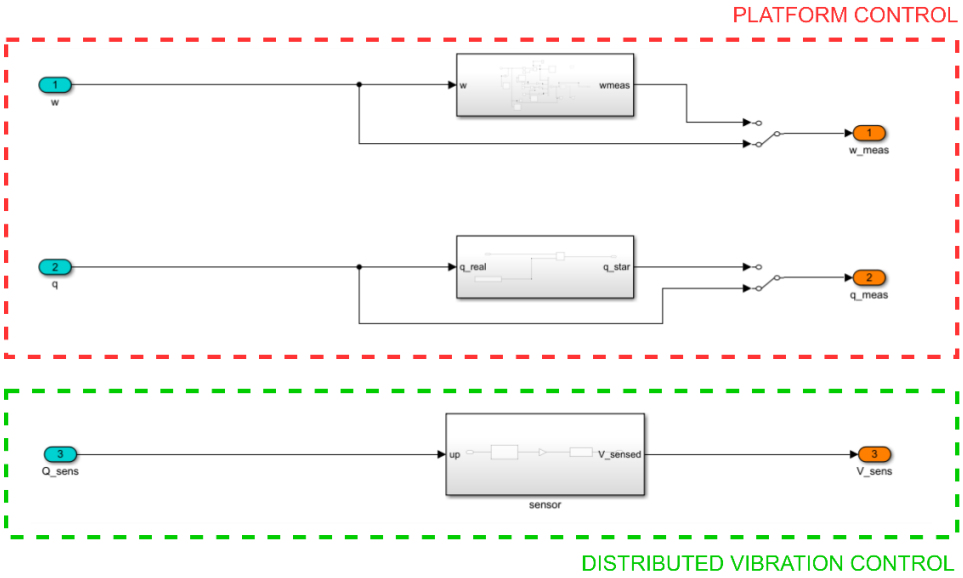

Fig. 7-5: Sensors overview

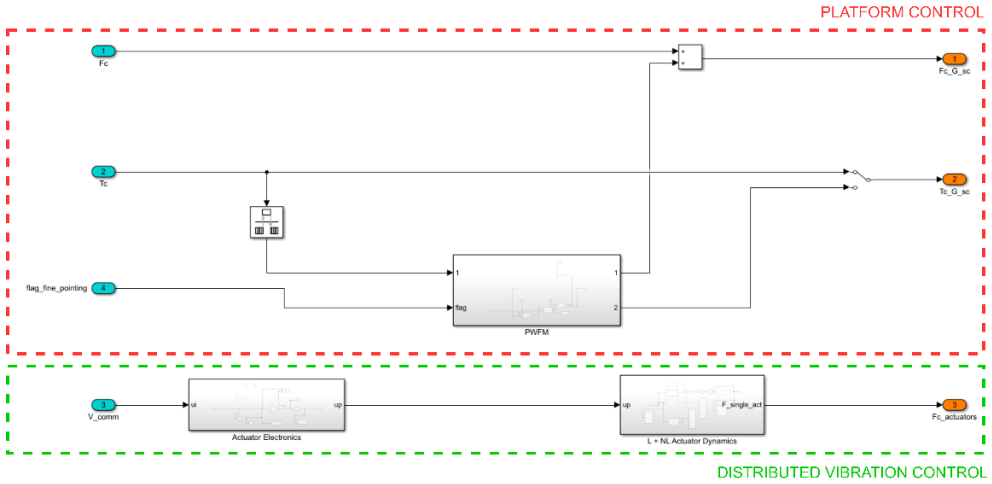

Fig. 7-6: Actuators overview

Concerning the vibration control system, a PD controller is used to generate the desired input voltage to be fed to the piezoelectric actuators. In Fig. 7-5 and Fig. 7-6, an overview of the *Actuators* and *Sensors* block is reported. More details about the implemented hardware will be given in the next sections.

7.2 ACTUATORS & SENSORS MODELS

In this section, the models of the actuators and sensors considered in the flexible spacecraft simulator are reported. In detail, as it is assumed to have a distributed control system on the flexible structures in this thesis, devices at both platform and structural level are introduced. In particular, the hardware will be chosen to accommodate the major requirements of the control system for both the hub and the appendages. In this research, the following main objectives can be deduced for the control/vibration systems:

- Capability to fulfil specific pointing requirements and complete a typical attitude mission profile in a limited time period;
- Capability of performing fast attitude manoeuvres at the targeted angular rate by minimizing the tranquilization time of the structure to allow a prompt data acquisition;
- Capability of compensating elastic and quasi-static deformations of the payload, as misalignments due to thermal loads and launch load;

- Capability of compensating sudden changes on spacecraft dynamic conditions, as thruster pulsing.

To achieve simultaneously the presented objectives, a distributed control system to obtain authority over the elastic modes of the structure, aimed at increasing the natural damping of the system, is actually required.

7.2.1 ACTUATORS AND SENSORS FOR DISTRIBUTED CONTROL

In this section, the implemented models for piezoelectric actuators and sensors are introduced, with the aim to illustrate how such devices have been built inside the simulator.

7.2.1.1 ACTUATORS

In detail, the non-linear model of a piezo-electric stack is shown in Fig. 7-7. In line with literature modelling the PZT devices [1][2][3], the multi-domain model for representing a Piezo Stack Actuator (PSA) is considered to be composed of electrical, piezoelectric and mechanical domains.

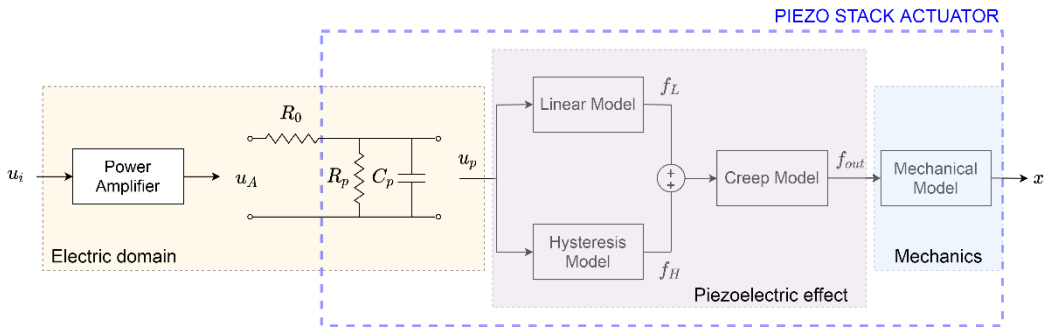

Fig. 7-7: Piezoelectric non-linear model

In the first-mentioned domain, the electric circuit is represented by a driver with amplification. Then, the piezoelectric effect is modelled by considering both hysteresis and creep effects. Finally, the mechanical model is described by a spring-mass-damper system composed of the equivalent mass, stiffness and damping of the device. Therefore, by applying a voltage u_p to the actuator, a linear force f_L and a hysteresis force f_H is generated (see also Fig. 7-7). The total

produced force, which has been impacted by both creep and hysteresis phenomena, will result in the forced vibration of the bonded piezoelectric layers.

Hence, the modified comprehensive model for the PSA can be expressed as

$$\begin{aligned} f_L &= L(u_P) = k_L u_P + f_0 \\ f_H &= H(u_P) \\ f_{out} &= C\left(f_L + f_H\right) \\ f_{out} &= m_p \ddot{x} + c_p \dot{x} + k_p x \end{aligned} \tag{7.1}$$

where

- $L(u_P)$ and $H(u_P)$ are the linear and hysteresis operators to model the linear and hysteresis forces;
- $C(\cdot)$ is the creep function that models the creep phenomenon;
- k_L is a constant describing the electro-mechanical ratio between input voltage and generated force, which can be considered equal to $n_l d_{33} k_P$ for a multi-stack piezo-actuator, with d_{33} electromechanical constant, n_l number of layers and k_p PSA equivalent stiffness;
- f_0 is the initial force applied to the PSA;
- f_{out} is the total force generated by the PSA with the applied voltage;
- m_p, c_P, k_p are the equivalent piezoelectric mass, damping and stiffness respectively;
- x is the displacement output of the PSA.

In detail, Buoc-Wen hysteresis relations are implemented [4], as the hysteresis of piezo material is asymmetrical and it results to be the more complete and adopted model in most experiments-based literature:

$$\dot{f}_H = \dot{H}(u_P) = \alpha \dot{u}_P - \beta |\dot{u}_P| |f_H|^{n-1} f_H - \gamma \dot{u}_P |f_H|^n + \delta u_P \, sign(f_H) \tag{7.2}$$

with α, β, γ and n parameters of the hysteresis, δ is the asymmetrical factor. Such coefficients may be provided by the manufacturer or be deduced via experimental tests (see Fig. 7-7). The hysteresis expression may be further simplified ($n=1$) according to the case in analysis.

The creep phenomenon can be described as a change in the piezo stack displacement over time under an unchanged drive voltage, therefore, it will be relevant at steady-state and quasi-static conditions, and be negligible for higher frequencies [5]. Two main categories of models are used to describe the creep effect

for piezo stack devices: time domain-based (exponential and logarithmic, mainly used for positioning applications) and frequency domain-based (such as spring-mass and Fractional Order Transfer Function, FOTF) approaches. In this thesis, both an exponential-based and a FOFT-based approaches have been considered. The exponential model predicts how the output force will be affected by a creep-like characteristic as described below

$$f_{out} = \left(1 - e^{-t/\tau}\right)\left(k_L u + f_0 + f_H\right) \tag{7.3}$$

where τ is the time constant of the creep. On the contrary, the FOTF model relies on the implementation of a fractional order creep acting on the linear and hysteretic force as

$$C_S(s) = K_S\left(\frac{1}{s}\right)^{\mu} \tag{7.4}$$

where K_S is a gain (which can be assumed as equal to 1 in most cases) and μ is the order of the fractional order model (set as equal to 0.0056). However, in both models, the impact of the creep phenomenon on the final actuator behaviour resulted to be negligible for the applications described in this thesis.

Concerning the electric circuit, an input voltage u_i is provided to an amplification stage. Therefore, a modified voltage u_A is obtained. From an electrical circuit point of view, the capacitance–resistance parallel connected equivalent circuit could be employed to represent the PSA under dynamic working conditions, and the electrically driven circuit can be illustrated in as

$$R_0\left(C_p \dot{u}_P + \frac{u_P}{R_P}\right) + u_P = n d_{33} u_A = n_l d_{33} K_{Amp} u_i \tag{7.5}$$

where R_0 is the equivalent resistance of the amplifier, C_p and R_P are the equivalent capacitance and resistance of the piezo-stack actuator, K_{Amp} is the amplification factor (the model is implemented in Simulink in. Finally, the equation of a flexible structure where a piezo-stack actuator has been implemented can be written as

$$\ddot{\eta}_{n_i}^{A_i} + 2\xi_{n_i}^{A_i}\boldsymbol{\omega}_{n_i}^{A_i}\dot{\eta}_{n_i}^{A_i} + \left(\left(\boldsymbol{\omega}_{n_i}^{A_i}\right)^2 + \boldsymbol{\phi}_{jm}^{A_i\,T} b b^T K_P \boldsymbol{\phi}_{jm}^{A_i}\right)\eta_{n_i}^{A_i} = \boldsymbol{\phi}_{jm}^{A_i\,T} b^T\left[\left(1 - e^{-t/\tau}\right)\left(k_L u_P + f_0 + f_H\right)\right] \tag{7.6}$$

where b is the influence vector mapping the piezoelectric forces on the structure.

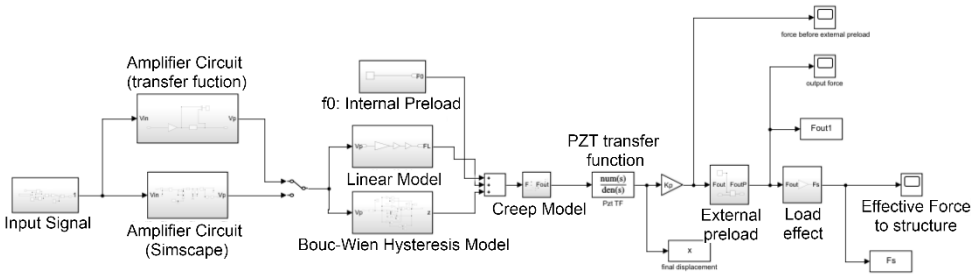

Fig. 7-8: Implemented model of a PSA actuator

In Fig. 7-8, the implemented model of a piezoelectric stack in Simulink is depicted. In particular, an amplifier is adopted to amplify the voltage to be fed to the piezoelectric device. Indeed, as the maximum voltage that can be generated on-board the spacecraft is limited (usually equal to 28V for middle-class satellites and up to 100V for large class communication satellites), it should be adapted to fully exploit the application range of piezoelectric devices.

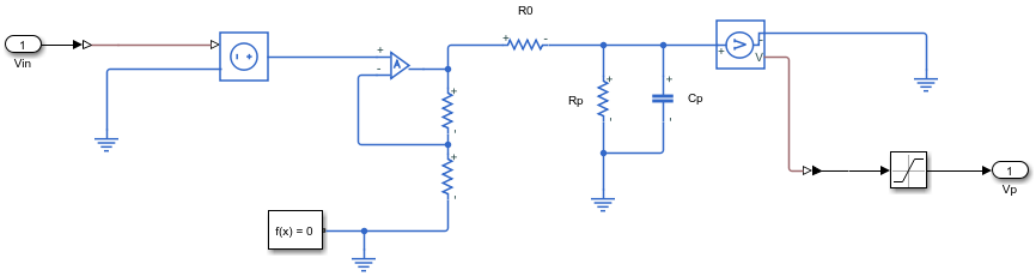

Fig. 7-9: Amplifier in Simscape Electric

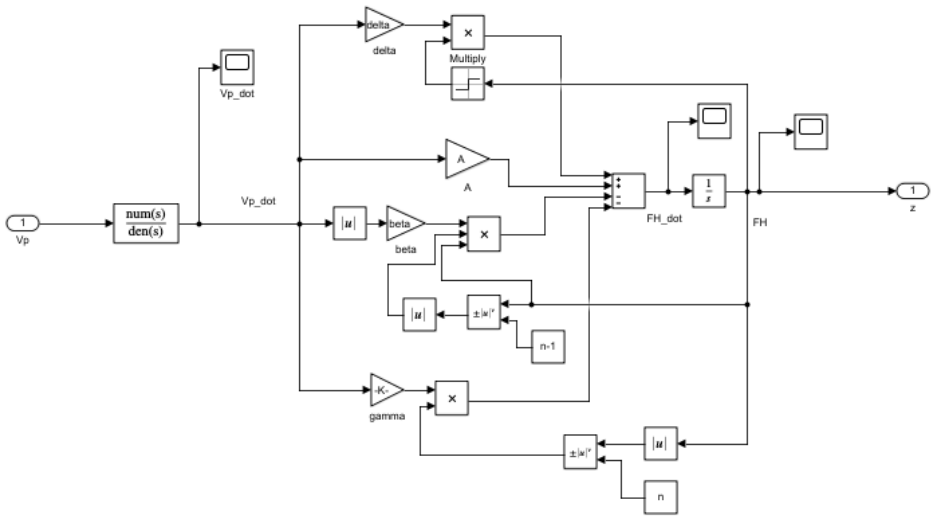

Fig. 7-10: Hysteresis model in Simulink

A comparison between the tested behaviour of commercial stack actuators and the proposed model has been performed to validate the formulation. A model of the piezostack actuator PI P885.51 device has been realized by implementing the above equations in SIMULINK environment. The relevant data of the piezo are listed in Table 7-1.

Table 7-1: Actuator properties

$k\ (\mu m/V)$	V_{max} (V)	C_P (μF)	$\Delta l_{max}(\mu m)$	$W \times H \times L$ (mm)
0.1858	120	1.5	18	$5 \times 5 \times 18$
α	β	n	γ	δ
-0.0724	0.0234	1.52	-0.025	0.0075

Such a device has been selected as test case due to the fact experimental data concerning its hysteresis curve are available in the work of Yang and Zhu [3]. In Fig. 7-11 and Fig. 7-12 the two trends are portrayed: it can be noticed a good correspondence between numerical and experimentally obtained data.

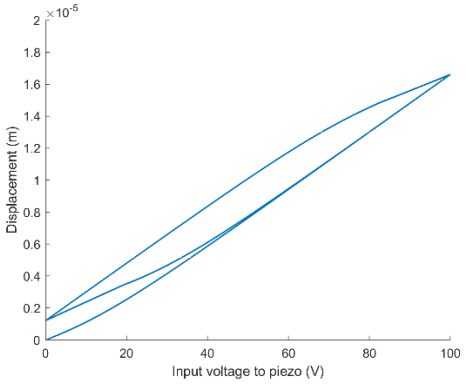

Fig. 7-11: Modelled hysteresis curve for P885.51 stack actuator

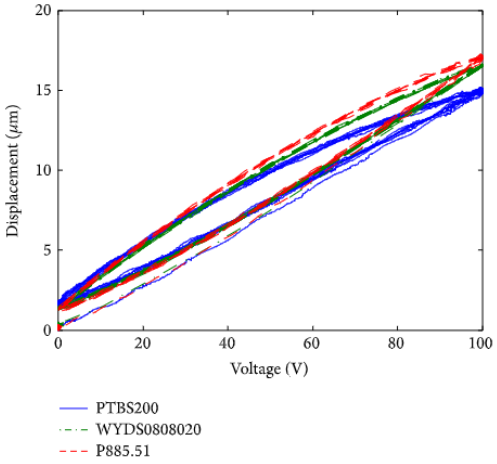

Fig. 7-12: Measured hysteresis curves of different PSAs [3]

When using piezoelectric actuators to perform vibration control, the devices are required to generate a displacement (or forces when constrained) in a two-sided way, which means they are required to both extend and contract to follow the trend of the input voltage. However, most of such devices, due to physical properties of the piezoelectric material, are defined *unipolar* and cannot be fed with negative voltage to reverse the motion. Even though some *bipolar* components are available at commercial level, the range of available input voltage is not symmetric

with respect to the zero, so that the maximum negative voltage that can be provided to the devices is often below one third of the positive limit value (typical ranges are [120, -30] V). Hence, if a minimum force is required to obtain a certain vibration damping efficacy, one should check to satisfy the negative voltage limit, thus leading to oversize the response of the piezo in the voltage positive range (implying bigger and more massive devices to perform a same damping action). Furthermore, it has been found [6] that even bidirectional piezoelectrics were damaged easily when applying negative voltages during experimental tests. Therefore, a positive voltage should be in general fed to piezo-stack devices to avoid potential failures and to ensure to use the proper actuator for the required application. In this thesis, only unidirectional stack devices will be considered.

To deal with such issues, some solutions may be proposed. The first one is to bias the input voltage to the half of the input voltage range (so if the piezo works in the interval [0,100] V, the bias will be equal to 50V). However, this strategy implies to continuously feed the piezoelectric with the constant bias value to be in a steady-state condition. As an alternative, some design changes may be adopted to avoid imposing a constant input signal. In the work of Luo et al. [6], an interesting concept employing bidirectional devices is developed - and experimentally tested – to provide a bidirectional output force. In this thesis, the proposed model will be adapted and extended to consider also the non-linearities of the piezoelectric materials. The solution will be implemented in Simulink environment to be easily included as a building block of a general vibration control architecture. The system operating principle is depicted in Fig. 7-13.

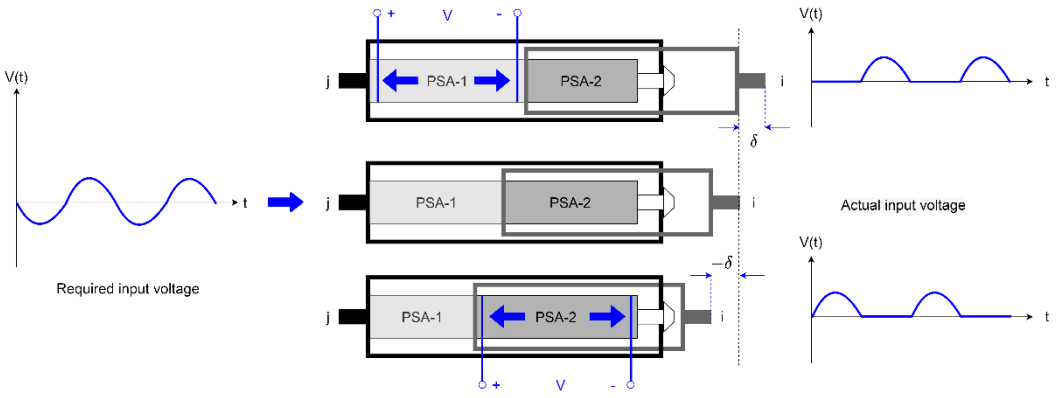

Fig. 7-13: Operating principle of a dual stack piezoelectric actuator

To achieve a bidirectional motion capability, two stack actuators are inserted in a same case to make them work in a coordinate alternate motion. When one of the

two actuators is fed with a positive voltage and expands, the other one is switched off and acts as a passive preload, taking the compressive load of the other device. To achieve such result when implementing the device in Simulink environment, the input voltage signal is decomposed as the sum of the positive u^+ and the absolute value of the negative part of the signal u^- (as indicated in Fig. 7-13).

$$u_P = u^+ + u^- \tag{7.7}$$

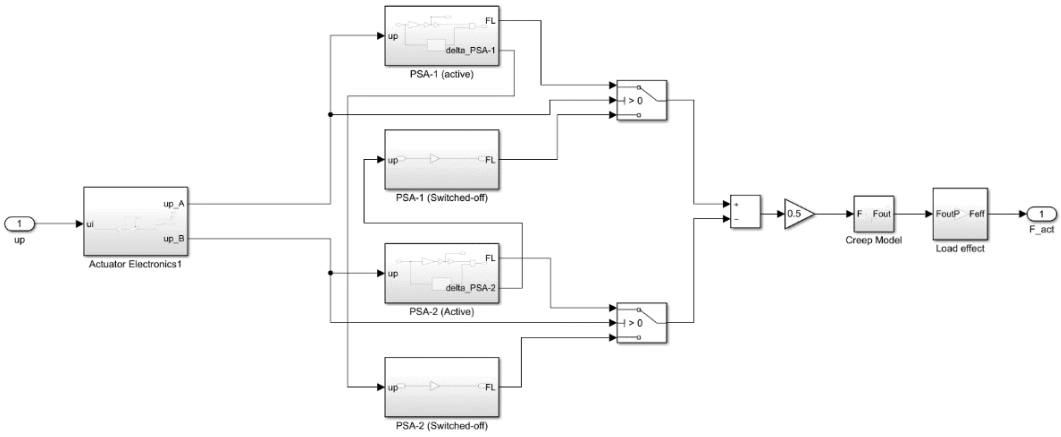

Fig. 7-14: Dual PSA model in Simulink

Then, such voltages as alternatively fed to the PSA-1 and PSA-2. A switch block is used to coordinate the movement between the two devices. When one actuator is switched-off, it acts against the displacement produced by the active one, acting as a passive preload as

$$F_L = -k_p \delta \tag{7.8}$$

where k_p is the stiffness of the piezoelectric device and δ is the produced displacement according to the relation $\delta = nd_{33}u$, with n number of layers of the stack, d_{33} piezoelectric constant and u voltage applied to the electrodes of the piezo.

7.2.1.2 SENSORS

When used in sensing mode, a piezoelectric transducer is coupled to an operational amplifier, which can be either a current amplifier or a charge amplifier [7]. As a result, when the electrodes of a piezoelectric transducer are connected to

an operational amplifier, they can be regarded as short-circuited and the electric field through the piezo can be considered as equal to zero. Then, the piezoelectric constitutive equation can be written to derive the charge per unit area D_3 as

$$D_3 = e_{31} S_1 \tag{7.9}$$

where e_{31} is the piezoelectric constant. Therefore, by considering the Euler-Bernoulli theory – assuming the strain and stress fields are uniaxial – the strain S_1 can be considered as proportional to the curvature w'' as described below

$$D_3 = -e_{31} z w'' \tag{7.10}$$

where z is the distance from the neutral axis. By integrating over the area of the electrodes, one can obtain for an electrode of constant width

$$Q = \int_A D_3 dA = -e_{31} z b \left(w'(x_b) - w'(x_a) \right) \tag{7.11}$$

with b width of the sensor, x_b and x_a coordinates describing the length of the device. Hence, the sensor output is proportional to the difference of slopes (i.e. rotations) at the extremities of the sensor strip. Once the sensor measures a physical response, the value of the charge (or current) should be amplified to be used by the controller system in a closed loop. Different types of amplifiers can be used with such aim, as the ones depicted in Fig. 7-15.

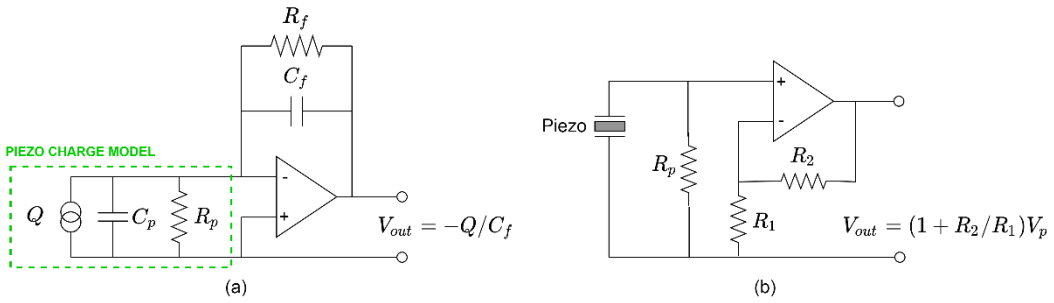

Fig. 7-15: (a) Charge amplifier (b) Non-inverting voltage amplifier

In this thesis, a sensor coupled with a charge amplifier is selected as, in general, voltage-mode amplification can be heavily affected by piezo and cable capacitance, length and type (whose exact value would be difficult to assess properly [8]). Indeed, the charge generated by the sensor is transferred to the feedback capacitance C_f and discharged by the resistor R_f to prevent the amplifier

saturation, as represented in Fig. 7-15-a. Therefore, the produced output voltage is generally assumed proportional to the amount of electric charge generated on the electrode and the amplifier gain is fixed by the feedback capacitance C_f as

$$V_{out} = -\frac{Q}{C_f} \tag{7.12}$$

However, a real piezo component does not behave the same at all frequencies. Indeed, the conditioning signal circuit's response has to be considered: the piezo device will experience a gain attenuation both at low frequencies (mainly due to the feedback resistor R_f) and high frequencies (due to input resistors and capacities). Nevertheless, in this study the high-frequency roll-off is neglected as outside the bandwidth of interest. Therefore, to reproduce a more realistic behaviour of a piezoelectric sensor at low frequencies, the gain of the device can be coupled with a first-order high-pass filter

$$V_{out} = -\frac{1}{C_f} F(s) Q = -\frac{1}{C_f} \frac{R_f C_f s}{R_f C_f s + 1} Q \tag{7.13}$$

where the cut-off frequency – that is the frequency at which the output is reduced by 3 dB – can be computed as

$$f_c = \frac{1}{2\pi R_f C_f} \tag{7.14}$$

The correspondent model implemented in Simulink environment is presented in Fig. 7-16. Hence, the behaviour at low frequencies can be modulated by choosing properly the values of the R_f and C_f parameters, usually varying between $[1M\Omega, 1G\Omega]$ and $[10pF, 100nF]$ [9]. However, even though a high R_f is necessary to reduce the cut-off frequency, the value of such resistance cannot be increased indefinitely, as it will introduce additional noise in the system. Consequently, piezo sensors have some limitations in sensing static deformations due to the properties of the electronics equipment they are coupled with.

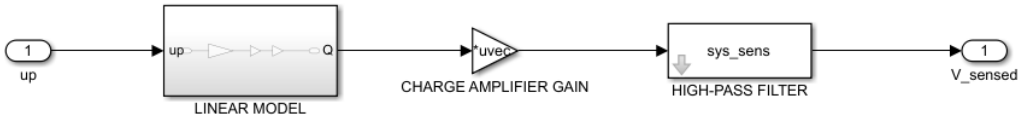

Fig. 7-16: Model of the piezoelectric transducer in Simulink

In conclusion, strain events occurring at a frequency below 1Hz can be measured by properly tuning the cut-off frequency of the filter. However, realistic piezo

sensor models will exhibit less sensitivity towards very-low frequency oscillations (related to attitude manoeuvres) than ideal sensors model. Nevertheless, in this regard, some solutions have been presented to solve this problem, as store&hold techniques which transfer the generated charge to a high-end, leakage free capacitor, while the charge proportional voltage across the capacitance can be measured closely load-free with a high impedance operational amplifier.

7.2.2 PLATFORM LEVEL ACTUATORS AND SENSORS

Concerning the platform actuators, according to the current state of the art, both Reaction Wheels (RWs) and thrusters (THRs) are presently used in modern spacecraft to ensure the capability to move (rotate and translate) in space.

7.2.2.1 ACTUATORS

In detail, as this thesis is focussed on the opportunity to reduce both the duration and the tranquilization time of spacecraft manoeuvres, a system based on THRs has been considered. In particular, to take the different operative modes of the satellite into account, a gain scheduling is assumed when performing coarse or fine pointing. Concerning thrusters, the way they are used depends on the type of operations they are assigned to. The force vector produced by the propulsion system can be considered as generated by the individual thrusters forces F_{thi}

$$F_T = \sum_{i=1}^{N} F_{thi} \tag{7.15}$$

The torque vector can be computed as the sum of the torques produced by each single thruster with respect to the CoM of the spacecraft as

$$N_T = \sum_{i=1}^{N} \left(d_{OG} - d_{th_i} \right) \times F_{thi} \tag{7.16}$$

In both cases, the general approach to determine what thrusters to fire makes use of a thruster configuration matrix $\mathbf{A}_T$, described in an equation written in the body reference frame

$$F = \mathbf{A}_T T \tag{7.17}$$

with

$$\mathbf{A}_T = \begin{bmatrix} e_{th1} & \cdots & e_{thi} & \cdots & e_{thN} \\ \left(d_{OG} - d_{th1} \right) \times e_{th1} & \cdots & \left(d_{OG} - d_{thi} \right) \times e_{thi} & \cdots & \left(d_{OG} - d_{thN} \right) \times e_{thN} \end{bmatrix} \tag{7.18}$$

where F is force and torque vector in the body reference frame, T is the $N \times 1$ thrust command vector, e_{thi} is the unit vector indicating the thrust direction and d_i is the vector representing the distance between the spacecraft CoG and the thruster position. In detail, N is the number of used thrusters in the selected arrangement. In order to achieve a six degrees of freedom control, it can be demonstrated [10] that at least six bidirectional or two-sided (capable of exhausting in two opposite directions) or seven unidirectional or one-sided (able to fire in one direction) thrusters are required. Therefore, if one direction is identified as positive, bidirectional devices are able to produce both a positive and a negative thrust, by using the opposite exhaust. In general, to solve eq. (7.17) the thrust command vector T is optimized with respect to a vector norm, as 1-norm, 2-norm or ∞-norm. One of the most widely used controllers due to its simplicity and reduced computational time, tries to minimize the 2-norm as

$$T^* = \min_T \|T\|_2 \tag{7.19}$$

which has a very simple solution [10] as

$$T^* = (\boldsymbol{A}_T)^\dagger F \tag{7.20}$$

with $(\boldsymbol{A}_T)^\dagger$ pseudoinverse of the configuration matrix

$$(\boldsymbol{A}_T)^\dagger = (\boldsymbol{A}_T)^T \left((\boldsymbol{A}_T)(\boldsymbol{A}_T)^T \right)^{-1} \tag{7.21}$$

In this thesis, a system of six bidirectional thrusters is considered to be positioned at the corners of the spacecraft face corresponding to the payload adapter surface. The thrusters were implemented in a way to not fire on the side of the satellite where the payload is mounted. In particular, as it is not the goal of this work to analize the optimal configuration for the proposed satellite, no in-depth analyses have been performed to assess the arrangement guaranteeing the optimal redundancy, lowest fuel consumption or time duration of the manoeuvres.

A major part of thrusters can only generate a constant thrust, so to control them it is necessary to change at least the length of their firing period (or pulse width) by using a Pulse Width Modulation (PWM) technique. In the last decades, spacecraft have demonstrated the possibility to use more advanced techniques to modulate not only the pulse, but also the frequency of the firing by adopting a

Pulse Width Frequency Modulation (PWFM) strategy. The method to implement attitude control is based on PWFM, which compared to other methods has superior advantages as high accuracy, adjustable frequency and better behaviour in presence of vibrations. When operating close to its linear behaviour, it produces an average torque equal to the demanded input torque. The standard scheme, adopted in this thesis, for a PWFM modulator is presented in Fig. 7-17. A first-order pre-filter with gain K_m and time constant T_m is used to process the error signal in input to provide a quasi–linear steady–state response. Then, the resulting signal is fed to a Schmidt trigger, which is a relay with a deadzone and a hysteresis cycle. The parameters defining the component are the activation threshold U_{on}, the hysteresis $h = U_{on} - U_{off}$, where U_{off} is the switch-off threshold, and the maximum output U.

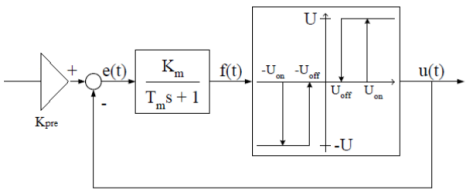

Fig. 7-17: Standard scheme for a PWFM modulator

To simplify the tuning operations, which could be not trivial for complex non-linear systems, the value of the maximum output is put equal to one and a gain K_G is added at the output of the modulator to be equal to the maximum allowed value of the thrust.

7.2.2.2 SENSORS

Concerning the sensors at platform level, two devices are considered in this thesis. To sense the attitude rate of the spacecraft, a gyro assembly is assumed to be implemented on the satellite [11], so that the output rate can be expressed as

$$\omega_g(t) = (1 + k_g)\omega(t - \tau) + d_g + n_{\mathrm{RRW}} + \dot{n}_{\mathrm{ARW}} \tag{7.22}$$

where k_g is the scale factor, ω is the real state angular speed in the body reference frame with respect to the inertial frame, d_g is the vector of drift and n_{RRW} is the vector of rate random walk (Gaussian) and n_{ARW} is the angular random walk.

Therefore, it is assumed to be a Gaussian distribution with zero mean and Σ_ω standard deviation, i.e. $n_{RRW} \sim N(0,\Sigma_\omega)$. In case the sensor is properly calibrated, the measurements in the three gyroscope axes are independent and the following relation yields

$$\Sigma_\omega = \begin{bmatrix} \sigma_x^2 & 0 & 0 \\ 0 & \sigma_y^2 & 0 \\ 0 & 0 & \sigma_z^2 \end{bmatrix} \tag{7.23}$$

The slowly time-variant term d_g can be assumed as constant in the simulation time interval. Typical value are a delay are 0.1 s and a sampling frequency of 10 Hz [11].

At the same time, a star sensor is contemplated in the hardware matrix at platform level. The sensor output is considered to be in quaternion, so to have

$$q_{str}(t) = q(t) \odot \left[1, N(0,\Sigma_c), N(0,\Sigma_c), N(0,\Sigma_b)\right]^T \tag{7.24}$$

where $N(0,\Sigma_c)$ is a random value coming from a Gaussian distribution, where Σ_c is the standard deviation across boresight and Σ_b along boresight. Typical modern values for the update rate are up to 10 Hz, accuracy of less than 20 arcsec [11].

7.3 SIMULATIONS

In this paragraph, an active vibration control system coupled with attitude controller is tested on two study cases, representative of large flexible payload for Earth Observation (EO) missions. Some considerations are reported in terms of feasibility of the proposed architecture. In detail, specific manoeuvres have been considered for each study case, as reported in Table 7-2.

Table 7-2: Overview of the considered manoeuvres

	K-Band Interferometer	Mesh Reflector
Manoeuvres type	1-axis (roll) RW-like	3-axes re-reorientation RW-like
	3-axes re-reorientation RW-like	3-axes re-reorientation Thrusters (PWFM)

Indeed, only specific slew manoeuvres, which are more representative for the type of analyzed spacecraft, have been reported in this thesis. In general, piezoelectric

devices proved to enhance the pointing performance of the systems and to avoid potential instability situations related to the use of thrusters, when used by considering also actuators and sensors delays and noise.

7.3.1 TEST CASE: K-BAND INTERFEROMETER

As first study case, an active collocated control distributed on a K-Band Interferometer, described in Par. 5.6.1, is tested along with platform classic control. Therefore, a typical profile for a re-orientation manoeuvre for a satellite equipped with such a flexible appendage is studied[4].

In particular, the control torque τ_C exerted ideally by the platform actuators is defined as [12]

$$\tau_C = -\sigma(\omega \wedge \boldsymbol{J}\omega) + u \tag{7.25}$$

where u is a linear feedback control law based on a Proportional Derivative (PD) approach and σ a constant between 0 and 1. The decoupling term is considered to compensate for the nonlinear gyroscopic term in the attitude equations. The feedback control on quaternions studied in [13][14] has proved to be globally stable in the case of uncertainties on spacecraft properties and will be adopted in this study. The feedback control around Euler's axis can be then expressed as

$$u = -\boldsymbol{K}_D\omega - \boldsymbol{K}_P\bar{q}_e^I sign(q_0) \tag{7.26}$$

where $\boldsymbol{K}_D$ and $\boldsymbol{K}_P$ are properly selected gains matrices [15]. To take the possible change of sign of the quaternion into account, the term $sign(q_0^I)$ is introduced in eq. (7.26). By considering a set of desired Euler's angles $[\phi_d, \theta_d, \varphi_d]$, it is possible to define the rotation matrix $\boldsymbol{R}_3(\phi_d, \theta_d, \varphi_d)$ describing the attitude of the spacecraft with respect to the LVLH orbital frame. Finally, the desired quaternion can be derived from the equivalence

$$\boldsymbol{R}_3(\phi_d, \theta_d, \varphi_d) = \boldsymbol{R}_3\left(\tilde{q}_d^O\right) \tag{7.27}$$

with $\tilde{q}_e^O = \left[q_{1_d}^O, q_{2_d}^O, q_{3_d}^O, q0\right]$.

[4] Part of the results in this section was published by the thesis author in F. Angeletti et al., *Design and performance assessment of a distributed vibration suppression system of a large flexible antenna during attitude manoeuvres*, Acta Astronautica, Volume 176, November 2020, Pages 542-557

Given the quaternions in the orbital reference frame, it is possible to find the desired quaternions with respect to the inertial reference frame $\tilde{q}_d^I$. The error on the final desired configuration $\tilde{q}_e^I = \left[\tilde{q}_e^I, \tilde{q}_0^I\right]$ will be then expressed as in eq. (7.28).

$$\begin{pmatrix} q_{1_e}^I \\ q_{2_e}^I \\ q_{3_e}^I \\ q_{0_e}^I \end{pmatrix} = \begin{bmatrix} q_{0_d} & q_{3_d} & -q_{2_d} & -q_{1_d} \\ -q_{3_d} & q_{0_d} & q_{1_d} & -q_{2_d} \\ q_{2_d} & -q_{1_d} & q_{0_d} & -q_{3_d} \\ q_{1_d} & q_{2_d} & q_{3_d} & q_{0_d} \end{bmatrix} \begin{pmatrix} q_1^I \\ q_2^I \\ q_3^I \\ q_0^I \end{pmatrix} \tag{7.28}$$

In parallel to the attitude control, during the manoeuvre, a PD-feedback law has been implemented to control the elastic vibrations the antenna is affected by. The actuating voltages are computed as

$$\psi_{ACT} = -k_P \psi_{SEN} - k_D \dot{\psi}_{SEN} \tag{7.29}$$

To simulate a realistic scenario, the selected orbit data are derived from the available information about SWOT mission (see Par. 5.6.1). The chosen parameters are reported in Table 7-3. Furthermore, as the structure is equipped with piezo devices, their properties are listed in Table 7-4 (deduced from commercially available data reported by Physik Instrumente, PI, producer). Moreover, the data about the platform are reported in Table 7-5.

Table 7-3: Orbital data

	Symbol	Value
Eccentricity	e	0.00104
Semi-major axis	a	7268.72 km
Inclination	i	77.6°
RAAN	Ω	22.36°
Argument of perigee	ω_p	10°

Table 7-4: Actuators/sensors physical properties

	Symbol	Value		Symbol	Value
Area	A_{PZ}	$0.00104 m^2$	P-PSA offset	h_a	$0.05\ m$
Young Modulus	E_{PZ}	$100 GPa$	Resistance	R_f	$2000\ \Omega$
Length	l_{PZ}	$0.1\ m$	Capacity	C_f	$30 \mu F$
Density	ρ_{PZ}	$7000\ kgm^{-3}$	Max/Min voltage	V_M	$\pm 150\ V$
Piezo-coefficient	d_{33}	$4e-10\ Vm^{-1}$			

Table 7-5: Platform properties

	Symbol	Value
Dimensions	D	$1\,m$
	W	$1\,m$
	H	$2m$
Inertia	I_{XX}	$833.3\,kg\,m^2$
	I_{YY}	$833.3\,kg\,m^2$
	I_{ZZ}	$333.3\,kg\,m^2$
Mass	M_{SAT}	$2000\,kg$

The satellite attitude and its orbit are propagated and visualized during the simulation in Matlab environment, where the axes of both the LVLH and the body reference frame are reproduced as well (the nadir direction being the dotted black line in Fig. 7-18).

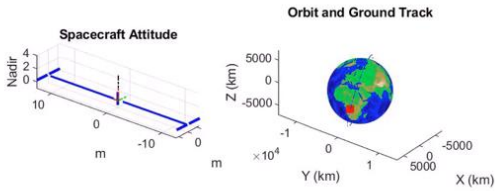

Fig. 7-18: Simplified spacecraft attitude and orbit visualization

In the following sections, two attitude manoeuvres are performed, and the control system performance evaluated.

7.3.1.1 ROLL-AXIS ATTITUDE MANOEUVRE

In most of remote sensing and surveillance missions the spacecraft is required to sweep a specific area with the same orientation orbit after orbit. The general objective is to acquire data of a strip, parallel to the satellite ground track. In such a scenario, the mission can be divided into two phases: a roll-attitude manoeuvre to re-orient the payload and a sensing phase. In this section, only the first part of the mission is considered, as the sensing phase is a stabilization problem around the nadir-pointing condition (if not considering compensations due to the Earth rotation). The final roll angle is set to $\varphi_d = 40°$. The system is able to reach the desired configuration in about 80 seconds (see Fig. 7-19).

The displacement of the tip of the antenna reflector with and without active control is reported in Fig. 7-20. In this study, the tip has been considered as the reflectors farthest point from the attachment with the mast, as indicated in Fig. 7-20. In particular, the plotted quantity refers to the module of the displacement computed by its components in the Cartesian space. It can be noticed how the manoeuvre was able to excite the flexible dynamics to cause a tip displacement of millimetres. As future Earth and Universe Observation missions will require the maximum tip displacement to be below submillimetre limit also for very large structures, the observed elastic perturbation could be considered as a relevant issue for the proper execution of next space operations.

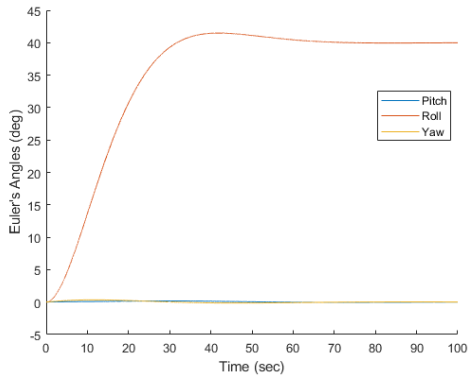

Fig. 7-19: Euler's angles – roll manoevres

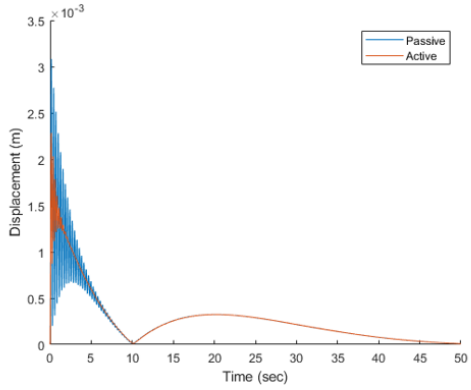

Fig. 7-20: Displacement of the tip of the antenna – Module (roll attitude manoeuvre)

To assess the actual enhancement in the damping capability of the system the value of the logarithmic decrement for the tip displacement has been derived as

$$\tilde{\delta} = \frac{1}{n_C} \ln\left(\frac{x_j^{TIP}}{x_{j+n_C}^{TIP}} \right) \tag{7.30}$$

where x_j^{TIP} and $x_{j+n_C}^{TIP}$ are two peaks in the considered time history and n_C indicates the number of consecutive peaks between them. The passive structural damping implies a logarithmic decrement $\delta_{PASSIVE} = 0.052$. The active control system guarantees instead an improvement of the decrement up to $\delta_{ACTIVE} = 0.072$. A good enhancement of the structural damping capability can be clearly noticed when using the piezo actuators devices.

The voltage required to activate all the actuators is reported in Fig. 7-21. The maximum voltage does not exceed the allowed value.

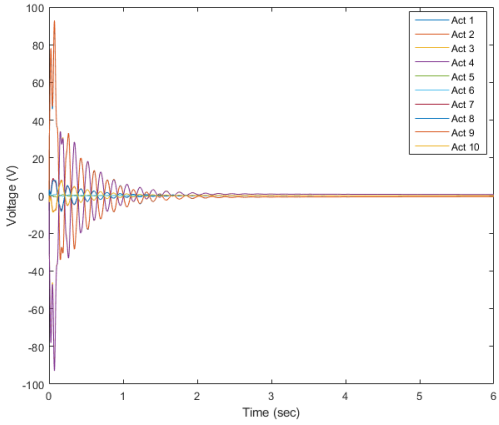

Fig. 7-21: Voltage in the first six seconds of the roll attitude manoeuvre

The system can damp out vibrations in the first six seconds of the manoeuvre, thus allowing to precisely acquire scientific data during the spacecraft movement (e.g. in the case of sensing a strip that is not parallel to the satellite ground track). Moreover, an evaluation of the power consumption during the attitude manoeuvre is presented in Fig. 7-22 (the numbers reported on the horizontal axis refer to Fig. 5-18). The mean power consumption of each actuator has been computed as

$$\overline{P}_i = \frac{1}{T_F}\int_0^T P_i(t)dt = \frac{1}{T_F}\int_0^T C_P \Psi_{ACTi}^2(t)dt \tag{7.31}$$

where the i-th index indicates the actuator number, T_F is the total manoeuvre time, C_P the electrical capacitance (as reported in Table 7-4) and Ψ_{ACT} the voltage supplied to each device.

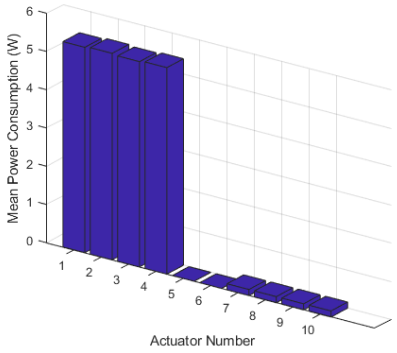

Fig. 7-22: Mean power consumption referred to each actuator

It can be noticed the actuators requiring most of the power are those placed near the root of the mast. This result is expected if considering a roll manoeuvre is mainly exciting the third elastic mode of the structure, which is an asymmetric bending mode around the roll axis (X-axis of the body reference frame). It is also interesting to note that the actuators 1 and 2 are driven with the same voltage, while actuators 3 and 4 show opposite sign with respect to them. This is also expected if considering that in the asymmetric bending mode the top surfaces of the two halves of the mast (along +Y-axis and –Y-axis in the body reference frame) are alternatively extending and contracting. The total mean power consumption is defined as the sum of the contributions of each actuator and it is equal to 25.6 W. Furthermore, according to the results of the closed loop simulations, when considering the displacements at the nodes where the actuators are located, the devices can impress an elongation not greater than 20 μm. This value corresponds to the one able to be generated by the off-the-shelf axial actuators.

7.3.1.2 GENERAL ATTITUDE MANOEUVRE

In this case, a general manoeuvre is considered in order to generate a more complex elastic displacement of the appendages with respect to the previous case. Accordingly, the desired final Euler's angles in the LVLH orbital frame are set to $[\phi_d, \theta_d, \varphi_d] = [10°, 30°, 20°]$. The attitude manoeuvre is simulated to verify the effectiveness of the active control system in damping out the vibrations. For this manoeuvre the gains of the PD control are kept unchanged. As shown in Fig. 7-23 the system is able to reach the desired attitude configuration in about 100 seconds.

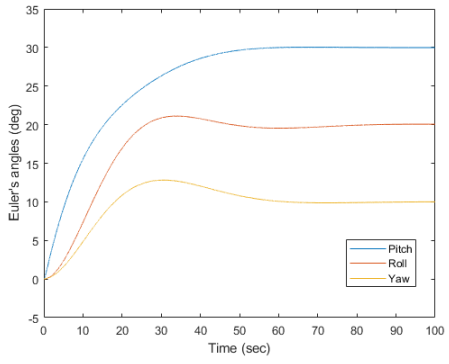

Fig. 7-23: Euler's angles - general manoeuvre

The time history of the tip displacement is presented from Fig. 7-24 to Fig. 7-27,

where the (X,Y,Z) components and the magnitude of the displacement are reported. It can be noticed the network is significantly able to reduce the undesired elastic vibrations in the first few seconds of the manoeuvre.

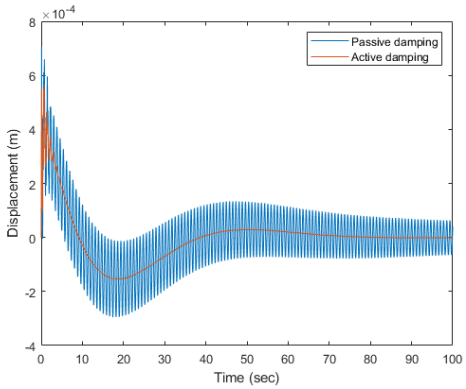

Fig. 7-24: Displacement of the antenna tip: X-component – general attitude manoeuvre

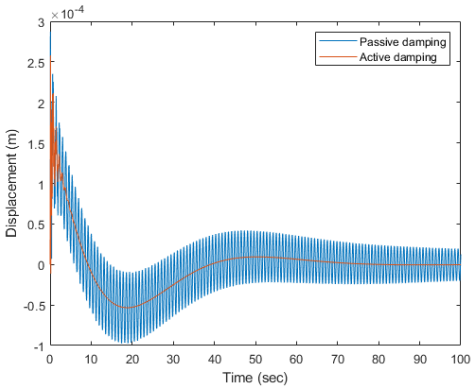

Fig. 7-25: Displacement of the antenna tip: Y-component – general attitude manoeuvre

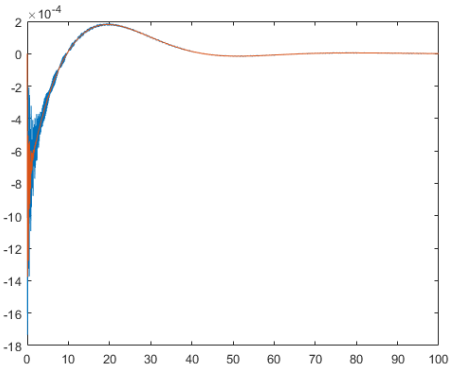

Fig. 7-26: Displacement of the antenna tip: Z-component – general attitude manoeuvre

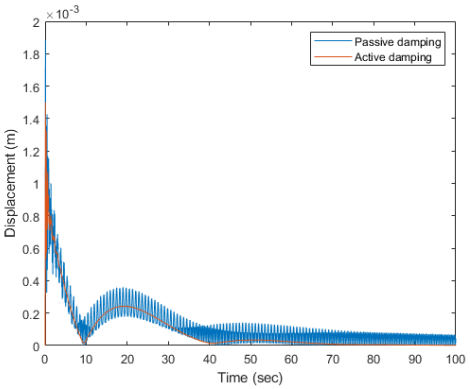

Fig. 7-27: Displacement of the antenna tip: module – general attitude manoeuvre

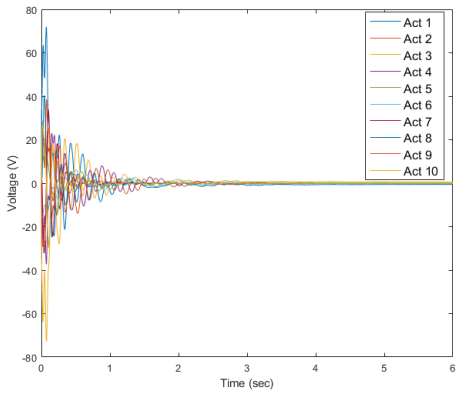

Fig. 7-28: Input voltage in the first seconds of the manoeuvre – general attitude manoeuvre

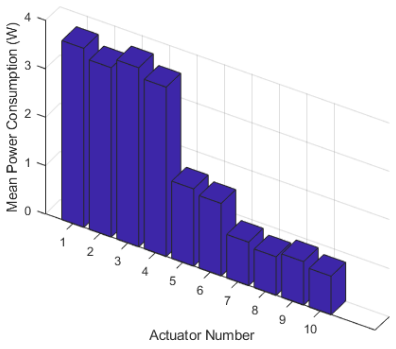

Fig. 7-29: Mean power consumption referred to each actuator

The active control system provides an enhancement of the logarithmic decrement up to $\delta_{ACTIVE} = 0.081$. The required input voltage is presented in Fig. 7-28. The mean power consumption, as described in Section 6.2, is shown in Fig. 7-29. In this case, all the actuators are required to efficiently damp out the induced vibrations on the antenna tip, as the manoeuvre is exciting different elastic modes from the third one. The total mean power consumption results to be roughly 20.5 W. In the two cases here examined, the required power consumption is compatible with modern satellites on-orbit available power. Finally, also in this case, the evaluated maximum displacement of the actuators does not exceed the value of 15 μm. Again, the voltage required to excite the vibration control action is below the maximum allowed voltage value for the considered actuators.

7.3.2 TEST CASE: MESH REFLECTOR AND SOLAR PANELS

Being motivated by the current interest in such a type of scientific instrument (as already mentioned in Ch. 1), the large mesh reflector introduced in Par. 5.6.2 has been selected as the payload of the analysed satellite for the second test-case. Moreover, the platform is equipped with two large solar panels (already considered in Par. 5.6.4). Such a model, representative of a realistic Earth Observation (EO) satellite, is composed of a central platform of prismatic shape, two solar arrays ($\sim 3\times 8\,m$) and a large mesh reflector (diameter $\sim 12\,m$). A schematic of the model is presented in Fig. 7-30.

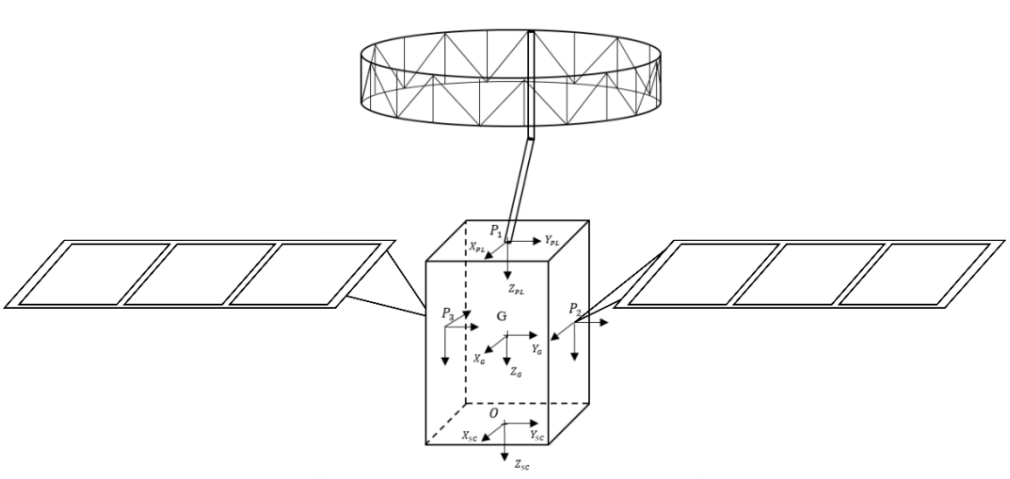

Fig. 7-30: Schematic of the case study

The properties of the platform have already been introduced in Table 6-1. The properties of the piezoelectric actuators (deduced from available data of NOLIAC company, as in Par. 6.3.1) are listed in Table 7-6. The considered sensors are standard piezo patches (selected as PI DuraAct Transducers). Moreover, the positions of all the attachment points are listed in Table 7-7.

Table 7-6: Actuators physical properties

	Symbol	Value		Symbol	Value
Area	A_{PZ}	$0.0001m^2$	P-PSA offset	h_a	$0.02\ m$
Young Modulus	E_{PZ}	$52GPa$	Resistance	R_f	$50\ M\Omega$
Length	l_{PZ}	$0.1\ m$	Capacity	C_f	$100nF$
Density	ρ_{PZ}	$7800\ kgm^{-3}$	Max/Min voltage	V_M	$\pm 150\ V$
Piezo-coefficient	d_{33}	$4e-10\ Vm^{-1}$	Layer number	n	1250

Table 7-7: Attachment Points

Substructure	Description	Attachment in S/C frame (m)
1	Payload	[0 ; 0 ; -3]
2	Solar Array 1 (+Y axis)	[0 ; 1 ; -2]
3	Solar Array 2 (-Y axis)	[0 ; -1 ; -2]

The relevant data concerning the inertial properties, participation factors, modes, and frequencies of the single substructures are extracted from the MSC Nastran tool and imported in Matlab environment. The data are then assembled to compute the dynamics of the complete system payload and solar arrays – retaining only a certain number of modes according to the Craig-Bampton approach. In particular, with the aim of assessing the correctness of the procedure, a model of the assembled spacecraft is designed in MSC Nastran to compare the main outcomes, as depicted in Fig. 7-31. The flexible appendages are anchored to a central lumped 0-D mass element (representing the satellite platform) by means of a RBE2 MPC (Multi-Point Constraint) connection.

Therefore, the attachment points P_1, P_2, P_3 in Table 7-7 are constrained to have the same displacements (in terms of both translation and rotation) of the platform (lumped in its CoG). The first frequencies obtained by assembling the three substructures (namely Payload, Solar Array 1 and Solar Array 2) in Matlab and extracting the related frequencies (either as deriving from the assembled mass and

stiffness matrices or by looking at the poles of the open loop dynamic system) are listed and compared to the ones derived by using Nastran in Table 7-8. The assembled model has been built based on the first 4 modes of the payload and the first 6 of the two solar arrays, for a total of 16 modes.

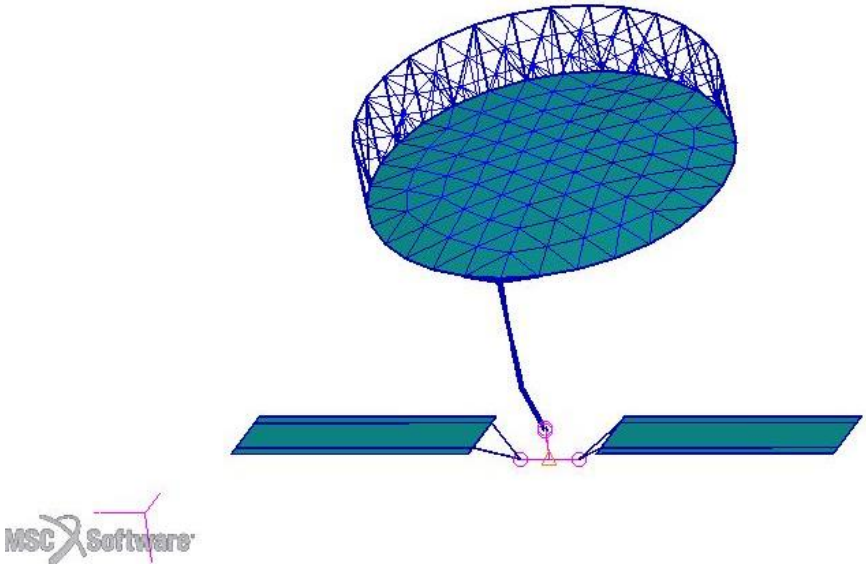

Fig. 7-31: Assembled case study in MSC Nastran environment

Table 7-8: Assembled case study verification based on frequencies check

Modes	LFT Assembly	Nastran Model	Error (%)
1st	0.1703 Hz	0.1702 Hz	0.05
2nd	0.2556 Hz	0.2556 Hz	0
3rd	0.3207 Hz	0.3207 Hz	0
4th	0.5041 Hz	0.5035 Hz	0.1
5th	0.7428 Hz	0.7428 Hz	0
6th	0.7783 Hz	0.7781 Hz	0.03
7th	0.9970 Hz	0.9968 Hz	0.02
8th	1.0338 Hz	1.0328 Hz	0.09
9th	1.1607 Hz	1.1608 Hz	0.01
10th	1.4206 Hz	1.4029 Hz	1.2
11th	1.5711 Hz	1.5367 Hz	2
12th	2.2821 Hz	2.2801 Hz	0.1
13th	2.3305 Hz	2.3236 Hz	0.3
14th	2.4504 Hz	2.4434 Hz	0.3
15th	2.5908 Hz	2.5461 Hz	2
16th	3.4466 Hz	3.0656 Hz	12

Also, the total mass, inertia and position of the CoG were compared between the two models, obtaining a very good agreement. It should be noticed however that using mode shape solutions of the individual substructures to obtain an approximation – via Craig-Bampton - to the exact first frequencies and mode shapes of the complete model generally leads to an error in the solution for higher order modes [16]. Therefore, a preliminary investigation aimed at retaining a significant number of modes so to properly approximate the modes in the bandwidth of interest should be performed.

7.3.2.1 TEST ATTITUDE/VIBRATION CONTROL

In this section, the results of a three-axis attitude manoeuvre performed by using a PID-attitude controller in parallel to a PD-vibration controller is presented. In Fig. 7-32 to Fig. 7-34 the displacement (in terms of the three components on the coordinated axis) of the tip of the mesh reflector are depicted. A very good vibration suppression action is performed by the distributed control. The same result can be noticed for the displacement of the tip of Solar Array 1, in Fig. 7-35 to Fig. 7-37.

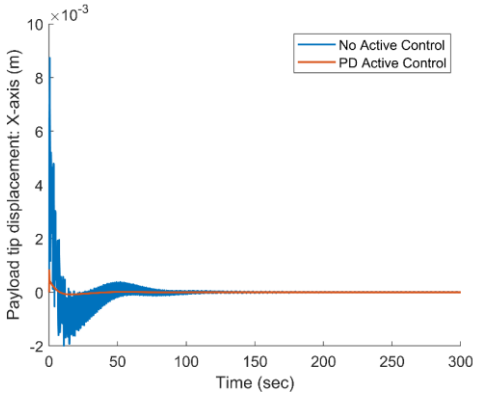

Fig. 7-32: Tip displacement of the Payload – X-axis component

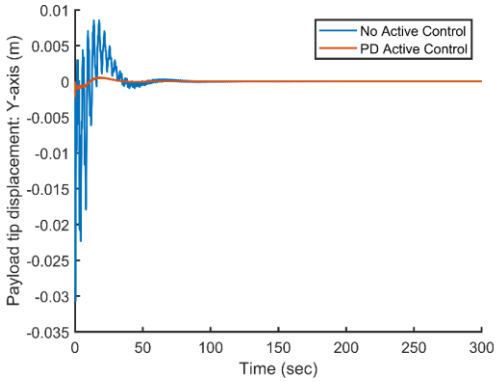

Fig. 7-33: Tip displacement of the Payload – Y-axis component

The trend of the Euler's angles is reported in Fig. 7-38. The spacecraft reach the steady-state condition at around 200 seconds, with an error of about 0.01 deg. The required torques for the manoeuvre are reported in Fig. 7-39. A saturation limit has been added to simulate the limits of most actuators.

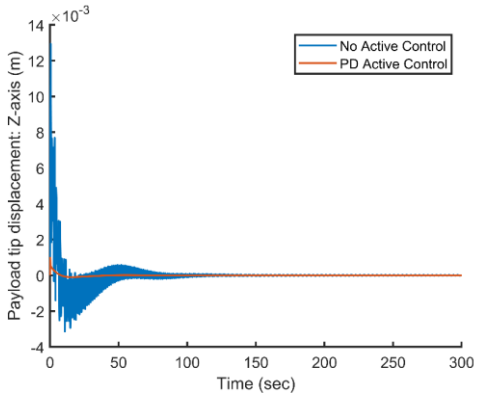

Fig. 7-34: Tip displacement of the Payload – Z-axis component

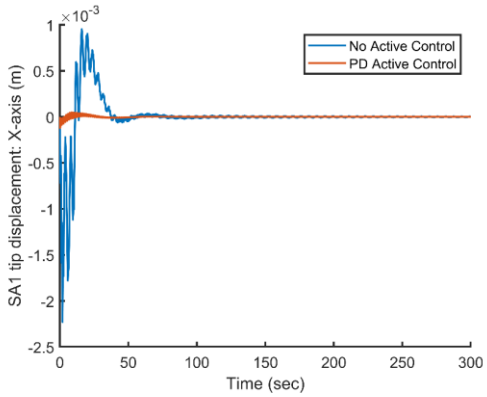

Fig. 7-35: Tip displacement of the Solar Array 1 – X-axis component

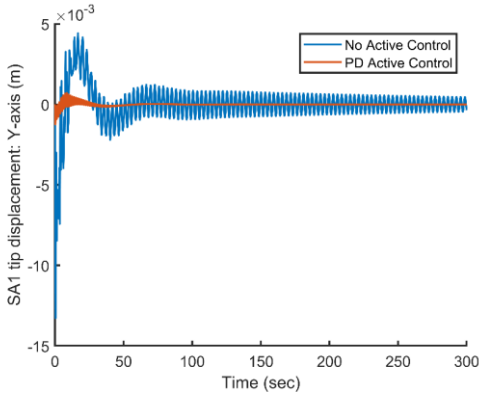

Fig. 7-36: Tip displacement of the Solar Array 1 – Y-axis component

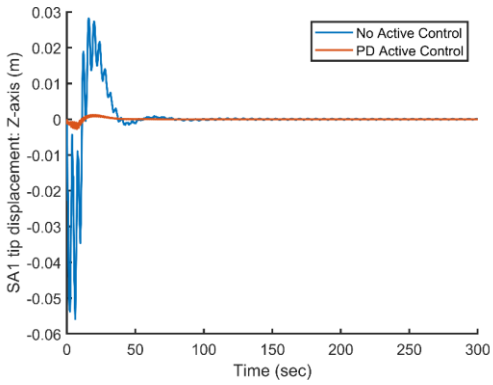

Fig. 7-37: Tip displacement of the Solar Array 1 – Z-axis component

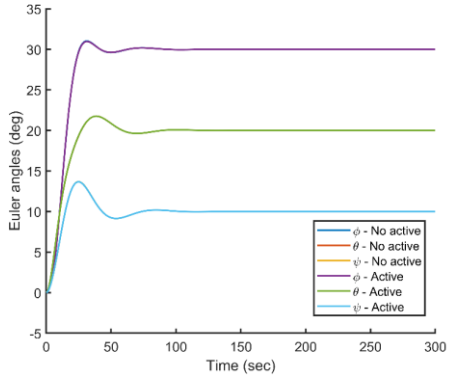

Fig. 7-38: Euler's angles

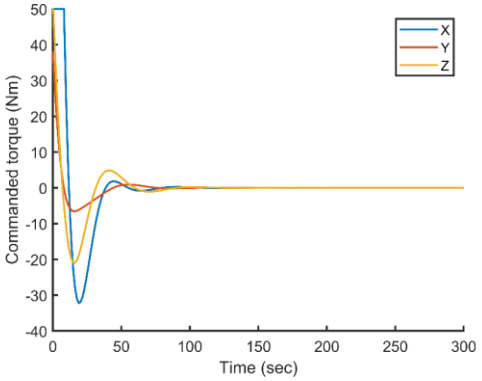

Fig. 7-39: Commanded torques

The trends of the input and output voltages are reported in Fig. 7-40 and Fig. 7-41. In detail, it can be noticed that the input voltages reach the saturation limit for the very first instant of the manoeuvre, thus not compromising the damping decrease.

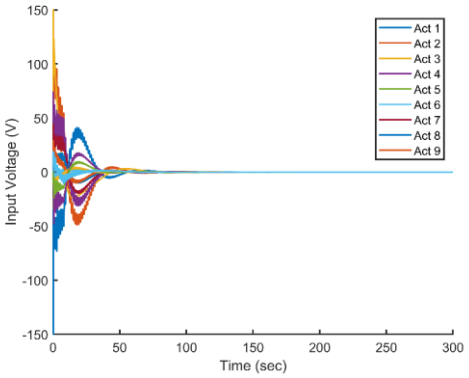

Fig. 7-40: Input Voltages

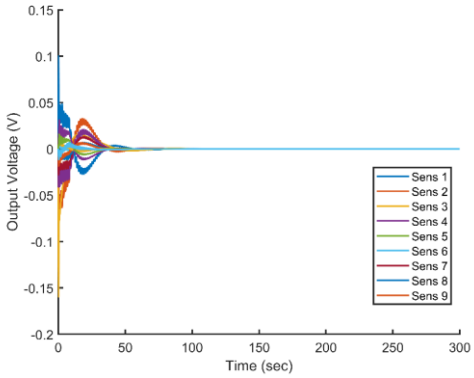

Fig. 7-41: Output Voltages

The mean power required to the system is estimated by using the method reported in eq. (7.31), resulting to be below 15 W.

Also, to further assess the performance of the proposed vibration system, a set of 100 manoeuvres (including single axis, two-axis and three-axis reorientation profiles) have been considered by sampling roll, pitch and yaw angles in the range between 0 and 90 degrees. Performance indexes are computed as the norm of the module of the elastic tip displacement for both the payload P_i^P and the solar array P_i^S , as indicated below

$$P_i^P = \left\| \sqrt{x_{TIP}^P(t)^2 + y_{TIP}^P(t)^2 + z_{TIP}^P(t)^2} \right\| \qquad P_i^S = \left\| \sqrt{x_{TIP}^S(t)^2 + y_{TIP}^S(t)^2 + z_{TIP}^S(t)^2} \right\| \tag{7.32}$$

where x_{TIP}^P , y_{TIP}^P , z_{TIP}^P are the coordinates of the payload tip displacement over time, while $x_{TIP}^S(t)$, $y_{TIP}^S(t)$, $z_{TIP}^S(t)$ are the coordinates of the solar array tip displacement. The performance indexes for each manoeuvre are reported in Fig. 7-42 and Fig. 7-43 for the payload and the solar array respectively.

Also, Fig. 7-44 and Fig. 7-45 depict an example of the tip displacement module of the two appendages, both in the case of no control and PD active control.

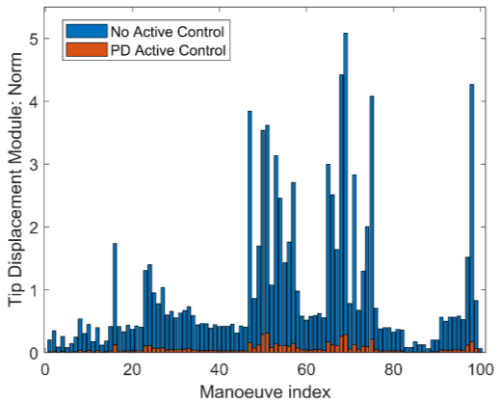

Fig. 7-42: Payload Performance Indexes

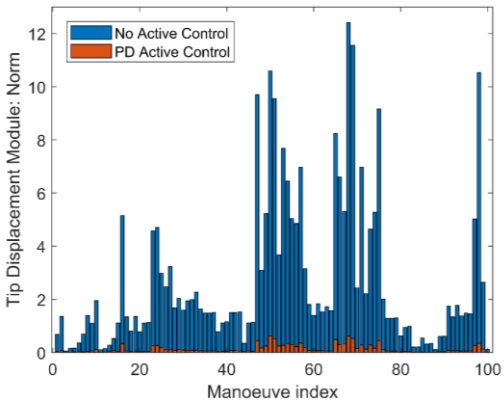

Fig. 7-43: Solar Array Performance Indexes

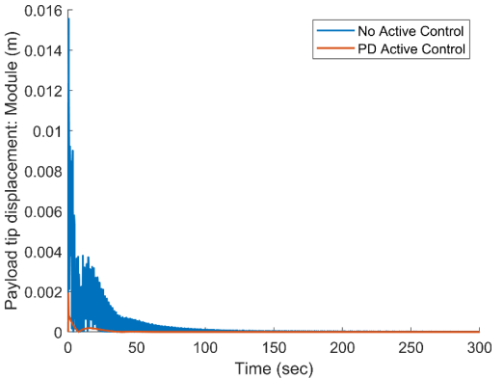

Fig. 7-44: Payload Tip Displacement: module

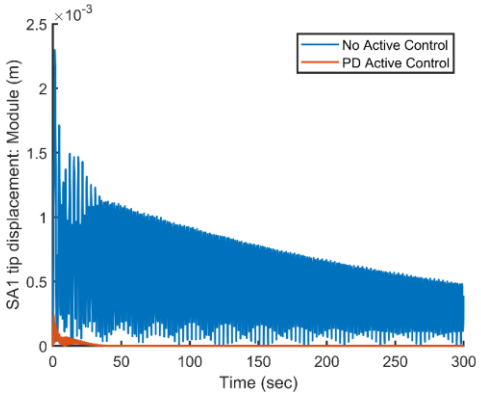

Fig. 7-45: Solar Array Tip Displacement: module

7.3.2.2 TEST ATTITUDE/VIBRATION CONTROL (WITH PWFM)

In this section, the results of a specific three-axis attitude manoeuvre performed by using a standard PID-attitude controller in parallel to a PD-vibration controller is presented. Moreover, a PWFM modulation of the command sent to the spacecraft thrusters is considered. Inn particular, this paragraph focuses on a particular case in which a relevant interaction between the rigid and the flexible dynamics (as in Fig. 7-52), which compromises the manoeuvre and the pointing performance, has been observed. In this case, in addition to guaranteeing an enhancement in the pointing performance of the satellite, the vibration control system is crucial to ensure the stability of the structure by actively rigidizing it, thus leading to a correct manoeuvre and a steady-state error below 0.02 deg. In Fig. 7-46 to Fig. 7-48 the displacements (along the three coordinated axis) of the mesh reflector tip are depicted. It can be noted that an effective vibration

suppression action is performed by the distributed control. The same result can be noticed for the displacement of the tip of Solar Array 1, in Fig. 7-49 to Fig. 7-51.

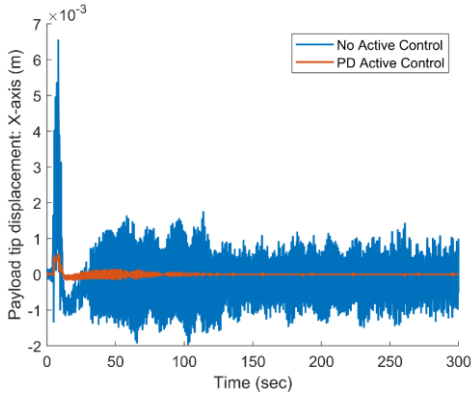

Fig. 7-46: Tip displacement of the Payload – X-axis component

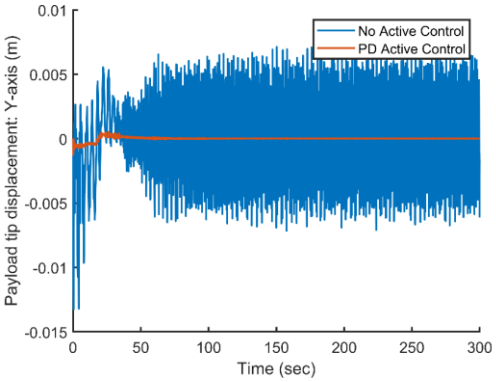

Fig. 7-47: Tip displacement of the Payload – Y-axis component

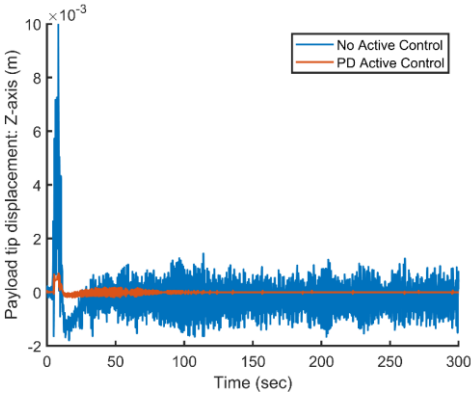

Fig. 7-48: Tip displacement of the Payload – Z-axis component

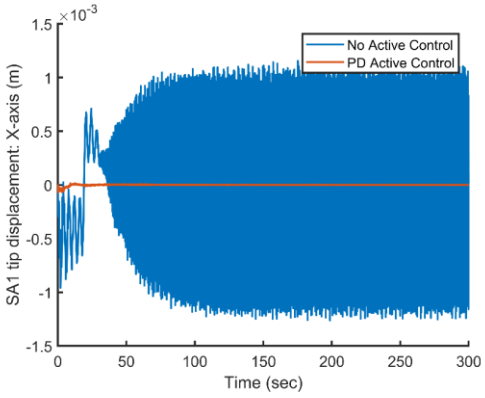

Fig. 7-49: Tip displacement of the Solar Array 1 – X-axis component

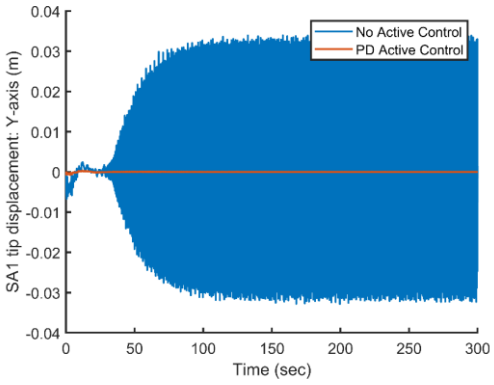

Fig. 7-50: Tip displacement of the Solar Array 1 – Y-axis component

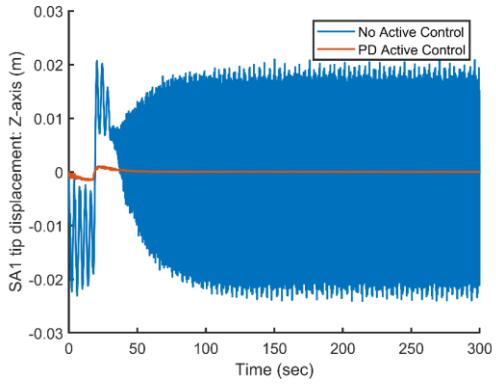

Fig. 7-51: Tip displacement of the Solar Array 1 – Y-axis component

The time histories of the Euler's angles are depicted in Fig. 7-52. It can be noticed how the spacecraft is not able, in this case, to ensure a proper pointing at the end of the re-orientation manoeuvre without activating the vibration suppression system. The commanded fires to the spacecraft thrusters in case of active control are therefore reported in Fig. 7-53.

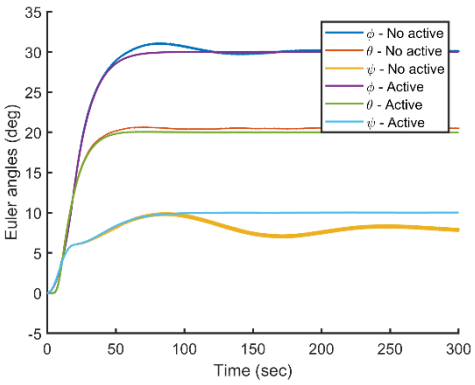

Fig. 7-52: Euler's angles

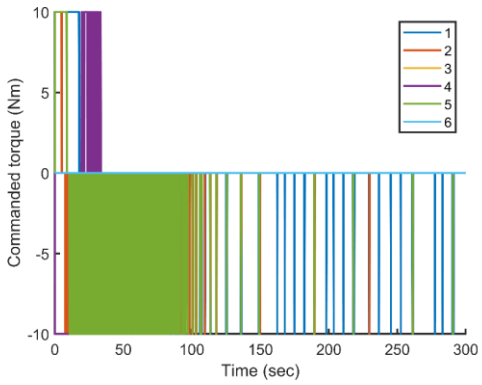

Fig. 7-53: Commanded force to thrusters

The behaviour of the input and output voltages is illustrated in Fig. 7-54 and Fig. 7-55. The input voltages do not reach the saturation condition, and it can be observed the action of the thrusters firing after 150 seconds, thus requiring the active vibration control to occasionally damp out the vibration when the RCT system is switched on. Again, the mean power required to the system is computed based on the method described in eq. (7.31), resulting to be about 25 W.

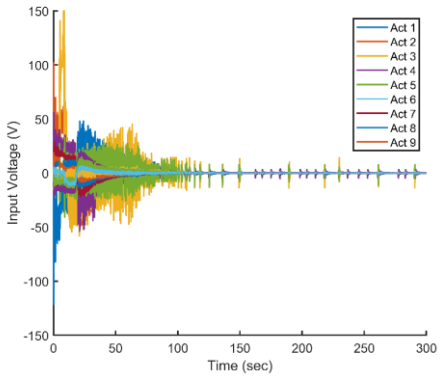

Fig. 7-54: Input Voltage

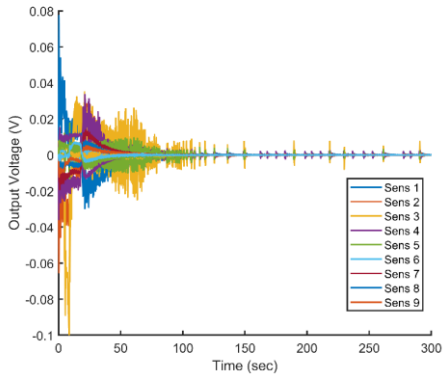

Fig. 7-55: Output Voltage

In Fig. 7-56, the spacecraft attitude before and after the re-orientation manoeuvre is depicted in the simulator data post processing tool. In detail, the coloured axes

indicate the orbital reference frame (in a black dotted line the nadir axis and in green the other two) and the body reference frame (in a red dotted line).

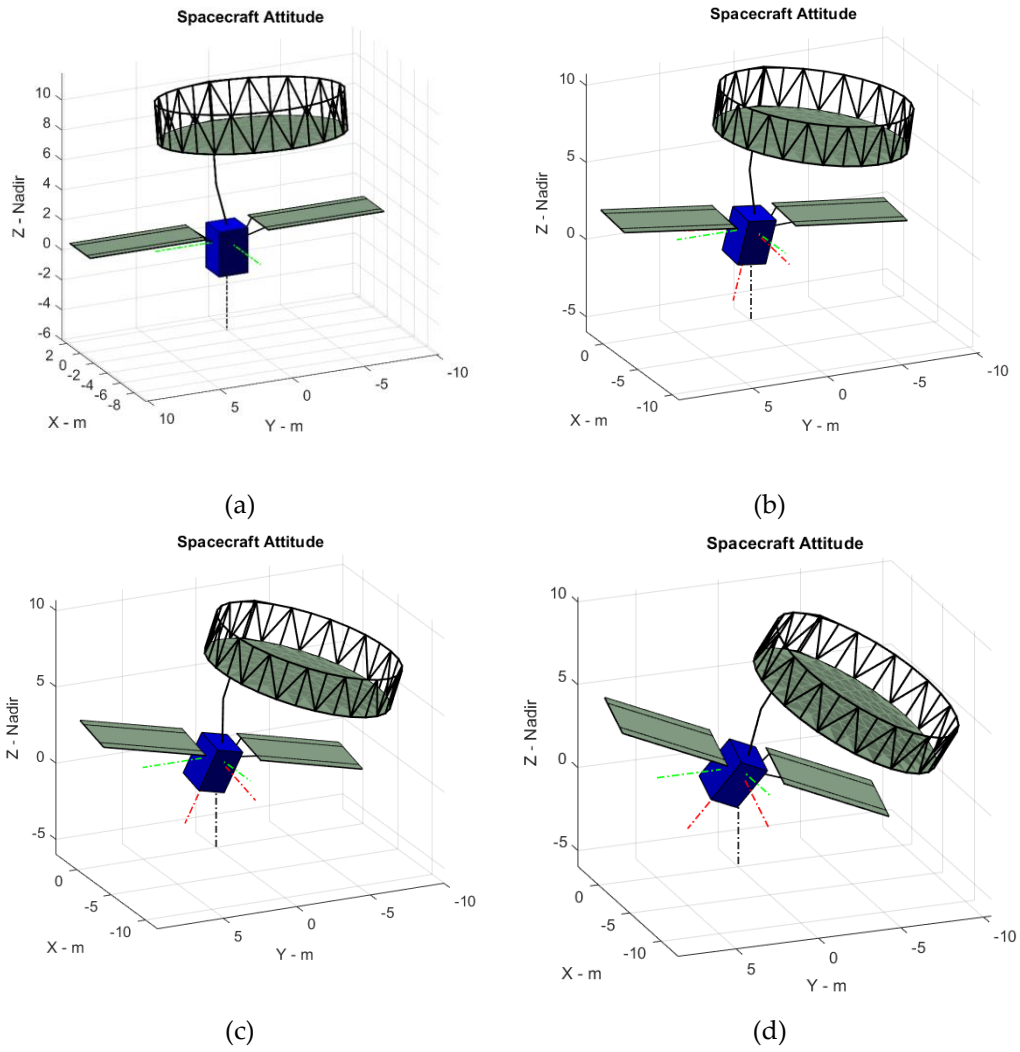

Fig. 7-56: (a) Spacecraft attitude at the beginning of the manoeuvre; (b) spacecraft after t=20 s; (c) spacecraft after t=60 s; (d) spacecraft after t=150 s

7.3.3 CONCLUSIONS

In this chapter, a simulator of an in-orbit flexible spacecraft has been presented. In detail, attention has been paid particularly to the implementation of realistic models of piezoelectric actuators and sensors for a distributed active vibration control system based on the results presented in Chapter 5. The system proved to be able to damp out undesired vibration and to avoid a coupling

between rigid and flexible dynamics, being also affordable, from a required power point of view, from most of Earth Observation (EO) modern missions. Future work will require the implementation of orbital environment as drag, magnetic and solar radiation pressure torques, as well as different types of actuators (as control moment gyros, magnetorquers and others) and attitude estimation algorithms.

BIBLIOGRAPHY

[1] C. Lin et al., *Modelling and Analysis of Characteristics of a Piezoelectric-Actuated Micro-/Nano Compliant Platform Using Bond Graph Approach*, Micromachines (Basel). 2018 Oct; 9(10): 498;

[2] J. Tzen et al., *Modeling of piezoelectric actuator for compensation and controller design*, Precision Engineering, 27 (2003), 70-86

[3] H. Yang, W. Zhu, *A Modified Comprehensive Model for Piezoelectric Stack Actuators and Corresponding Parameter Identification Method*, Advances in Materials Science and Engineering, Vol. 2015;

[4] Z. Zhou, X. Zhou, *A Novel Fractional Order Model for the Dynamic Hysteresis of Piezoelectrically Actuated Fast Tool Servo*, Materials, 2012, 5, 2465-2485

[5] H. Jung, D.G. Gweon, *Creep characteristics of piezoelectric actuators*, Review of Scientific Instruments 71(4):1896-1900, April 2000;

[6] Y. Luo et al., *Active vibration control of a hoop truss structure with piezoelectric bending actuators based on a fuzzy logic algorithm*, Smart Materials and Structures, Volume 27, Number 8, 2018;

[7] A. Preumont, *Vibration Control of Active Structures, Solid Mechanics and Its Applications*, Third Edition, Springer Netherlands, 2011;

[8] https://www.st.com/resource/en/application_note/dm00188713-signal-conditioning-for-shock-sensors-stmicroelectronics.pdf, accessed on December 1st 2020;

[9] J. S. Wilson, *Sensor Technology Handbook*, Newnes, 2005

[10] J. Chen, *Helium thruster propulsion system for precise attitude control and drag compensation of the Gravity Probe-B satellite*, PhD thesis, Department of Aeronautics and Astronautics , Stanford University, 2003

[11] F. Ankersen, *Guidance, Navigation, Control and Relative Dynamics for Spacecraft Proximity Maneuvers*, Doctoral thesis, Aalbord University, December 2015;

[12] F. Angeletti, P. Gasbarri, M. Sabatini, P. Iannelli, *Design and performance assessment of a distributed vibration suppression system of a large flexible antenna during attitude manoeuvres*, Acta Astronautica, Volume 176, November 2020, Pages 542-557;

[13] S. R. Vadali, J. L. Junkins, *Optimal open loop and stable feedback control of rigid spacecraft attitude maneuvres*, J. Astronaut. Sci. 32 (January–March) 105–122, 1984;

[14] B. Wie, P. M. Barba, *Quaternion feedback for spacecraft large space maneuvres*, J.

Guid. Contr. Dynam. 8 (May–June, 360–365, 1985;

[15] B. Wie, H.Weiss, A. Araphostasis, *Quaternion feedback regulator for spacecraft eigenaxis rotations*, J. Guid. Contr. Dynam. 12 (May–June), 375–380., 1989;

[16] K. J. Bathe, J. Dong, *Component mode synthesis with subspace iterations for controlled accuracy of frequency and mode shape solutions*, Computers and Structures 139, 28–32, 2014.

Part II

Chapter 8
LEARNING-BASED APPLICATIONS

The aim of this chapter is to design and implement learning-based strategies suitable to address specific issues of modern space activities. Concerning failure identification problem, a supervised Deep Learning technique is presented to identify the damage in large space structures. Regarding repetitive in-orbit operations, typical for EO manoeuvres, the attitude control of a spacecraft with sloshing propellant and of a small platform (as a CubeSat) is addressed. The strategies are verified by developing suitable mathematical models for numerical simulations.

Many in space activities could benefit by modern machine learning-based algorithms. Currently, a large share of space research activities is focussing on increasing the on-board autonomy and awareness of the future generation of satellites. Indeed, cutting-edge solutions to improve spacecraft decision-making capabilities and enable autonomous in-orbit operations have been given growing interest in recent years. In this scenario, two main fields have been addressed in this chapter: to improve the awareness of the system, a Fault Detection and Identification (FDI) scheme is developed based on Deep Learning, and to increase the autonomy of the satellite in performing specific repetitive tasks, as data acquisition, an attitude controller based on the concept of Iterative Learning Control (ILC) is proposed.

8.1 DEEP-LEARNING FOR FAILURE DETECTION AND IDENTIFICATION

Nowadays, the interest in autonomous on-board failure detection capabilities is constantly increasing, both to guarantee a prompt responsiveness to

emergency/damage situations and to avoid processing the huge amount of telemetry data downlinked from the spacecraft [1]. Furthermore, in view of the future spacecraft maintenance missions, there exists a relevant need to assess the conditions of spacecraft candidates for prospective repairing, in order to decide whether the operation is convenient, for instance by implementing a FDI approach. Therefore, researching possible techniques aimed at identifying local damages will be a crucial step to boost the technological advancement of in-orbit services.

8.1.1 Overview of FDI approaches for space systems

Over the past decades, several techniques have been studied to perform diagnosis and failure analysis for space systems. Such strategies are still mostly based on traditional methods, which can be divided into two branches [2]: *physical redundancy*-based approaches, where the presence of redundant hardware system is needed (with consequent increase in weight and costs of the satellite system), and *analytical redundancy*-based systems, which use models reproducing the physical system to simulate certain processes and compare them with the behavior of real hardware. In particular, the second philosophy has the advantage of not having to mount additional components on the satellite and will be the approach followed in this thesis.

Among traditional methods that have been investigated and implemented in the framework of analytical redundancy for space systems, one can mention parity space [3], observers-based (such as Unknown Input Observers [4][5]) approaches, Kalman Filters or Particle Schemes [6]. Recently, methodologies based on data analysis - such as Machine Learning – are being increasingly adopted to address damage/failure detection and identification problems to achieve a wider range of applicability. Neural Networks, or Artificial Neural Networks (ANNs), have been used in the field for years. However, such systems initially found only partial success, as their performance can be influenced - without the necessary precautions - by some disturbances, such as the presence of noise in the training-sets. Therefore, in order to overcome such limitations, Deep Learning (DL) techniques have been introduced both as data extractors and classifiers. Some of the most diffused techniques to automatically extract fault features are indeed Convolutional Neural Networks (CNNs), obtaining excellent results even for noisy data-sets [7][8]. Also, Support Vector Machine (SVM) philosophy has been

used to regress satellite data to identify satellite operating modes and telemetry parameters for Fault Diagnosis, as described in [9]. Another major field of research in this field is Data Mining: such an approach allows to obtain a more detailed knowledge of the state of the satellite from the enormous amount of data transmitted to the ground (such as the operational state of each subsystem of the satellite), by identifying patterns and tendencies in the received data [10]. In general, DL techniques – being data driven - are also very efficient in predicting failures considering the non-linearities related to satellite dynamics [9]. In particular, two studies funded by the European Space Agency (ESA) can be mentioned as preliminary studies of FDI solutions aboard satellites using Artificial Intelligence The first, SMART-FDIR (2003) [11], investigated the possibility to implement a software based on Fuzzy Inductive Reasoning (FIR), developing a demonstrative prototype on which to test the algorithm; the second, AFDIR (2001) [12] proposed a methodology based on Kalman filtering, Bayesian networks and causal networks.

An up-to-date classification of machine learning-based methods for FDI can be found in [13], where an evaluation of the Machine Learning methods is proposed based on some fundamental parameters for an FDI architecture. In detail, DL algorithms can offers relevant advantages – such as recognizing features automatically, learn complex data structures due to their deep architecture and avoid using feature extractors – with respect to other approaches as SVM, ANN and Naïve Bayes. Also, DL networks results to be very effective when dealing with big amount of data, at the expense of a loss of physical meaning of their configuration and long training processes, common to methods based on Neural networks. Recently, a new type of DL algorithms, known as Long Short-Term Memory Neural Networks (LSTM-NN), have been applied to Failure Identification problems. In 2020, Lee et al. [14] proposed a DL model based on LSTM-NN to identify the failures of an attitude control system of a CubeSat, based on three reaction wheels. However, applications of such networks for FDI at structural level are still quite limited.

Hence, a methodology based on a state-of-the-art supervised Deep Learning (DL) technique is here proposed for the study of a large in-orbit flexible spacecraft. A framework composed of a stacked Long Short-Term Memory Neural Network (LSTM-NN) is presented to address the structural failure identification problem in large space flexible appendages. Therefore, the problematic can also be thought as

a Structural Health Monitoring (SHM) issue. The procedure is set as a sequence-to-label classification problem: time histories of the acceleration profile of some points in the structure (assuming to have three-axis accelerometers hosted on the structure) are acquired, pre-processed and then fed to the LSTM to classify the damage condition.

8.1.2 PROBLEM SETUP

This section presents the study case on which the presented Deep Learning scheme will be applied. To propose a model to be representative of the dynamics of an Earth Observation (EO) satellite, the spacecraft equipped with a mesh reflector and two solar panels (introduced in Par. 5.6.2) is selected. The model has been reproduced in MSC Nastran and discretized in a rich mesh (about 3000 nodes) to ensure modelling properly its dynamic behaviour. An overview of the model is reported for clarity's sake in Fig. 8-1.

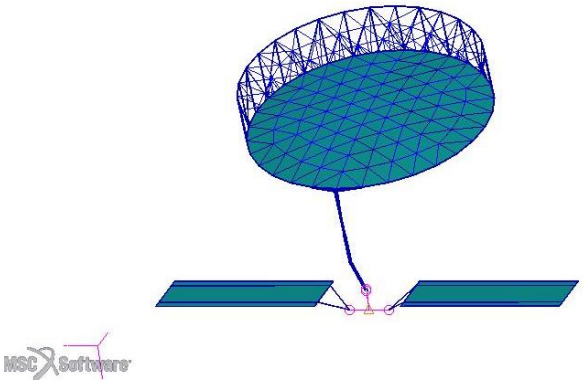

Fig. 8-1: Test case overview (MSC Nastran model)

As the proposed DL method adopts a supervised classification algorithm, a training dataset has to be generated. Therefore, several simulations of different three-axis attitude manoeuvres have been performed to collect realistic time histories from the accelerometer sensors hosted on the structure.

For what concerns the damages considered in this study, failures are expected to entail major repercussions on the system performance if occurring in one of the supporting elements of the mesh reflector. Indeed, a sudden decrease in the mechanical properties of a single critical member in the truss structure may lead to an unexpected redistribution of dynamic forces in the remaining members and also lead to the failure of the entire structure [15]. In this case, the damage is

defined as the total failure of one or more beam elements in the structural model of the truss, to reproduce either a possible fault of a joint/deployment mechanism or a failure related to debris impact or other causes. To reproduce the dynamic behaviour of a damaged structure, the pre-defined faulty elements are directly deleted from the finite element model. Once the number of damaged structural sub-models – as deriving from the original undamaged one – is defined, the data are extracted from the finite element suite and imported in Matlab to perform further analysis (see Fig. 8-2). At this point, a non-linear simulator of the flexible dynamics of spacecraft (implementing the equations reported in Chapter 3) is used to carry out several attitude manoeuvres to produce measurements from accelerometers sensors mounted in some specific points of the structure.

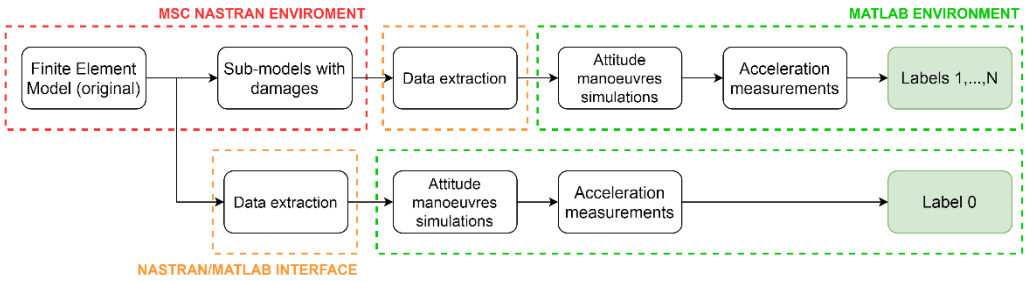

Fig. 8-2: Training-set generation logic

In this work, a PD-controller is assumed to produce the desired command torque profile u to be exerted on the spacecraft, as in

$$u = -\boldsymbol{K}_D \omega - \boldsymbol{K}_P \bar{q}_e^I \, sign(q_0) \tag{8.1}$$

where ω is the angular rate of the satellite, $\bar{q}_e^I$ is the error quaternion as defined in Par. 7.3.1, q_0 is the scalar component of the quaternion, $\boldsymbol{K}_D$ and $\boldsymbol{K}_P$ are the derivative and proportional gain of the controller respectively. The dataset of possible manoeuvres is built by varying properly both the desired final Euler's angles of the manoeuvre (considering also one and two-axis manoeuvres to improve the variation of the data collection) and the gains of the controller. Then, data for the accelerometers are collected to build the Input dataset to the LSTM network. Finally, a specific label is associated to each acceleration time history to build the Output dataset. In detail, the label 0 corresponds to an acceleration profile deriving from the undamaged model, and labels with numbers from 1 to N – where N is the total number of damage configurations considered in the study – to different damage arrangements. Once the final dataset is assembled, the data

are fed to the network for the training and validation process.

8.1.2.1 TRAINING-SET GENERATION FOR THE STUDY CASE

In this study, for demonstration purposes, three models have been realized: a nominal model (the undamaged structure) and two sub-models with a failure in different elements of the mesh reflector supporting structure, namely Failure 1 and Failure 2, as indicated in Table 8-1. However, the approach can be easily extended to consider more configurations of damage to be classified. An overview of the physical failures in the finite element model is reported in Fig. 8-3 and Fig. 8-4.

Table 8-1: Damage configurations and related labels

Damage configuration	Damaged Element ID	Associated label
Undamaged	-	0
Failure 1	Elm 4137	1
Failure 2	Elm 4152	2

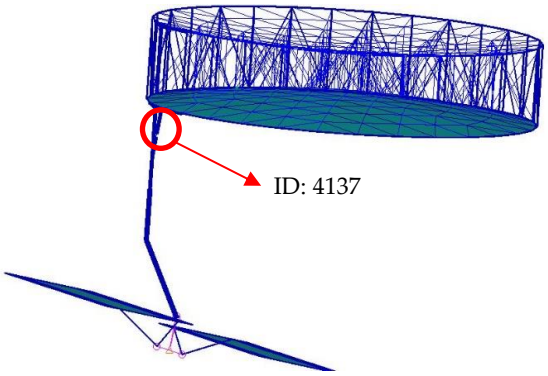

Fig. 8-3: Failure 1 (Element ID: 4137)

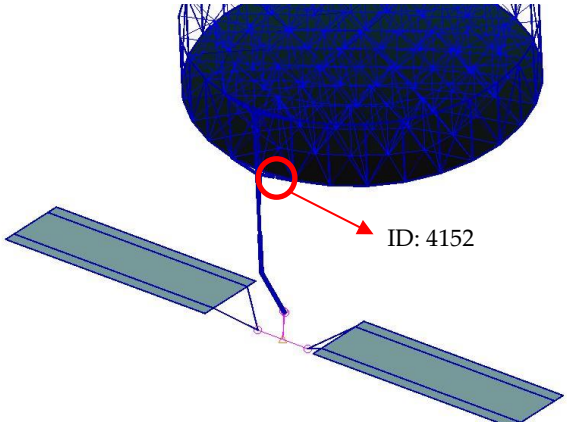

Fig. 8-4: Failure 2 (Element ID: 4152)

As already mentioned, it is assumed to have mounted on the appendage accelerometer sensors to measure the time response of some critical points of the model in different attitude manoeuvres. In detail, two accelerometers are considered: the first one is hosted at the tip of the antenna, while the second one is assumed to be positioned at the center of the supporting net of the antenna.

Table 8-2: Sensors position

Sensor ID	Position (Element ID)	Measured quantity
1	Elm 75	X,Y,Z acceleration (m/s²)
2	Elm 1246	X,Y,Z acceleration (m/s²)

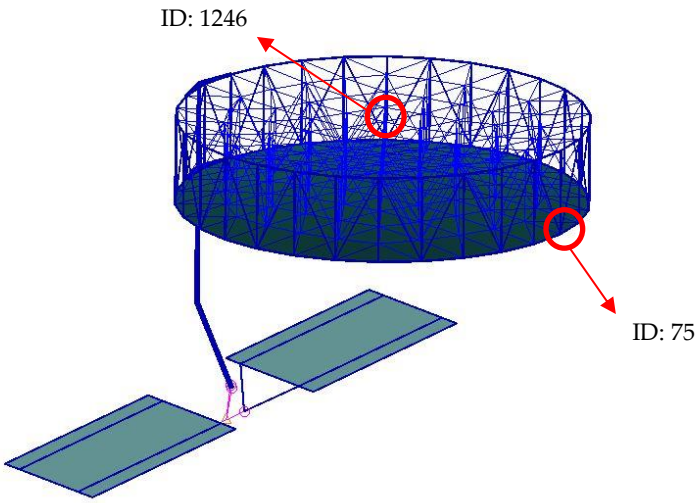

Fig. 8-5: Sensors location

Once defined the architecture of the system, the data are prepared to be fed to the neural network. However, some considerations have to be made:

- The most relevant dynamic content of the acceleration time sequences is detected in the first-time instants of the manoeuvre. Indeed, after the rotation of the satellite has occurred, the system returns to a stationary condition and the measurements go to zero. Therefore, the time histories have to be trimmed to avoid including in the dataset the components (equal to zero or under a certain threshold) which not only would not be representative of the specific dynamic behaviour, but would also contribute to flatten the dataset and compromise a proper classification of the failure;

- A pre-processing of the data is required to re-scale all the variables belonging

to the multi-dimensional training-set by using a standardization process, which is more practical for most machine-learning algorithms. According to such method, all the variables X (which are different acceleration time sequences in this case) are brought on the same scale. In particular, a strategy to centre the variables at their mean zero with a unit standard deviation is utilized, as reported below

$$\bar{X}(i,j,k) = \frac{X(i,j,k) - \mu_X(i,j)}{\sigma_X(i,j)}, \quad i = 1,...,N_A, \quad j = 1,...,N_M, \quad k = 1,...,T \tag{8.2}$$

where $\bar{X}$ is the standardized variable, μ_X is the mean value of the variable, σ_X is the standard deviation of the variable, N_A is the number of accelerations time sequences (i.e. $N_A = 3 \cdot n_S$, where n_S is the number of sensors, which collect data along the three coordinated axis X,Y,Z), N_M is the number of manoeuvres which have been performed to produced the training set and T is the number of time samples of the acceleration time histories. Concerning this study case, more information on the architecture of the multivariate training-set is reported in Table 8-3.

Table 8-3: Details on the multidimensional training-set

	N_A	N_S	T
Training-set details	6	38	301

In particular, a sampling time of 0.1 seconds is considered for the accelerometers, so that $T = 301$ samples correspond to the first 30 seconds of the spacecraft dynamics. By using this method, the variables are normally distributed, making the learning process faster and easier. Also, a Gaussian noise equal to the 2% of measured values is considered when acquiring the data from the accelerometers to simulate a realistic condition.

8.1.3 LSTM ARCHITECTURE AND RESULTS

Recently, Long Short-Term Memory Neural Networks (LSTM-NNs) [16] have become increasingly adopted to take advantage of data long-term dependencies,

in order to overcome the error flow in the existing Recurrent Neural Networks (RNN) and to efficiently tackle problems where the current time step is very far from relevant information. Indeed, by connecting several layers of LSTMs, thus introducing the capability of handling past information in a single cell, it has been found that Deep Neural Networks architectures can improve their performance. Such results have been confirmed in several studies, including time series forecasting [17][18][19] and for both univariate and multivariate time sequence classification problems [20].

In detail, a LSTM layer is composed of a group of N_H hidden units – which are recurrently connected blocks. Each unit computes at time n a scalar output or hidden state h_n^m and a scalar cell state c_n^m, with $m = 1,...,N_H$. Therefore, the output of a set consists in the vectors h_n and c_n, which represent the whole hidden and cell states of the layer at that time instant (see Fig. 8-6).

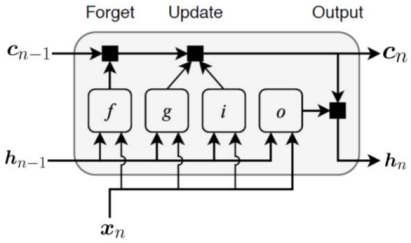

Fig. 8-6: Hidden unit

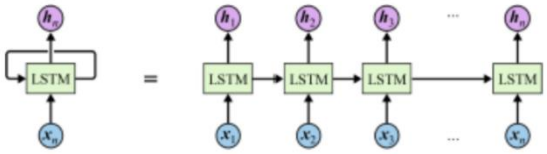

Fig. 8-7: Equivalence of un-folded LSTM network

The inputs of each hidden units are the current and n_{i-1} previous samples, previous hidden states h_{n-1} and cell states c_{n-1} (stemming from itself and other units). At each time instant, the layer updates itself by adding or removing information from the cell state. This process is performed through the gates of each hidden unit, which are:

- Input gate i, which regulates how much of the current state has to be imputed to the layer to compute the new state

$$i_n^m = \sigma_g\left(w_i^m x_n + r_i^m h_{n-1} + b_i^m\right) \tag{8.3}$$

- Forget gate f, which regulates how much of the previous state has to be retained

$$f_n^m = \sigma_g\left(w_f^m x_n + r_f^m h_{n-1} + b_f^m\right) \tag{8.4}$$

- Cell candidate g, which regulates the memory of the past

$$g_n^m = \sigma_c\left(w_g^m x_n + r_g^m h_{n-1} + b_g^m\right) \tag{8.5}$$

- Output gate o, which regulates how much of the internal state has to be let though other layers and successive time instants

$$o_n^m = \sigma_g\left(w_o^m x_n + r_o^m h_{n-1} + b_o^m\right) \tag{8.6}$$

where $\sigma_g = \left(1 - e^{-\alpha}\right)^{-1}$ and $\sigma_g = \tanh(\alpha)$ are a sigmoid and hyperbolic activation functions, w vectors represent the input weights to the gates, r the recurrent weights, b scalars representing the LSTM biases. Then, the cell state is given by

$$c_n^m = f_n^m c_{n-1}^m + i_n^m g_n^m \tag{8.7}$$

while the hidden state is

$$h_n^m = o_n^m \sigma_c\left(c_n^m\right) \tag{8.8}$$

In Fig. 8-7, the equivalence between a recurrent representation and unfolded version of the LSTM layer is presented. This means the recurrent network (RNN) can be effectively replaced by cascade blocks where the hidden states are propagated. The final output y_n of the LSTM network a the n time instant is

$$y_n = \mathbf{W}_d h_n + b_d \tag{8.9}$$

with $\mathbf{W}_d$ and b_d are the terms indicating the weights and the biases of the layer.

8.1.3.1 PROPOSED ARCHITECTURE FOR CLASSIFICATION PURPOSES

In this research, a LSTM architecture will be used to carry out multivariate time sequences classification, as illustrated in Fig. 8-8. The neural network has been implemented in Matlab environment. A first sequence layer is set to fix the data structure for backward training and feedforward test at each time instant. Then, two bi-directional LSTM (or Bi-LSTM) are interspersed by a drop-out layer. In detail, as opposed to standard unidirectional LSTMs, which only preserve information of the past time instants of a sequence, Bi-LSTMs have the capability

to preserve both information from the past and the future time steps. Therefore, causal classification can be improved by letting each time sequence through two recurrent networks both forwards and backwards. In addition, the drop-out layer is used to limit the overfitting problem: at each time step, some random outputs of the first Bi-LSTM are hidden from the inputs of the second Bi-LSTM. Then, after the second Bi-LSTM, a fully connected network composed of three layers is stacked to the architecture to connect the hidden units of the LSTM to the output. Finally, the output layer is characterized by a cross-entropy error function and softmax activation function – which are a standard for classification [21].

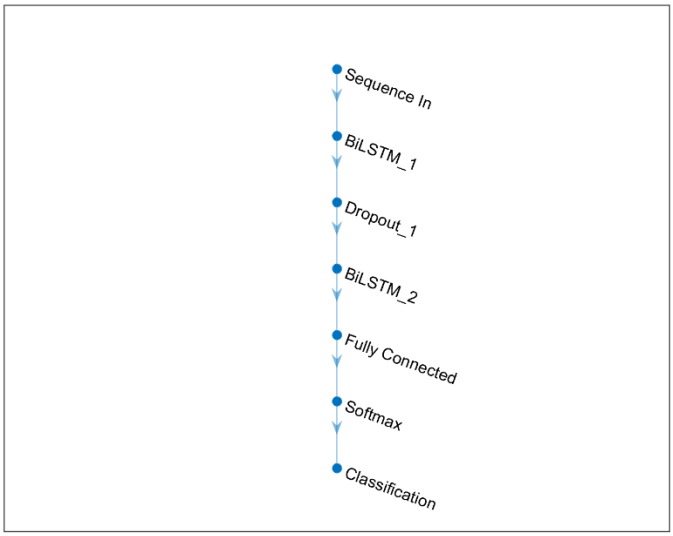

Fig. 8-8: LSTM-NN architecture overview

The training process consists in feeding the LSTM architecture with the prepared training-set (input-output pairs) to identify the matrices and bias reported in eq. (8.9) and train the network the non-linear relation which allows to classify them. Concerning the training algorithm, the adaptive moment estimation (ADAM) is used. The learning rate is initially set to 0.08 to train all models and gradually halved every 20 epochs. The hyperparameters of the architecture (as the number of dropout elements, hidden units, fully connected neurons) have to be decided. To set the best combination of these terms, preliminary tests are performed to heuristically select the parameters by observing their influence on the training process. In particular, the approach used to train the LSTM architecture is the so-called "key-folding", which consists in alternately selecting a sub-group of input-output pairs of the training set to test the performance of the

network. In detail, in this case, a 4-fold method have been adopted. Indeed, out of the total number of input-output pairs ($3 \cdot N_M = 114$, where 3 indicates the three considered labels 0, 1 and 2) for each fold $1/4$ of the data are used to test the LSTM trained with the remaining $3/4$ of the training set. The testing sub-set is repetitively chosen in a random way, being careful to not include any pairs that have been used in previous tests, so to fully exploit all of the available data at the end of the process. The procedure is repeated 20 times, initializing the network with different sets of parameters, so to gather a satisfactory statistic and decreasing the performance dependence upon the specific initial sets of matrices of the LSTM. A part from the use of a drop-out layer, further precautions have been taken to avoid the network overfitting, such as keeping the network architecture as simple as necessary (i.e. including only up to 60 and 30 neurons for the first and second Bi-LSTM layers respectively), use a k-folding training technique and applying an early stopping criterion (i.e. defining the number of times - set as 3 - that the loss on the validation set can be larger/equal to the previously smallest loss before network training automatically stops).

8.1.3.2 RESULTS

The effectiveness of the proposed Deep Learning Neural Network is verified through the k-fold process. The main results are reported in this paragraph. The performance of the LSTM architecture in terms of classification accuracy and error for a time sequence composed of 301 samples (30 seconds) is listed in Table 8-4.

Table 8-4: LSTM-NN performance after training (T=301)

LSTM Performance	Mean Value	Deviation
Classification accuracy	94.79%	1.89%
Classification error	5.21%	1.89%

The network guarantees good results, being able to associate an acceleration time sequence with the correspondent model with an accuracy of above 95%. It should be remarked that the accuracy of the network depends also on the pre-processing of the training-set. Indeed, it has been noted that, by implementing a different standardization on the overall dataset – although without re-tuning the hyperparameters of the network - the results can also reduce to reach a minimum

accuracy of above 45% in case of a standardization based on the minimum-maximum values of the dataset, which re-scales the variables in a range between 0 and 1. Therefore, the standardization based on the mean value/standard deviation of the training set is to be preferred in this case. The mean confusion matrix of the trained LSTM network is illustrated in Table 8-5. This solution allows to visualize the performance of the algorithm in classifying the acceleration measurements and associated them with the corresponding undamaged or damaged condition.

Table 8-5: Average confusion matrix (T=301)

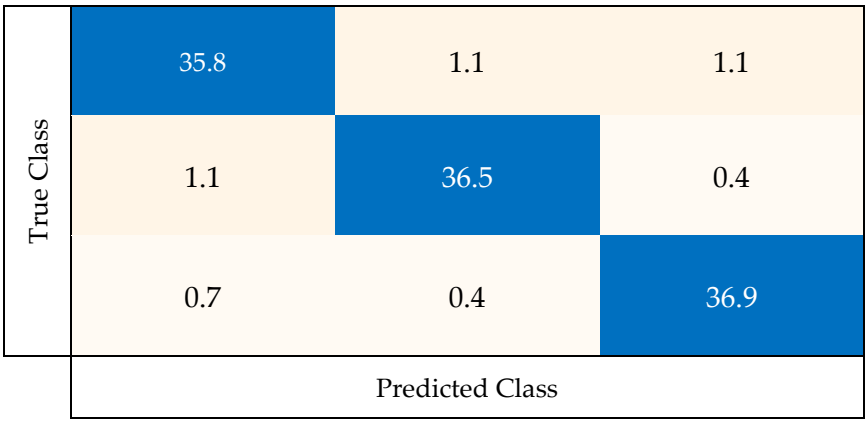

In addition, the behaviour of the LSTM has been studied when changing the length of the measurement time sequence in the training set. Indeed, three two additional tests have been performed: one truncating the sequence at the first second of the manoeuvre, the other one by increasing the length of the time history from 30 sec to 60 sec. In Table 8-6, the results are illustrated based on the length of the time sequence (the term $\boldsymbol{t_f}$ indicates the corresponding duration in seconds).

Table 8-6: LSTM-NN performance after training

LSTM Performance	$\boldsymbol{t_f = 1s}$	$\boldsymbol{t_f = 30s}$	$\boldsymbol{t_f = 60s}$
Classification accuracy	96.27% ±1.66%	94.79%±1.89%	91.31%±5.79%
Classification error	3.73%±1.66%	5.21%±1.89%	8.69%±5.79%

The network demonstrates to be able to effectively associate a time sequence to the corresponding label even if just one second of the acceleration time history is considered. Also, the mean confusion matrix of the trained LSTM network when considering time sequences up to 1 second is illustrated in Table 8-7.

Table 8-7: Average confusion matrix ($t_f = 1s$)

True Class \ Predicted Class			
	36.2	0.8	1.0
	0.6	36.9	0.4
	0.9	0.4	36.65

The network demonstrates to be able to effectively associate a time sequence to the corresponding label even if just one second of the acceleration time history is considered. This means that the proposed architecture can effectively produce a prompt response, as a FDI method, to make the satellite autonomously aware of an issue in the very first instant of an attitude manoeuvre. This result can be used, for instance, to produce an alarm signal and/or to promptly discard data acquired during a manoeuvre which is not nominal, saving time and on-board memory.

8.1.4 CONCLUSIONS

This study aimed at demonstrating that LSTM-NNs can be a promising candidate to perform FDI tasks on-board satellite, to improve their autonomy and awareness. In particular, the considered application, i.e. damage classification for large space structures, has proved to lead to very good performance. The results pointed out the importance of selecting a proper method for pre-processing the data and the impact of the time sequence length on the final performance of the network. Also, the LSTM network proved to be able to identify damage even if the damaged elements are close to each other.

As future developments, to design a general framework to classify failures in different areas of the structure, a larger dataset of damaged configurations will be considered, eventually also introducing several levels of damage to be identified. However, even though in this preliminary study the dataset is reduced, the LSTM

architecture still managed to produce good results. Hence, the accuracy of the neural network is not expected to decrease if enlarging the dataset (by re-tuning the hyperparameters). To conclude, automatic tailoring of the input time sequence could be introduced to let the network decide which time instants are more relevant for classification purposes.

8.2 CONTROL OF A SPACECRAFT WITH SLOSHING PROPELLANT

Currently, most of remote sensing and surveillance space missions are required to perform a periodical sweep over a prescribed terrestrial area to detect eventual changes at different times but with same illumination conditions and spacecraft orientation. In general, those space systems take repetitive ground track orbits to obtain revisiting capability over the desired area. Therefore, the entire mission can be considered as the repetition of several identical tasks. The spacecraft orientation should be cyclically modified to be identical during the data acquisition process orbit after orbit. In this case, the spacecraft is a repetitive dynamic system and major disturbances are repeating themselves as well. Therefore, learning from the available on-orbit data collected during the mission can be a relevant advantage. An effective improvement in control system performance and autonomy can be obtained implementing learning-based strategies, opportunely modified to adapt themselves to specific mission requirements. Due to the repetitive nature of most space operations, the Iterative Leaning Control (ILC) appears to be a promising tool for the purpose. In general, ILC approach can be applied to repeatedly operated dynamic systems. Indeed, the ILC is well suited for self-improving attitude control performance of satellites due to the possibility to collect and elaborate information gained during the previous consecutive orbits. The control system can improve attitude tracking precision for those manoeuvres that are repeated orbit by orbit, compensating for cyclic orbital disturbances such as gravity gradient, atmospheric drag, solar radiation pressure and liquid fuel sloshing effects.

In literature, different methods for improving space systems performance when performing re-orientation manoeuvres can be found. To cite some of them, the attitude tracking of a spacecraft impacted by periodic disturbances is improved by using a learning-based strategy in [22]. The evaluation of a fitness function of the satellite attitude error is used to optimize the parameters of a satellite control scheme in [23]. Concerning target capturing, a Reinforcement Learning technique is adapted to re-stabilize the attitude of a spacecraft after the contact phase. Moreover, one of the uses of learning-based methods is to compensate for un-modelled dynamics, which is an advantageous characteristic suitable to control design for space systems. Indeed, modern satellites are often equipped with large tanks containing a relevant amount of liquid fuel to accomplish both attitude manoeuvres and station keeping. Consequently, the periodic movement of the

spacecraft provoke a cyclic agitation of the fuel. The slosh phenomenon may be defined as oscillations of the free surface of a fluid on a partially filled container. Therefore, the GN&C (Guidance, Navigation and Control) subsystem performance may be heavily affected by the sloshing effects of the liquid put in motion inside the propellant containers, also due to possible coupling between fuel and structure dynamics [25][26]. However, in general, the combined liquid-spacecraft dynamics is difficult to be analysed and some simplification have to be carried out. Hence, equivalent mechanical models can be designed to consider the complete system dynamics while deriving a control strategy. Some examples are: spring-mass-damper idealization to reproduce the linear lateral sloshing modes [26][27], pendulum model to represent the variation of the natural frequencies when acceleration of the system is modified [28][29] and a spherical pendulum model to simulate nonlinear rotary sloshing [30][28].

Thus, the on-orbit available information can be processed by a learning algorithm to reconstruct the dynamics of the system in more detail and to directly change the control actions to reduce the satellite instrument pointing errors deriving from couplings between the fluid and the structural dynamics. In [31], the sloshing effect is reduced by using optimization techniques based on evolutionary methods as Neural Networks and Genetic Algorithms applied to a system hosting a rectangular tank.

However, still very few literature can be found related to the application of machine learning to the attitude control of a spacecraft with fuel slosh. Moreover, in general such methods implies high computational costs, often not affordable for current on-board spacecraft computation and memory capacities. In this thesis, a learning-based control law – based on available platform measurements, and also computationally efficient and compatible with on-board limitations - is applied to improve the attitude tracking performance of a satellite repeating the same orientation manoeuvre to acquire scientific data in different orbits [32].

8.2.1 MATHEMATICAL MODEL

In this section, a mechanical-analogy model is implemented to characterize the propellant sloshing phenomenon during a typical orientation manoeuvre for an Earth Observation (EO) spacecraft. The bus is modelled as a rigid body while the sloshing masses as internal bodies. The spacecraft is also equipped with two flexible solar arrays to investigate the interaction between the liquid movement

and the elastic dynamics of the panels (see Fig. 8-9). In the following sections, the mathematical formulation of the equivalent model is presented and the implementation of the system in a commercial multibody dynamics tool is discussed.

8.2.1.1 LATERAL SLOSHING EQUIVALENT MODEL

Lateral sloshing phenomenon can be considered as occurring when performing an attitude manoeuvre around a single axis (the X-axis in Fig. 8-9). In particular, a spring-mass-damper model has been adopted to simulate the dynamics of the fluid inside the tanks. This approach is based on transforming the liquid motion into some sloshing masses attached to springs and dampers. Either experimental tests or numerical tools can be used to determine the corresponding physical parameters.

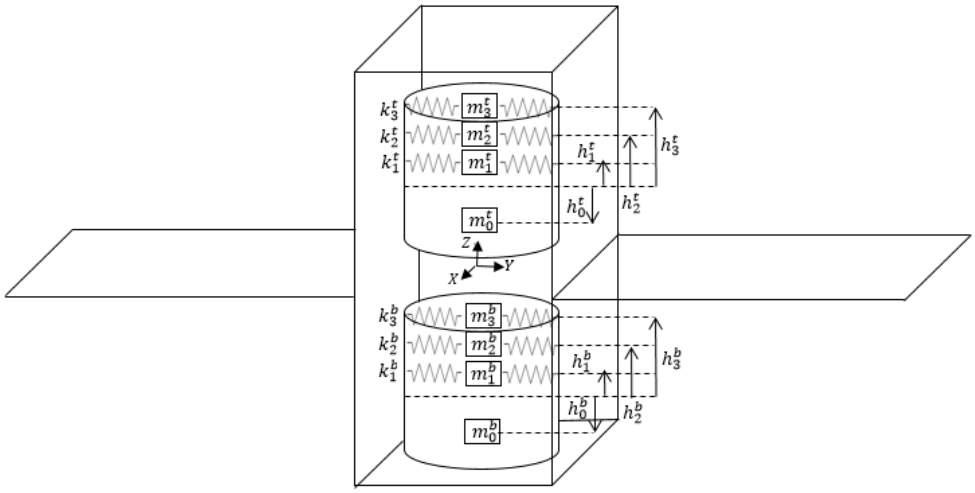

Fig. 8-9: Equivalent mechanical model of a spacecraft equipped with two solar panels and two tanks with fuel slosh

The spacecraft platform hosts two tanks, each containing different amounts and types of liquid propellant. In most literature, only the first sloshing mode represented by a single mass-spring model is considered and higher-order modes are neglected. In this study, more than one sloshing mass is instead considered in modelling the dynamics.

The fluid can be represented by both static and moving masses. The motionless part of the fuel is identified by a moment of inertia I_0 assigned to mass m_0 rigidly attached to the tank. The sloshing modes are modelled by using point

masses m_i, $i=1,...,N$, whose relative positions along the satellite Z-axis are defined by h_i, referred to the centre of the tank (as indicated in Fig. 8-9). The moments of inertia of the masses m_i are usually not taken into account. When perturbed from their neutral positions, those masses are subjected to an elastic force proportional to the spring constants k_i. The parameters $I_0, m_0, m_i, h_0, h_i, k_i$ are highly dependent on the properties of the fluid, the geometry of the tank and the fill ratio of the fuel tank [28]. The sum of all the masses should be equal to the fuel mass m_f and the centre of mass of the system at the same height as that of actual fuel. Such considerations can be translated into the following relations

$$m_0 + \sum_{i=1}^{N} m_i = m_f \tag{8.10}$$

$$m_0 h_0 + \sum_{i=1}^{N} m_i h_i = 0 \tag{8.11}$$

so that the properties m_0 and I_0 can be computed. Then, a 3D equivalent cylindrical tank is considered to derive the sloshing parameters. By assuming a constant propellant density, the height of the liquid inside the tanks is

$$h = \frac{4m_f}{\pi\varphi^2\rho} \tag{8.12}$$

where φ and ρ are respectively the diameter of the tank and the propellant density. Each sloshing mass is defined as follows

$$m_i = m_f \left[\frac{\varphi \tanh\left(2\xi_i h/\varphi\right)}{\xi_i\left(\xi_i^2 - 1\right)h} \right] \tag{8.13}$$

$$h_i = \frac{h}{2} - \frac{\varphi}{2\xi_i}\left[\tanh\left(\frac{\xi_i h}{\varphi}\right) - \frac{1-\cosh\left(2\xi_i h/\varphi\right)}{\sinh\left(2\xi_i h/\varphi\right)} \right] \tag{8.14}$$

$$k_i = \frac{m_i g}{\varphi} 2\xi_i \tanh\left(\frac{2\xi_i h}{\varphi}\right) \tag{8.15}$$

where g is the axial acceleration of the spacecraft (i.e. the acceleration along its z-axis depicted in Fig. 8-9) and ξ_i are constant parameters given by

$$\xi_1 = 1.841, \qquad \xi_2 = 5.329, \qquad \xi_i \simeq \xi_{i-1} + \pi \tag{8.16}$$

The acceleration is considered to be of the order of milli-g to reproduce a low-

gravity environment. By assuming that the liquid depth ratio for the cylindrical tank h/φ is lower than one (in this case radius equal to 0.7 m and height of 1.2 m), the following relation can be applied

$$I_0 = \left(1 - 0.85\frac{h}{\varphi}\right) m_f \left(\frac{3\varphi^2}{16} + \frac{h^2}{12}\right) - m_0 h_0^{\,2} - \sum_{i=1}^{3} m_i h_i^{\,2}, \qquad \text{if} \quad \frac{h}{\varphi} < 1 \tag{8.17}$$

Two tanks are considered in the model shown in Fig. 8-9, so that the variables referred to the top tank are defined by the apex "t" and those referred to the bottom tanks with the apex "b". The aforementioned equations have been used to obtain the sloshing parameters to be implemented in a commercial suite to simulate the dynamics of the system.

8.2.1.2 DYNAMIC MODEL ON MSC ADAMS SUITE

The system has been modelled by using a multibody dynamics software, namely MSC Adams. This is a Multibody Dynamics (MBD) commercial tool used to analyse articulated mechanical systems based on the principles of Lagrangian Dynamics. The code can solve both algebraic and differential highly non-linear equation as functions of time.

As far as the solar arrays are concerned, a realistic system would also include the presence of hinges, torsional springs and dampers to connect consecutive sections (see Fig. 8-10).

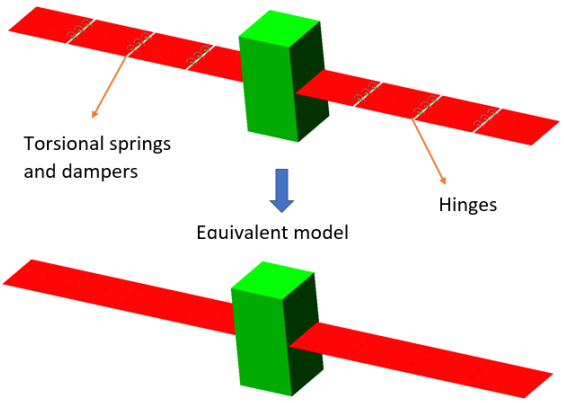

Fig. 8-10: MSC Adams solar arrays equivalent model

Due to the high computational costs related to such model in the Adams-Simulink simulation architecture, an equivalent monolithic structure has been adopted to perform the analyses. According to this approach, the allowed relative rigid rotations between each section of the panels are reproduced as an increased flexibility of the overall array.

The spacecraft is hereby represented as a parallelepiped platform with solar panels as appendages (respectively in green and in red in Fig. 8-11). The two tanks are modelled as bodies with assigned mass and inertia to reproduce a hollow cylindrical tank.

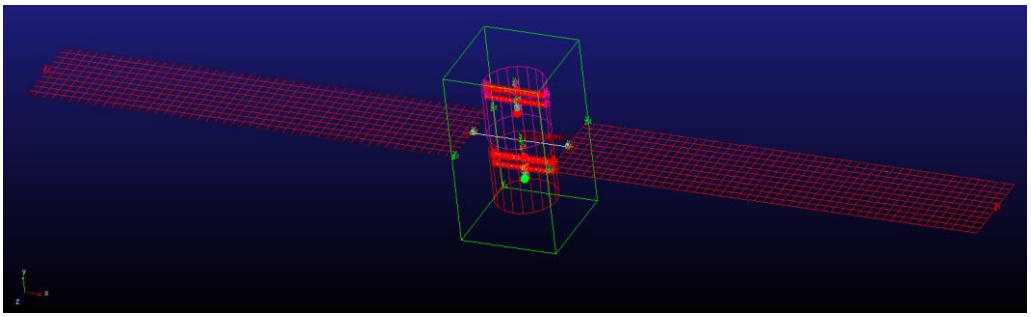

Fig. 8-11: MSC Adams dynamic model

The flexibility of the two solar panels is simulated by using FEM techniques. In particular, the two arrays are shell bodies meshed with Quad4 elements. The two tanks are rigidly connected to the platform to simulate their fastening to the satellite. A detailed image of a single tank is provided in Fig. 8-12.

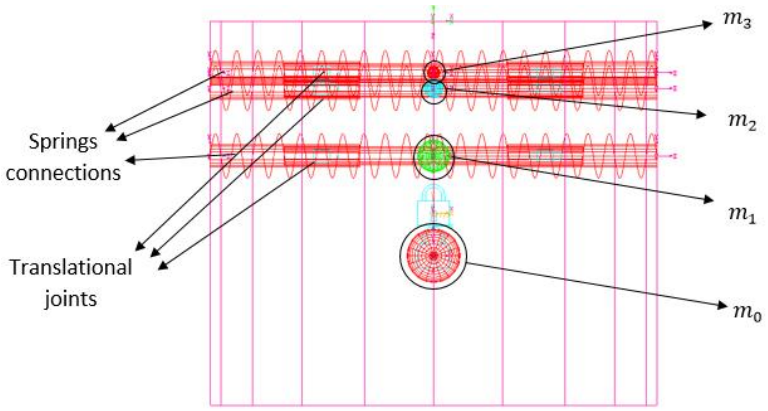

Fig. 8-12: Particular of the sloshing equivalent mechanical model in MSC Adams

The sloshing masses (m_1 in green, m_2 in blue and m_3 in red) have been modelled has spherical bodies with assigned mass deriving from eq. (8.13) and

negligible inertia. Their location with respect to the centre of the filled tank respects what expressed by eq. (8.14). Those masses have been connected via translational joints to the walls of the tank, so that they are constrained to move only in the horizontal direction to simulate the lateral sloshing behaviour. At the same time, two spring-damper forces are acting on each mass to reproduce the elastic forces they are subjected when moving from their equilibrium position (these forces are representative of the "elastic" properties of the fluid). The stiffness of each spring is computed by using eq (8.15). The red sphere in the lower part of the tank in Fig. 8-12 represents m_0 . Its position and value are derived from eq.s (8.10)(8.11), while its moment of inertia from eq. (8.17).

8.2.2 LEARNING-BASED CONTROL FOR ATTITUDE TRACKING

In most Earth Observation missions, the spacecraft is required to sweep a specific area with the same orientation orbit after orbit. One possible objective is to use the scientific instrumentation to acquire data of a strip, parallel to the satellite ground track (see Fig. 8-13). In this case, the mission can be divided into two phases: a first attitude manoeuvre to re-orient the payload and a sensing phase. In this investigation, only the first part of the mission is considered, as the sensing phase is a stabilization problem around the nadir-pointing condition.

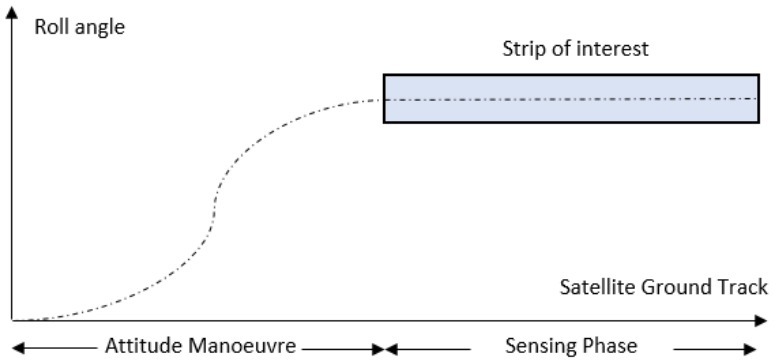

Fig. 8-13: Problem statement for an EO mission

As the satellite is repeatedly operated, the attitude control system could benefit by data available in-orbit to improve its attitude tracking performance. In this thesis, an Iterative Learning Control algorithm is used by exploiting the attitude errors and the control inputs from previous operations.

8.2.2.1 ITERATIVE LEARNING CONTROL (ILC)

The aim of the Iterative Learning is to generate a sequence of inputs such that the output of the system is as close as possible to the desired one, being the input the attitude control torque exerted about the spacecraft centre of mass while the output the desired attitude trajectory [33]. The inner core of the ILC strategy is to improve control inputs on the basis of previous operation data. The controller can learn to produce zero tracking error during repetition of a command or to eliminate the effects of a repeating disturbance.

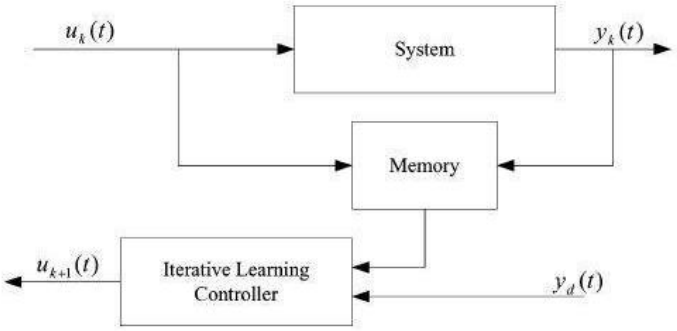

Fig. 8-14: Classical Arimoto's type ILC

To counteract a-periodic disturbances, a conventional feedback controller can be added in the control strategy to work in parallel with ILC. The scheme is named Current Cycle Feedback Iterative Learning Control (CCF-ILC). For those systems with dynamics uncertainties through iterations, a High-Order Iterative Learning Control (HOILC) is usually applied to the problem of tracking control [34]. The mentioned strategy uses more than one past error history in different iterations. In this section, a CCF-HOILC scheme is proposed. The control action at the iteration k (i.e. in a specific orbit) is given by the sum of the contributions as follows

$$
\begin{aligned}
&u_k = u_k^{FB} + u_k^{FF} = u_k^{FB} + u_k^{ILC} \\
&u_k^{FB} = K_P\left(\theta_d - \theta^k\right) + K_D\left(\dot{\theta}_d - \dot{\theta}^k\right) \\
&u_k^{ILC} = u_{k-1} + L\left(\sum_{i=1}^{3} l_i\left(\theta_d - \theta^{k-i}\right)\right) + D\left(\sum_{i=1}^{3} d_i\left(\dot{\theta}_d - \dot{\theta}^{k-i}\right)\right) \\
&\textit{with} \quad \sum_{i=1}^{3} l_1 = \sum_{i=1}^{3} d_1 = 1
\end{aligned}
\tag{8.18}
$$

where u_k^{FB} is the feedback control torque and u_k^{FF} is the HOILC feedforward term using data from up to three iteration before.

As a summary, the control strategy can be resumed in three steps:

- Choosing feedback gains so that the error dynamics along the desired trajectory is stable;
- Updating the feedforward term by the means of the learning rule;
- Composing the actual control input signal by using both HOILC and PD-feedback contributions (see Fig. 8-15).

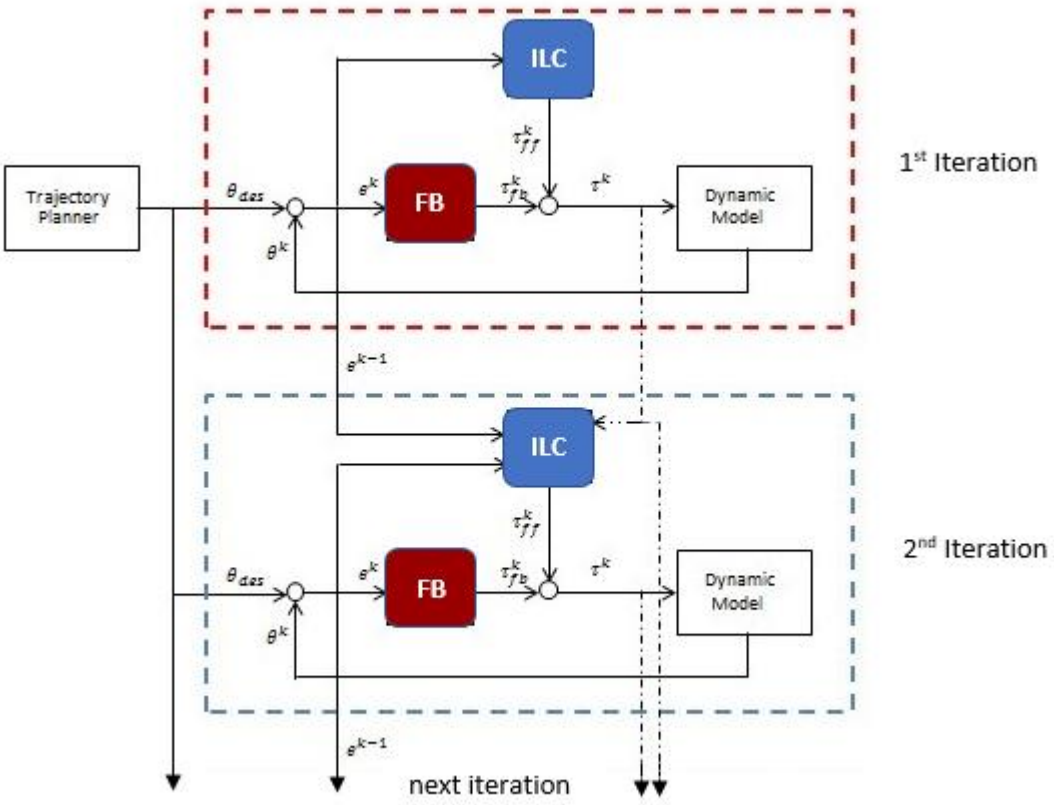

Fig. 8-15: Adopted control scheme

In this study, the selected gains are $K_P = 200$, $K_D = 500$, $L = 0.1$, $D = 300$, $l_1 = d_1 = 0.7$, $l_2 = d_2 = 0.2$, $l_3 = d_3 = 0.1$. In the next section, the simulation architecture is described by introducing the tools used for performing the dynamic analyses. The main results of the study are introduced and commented.

8.2.3 SIMULATIONS AND RESULTS

In this section, the manoeuvre depicted in Fig. 8-13 is investigated. A roll tilt of 35 degrees is considered to be required to accomplish the mission and reach the

sensing phase. The relevant data concerning the equivalent mechanical model used in the simulation is reported in Table 8-8, while Table 8-9 lists the bus and solar panels features.

Table 8-8: Propellant physical parameters

Parameter	Upper Tank	Lower Tank	Parameter	Upper Tank	Lower Tank
ρ	846 kg/m^3	1447 kg/m^3	k_1	1.12 N/m	1.91 N/m
h	1.12 m	1.05 m	k_2	0.1 N/m	0.16 N/m
m_0	1032 kg	1610 kg	k_3	0.04 N/m	0.07 N/m
I_0	188.49 $kg\ m^2$	348.14 $kg\ m^2$	h_1	0.22 m	0.19 m
m_1	412.23 kg	703.33 kg	h_2	0.43 m	0.39 m
m_2	12.49 kg	21.35 kg	h_3	0.48 m	0.44 m
m_3	3.04 kg	5.20 kg	h_0	0.09 m	0.09 m

Table 8-9: Platform properties

Parameter	Bus	Parameter	Solar Panel
m	2000 kg	m	191 kg
h	4 m	h	0.03 m
L	2.2 m	L	10 m
W	2.2 m	W	2 m
I_{XX}	3473.3 $kg\ m^2$	I_{XX}	63.9 $kg\ m^2$
I_{YY}	1613.3 $kg\ m^2$	I_{YY}	8650.8 $kg\ m^2$
I_{ZZ}	3473.3 $kg\ m^2$	I_{ZZ}	8626.7 $kg\ m^2$

The reorientation manoeuvre is carried out by means of a control torque exerted by on-board devices (e.g. reaction wheels or control moment gyros). Even if the fuel mass varies with respect to time during the manoeuvre, in this study the fuel consumption has been considered as negligible.

8.2.3.1 CO-SIMULATION

MSC ADAMS is a Multibody Dynamics (MBD) commercial tool used to analyse articulated mechanical systems. Based on the principles of Lagrangian Dynamics, the code solves both algebraic and differential highly non-linear equations as functions of time. A co-simulation between MSC ADAMS and SIMULINK has been used to analyse the system dynamics by providing the output of the control system to the model. The control laws have been designed in SIMULINK software and the ADAMS multibody code reproduces the system dynamic plant (see Fig. 8-16).

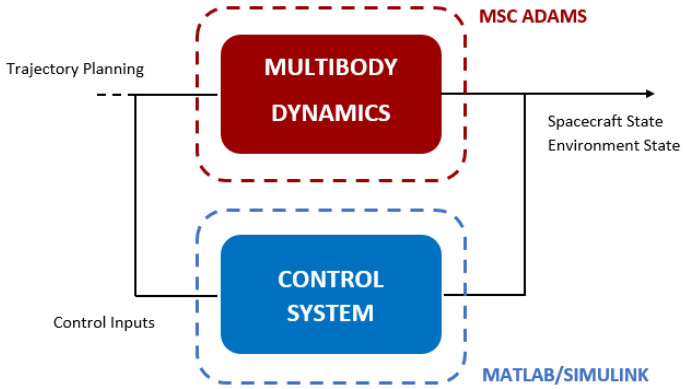

Fig. 8-16: Co-simulation logic

The technique is suitable for conducting tests on space robotic systems [35][36]. The choice is justified by the need of validating a control algorithm on a complex multibody structure. To run the simulation, the ADAMS multibody model has been imported as an S-function in SIMULINK workspace. The control inputs to the dynamic model are calculated by using Matlab scripts. The outputs of ADAMS solver are then exploited to compute control actions thus closing the loop.

8.2.3.2 RESULTS

The Root Mean Squared Error (RMSE) index has been chosen as quality parameter for evaluating the learning performance of the controller. Simulations show that the ILC control scheme reduces the trajectory error in a monotone way iteration by iteration. The achieved convergence is monotone and not exponential. In particular, in Fig. 8-17-(a) the trend of the RMSE with respect to iterations (where one iteration corresponds to one orbit) is reported. Even if the first guess of the NN implies an initial RMSE of some degrees, the ILC controller proved to reduce the

RMSE by an order of magnitude in the first 170 orbits. As an EO spacecraft has an orbital period of around 90 minutes, the end time of the simulation is around ten days. The intelligent control system is able to improve significantly the tracking performance of the satellite just by using available in-orbit data or attitude orientation and angular velocities. It should be noticed that no knowledge of the interaction between the flexible solar panels and sloshing masses dynamics is required to achieve this result.

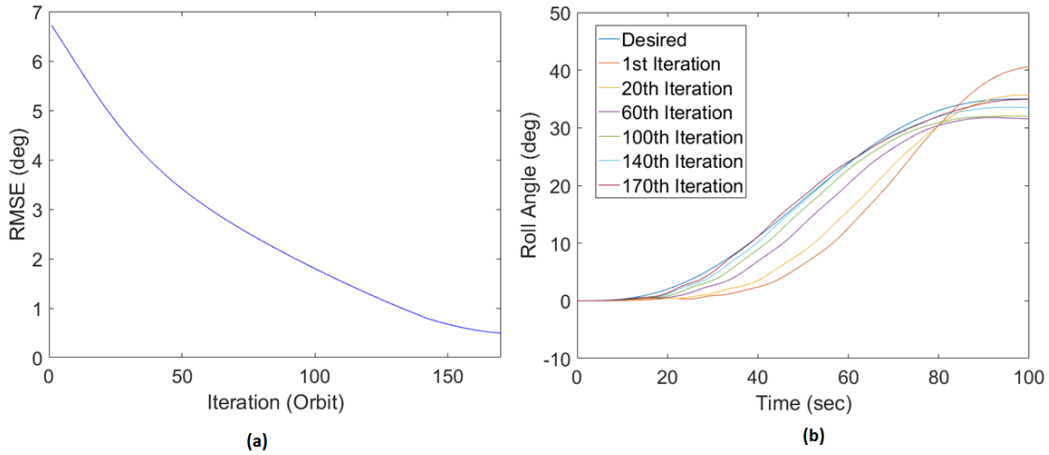

Fig. 8-17: (a) RMSE of the roll angle trend through iterations (b) Roll trajectory evolution through iterations (orbits)

In Fig. 8-18, a 3D plot of the evolution of the trajectory is depicted, to better show the change and the modifications of the trajectory orbit after orbit.

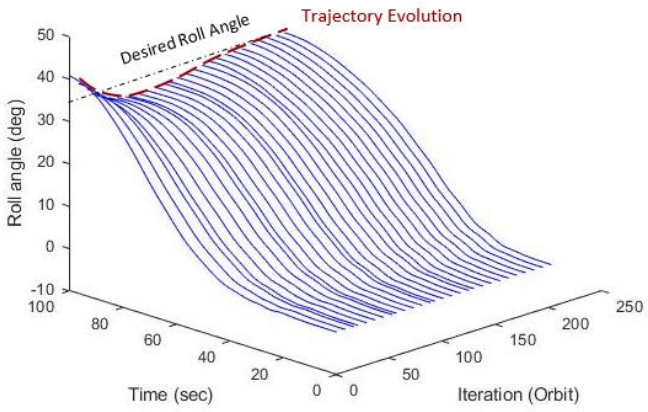

Fig. 8-18: Trajectory evolution through iterations (orbits)

The combination of the HOILC and FB controller has proved to be successful in enhancing the precision of the attitude tracking when performing repetitive

manoeuvres. As mentioned in Section 8.2.2.1, the control input is composed of two terms: a feedback and a feedforward signal. As the feedback term decreases iteration by iteration (see Fig. 8-20), the feedforward corrective term gradually increases (see Fig. 8-19). This means that the controller has learnt the amount of supplementary torque to add to the standard PD controller to track the trajectory in presence of disturbances given by elastic panels and sloshing masses.

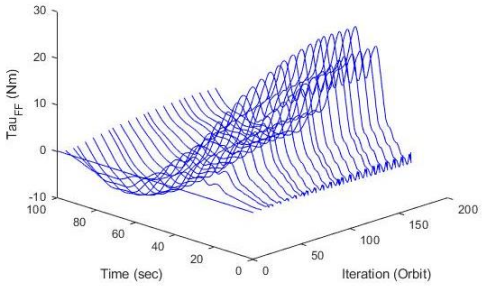

Fig. 8-19: Trend of the torque correction term (feedforward term)

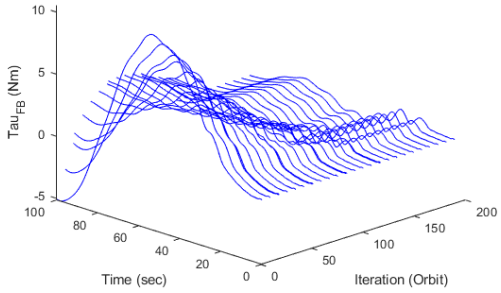

Fig. 8-20: Trend of the feedback torque

The left solar panel tip displacement is shown in Fig. 8-21. The order of magnitude of the maximum deflection is 20 cm, but it is expected if considering the assumptions made in Par. 8.2.1.2. The reported tip displacement would correspond to a roughly half-degree relative rotation between two adjacent sections (if the array segments were considered to be rigid).

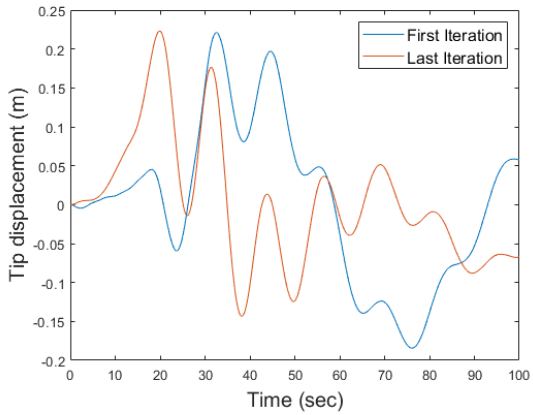

Fig. 8-21: Tip displacement of the left solar panel

As the manoeuvre is symmetric, the tip displacement of the right panel has equal norm and opposite sign with respect to the left one and it is not reported for

the sake of brevity. In Figures from 8.14 to 8.16, the displacement of the sloshing masses with respect to their equilibrium position inside the tanks are plotted. The maximum displacements of the first sloshing masses (m_1^{DOWN} and m_1^{UP}) in both tanks are one order of magnitude higher than the other ones as they represent the modes associated to predominant "modal masses". It is worth noting the last iteration displacements of m_1^{DOWN} and m_1^{UP} show a phase inversion if compared to the first one. The same behaviour can be partially observed for the second sloshing masses m_2^{DOWN} and m_2^{UP}, while it cannot be detected for the third sloshing masses m_3^{DOWN} and m_3^{UP}.

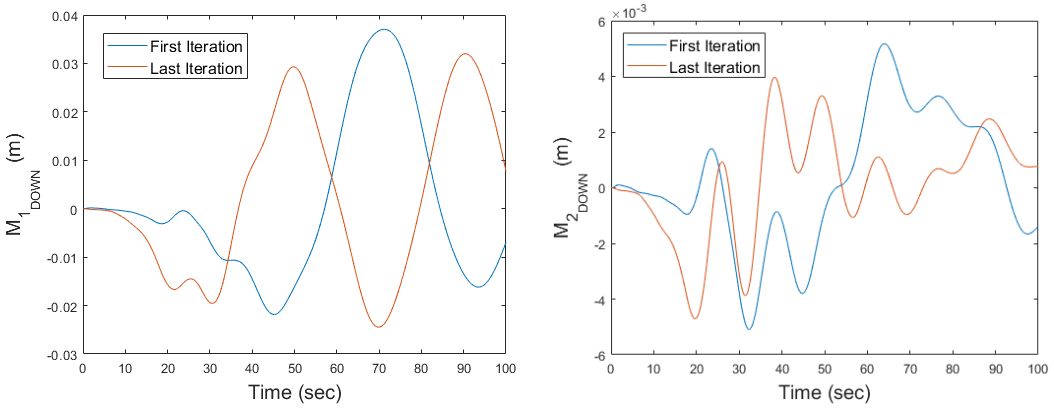

(a) (b)

Fig. 8-22: (a) First sloshing mass m_1^{DOWN} displacements in the lower tank (b) Second sloshing mass m_2^{DOWN} displacement in the lower tank

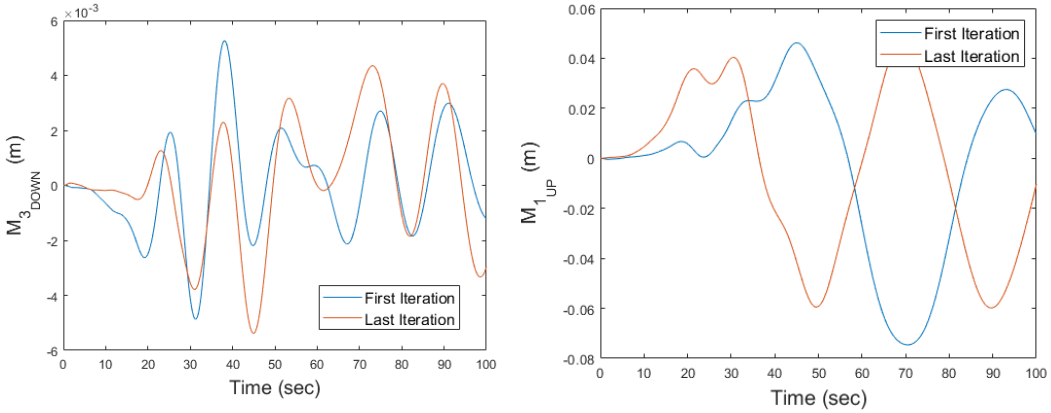

(a) (b)

Fig. 8-23: (a) Third sloshing mass m_3^{DOWN} displacement in the lower tank (4) First sloshing mass m_1^{UP} displacement in the upper tank

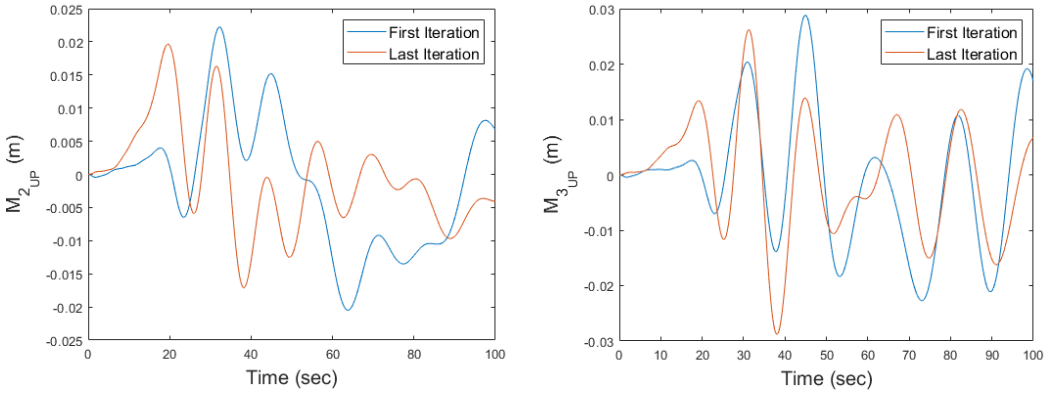

(a) (b)

Fig. 8-24: (a) Second sloshing mass m_2^{UP} displacement in the upper tank (4) Third sloshing mass m_3^{UP} displacement in the upper tank

The displacements of all the sloshing masses are compatible with the geometric dimensions of the tanks (i.e. the masses displacements do not exceed the maximum allowed value given by the tanks radius).

8.2.3.3 CONCLUDING REMARKS

The learning control can effectively cope with uncertainties or lacking knowledge of the model. The controller sees the flexible deformations and sloshing phenomena induced by the attitude control system as external disturbances. The control system can generate an on-line supporting signal co-operating with a traditional PD controller with fixed gains to achieve better tracking precision before the sensing phase and to counteract to both periodical and non-periodical disturbances. A combination of a High-Order ILC and a PD feedback law has proved to be effective in addressing such issue one orbit after the other.

To further examine the control problem, more details should be included in the environment model. The contribution of orbital disturbances as solar radiation pressure, atmospheric drag and gravity gradient could be considered when carrying out the simulations (as they will be in the next paragraph). Nevertheless, ILC is expected to be able to counteract their effects as these disturbances are mostly periodic. Furthermore, the values of the propellant sloshing masses could be set as varying with time (due to the consumption of the propellant itself) to evaluate their impact during mission. Moreover, the dynamic model could be complicated by adding other flexible appendages or more sloshing

masses and tanks, even of different geometry. A sliding surface could be introduced in MSC Adams to obtain the possibility of studying lateral sloshing along different axes of the spacecraft.

8.3 ITERATIVE LEARNING CONTROL PROCESSES ON-BOARD CUBESATS

Nowadays, small orbiting platforms as CubeSats are becoming more and more capable to perform challenging technological missions [37]. Lately, they have granted a viable and economic access to space to commercial, scientific and educational purposes. Such tiny spacecraft are particularly employed for fulfilling short-duration missions, yet producing valuable scientific outcomes, due to their various advantages, as low development costs and innovative hardware [24][25]. Currently, space missions for Earth and universe observation, as well as telecommunication and technology demonstration are already going through a radical change to take advantage of such smaller and cost-effective satellites. Such a success mostly lies on the recent miniaturization technology advancement, but it is – and will also be in the near future – also due to improvements in the on-board intelligence, which allows to optimize operations and hardware possibilities.

To follow the path of increasing the autonomy and relevance of smart processes on-board, Artificial Intelligence (AI) techniques can be surely implemented. In this scenario, future space mission will benefit by intelligent and autonomous on-board systems to improve their reliability, promptness and overall performance, in particular when high latency time is involved (as missions around celestial bodies other than the Earth). Both Machine Learning (ML) and Artificial Intelligence (AI) fields advanced in the last decades in a wide variety of scientific areas, also due to the evolution and extensive use of GPUs [40][41]. Regarding CubeSats, ML and AI can be convenient to enhance the system autonomy, to decrease the costs associated to the ground segment by implementing a certain level of decisional capabilities and to learn how to react to the surrounding orbital environment [42]. However, high computational costs are still related to the use of intelligent algorithms, which are in general difficult to be sustained by miniaturized on-board computers.

In this direction, the Iterative Learning Control (ILC) consists in an already available and yet computational efficient small step towards intelligent systems – as opposed to as opposed to current ML methods [43] - suitable to the scenarios where a set of repetitive actions is expected to be taken by the satellite. Such an algorithm aims at exploiting past experience, intended as the memorized data during previous tasks, to shape more conveniently the future operations of the

system. Indeed, the purpose of this controller is to produce a sequence of control signals such that the output of the system is as close as possible to the desired one. In the particular case of CubeSat missions, the ILC is an interesting and viable option due to the reduced computational burden consequent to the real implementation of the algorithm – which is currently diffused in the robotic industrial field. As in a major part of remote sensing missions the spacecraft should be commanded to sweep over a prescribed terrestrial area with the same viewing conditions, the dynamic system can be then actuated in an iterative way to control the attitude while guaranteeing at the same time an improve pointing precision.

In this chapter, ILC is considered to be applied to the case of attitude manoeuvre – as the slewing often performed for Earth Observation purposes – but could be suitable also to correct the frequent, off-nominal behaviour of the subsystems onboard these miniaturized platforms. Due to the inner periodic nature of spacecraft missions, related to their orbital period, CubeSats are mostly subjected to repeated environmental disturbances, such as aerodynamic drag, magnetic field and gravity gradient action [22]. The Iterative Learning Control has been successfully applied to improve the attitude manoeuvres accuracy in [44]. Conversely to the little available literature, the main aim of this research is to advance the state-of-the-art of such approach by implementing a High-Order Iterative Learning Control to the problem of tracking both a parallel and an oblique terrestrial strip in the case of an Earth Observation (EO) CubeSat platform under orbital perturbances, as gravity, drag and magnetic disturbance torques. Indeed, on of the additional advantage the ILC method guarantees with respect to standard controllers is the ability to preventively react to repetitive disturbances[5].

8.3.1 Problem Statement

Some remote sensing space missions require the spacecraft to observe specific areas with the same viewing conditions [38]. To complete the task, the satellite assumes identical orientation when passing over a target object or surface. In general, space systems performing such a mission take repetitive ground track orbits in order to give to the satellite revisiting capability of the desired area. In

[5] The results in this section were published by the thesis author in F. Angeletti, P. Iannelli, *Iterative Learning Control Processes On-Board Cubesats*, 5th IAA Conference on University Satellite Missions, January 28-31, Rome, 2020;

this case, the entire mission can be considered as the repetition of several tasks during the system operative life. A typical mission profile would consist in sensing a strip of terrestrial area that is parallel to the satellite ground track (visualized in green in Fig. 8-25). The satellite, assumed to be in nominal nadir pointing condition, performs a roll-tilt φ so that the payload can observe the interested strip without changing its attitude. Another possible scenario would consist in sensing a strip that is oblique with respect to the satellite ground track (as visualized in green in Fig. 8-26). The spacecraft performs two subsequent roll-tilts: the first to reach the desired initial roll angle to perform the observation and the second one to track a desired trajectory during the sensing phase.

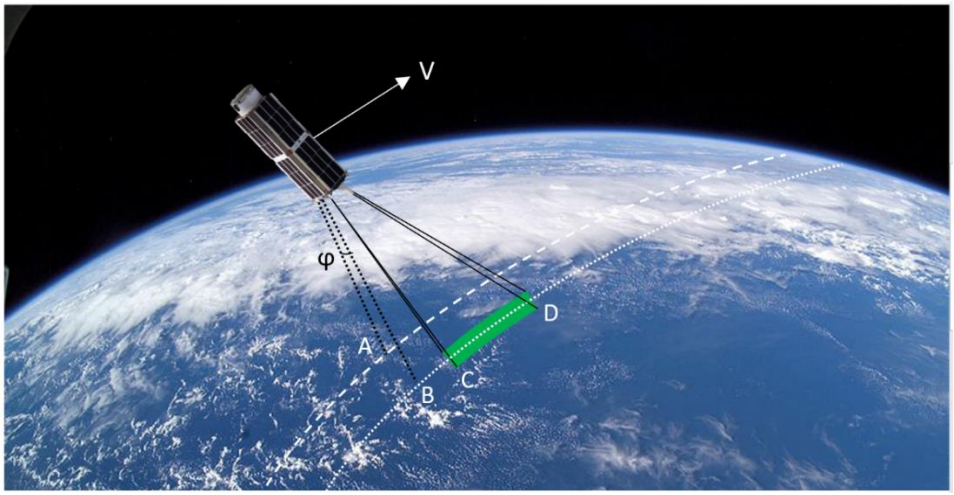

Fig. 8-25: Attitude Control Problem Description: Case A (Parallel Strip)

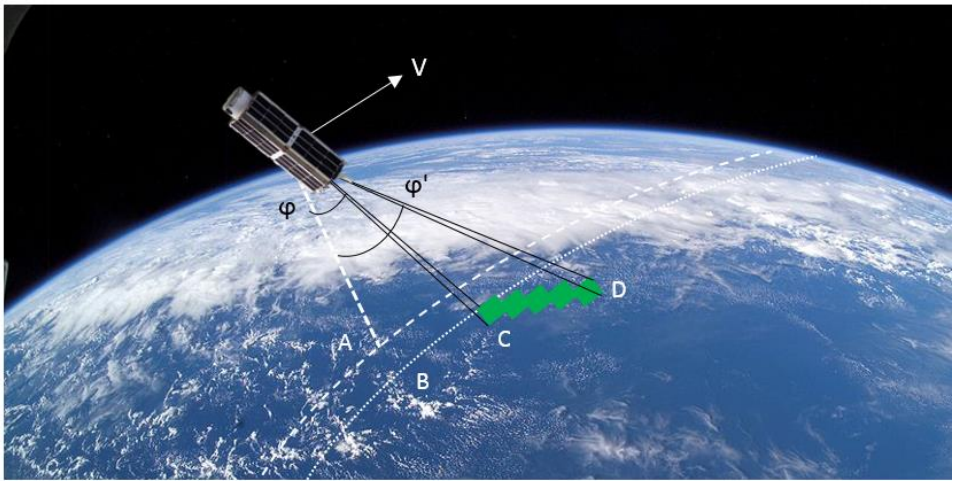

Fig. 8-26: Attitude Control Problem Description: Case B (Oblique Strip)

In both cases, the manoeuvre can be divided into two phases: a first attitude manoeuvre to reach the desired roll angle (from point A to point C in Fig. 8-25 and Fig. 8-26) and a sensing phase (from point C to point D in Fig. 8-25 and Fig. 8-26). If considering no yaw compensation due to the rotation of the Earth, the sensing phase is an attitude stabilization problem. As the satellite is repeatedly operated, the attitude control strategy could benefit by using data available from previous orbits to improve its tracking performance.

8.3.1.1 SATELLITE DYNAMICS

The governing equations for an in-orbit satellite that have been already defined in Chapter 3 are used to perform dynamic simulations in this paragraph. By performing the relevant algebra, not reported here for the sake of brevity, the equations of motion of a rigid spacecraft can be reduced to

$$\begin{cases} \boldsymbol{M}\ddot{X}_P + \boldsymbol{R}^T\left[\omega\wedge\left(\omega\wedge p\right)\right] + \boldsymbol{R}^T\left(\dot{\omega}\wedge p\right) = F_{Env} \\ p\wedge\boldsymbol{R}\ddot{X}_P + \boldsymbol{J}\dot{\omega} + \omega\wedge\boldsymbol{J}\omega = C_{Env} + u_C \end{cases} \tag{8.19}$$

where $\boldsymbol{M}$ is the mass matrix of the satellite, $\boldsymbol{J}$ is the inertia matrix, p is the static moment, ω is the angular velocity of the spacecraft with respect to the inertial frame (written in the body reference frame). The terms F_{Env} and C_{Env} indicate the generalized forces related to the orbital environment, which are presented in the next paragraph, while u_C represents the control torque exerted on the spacecraft. In Fig. 8-27, the reference frames of the satellite are illustrated, as introduced in Par. 3.1.1

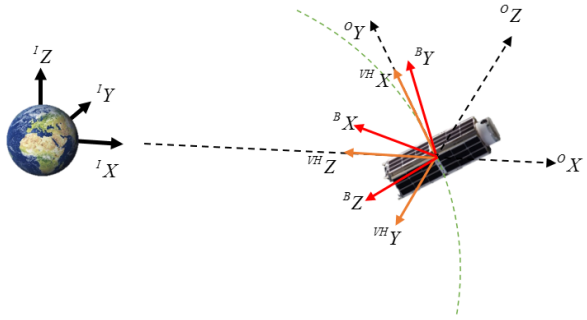

Fig. 8-27: Reference Frames Visualization: ${}^{I}I$, ${}^{O}I$, ${}^{VH}I$, ${}^{B}\boldsymbol{I}$

In the next section, the environment model to which the CubeSat has been exposed is considered and the main disturbance torques are presented.

8.3.1.2 ENVIRONMENT MODEL

In general, CubeSat platforms are subjected to various types of disturbances which affect their dynamics in space [47]. The main sources of attitude disturbance torques are the gravity related forces, aerodynamic drag and magnetic disturbance, as follows:

$$\begin{cases} F_{Env} = F_G + F_{aero} \\ C_{Env} = C_G + C_{aero} + C_{magn} \end{cases} \tag{8.20}$$

8.3.1.3 GRAVITATIONAL FORCES

The gravitational generalized forces are expressed as

$$F_G = -\boldsymbol{M}\mu_{\oplus}\frac{\hat{s}}{\left|X_P\right|^2} \quad with \quad \hat{s} = \frac{X_P}{\left|X_P\right|} \tag{8.21}$$

$$C_G = -\frac{\mu_{\oplus}\hat{s}}{\left|X_P\right|^2}\left(\tilde{p}\wedge\hat{s}\right) - \frac{3\mu_{\oplus}}{\left|X_P\right|^3}(\hat{s}\wedge\boldsymbol{J}\hat{s}) \tag{8.22}$$

where $\mu_{\oplus}$ is the Earth gravitational parameter. The vector C_G describes the effect of the gravity gradient (GG) torque on the spacecraft. Such a torque is one of the largest sources of disturbance that would affect the low earth orbit CubeSats, due to the variation in the Earth's gravitational force over the object.

8.3.1.4 AERODYNAMIC DRAG

The interaction of the upper atmosphere with the surfaces of the satellite induces forces and torques about the spacecraft center of mass. If considering the energy of the particles is totally absorbed on impact with the satellite, the aerodynamic force acting on a surface element *dA* can be expressed as [48]

$$dF_{aero} = \begin{cases} -\frac{1}{2}C_D\rho v^2\left(\hat{n}\cdot\hat{v}_b\right)\hat{v}_b dA & \left(\hat{n}\cdot\hat{v}_b\right) > 0 \\ 0 & \left(\hat{n}\cdot\hat{v}_b\right) \le 0 \end{cases} \tag{8.23}$$

where $\hat{n}$ is the unit normal vector of the surface element, C_D is the drag coefficient (usually considered equal to 2-2.5), ρ is the atmospheric density according to the International Standard Atmosphere (ISA), $\hat{v}_b$ is the unit vector of the translational velocity of the spacecraft. The total aerodynamic force F_{aero} can be obtained by integrating eq. (8.23) over the exposed surface of the satellite. As CubeSats can be considered cubic or parallelepiped-shaped objects, they are generally composed of six surfaces. In such case, the aerodynamic torque C_{aero} can be computed as the sum of the torques on individual planes as

$$C_{aero} = \sum_{i=1}^{6} r_i \wedge F_{aero_i} = \frac{1}{2} C_D \rho v^2 \sum_{i=1}^{6} A_i \left(\hat{n}_i \cdot \hat{v}_b\right) \hat{v}_b \wedge r_i \tag{8.24}$$

with r_i vector from the spacecraft center of mass to the center of pressure (CP) of the surface A_i.

8.3.1.5 MAGNETIC FIELD

Magnetic torques are generated due to the interaction of the Earth magnetic field with the satellite's residual magnetic moment, which is the result of the presence of electronic equipment onboard. Therefore, the Earth's magnetic field must be modelled in order to simulate its perturbative effects on the attitude of the satellite. One important global model of the geomagnetic field is the International Geomagnetic Reference Field (IGRF) [49][50]. This model computes the geomagnetic field as a gradient of a scalar potential V, which is expressed as an orthogonal expansion of spherical harmonics.

$$B_{earth} = -\nabla V \tag{8.25}$$

$$V(r,\theta,\phi,t) = R_e \sum_{n=1}^{N} \sum_{m=0}^{n} \left(\frac{R_e}{r}\right)^{n+1} \left[g_n^m(t)\cos(m\phi) + h_n^m(t)\sin(m\phi)\right] P_n^m(\cos\theta) \tag{8.26}$$

where r, θ and ϕ are distance, latitude and longitude of the spacecraft, R_e is the mean radius of the Earth (6371.2 Km) and $P_n^m(\cos\theta)$ are the quasi Schmidt normalized associated Legendre function of degree n and order m. The coefficients g_n^m and h_n^m are determined experimentally by combining earth-based and satellite measurements and updated periodically and given for specific epoch

(generally each 5 years) in the IGRF model.

The magnetic torque C_{magn} is computed as the cross product between the spacecraft dipole m_{sat} and the magnetic field vector in the body reference frame B^B_{earth}:

$$C_{magn} = m_{sat} \wedge B^B_{earth} \tag{8.27}$$

According to NASA [51], the residual magnetic dipole of a spacecraft can be estimated either on measurements made on the flight hardware or based on known parameters of the spacecraft, such as mass and on-board equipment, as

$$m_{sat} = c\ 10^{-3}\, m_{sc} \tag{8.28}$$

where c is a constant in the range of 1 to 10 depending on the level of magneticity of the spacecraft and m_{sc} is the mass of the satellite.

8.3.2 ITERATIVE LEARNING CONTROL

The Iterative learning method aims at producing a sequence of inputs such that the output of the system is as close as possible to the desired one [33]. To this purpose, the ILC strategy is able to improve control input based on previously memorized operation data. The controller can learn to produce zero tracking error during the repetition of a task, also by eliminating the effects of repeating disturbances, as environmental torques. The classical ILC algorithm has been formulated by Arimoto [50] as

$$\tau^{k+1}(t) = \tau^k(t) + \Gamma e^k(t) \tag{8.29}$$

where τ^{k+1} is the control input to be computed for the next k+1-th operation, τ^k is the control input exerted on the system to perform the k-th iteration, Γ is a learning matrix and $e^k(t)$ is the tracking error, expressed as the difference between the desired output $y_{des}(t)$ and the actual output $y^k(t)$ of the considered dynamic system.

The ILC is classified as a feedforward control system. However, according to this definition, the ILC method is not able to compensate for non-repetitive disturbances and random noise [52]. To extend its range of applicability and overcome such issues, a conventional feedback controller can be considered to

work in parallel with the ILC:

$$\tau^k(t) = \tau^k_{fb}(t) + \tau^k_{ff}(t) = \tau^k_{fb}(t) + \tau^k_{ILC}(t) \tag{8.30}$$

According to this approach, the control input at the current k-th iteration is composed of a feedback action $\tau^k_{fb}(t)$ and a feedforward term (associated to the ILC). The modified control strategy is named Current Cycle Feedback Iterative Learning Control (CCF-ILC) and is illustrated in Fig. 8-28.

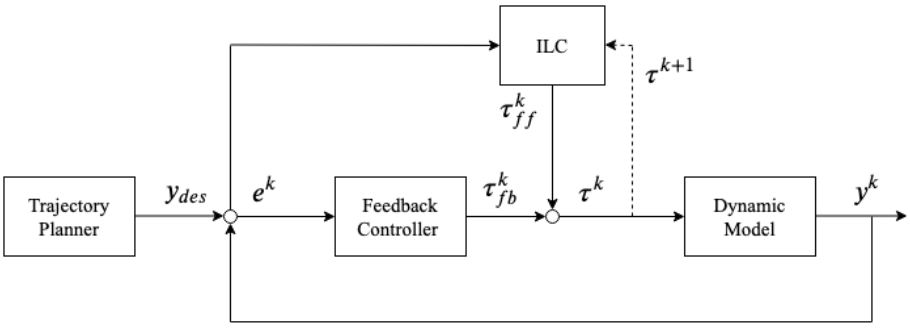

Fig. 8-28: CCF-ILC Scheme

To deal with those systems with dynamics uncertainties through iterations, and generally to increase the learning velocity and improve the capacity to react to periodic disturbances, a High-Order Iterative Learning Control (HOILC) is usually applied to the problem of tracking control [34]. The mentioned strategy uses more than one past error history in different iterations.

8.3.2.1 *HIGH-ORDER ITERATIVE LEARNING CONTROL FOR ATTITUDE MANOEUVRES*

In this section, the proposed control scheme for attitude manoeuvres of CubeSats subjected to environmental disturbances as gravity gradient, aerodynamic and magnetic torques is presented. In particular, the control torque u_C exerted ideally by the platform reaction wheels at k-th iteration (orbit) is defined as

$$u^k_C(t) = -\sigma(\omega^k(t) \wedge \boldsymbol{J}\omega^k(t)) + \tau^k(t) \tag{8.31}$$

where σ is a constant between 0 and 1 to compensate for the nonlinear gyroscopic term in eq. (8.19). The term $\tau^k(t)$ can be expressed as

$$\begin{aligned}
&\tau^k(t) = \tau^k_{fb}(t) + \tau^k_{ILC}(t) \\
&\tau^k_{fb}(t) = \boldsymbol{K_P}\left(\Theta_{des} - \Theta^k(t)\right) + \boldsymbol{K_D}\left(\omega_{des}(t) - \omega^k(t)\right) \\
&\tau^k_{ILC} = \tau^{k-1} + \boldsymbol{L}\left(\sum_{i=1}^{2} l_i\left(\Theta_{des} - \Theta^{k-i}(t)\right)\right) + \boldsymbol{D}\left(\sum_{i=1}^{2} d_i\left(\omega_{des}(t) - \omega^{k-i}(t)\right)\right) \\
&\sum_{i=1}^{2} l_i = \sum_{i=1}^{2} d_i = 1
\end{aligned} \tag{8.32}$$

where $\boldsymbol{K_D}$ and $\boldsymbol{K_P}$ are properly selected gains matrices to ensure the error dynamics along the desired trajectory is stable and $\Theta = [\phi, \theta, \varphi]$ is the set of Euler's angles (Roll, Pitch and Yaw) describing the attitude of the spacecraft with respect to the LVLH orbital frame through the rotation matrix $\boldsymbol{R_3}(\phi, \theta, \varphi)$.

The Iterative Learning scheme applied in this research is the CCF-HOILC in eq. (8.32), where $\boldsymbol{L, D}$ are the proportional and derivative learning gains respectively, and l_i, d_i are weight coefficients introduced to define the importance of previous iterations or orbits data. Such gains have been selected heuristically to avoid instability of the learning process.

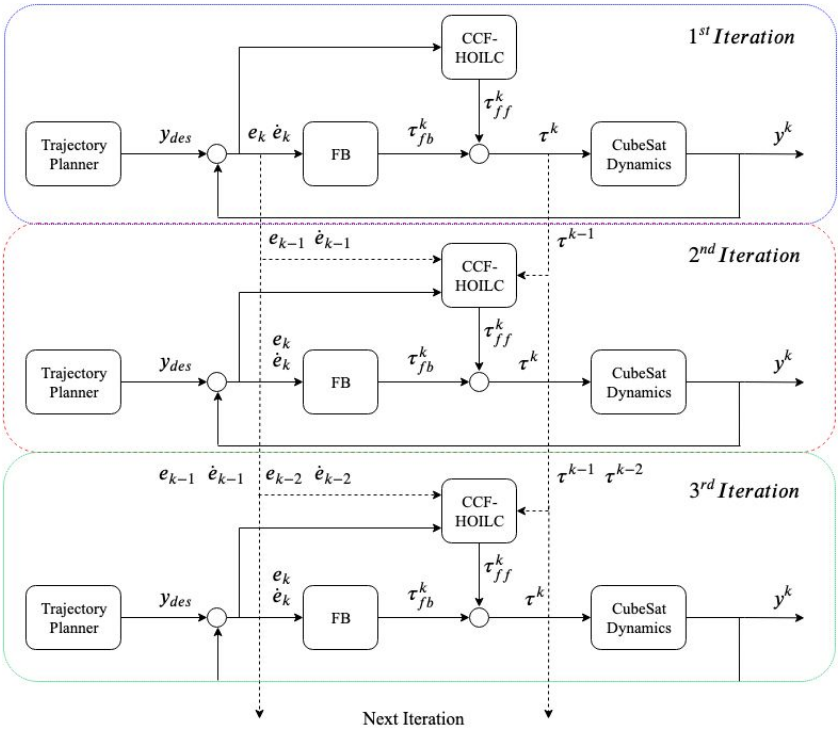

Fig. 8-29: Implemented Control Strategy

8.3.3 SIMULATIONS AND RESULTS

In this section, the manoeuvres for sensing both a parallel and an oblique strip of terrestrial area are investigated, as descripted in Fig. 8-25 and Fig. 8-26. In particular, the former mission profile (Case A) focuses on tracking a trajectory to a final roll tilt of 20 degrees at the beginning of the sensing phase (or stabilization phase, see Fig. 8-30-(a)). On the contrary, the latter observation mission (Case B), after having reached 20 degrees roll tilt at the end of the first manoeuvre phase, aims at obtaining a final roll angle of 30 degrees by tracking a desired trajectory (see Fig. 8-30-(b)).

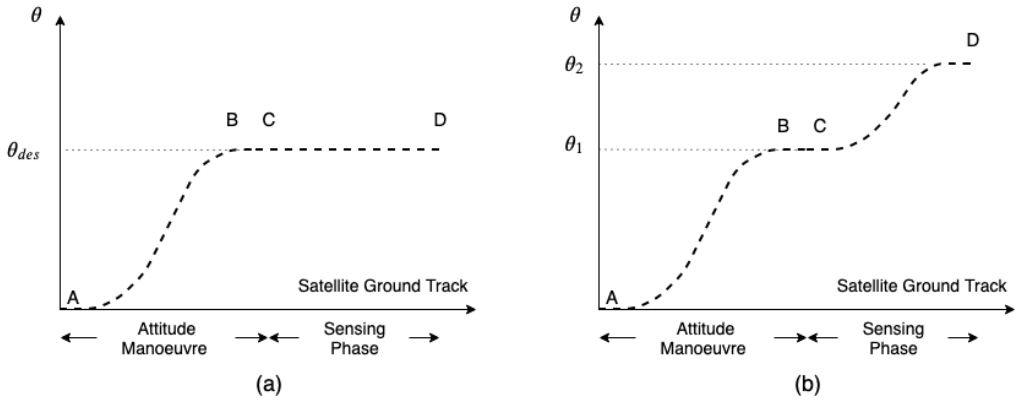

Fig. 8-30: Mission Profiles: (a) Case A; (b) Case B

The relevant data concerning the orbit and the inertial characteristics of the satellite are reported in Table 8-10 and Table 8-11.

Table 8-10. Orbital Data

	Symbol	Value
Eccentricity	e	0.001
Semi-major axis	a	6871 km
Inclination	i	77.6 deg
RAAN	Ω	22 deg
Argument of perigee	ω_p	0 deg

Table 8-11. Platform properties

	Symbol	Value
Dimensions	H	0.2 m
	W	0.2 m
	D	0.2 m
Inertia	I_{XX}	0.166 kg m²
	I_{YY}	0.166 kg m²
	I_{ZZ}	0.166 kg m²
Mass	M	25 kg

8.3.3.1 CASE A: PARALLEL STRIP

The maximum absolute error between the actual trajectory and the desired one has been chosen as quality parameter for evaluating the learning performance of the controller. Simulations prove that the ILC strategy effectively decreases the trajectory error in a monotone way orbit after orbit. The achieved convergence is monotone and not exponential. In particular, in Fig. 8-31 the error with respect to iterations (where one iteration corresponds to one orbit) is depicted.

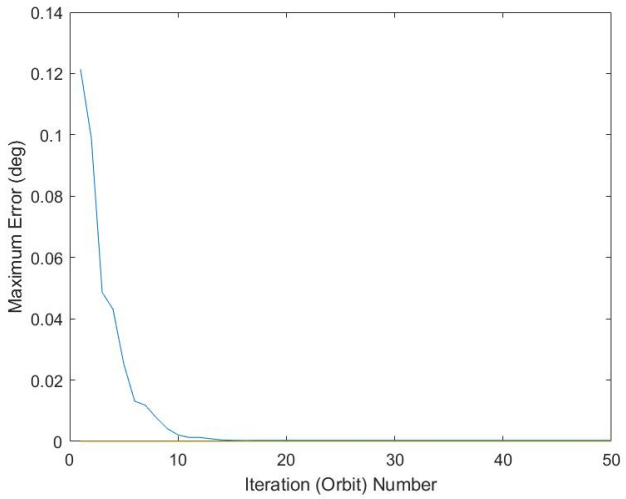

Fig. 8-31: Maximum Error vs. Iteration (Orbit) Number

The CCF-HOILC scheme demonstrated to reduce the error by two orders of magnitude in the first fifteen orbits. The intelligent control system is the able to improve significantly the tracking performance of the controller just by exploiting few available in-orbit information as attitude orientation and angular velocities. In Fig. 8-32, the trend of the Euler's angles with respect to time is reported. In particular, the first phase of the manoeuvre, from points A to C in Fig. 8-25-(a), is considered. The controller was able to reach the desired roll angle in 100 seconds. In detail, Fig. 8-33 shows how the ILC scheme was able to compensate for an error of 0.05 degrees in the first iteration, while the trend of the roll angle coincides with the desired one in the last iteration.

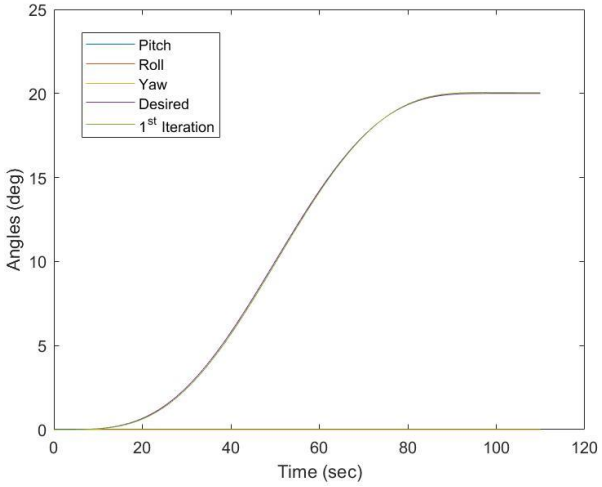

Fig. 8-32: Trend of Euler's Angles

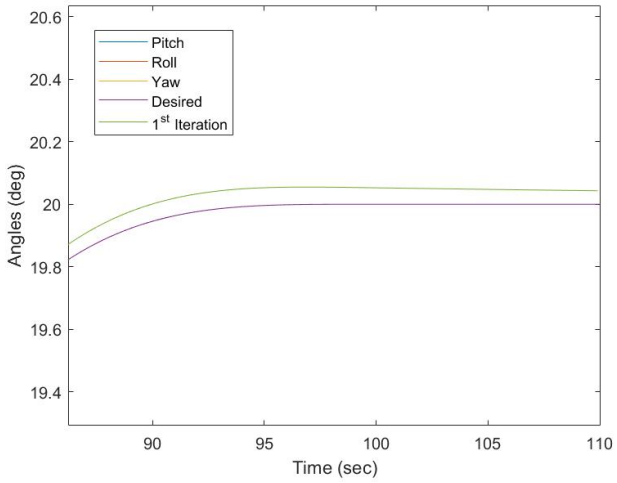

Fig. 8-33: Trend of Euler's Angles: particular (Initial Error of 0.05 Degrees)

As illustrated in eq. (8.32), the control input is composed of two signals: a feedback and a feedforward term. As the feedback input reduces orbit by orbit (see Fig. 8-35), the feedforward corrective term gradually increases (see Fig. 8-34). This means that the controller has learnt the amount of torque needed to track the trajectory even in presence of disturbances given by the environmental torques.

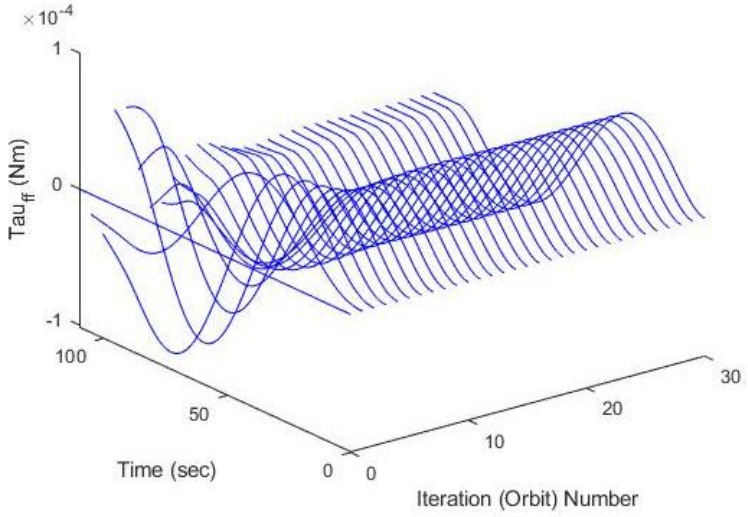

Fig. 8-34: Trend of the torque correction term (feedforward term) – X-axis (roll)

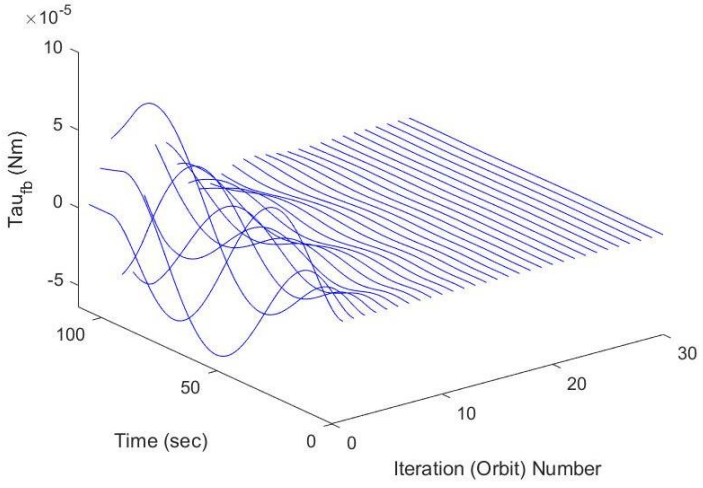

Fig. 8-35: Trend of the feedback torque term – X-axis (roll)

8.3.3.2 CASE B: OBLIQUE STRIP

As in the first case, the maximum absolute error between the actual trajectory and the desired one is the quality parameter of the learning performance of the

controller. Also concerning the mission profile related to an oblique strip with respect to the ground track, simulations show that the ILC strategy effectively decreases the trajectory error in a monotone way orbit after orbit.

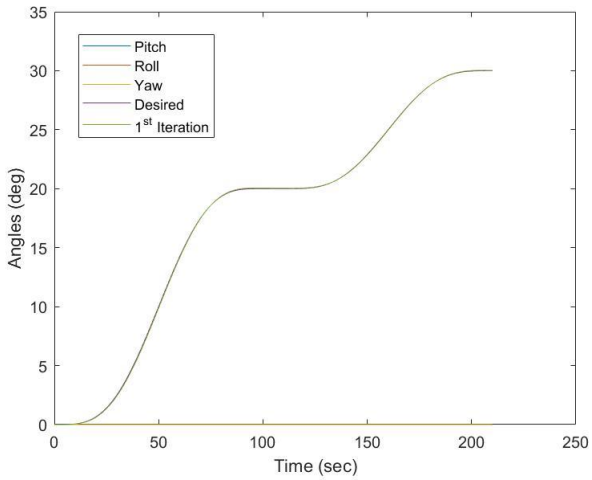

Fig. 8-36: Trend of Euler's Angles

In Fig. 8-36, the trend of the Euler's angles with respect to time is reported. In particular, the whole manoeuvre, from points A to D in Fig. 8-26-(b), is considered. The controller was able to track the first trajectory both in the first phase (from A to C) and in the sensing phase (from C to D). In particular, the ILC scheme was able to compensate for an error of 0.04 degrees in the first iteration, while the trend of the roll angle coincides with the desired one in the last iteration (see Fig. 8-37)

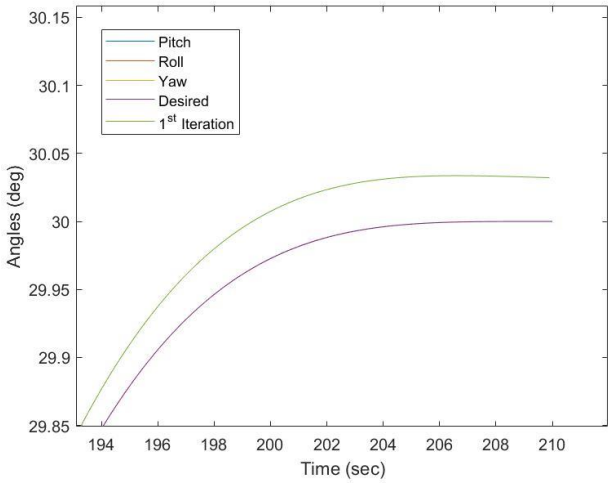

Fig. 8-37: Trend of Euler's Angles: Particular (Initial Error of 0.04 Degrees)

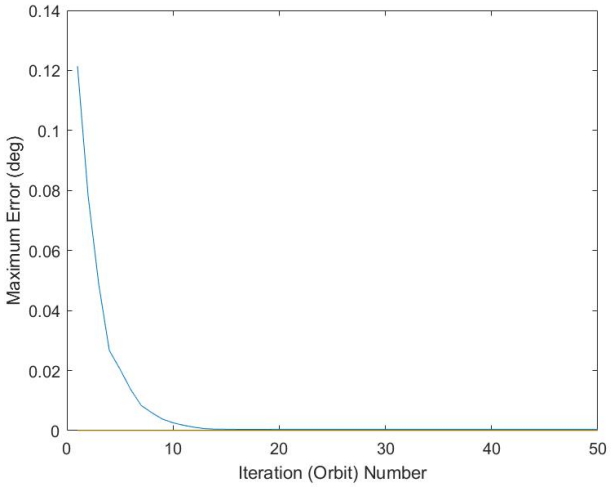

Fig. 8-38: Maximum Error vs. Iteration (Orbit) Number

In Fig. 8-38, the error with respect to iterations (where one iteration corresponds to one orbit) is illustrated. The learning-based controller demonstrated to greatly reduce the error by two orders of magnitude in the first twelve orbits.

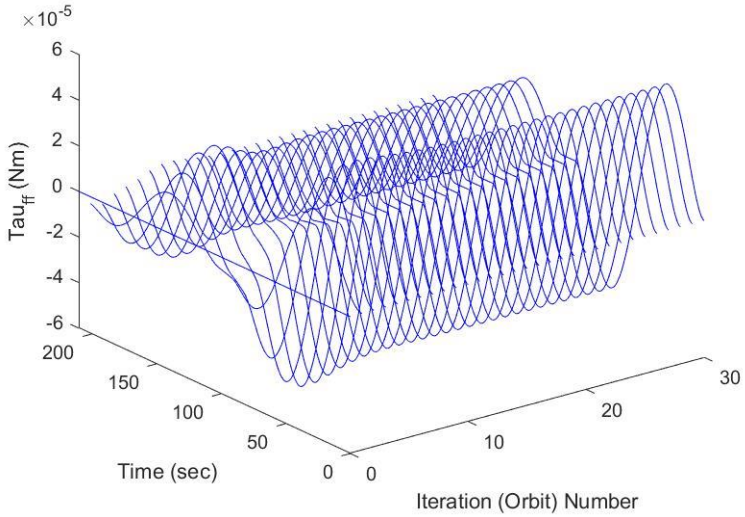

Fig. 8-39: Trend of the torque correction term (feedforward term) – X-axis (roll)

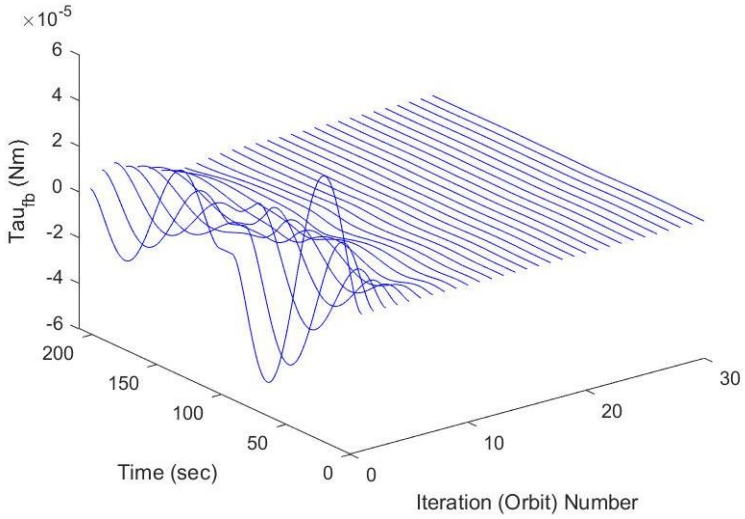

Fig. 8-40: Trend of the torque feedback term – X-axis (roll)

As in the previous case, the feedback input reduces orbit by orbit (see Fig. 8-40) while the feedforward corrective term gradually increases (see Fig. 8-39). This means that the controller has learnt the amount of torque needed to track the trajectory even in presence of disturbances given by the environmental torques.

8.3.4 CONCLUSION

The possibility to use on-orbit available data, which can be memorized among successive orbits, naturally calls for exploiting the gathered information to improve the system performance. Indeed, the controller sees the environmental torques, as gravity gradient, drag and magnetic field torques, as periodic external disturbances, being able to counteract them orbit after orbit. In particular, two manoeuvres have been simulated for sensing a parallel and an oblique strip with respect to the spacecraft ground track. In both cases, the controller demonstrated to reduce the maximum absolute tracking error by more than one order of magnitude in the first fifteen orbits. By observing the required control torques, the learning processes can be considered as successful, as the feedforward term related to the ILC converges to the value needed to perform such manoeuvres, while the feedback terms go to zero. The learning gains associated to the controller have been chosen heuristically to avoid instability of the system.

BIBLIOGRAPHY

[1] J. Mess et al., *Techniques of Artificial Intelligence for Space Applications – A survey*, 2019;

[2] S. Osder, *Practical View of Redundancy Management Application and Theory*, Journal of Guidance, Control, and Dynamics, 1999 Vol. 22 Issue 1, pp 12-21;

[3] J. Patton, Chen, *A Review of Parity Space Approaches to Fault Diagnosis*, IFAC Proceedings Volumes Volume 24, Issue 6, September 1991, Pages 65-81.

[4] D. Henry, F, Ankersen, L. Strippoli, *Chapter 9 - A Class of Unknown Input Observers Under H∞ Performance for Fault Diagnosis: Application to the Mars Sample Return Mission*, In Emerging Methodologies and Applications in Modelling, New Trends in Observer-based Control, Academic Press, 2019, pp. 225-266.

[5] Patton et. al, *Robust FDI applied to thruster faults of a satellite system*, Control Engineering Practice 18 (2010) 1093–1109.

[6] F.N. Pirmoradi, F. Sassani, C.W. de Silva, *Fault detection and diagnosis in a spacecraft attitude determination system*, Acta Astronautica, Volume 65, Issues 5–6, 2009, Pages 710-729.

[7] L. Yizhou et al., *Structural Damage Detection with Automatic Feature-Extraction through Deep Learning*, Computer-Aided Civil and Infrastructure Engineering, Nov. 2017.

[8] T. Guo et al., *Damage detection in a novel deep-learning framework: a robust method for feature extraction,* Structural Health Monitoring, Vol 19, Issue 2, 2020.

[9] S. K. Ibrahim, A. Ahmed, M. A. Eldin Zeidan, I. E. Ziedan, *Machine Learning Techniques for Satellite Fault Diagnosis,* Ain Shams Engineering Journal, Volume 11, Issue 1, 2020, Pages 45-56.

[10] Yang et al., *Data Mining-Based Fault Detection and Prediction Methods for In-Orbit Satellite,* 2013 2nd International Conference on Measurement, Information and Control, 2013.

[11] A. Guiotto, A. Martelli, C. Paccagnini et al, *SMART-FDIR: Use of Artificial Intelligence in the Implementation of a Satellite FDIR*, Proceedings of DASIA 2003 (ESA SP-532). 2-6 June 2003, Prague, Czech Republic. Editor: R.A. Harris.

[12] P. Massioni, G. Sangiovanni, M. Lavagna, *Innovative Software for Autonomous Fault Detection and Diagnosis on Space Systems*, Proceedings of the 9th ESA Workshop on Advanced Space Technologies for Robotics and Automation, ESTEC, Noordwijk, The Netherlands, Nov. 28-30, 2006;

[13] S. Voss, *Application of Deep Learning for Spacecraft Fault Detection and Isolation*, Master Thesis, Delft University of Technology;

[14] K. Lee et al., *Development of Fault Detection and Identification Algorithm Using Deep learning for Nanosatellite Attitude Control System*, International Journal of Aeronautical and Space Sciences, 21:576–585, 2020.

[15] R.B. Malla, P. Agarwal, R. Ahmad, *Dynamic analysis methodology for progressive failure of truss structures considering inelastic post buckling cyclic member behavior*, Engineering Structures 33(5), 1503-1513, 2011;

[16] Hochreiter S. et al., *Long short-term memory*, Neural Comput. 9 (8), 1735–1780, 1997;

[17] A. Rosato, M. Panella, R. Araneo, A. Andreotti, *A neural network-based prediction system of distributed generation for the management of microgrids*, IEEE Transactions on Industry Applications, vol. 55 (2019), no. 6, 7092-7102;

[18] A. Stolfi, F. Angeletti, P. Gasbarri, M. Panella, *A Deep Learning Strategy For On-Orbit Servicing Via Space Robotic Manipulator*, Aerotecnica Missili&Spazio, 98, pages273–282(2019);

[19] P. Iannelli, F. Angeletti, P. Gasbarri, M. Panella, A. Rosato, *Deep Learning for local damage identification in large space structures via sensor-measured time responses*, 71st International Astronautical Congress (IAC) – The CyberSpace Edition, 12-14 October 2020

[20] F. Karim, S. Majumdar, H. Darabi, S. Harford, *Multivariate LSTM-FCNs for Time Series Classification, Neural network*, 116 (2019) 237-245;

[21] C. Bishop, *Neural networks for pattern recognition*, Oxford University Press, Inc., Oxford, 1995;

[22] B. Wu, D. Wang, E.K. Poh. *High Precision Attitude Tracking Control via Iterative Learning Control*, Journal of Guidance, Control and Dynamics, Vol. 38, No. 3, March 2015;

[23] G. J. Sun et al., *The Satellite Attitude Control Law Design Based on Machine Learning*, Applied Mechanics and Materials, Vols. 519-520, pp. 741-746, 2014

[24] Z. Ma, Y. Wang, Y. Yang et al., *Reinforcement Learning-Based Satellite Attitude Stabilization Method for Non-cooperative Target Capturing*, Sensors (Basel), Vol. 18, No. 12, December 2018;

[25] N. Fries, P. Behruzi, T. Arndt, M. Winter, G. Netter, *Modelling of fluid motion in spacecraft propellant tanks – Sloshing*, Space Propulsion 2012 Conference Proceedings, Bordeaux, France, May 7-10, 2012;

[26] A.G. de Souza, L. C.G. de Souza, *Satellite Attitude Control System Design Taking into account the Fuel Slosh and Flexible Dynamics*, Mathematical Problems in

Engineering, Vol. 2014, September 2014;

[27] C. Zou, D. Wang, *A simplified mechanical model with fluid-structure interaction for rectangular tank sloshing under horizontal excitation*, Advances in Mechanical Engineering, Vol. 7, No. 5, 2015;

[28] J.R. Hervas, M. Reyhanoglu, *Thrust Vector Control of an Upper-Stage Rocket with Multiple Propellant Slosh Modes*, Mathematical Problems in Engineering, Vol. 2012, August 2012;

[29] P. Gasbarri, M. Sabatini, A. Pisculli, *Dynamic Modelling and Stability Parametric Analysis of a Flexible Spacecraft with Fuel Slosh*, Acta Astronautica, Vol. 127, 141-159, May 2016;

[30] D. D. Kana, *Validated Spherical Pendulum Model for Rotary Liquid Slosh*, Journal of Spacecraft and Rocket (JSR), Vol. 26, No. 3, May 1989;

[31] K. Soo, L. Young-Shin, *Optimization design techniques for reduction of sloshing by evolutionary methods*, Journal of Mechanical Science and Technology by evolutionary methods. Vol. 22, Issue 1, pp 25-33, January 2008;

[32] F. Angeletti, A. Stolfi, P. Gasbarri, *Learning-based control of a spacecraft with sloshing propellant*, Aerotecnica Missili&Spazio, Aerotecnica Missili & Spazio, Volume 99, Issue 1, p.33-42, 2020

[33] K.L. Moore, Y. Q. Chen and H. S. Ahn, *Iterative Learning Control: Brief Survey and Categorization*, IEEE Transactions on Systems, Man and Cybernetics, Part C, Applications and Reviews, Nov-2007;

[34] Y. Chen, *High-order iterative learning control: convergence, robustness and applications*, IMA Journal of Mathematical Control and Information, pp. 111–121, 2000;

[35] L. Felicetti, P. Gasbarri, A. Pisculli, M. Sabatini, and G.B. Palmerini, *Design of robotic manipulators for orbit removal of spent launchers' stages*, Acta Astronautica, vol. 119, pp. 118–130, Dec. 2015;

[36] F. Angeletti, P. Gasbarri, G.B. Palmerini, M. Sabatini, *Learning-based Control Scheme to Deploy Modular Space Structures*, 2018 IEEE Aerospace Conference Proceedings, pp. 1-15, Big Sky, MT, USA, 2018, DOI: 10.1109/AERO.2018.8396782;

[37] R. Jenet, J. Aremberg, H. Banich et al., *CubeSat Astronomical Telescopes and Research in the 2020s* , National Acad-emies Astro 2020 Decadal Study, July 10, 2019.

[38] F. Angeletti, P. Iannelli, *Iterative Learning Control Processes On-Board Cubesats*, 5th IAA Conference on University Satellite Missions, January 28-31, Rome, 2020;

[39] D. Selva, D. Krejci, *A survey and assessment of the capabilities of CubeSats for Earth observation*, Acta Astronautica,. Vol. 74, May-June 2012, pages 50-68;

[40] W. Xiang, P. Musau, A. A. Wild et al., *Verification for Machine Learning, Autonomy, and Neural Networks Survey*, arXiv:1810.01989v1, Oct. 2018;

[41] V. C. Muller, N. Bostrom, *Future Progress in Artificial Intelligence: A Survey of Expert Opinion*, Fundamental Is-sues of Artificial Intelligence, Vol 376, Springer, Cham, pages 555-572

[42] J. Manning, D. Langerman, B. Ramesh et al., *Machine-Learning Space Applications on SmallSat Platforms with TensorFlow*, Proceedings of the 32nd AIAA/USU Annual Conference on Small Satellites, 4-9th August, Utah, USA, 2018;

[43] K. L. Moore, *Iterative Learning Control: An Overview*, Iterative Learning Control for Deterministic Systems. Ad-vances in Industrial Control. Springer, London, 1993;

[44] B. Wu, D. Wang, E. Poh, *High Precision Satellite Attitude Tracking Control via Iterative Learning Control*, Journal of Guidance Control and Dynamics 38(3):528-534, March 2015;

[45] S. A. Rawashdeh, *Attitude Analysis of Small Satellites Using Model-Based Simulation*, International Journal of Aerospace Engineering, CubeSats and Small Satellite Special Issue, Vol. 2019, April 2019;

[46] F. Angeletti, P. Gasbarri, M. Sabatini, P. Iannelli, *Distributed network of smart actuators/sensors for active micro-vibration control in large space antenna structures,* Proceedings of the 70th International Astronautical Congress (IAC), Washington D.C., USA, October 2019;

[47] H. Shou, *Microsatellite Attitude Determination and Control Subsystem Design and Implementation: Software-in-the-Loop Approach*, Mathematical Problems in Engineering, Vol. 2014, May 2014;

[48] J.L. Doe and J.Q. Public, *Passive Aerodynamic Stabilisation of Low Earth Orbit Satellite*, Spacecraft Guidance, Navigation and Control Systems, Proceedings of the 3rd ESA International Conference., 26-29 November 1996, ESTEC, Noodwijk, The Netherlands;

[49] E. Thébault, C.C Finlay, C.D., Beggan, et al., *International Geomagnetic Reference Field: the 12th generation*, Earth Planet Sp 67, 79 (2015);

[50] M. S. Farissi, S. Carletta, A. Nascetti, P. Teofilatto, *Implementation and Hardware-In-The-Loop Simulation of a Mag-netic Detumbling and Pointing Control Based on Three-Axis Magnetometer Data*, Aerospace 2019, 6(12), 133;

[51] S. Schalkowski, M. Harris, *Spacecraft Magnetic Torque*, Electronics Research

Group, NASA, SP-8018, Springfield, Virginia, March 1969;

[52] S. Arimoto, S., Kawamura, and F. Miyazaki, *Bettering Operation Of Robots By Learning*, J. Of Robotic Systems, 1:123–140, 1984.

CONCLUSIONS

The Conclusions aim at highlighting the main contributions of this research, by pointing out relevant advantages and limitations. As mentioned before, two areas of study have been investigated during the PhD activities: a primary line of research about flexible spacecraft control and a side investigation on machine learning techniques for space systems. Accordingly, this thesis has been divided into two parts. More thoroughly, *Part I* examined the design of an end-to-end architecture for performing integrated attitude and vibration control of large space structures. To this purpose, several steps have been taken: starting from the structural design of study cases representative of realistic Earth Observation missions, placement processes for smart devices (according to both closed-loop and open-loop approaches) have been carried out, leading to the implementation of different control strategies. Finally, a simulator to reproduce the dynamics of in-orbit satellites has been presented, by considering realistic models of actuators and sensors for both attitude and vibration control. In addition, *Part II* investigated a second subject of interest: the application of modern machine learning-based algorithms to current problems of space activities. In detail, as one of the major trends for the future development of spacecraft is to improve their on-board autonomy and self-awareness, attention has been paid to two topics: Failure Detection and Identification at structural level in large flexible space appendages and the improvement of tracking performance during specific attitude manoeuvre profiles.

At the beginning of the thesis, an overview on the state-of–the-art of Large Space Structures (LSSs) has allowed to identify meaningful candidates for further analyses on vibration control. In addition, by conducting a survey on current solutions for active vibration control, piezoelectric materials have been selected as the most promising devices for the considered space applications. Then, a straightforward mathematical formulation for modelling LSSs assemblies has been presented based on a mass/inertia approach. Such a method has been extended with respect to available literature to consider also the presence of active

distributed control devices on the structure. The proposed formulation can be applied to star-like-type assemblies only (which where the focus of this research); consequently, further studies are needed to expand the equations for generic types of assemblies (as chain-like, closed-loop-like, and other configurations).

The first contribution in the field of smart actuators and sensors placement was the development of a closed-loop Direct Velocity Feedback (DVF) approach via optimized poles placement. An in-cascade optimization has been proposed by comparing non-deterministic methods (namely, genetic and Reinforcement Learning algorithms) coupled with deterministic gradient-based Sequential Quadratic Programming. At first, the procedure is carried out to find the optimal gains distribution for the DVF control law while respecting some imposed constraints on minimum structural damping enhancement. Furthermore, based on the obtained results, a reduced number of actuators has been actually placed on the structure. It should be therefore noticed that the outcome of the optimization process is not limited to find optimal gains for a specific manoeuvre, but it is proposed as general pole placement to ensure proper damping in various scenarios. As a corollary result, the robustness of the optimized DVF controller to damages of actuators and significant variation in the passive structure physical properties was verified. Although the approach proved to be promising on a planar dynamic model, further research should be performed to reduce the high computational costs related to apply such a procedure to complex tri-dimensional structures.

In this scenario, an alternative open-loop placement architecture, aimed at being straightforward and computationally efficient even for tridimensional structures, is proposed. An important result is that the presented method, based on both systems norms and on modal strain energy, as opposed to heuristic algorithms, lead to obtain an easily scalable placement framework for generically shaped LSSs. Moreover, the illustrated architecture adopts two in-parallel placement procedures for cross-check and validation. The framework is indeed designed to accept data from one of the most diffused commercial finite elements tools (namely MSC Nastran); input data are then processed to select elements to be included (or excluded, due to a practical impossibility to place devices on the structure) in the placement procedure. Conversely to most methods found in literature, the possibility to include several smart device orientations on a same finite element, in a tridimensional logic, was also considered in this thesis. Finally,

the method was applied and validated on four different LSSs study cases.

Following the same design philosophy, a general framework for an integrated attitude/vibration Multi-Input/Multi-Output (MIMO) controller based on μ-synthesis theory has then been proposed. The approach complemented robust control techniques with loop-shaping methods considering also requirements on spacecraft flexible structures, so that they could be fulfilled by using distributed control solutions. As a first step, an assembly technique – stemming from the theory presented in Chapter 3 - was used to automatically build a generic star-like assembled system. Then, a multi-channel architecture was arranged to select the variables of interest to be considered in the synthesis process. Finally, the synthesis was carried out and tested both on a linear and a non-linear simulator to study the effectiveness of the solution. In this context, future work could be focussed on the definition of guidelines to select weighting functions suitable to the specific application, as well as on the implementation of an automatic framework to optimally select parameters needed to run the control synthesis tasks.

Then, a different perspective has been considered by developing a simulation environment reproducing in-orbit behaviour of flexible space structures. The tool included the full-nonlinear in-orbit dynamics of the assembled satellite as presented in Chapter 3, including orbit propagation, realistic models of distributed actuators and sensors and attitude and vibration control laws to evaluate the performance of active vibration solutions. To this purpose, an advantageous model to interface piezo-stack actuators with the host structure in Simulink environment has been proposed and tested by performing different simulations. However, external disturbances (except for gravity gradient torque) as orbital perturbations, solar pressure and thermal gradients have not been considered at the current state of the research, even though they are not expected to compromise the performance of the system.

The second area of research was presented in *Part II*. The first proposed machine learning solution was applied to Failure Detection and Identification (FDI) tasks on-board satellites, with the aim of improving their self-awareness. In detail, a supervised Deep-Learning method (based on Long Short-Term Memory Neural Networks, LSTM-NNs) has been used to classify the damage occurring at local level in one of the Study Case introduced in Chapter 5. The results highlighted the relevance of selecting a proper method for pre-processing the data and the impact of the time sequence length on the final performance of the network. The

architecture proved to be very effective and to be able to identify damages even if the faulty elements are in the same area of the structure. However, in future research, attention should be paid to consider a larger training database, even though this is not expected to relevantly affect the prediction capability of the network. Moreover, the natural next step in this this work would be the validation of the trained FDI architecture on an experimental testbed (as a planar floating platform) equipped with scaled LSSs.

Also, to improve the autonomy of space systems, in-orbit data - memorized among successive simulated orbits - have been used to counteract periodic disturbances. To this purpose, a High-Order Iterative Learning Control (HOILC) scheme has been proposed to improve the tracking performance of two EO space systems: a CubeSat and a large satellite equipped with flexible solar panels and liquid fuel. The control system has been hence used to generate an on-line supporting signal coupled with a traditional PD controller to achieve a better tracking precision before the sensing phase orbit after orbit. Indeed, the controller proved to consider the fuel sloshing, flexibility effects and environmental torques as periodic external disturbances, being able to counteract them orbit after orbit and to reduce the maximum absolute tracking error by more than one order of magnitude. However, next research should focus on testing the ILC control solution on real spacecraft telemetry, also by setting-up a laboratory experiment to simulate repetitive manoeuvre and evaluate the related system tracking performance.

APPENDIX A

A.1 FEM FORMULATION

In this appendix, details on the derivation of the mass and stiffness matrices in eq. (4.5) are reported. The test case structure (see Par. 4.2.1) has been modelled as a truss composed of ten modules (or bays) with the same geometrical and physical properties. In this thesis, a F.E. approach has been selected to derive a formulation including active piezoelectric elements embedded in the passive truss structure. Each truss is further divided into three elements to enhance the finite elements representation of the system dynamics (see Fig. A-1). In this study, the structural components are modelled as beams with three degrees of freedom for each node (see Fig. A-2).

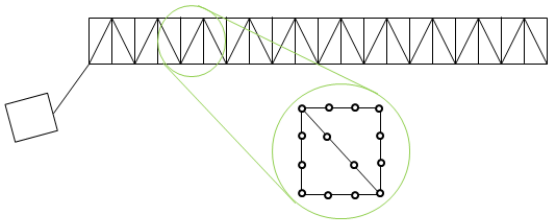

Fig. A-1: F.E. approach

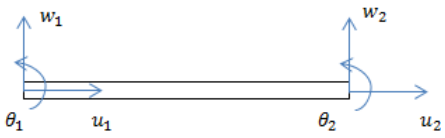

Fig. A-2: Passive beam element

The boom is made of eight beams elements. The system comprises 251 elements connected by 212 nodes, for a total of 636 degrees of freedom. The local stiffness and mass matrices of the passive two-node beam are presented as in [1]:

$$\mathbf{K}_p = \begin{bmatrix} \frac{EA}{L} & 0 & 0 & -\frac{EA}{L} & 0 & 0 \\ 0 & 12\frac{EI}{(L^3(1+\phi))} & 6L\frac{EI}{(L^3(1+\phi))} & 0 & -12\frac{EI}{(L^3(1+\phi))} & 6L\frac{EI}{(L^3(1+\phi))} \\ 0 & 6L\frac{EI}{(L^3(1+\phi))} & L^2(4+\phi)\frac{EI}{(L^3(1+\phi))} & 0 & -6L\frac{EI}{(L^3(1+\phi))} & L^2(2-\phi)\frac{EI}{(L^3(1+\phi))} \\ -\frac{EA}{L} & 0 & 0 & \frac{EA}{L} & 0 & 0 \\ 0 & -12\frac{EI}{(L^3(1+\phi))} & -6L\frac{EI}{(L^3(1+\phi))} & 0 & 12\frac{EI}{(L^3(1+\phi))} & -6L\frac{EI}{(L^3(1+\phi))} \\ 0 & 6L\frac{EI}{(L^3(1+\phi))} & L^2(2-\phi)\frac{EI}{(L^3(1+\phi))} & 0 & -6L\frac{EI}{(L^3(1+\phi))} & L^2(4+\phi)\frac{EI}{(L^3(1+\phi))} \end{bmatrix} \quad \text{A-1}$$

where E is the structure Young module, A the section area and L length of the truss. A shear-flexible Timoshenko plane beam has been chosen to model the flexible element in the stiffness local matrix. The dimensionless properties that characterize relative shear rigidity and rotary inertia are defined as

$$\phi = \frac{12EI}{GA_s L^2} \qquad G = E/2(1+\nu) \qquad A_s = 10A(1+\nu)/(12+11\nu) \tag{A-2}$$

$$\underline{\underline{M}} = \begin{bmatrix} \frac{5}{12}\rho AL & 0 & 0 & \frac{1}{12}\rho AL & 0 & 0 \\ 0 & \frac{156}{420}\rho AL & \frac{22}{420}\rho AL^2 & 0 & \frac{54}{420}\rho AL & -\frac{13}{420}\rho AL^2 \\ 0 & \frac{22}{420}\rho AL^2 & \frac{4}{420}\rho AL^3 & 0 & \frac{13}{420}\rho AL^2 & -\frac{3}{420}\rho AL^3 \\ \frac{1}{12}\rho AL & 0 & 0 & \frac{5}{12}\rho AL & 0 & 0 \\ 0 & \frac{54}{420}\rho AL & \frac{13}{420}\rho AL^2 & 0 & \frac{156}{420}\rho AL & -\frac{22}{420}\rho AL^2 \\ 0 & -\frac{13}{420}\rho AL^2 & -\frac{3}{420}\rho AL^3 & 0 & -\frac{22}{420}\rho AL^2 & \frac{4}{420}\rho AL^3 \end{bmatrix} \tag{A-3}$$

with ρ the material density and ν the Poisson ratio. The local matrices are then assembled in global ones by using a mapping matrix describing the interconnections and orientation of nodes and trusses in the plane. The complete stiffness and mass matrices, as well as the eigenvalue and modes originated from the assembled system, have been computed by the means of a MATLAB FEM code and then validated by comparison with a commercial software (i.e. MSC Nastran).

A.1.1 Active Finite Elements

To effectively counteract undesired elastic vibrations on both boom and antenna structures, a set of piezo-electric devices has been embedded within the beams. The mass associated to the active devices is not neglected in this study. The device action is meant to be applied only to the axial beam direction, due to the reticular nature of the structure.

As for that, the shape functions for an axial element can be formulated as

$$\Gamma_X = \begin{bmatrix} l - x/L & x/L \end{bmatrix} \tag{A-4}$$

$$B_X = \begin{bmatrix} \frac{\delta \Gamma_{X1}}{\delta X} & \frac{\delta \Gamma_{X2}}{\delta X} \end{bmatrix} = \begin{bmatrix} -\frac{1}{L} & \frac{1}{L} \end{bmatrix} \tag{A-5}$$

The electric field and relative shape function derivative can be written as

$$E_F = -\phi / L \tag{A-6}$$

$$B_\phi = -1 / L \tag{A-7}$$

Therefore, the aforementioned matrices from FEM theory can be written as

$$\begin{aligned} \boldsymbol{K}^e_{U\psi} &= \int_0^L A\, c^E \begin{bmatrix} -1/L \\ 1/L \end{bmatrix} \begin{bmatrix} -1/L & 1/L \end{bmatrix} dL = \\ &= \frac{A\, c^E}{L} \begin{bmatrix} 1 & -1 \\ -1 & 1 \end{bmatrix} \end{aligned} \tag{A-8}$$

$$\boldsymbol{K}^e_{U\psi} = \int_0^L A\, e \begin{bmatrix} -1/L \\ 1/L \end{bmatrix} \begin{bmatrix} 1/L \end{bmatrix} dL = \frac{A\, e}{L} \begin{bmatrix} -1 \\ 1 \end{bmatrix} \tag{A-9}$$

$$\boldsymbol{K}^e_{\psi\psi} = -\int_0^L A\, \varepsilon^S \begin{bmatrix} \frac{1}{L} \end{bmatrix} \begin{bmatrix} \frac{1}{L} \end{bmatrix} dL = \frac{A\, n\, \varepsilon^S}{L} \tag{A-10}$$

with n number of the layers of the piezo-stack actuator.

The lateral parts stiffness can be simply written as

$$K_1 = \frac{EA}{L_1} \tag{A-11}$$

Then, it is possible to determine the equivalent stiffness parameter to be used in the finite element formulation [2][3]. We can imagine to divide the adaptive-truss in three parts: a central active and two symmetrical passive parts.

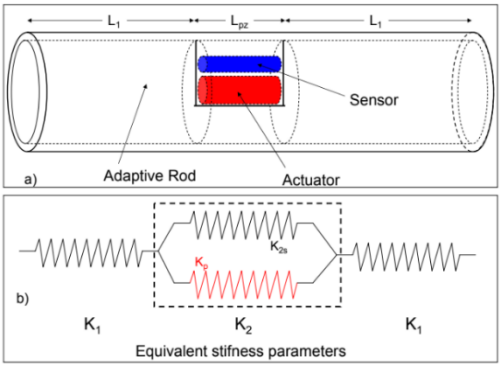

Fig. A-3: F.E. approach

The parts are considered as rigidly connected between them. The central part length is equal to the dimension of the piezo devices, while the lateral ones can vary accordingly to the selected structure. In this case, they have equal lengths. Concerning the central active part, an equivalent stiffness coefficient can be defined by considering the stiffness of the host structure (the truss itself) in parallel with the stiffness of the active device embedded in it.

In this case, we can write

$$K_2 = K_{2a} + K_{pz} = \frac{E(A - A_{pz})}{L_{pz}} + \frac{E_{pz} A_{pz}}{L_{pz}} \qquad \text{A-12}$$

The equivalent stiffness parameter for the whole element is finally defined as the series of three "elastic springs"

$$K_{eq} = \frac{K_1 K_2}{2K_2 + K_1} \qquad \text{A-13}$$

Some considerations in regard to the matrices $\boldsymbol{K}_{UU}$, $\boldsymbol{K}_{U\psi}$ and $\boldsymbol{K}_{\psi\psi}$ are therefore required to take the element equivalent stiffness into account and considering that the nodal potentials are applied exclusively to the central part of the FEM element. Indeed, we can write

$$\bar{\boldsymbol{K}}^e_{UU} = K_{eq} \begin{bmatrix} 1 & -1 \\ -1 & 1 \end{bmatrix} \qquad \text{A-14}$$

Bearing in mind the piezo material is only inside the central part, the piezo-coupling coefficient can be treated as a function depending on the truss coordinate x. Integrating, we have

$$\bar{\boldsymbol{K}}^e_{U\psi} = \int_0^L A\, e(x) \begin{bmatrix} -1/L \\ 1/L \end{bmatrix} \begin{bmatrix} 1/L_{pz} \end{bmatrix} dx = \frac{Ane}{L_{pz}} \begin{bmatrix} -1 \\ 1 \end{bmatrix} \qquad \text{A-15}$$

Considering that the voltage is actually applied to central active part of the element, we should integrate exclusively along the piezo length

$$\bar{\boldsymbol{K}}^e_{\psi\psi} = -\int_0^{L_{pz}} A\, \varepsilon^S \begin{bmatrix} \frac{1}{L_{pz}} \end{bmatrix} \begin{bmatrix} \frac{1}{L_{pz}} \end{bmatrix} dx = \frac{A\, n\, \varepsilon^S}{L_{pz}} \qquad \text{A-16}$$

That means that according to $E_F = -V/t$ with a smaller length and equal electric potential a higher electric field occurs inside the piezo than if applied to the very length of the total element.

The stiffness element used for the FEM matrices assembling is

$$\boldsymbol{K}_A = \begin{bmatrix} K_{eq} & 0 & 0 & -K_{eq} & 0 & 0 \\ 0 & 12\frac{EI}{(L^3(1+\phi))} & 6L\frac{EI}{(L^3(1+\phi))} & 0 & -12\frac{EI}{(L^3(1+\phi))} & 6L\frac{EI}{(L^3(1+\phi))} \\ 0 & 6L\frac{EI}{(L^3(1+\phi))} & L^2(4+\phi)\frac{EI}{(L^3(1+\phi))} & 0 & -6L\frac{EI}{(L^3(1+\phi))} & L^2(2-\phi)\frac{EI}{(L^3(1+\phi))} \\ -K_{eq} & 0 & 0 & K_{eq} & 0 & 0 \\ 0 & -12\frac{EI}{(L^3(1+\phi))} & -6L\frac{EI}{(L^3(1+\phi))} & 0 & 12\frac{EI}{(L^3(1+\phi))} & -6L\frac{EI}{(L^3(1+\phi))} \\ 0 & 6L\frac{EI}{(L^3(1+\phi))} & L^2(2-\phi)\frac{EI}{(L^3(1+\phi))} & 0 & -6L\frac{EI}{(L^3(1+\phi))} & L^2(4+\phi)\frac{EI}{(L^3(1+\phi))} \end{bmatrix} \quad \text{A-17}$$

For the parameter (ρAl) that exists in the mass matrix, a simple "equivalent" mean value of the adaptive truss (both piezo-device and host structure) is considered.

Finally, passive and active mass and stiffness matrices are assembled by adopting standard mapping techniques, connecting adjacent nodes. The final stiffness and mass matrices of the flexible substructure $\boldsymbol{K}_{FLEX}$ and $\boldsymbol{M}_{FLEX}$ comprehending the mechanical properties of both passive and active beams have been computed by the means of a MATLAB FEM code and then validated by comparison with a commercial software (MSC Nastran).

REFERENCES

[1] O. Zienkiewicz, R.t Taylor, J.Z. Zhu, *The Finite Element Method: its Basis and Fundamentals (seventh ed.)*, Butterworth-Heinemann, 2013;

[2] F. di Scioscio, P. Gasbarri, C. Marianetti, and C. Toglia, *Control of Vibrations of the International Space Station with Piezoelectric Actuators*, in Proceedings of the International Astronautical Federation, Fukoka, Japan, 2005, vol. 6, pp. 16–21.

[3] F. Angeletti, P. Gasbarri, M. Sabatini, *Optimal design and robust analysis of a net of active devices for micro-vibration control of an on-orbit large space antenna*, Acta Astronautica, Vol. 164, Nov. 2019, pp. 241-253;

ACKNOWLEDGEMENTS

It is my sincere pleasure to acknowledge the roles of several individuals who were beneficial to this research journey. To begin with, I would like to give proper credit to those who supported me from a technical point of view.

First of all, I would like to thank my supervisor, Prof. Paolo Gasbarri, for his expert guide and advice throughout these years. As a matter of fact, I benefited from his teachings ad trust well before this dissertation, through all the milestones of my academic career, from the Bachelor's to the Master's theses and, eventually, to the PhD studies. After so much time, I can state he has been much more than a invaluable asset to the development of my research activities. He has always been a person with whom to share my deep passion for the space field, and a never-ending source of motivation. His daily enthusiasm, thoughtfulness and high commitment in all his activities were fundamental to create that supportive and inspiring research atmosphere I experienced during my PhD journey.

Then, I would like to express my sincere gratitude to Prof. Fabio Celani and Prof. Giovanni B. Palmerini and for their insightful suggestions, opinions and discussions of these years. Their fruitful engagement helped me further shape and tailor my PhD project. Moreover, I would like to thank Dr. Marco Sabatini, not only for his valuable technical advice, but also for constantly brightening up the days at the *GNLab*, with a special mention to his punctual and very ironic comments to manuscripts and relations. My appreciation also extends to the people I shared this journey with, my PhD colleagues. In particular, it has been a honour to collaborate with Angelo, Paolo and Renato on so many challenging research topics, and to share with them pleasant moments during conferences and trips. I wish you all the best that competent and brilliant people like you deserve.

Since part of this thesis work has been carried out in the framework of a research study funded by the European Space Agency (ESA), in collaboration with Thales Alenia Space France (TASF), I had the opportunity to be a visiting researcher at TASF's GNC Department in Cannes. There, it has been a sincere pleasure to be supervised by Dr. José Alvaro Perez Gonzalez. I wish to thank him for his warm welcome, his technical advice and the precious support he offered me, especially when my visit was interrupted before time due to the pandemic outbreak in Europe. Likewise, I am grateful to have had the chance to work along with Dr. Nicolas Ellero. I would like to thank him for his useful teachings and very

agreeable chats. I would also like to mention the friendly people I met there, such as Elisa, Davide, Francesca, Mario, Vincent and Aurelian, thank you for the amusing lunch time together. I will always treasure those weeks as a remarkable formative experience.

I also had great pleasure of cooperating with Prof. Massimo Panella and Dr. Antonello Rosato (DIET, La Sapienza) to implement Deep Learning algorithms on-board modern satellites. I sincerely appreciate the enthusiasm they put in applying their knowledge to a new field, alongside their availability and invaluable technical advice.

Moreover, I gratefully acknowledge the people I met during the conferences, workshops and seminars I attended in these three years; every exchange of ideas, debate and cooperation contributed to my professional and personal growth. Among them, I desire to mention the skilled group of people I worked with at the *ESA Academy Concurrent Engineering Workshop* in 2018. To date, they represent to me the embodiment of those values of trust and international cooperation for which, among other things, I fondly love the space sector.

Getting through my dissertation required more than academic support, and I have many other people to thank. To begin with, I would like to thank the *Italian Association of Aeronautics and Astronautics (AIDAA)*, for which I have been Board Member as Student Representative for about two years, for providing me with constant opportunities for growth. Then, I would love to mention the impact that the international association Zonta International had on the quality of my research after being awarded with an Amelia Earhart Fellowship (AEF). Now, as a member of the *Zonta e-club of Italy*, surrounded by such skilled, proactive and determined women, I wish I can repay at least in part what I received. Thanks to Fernanda, Daniela, Lucia, Melissa, Donatella, Maria Vittoria and all the others for being such an example to follow. Finally, I would like to thank the amazing women of the *Rome Local Group of Women in Aerospace Europe (WIA-E)*. During my PhD journey, they have been at my side, encouraging and galvanizing me, and providing me with the tools I needed to be more assertive. Thank you, Annamaria and Cristina, for being such a bright role models, and for your wise advice and life lessons. Thanks to all my friends of the Committee, Alice, Aloisia, Alessia, Marzia, Eleonora, Maria Giulia, Anastasia, Maria, Laura, Fabiana and all the others, for showing me what amazing results we can achieve by working together, step by step. I really have to say: you all are my #InspirationalWomen!

In this regards, I wish to spend some more words on Alice, my university friend, educational projects companion and one of the most brilliant people I know. Thank you for having inspired me, day after day, with your determination, curiosity and willingness to take up new challenges. On this note, I cannot help but thanking all the other my friends from the amazing STRATONAV team: Paolo, Andrea, Federico and Lorenzo. Thank you for our amazing board games nights and the unforgettable moments we spent around the world. Some special words of gratitude go to all my other friends who have always been a major source of support. Among them, thank you Gioia, Federica, Alessandra and Stefania P. for your energy, kindness and empathy. Thank you Francesco C. for such stimulating conversations and debates. Thank you Tommaso for our delirious conversations and funny comments about TV series.

To my legen-dary friends from *Zazio!!*, Stefania, Daniele, Luca e Francesco, you should know that your support and encouragement is worth more than I can express on paper. You made me always believe in myself and have always given me the necessary rest from my hectic research life (especially during our memorable Black Friday nights!). Even though this last year we were mostly apart, you never made me miss your presence. In this regard, I would also like to add a special thank to Stefania, my best friend, who always managed to make me feel special and with whom I lived some of the best moments in my life. Thank you for listening, offering me advice, and supporting me through all these years, from the days we bonded on our school bus. Thank you for always being there for me!

Above ground, I am indebt to all my relatives: my uncles (especially my dear uncle Luciano), my cousins and my grandparents. You were the first supporting community that encouraged me nourish my passion for learning. A very special word of thanks goes to my parents, Marina e Mauro, for always showing how proud they are of me. Thank you for your efforts for educating and preparing me to my future. Your continuous and unparalleled love, unconditional trust and endless patience accompanied me throughout my journey. The last word goes for my brother, Stefano, who always has been my best friend and greatest companion of adventures, and who gave me his unconditional love. Having you in my life is what fills my heart with gratitude the most. Thank you for always being my Miguel. This thesis is dedicated to you.

LIST OF PUBLICATIONS

In this section, the list of the publications produced during the PhD research activities is reported, as well as the related impact factor.

Journal Papers:

- Angeletti, Iannelli, Gasbarri, Sabatini, *End-to-end design of a robust attitude control and vibration suppression system for large space smart structures,* Acta Astronautica, avilable online April 2021;
- Marzioli, Frezza, Curianò, Pellegrino, Gianfermo, Angeletti et al., *Experimental validation of VOR (VHF Omni Range) navigation system for stratospheric flight*, Acta Astronautica, Vol. 178, January 2021, pp. 423-431;
- Angeletti, Gasbarri, Sabatini, Iannelli, *Design and performance assessment of a distributed vibration suppression system of a large flexible antenna during attitude manoeuvres*, Acta Astronatica, Vol. 176, November 2020, Pages 542-557;
- Angeletti, Stolfi, Gasbarri, *Learning-based control of a spacecraft with sloshing propellant*, Aerotecnica Missili & Spazio, Volume 99, pages 33–42(2020);
- Stolfi, Angeletti, Gasbarri, Panella, *A Deep-Learning strategy for on-orbit servicing via space robotic manipulator, Aerotecnica Missili & Spazio, Volume 98, pages 273–282(2019);*
- Angeletti, Gasbarri, Sabatini, *Optimal Design and Robust Analysis of a Net of Active Devices for Micro-vibration Control of an on-orbit Large Space Antenna*, Acta Astronautica 164 (2019), 241-253, August 2019;

Conference Papers:

- Iannelli, Angeletti, Gasbarri, *Model-based FDI architecture applied to an Active Vibration Control system on a flexible spacecraft*, IAA/AAS SciTech Forum 2020 Cyber Edition, December 8-10, 2020;
- Angeletti, Iannelli, Gasbarri, Sabatini, *Control-oriented modelling of an active suppression system for large space smart structures*, 71st International Astronautical Congress (IAC), Cyber Edition, October 12-14, 2020;
- Iannelli, Angeletti, Gasbarri, Panella, Rosato, *Deep Learning for local damage identification in large space structures via sensor-measured time responses*, 71st

International Astronautical Congress (IAC), Cyber Edition, October 12-14, 2020;

- Palmerini, Angeletti, Iannelli, *Multiple Model Filtering for Failure Identification in Large Space Structures*, Lecture Notes in Civil Engineering, 2021, 128, pp. 171–181;
- Angeletti, Iannelli, *Iterative Learning Control Processes On-Board Cubesats, 5th IAA Conference on University Satellite Missions*, January 28-31, Rome, 2020;
- Angeletti, Latini, Willett et al., *Insight into the benefits of ESA Education activities: an overview of the next European space-related workforce*, 3rd Symposium on Space Educational Activities (SSEA), September 16-18, Leicester, UK, 2019;
- Angeletti, Stolfi, Gasbarri, *Learning-based control of a spacecraft with sloshing propellant, XXV AIDAA International Congress,* September 9-12, Rome, Italy, 2019;
- Angeletti, Gasbarri, Sabatini, Iannelli, *Distributed network of smart actuators/sensors for active micro-vibration control in large space antenna structures*, IAC-19, IAC-19-C2.3.6x50004, October 21-25, Washington DC, USA, 2019.
- Angeletti, Gasbarri, *Uncertainty Impact on Micro-vibration Control of an Orbiting Large Adaptive Space Structure*, IAA SciTech Forum 2018, Conference on Space Structures and Materials, November 13-15, Mosca, Russia, 2018;
- Angeletti, Gasbarri, Sabatini, *Optimal Design of a Net of Adaptive Structures for Micro-vibration Control in Large Space Mesh Reflectors*, IAC-18.C2.3.9.x43294;
- Angeletti, Gasbarri, Palmerini, Sabatini, *Learning-based Control Scheme to Deploy Modular Space Structures*, 2018 IEEE Aerospace Conference Proceedings, pp. 1-15, Big Sky, MT, USA, 2018, DOI: 10.1109/AERO.2018.8396782;

Impact factor h-index (Scopus): 3 (accessed 20th April 2021)

Ph.D. Thesis – University of Rome La Sapienza

Author's email: federica.angeletti.9@gmail.com